Dynamic modelling and control of a solid oxide reversible cell for power disturbance rejection in a mixed power grid

B.P.E. Numan

Master of Science Thesis

TU Delft Delft University of Technology

Dynamic modelling and control of a solid oxide reversible cell for power disturbance rejection in a mixed power grid

Master of Science Thesis

For the degrees of Master of Science in Mechanical Engineering at Delft University of Technology and Master of Science in Systems and Control at Delft University of Technology

B.P.E. Numan

March 2, 2020

Faculty of Mechanical, Maritime and Materials Engineering (3mE) · Delft University of Technology

Delft University of Technology
Department of
Process and Energy (P&E)
and department of
Delft Center for Systems and Control (dcsc)

The undersigned hereby certify that they have read and recommend to the Faculty of Mechanical, Maritime and Materials Engineering (3mE) for acceptance a thesis entitled

Dynamic modelling and control of a solid oxide reversible cell for power disturbance rejection in a mixed power grid

by

B.P.E. Numan

in partial fulfillment of the requirements for the degree of

Master of Science Mechanical Engineering

and the degree of

Master of Science Systems and Control

Dated: March 2, 2020

Supervisor(s):

Dr S. Hajimolana

Prof. P.V. Aravind

Dr E. Steur

Reader(s):

Dr A.J.J. van den Boom

Abstract

The integration of variable renewable energy sources (RESs) in the electrical power grid leads to larger and faster variations in the power demanded from controllable power sources. This is a problem, because flexibility of (base load) power plants is limited. Solid oxide reversible cells (SORCs) can be used as load-shifting devices to reduce these power variations by converting electricity to hydrogen (solid oxide electrolysis cell (SOEC) mode) when power demand is low and converting hydrogen to electricity (solid oxide fuel cell (SOFC) mode) when power demand is high. However, the introduction of SORCs is challenging. It is a promising long-term energy storage technology, but it is in its development stage. Apart from prohibitive costs, challenges also lie within durability and efficiency under dynamic operation. Development of control strategies is essential for maintaining optimal operating conditions. Therefore, this study researches the ability of SORCs to operate in a mixed power grid by developing an SORC model and power disturbance rejection controller which ensures safe operating conditions.

A dynamic 0D SORC model was developed. It describes a single cell at the center of a large stack of identical cells, which makes it representative for large-scale SORCs. The model is based on SOFC models and uses the current density to indicate the operating mode of the SORC. The benefit of this approach is that one continuous model describes both operating modes. Validation of the model is based on comparison of static cell voltage-current density curves from literature and from a small stack experiment. Open-loop analysis of the model showed that the system is stable and can be decoupled. It also showed that development of gain-scheduling controllers was necessary to handle the exothermic, hydrogen consuming SOFC mode and endothermic, hydrogen producing SOEC mode. This motivated the design of gain-scheduling $\mathcal{H}_\infty$ tuned proportional-integral (PI) controller, which were used to control the positive electrode, electrolyte, negative electrode (PEN) structure temperature and fuel channel composition by manipulating the air and fuel flow rate, respectively. Two methods were compared for specifying the performance of the controller. The first method was based on the desired closed-loop bandwidths and the second method was based on the bandwidth of the disturbance. The first method was superior to the second method, because the obtainable closed-loop bandwidths are faster than the bandwidth of the disturbance.

This study shows that gain-scheduling PI controllers allow SORCs to be used for load shifting applications in a mixed power grid. Further research is needed to validate the dynamics of the model and to identify the influence of balance of plant (BOP) dynamics on controller performance.

Table of Contents

List of Figures

List of Tables

Preface

This master thesis is the final deliverable of my double degree Mechanical Engineering and Systems & Control at Delft University of Technology. The idea for this thesis came during a meeting with Yashar Hajimolana where he asked me if I was interested in the novel field of control for solid oxide reversible cells. I realized that this was a perfect opportunity to combine both of my degrees and accepted the offer.

I would like to thank my supervisors Erik Steur, Yashar Hajimolana, and Aravind Purushothaman Vellayani for their advice, help, patience and feedback throughout the project and the writing of this thesis.

Delft, University of Technology
March 2, 2020

Bart Numan

Chapter 1

Introduction

Renewable energy is getting a lot of attention as the world is in a transition from finite energy resources to renewable energy sources (RESs). The goal of this transition is to reduce greenhouse gas emissions and keep global warming within acceptable limits. For example, the European Union has set the goal to reduce its emissions by 80 to 95 % in 2050 compared to 1990 [1]. Looking at the energy sector, the main goal is to phase-out coal-fired power plants. The void that is left is filled with RESs and natural gas-fired plants. RESs mainly considers wind and solar energy, which comes at the price of being variable energy sources. This means that there will be a time-based imbalance between renewable power production and consumption, if no measures are taken. Time-based imbalance or mismatch refers to (renewable) power production not matching the power demand from the grid at a certain time. It could be that the production is higher or lower than the power demand. An example of time-based imbalance is shown in Figure 1-1 where renewable energy and grid demand show a severe mismatch. This mismatch is the result of the intermittent nature of wind and solar energy.

In the current power gird, time-based power imbalances are not as intense as in Figure 1-1, because power production by variable RESs does not yet exceed power consumption. Variations arising from integration of RESs are taken care of by natural gas-fired plants in the current grid, because their power production can be adjusted quickly. However, this is a short-term solution, as it results in emission reductions, but still uses a finite energy source. Furthermore, gas-fired power plants are not able to deal with overproduction by RESs, because they are not able to take power from the grid and store it for later use. Therefore, it is important to look into non-finite options that are able to take care of the power imbalance that arises due to the integration of RESs.

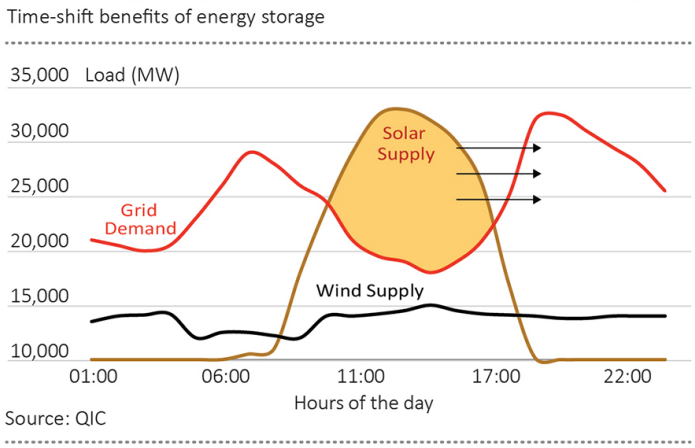

Figure 1-1: Possible power grid situation where there is a clear mismatch between renewable energy production and grid demand. Taken from [2].

1-1 Problem description: power imbalance due to the introduction of RESs

The energy transition is not only about energy sources, but also about balancing power supply and demand. The integration of RESs gives several challenges. Short-term challenges, such as power quality concerns, and long-term challenges, such as daily imbalances and seasonality due to the variable nature of solar and wind energy.

It is important to notice that these problems are not problems of the far future, but are also relevant during the energy transition itself. The integration of RESs results in steeper net load curves and even the risk of oversupply [3]. Therefore, flexible solutions are required to keep a reliable energy grid. One of these measures is storage of energy by converting electricity in a different form of energy.

1-2 SORC, an energy storage solution

The power imbalance problem does not have one solution. Some storage systems are suited for short term storage, such as flywheels or supercapacitors, while long term storage requires solutions such as pumped hydro or fuel cells and electrolysers. The basis of fuel cells and electrolysers is very similar, which gives rise to the question if it would be possible to combine them into one system, known as a reversible cell. A reversible cell has the potential of smaller space occupation and does not require to keep inactive systems at (high) temperature for a long time, when compared to separate fuel cells and electrolysers. However, the control of such a reversible cell is more challenging, because it should ensure suitable operating conditions in both modes and during mode switching from electrolyser to fuel cell mode, and vice versa.

One of the promising reversible cell technologies for energy storage is known as solid oxide reversible cell (SORC). An illustration of its operating principle is shown in Figure 1-2. In fuel cell mode, power is generated by converting hydrogen and oxygen in water. The opposite happens in electrolyser mode, where water is split in hydrogen and oxygen by providing

power to the cell. Consequently, SORCs have the ability to decouple energy production and consumption, which makes it possible to design renewable grid predominantly based on variable RESs.

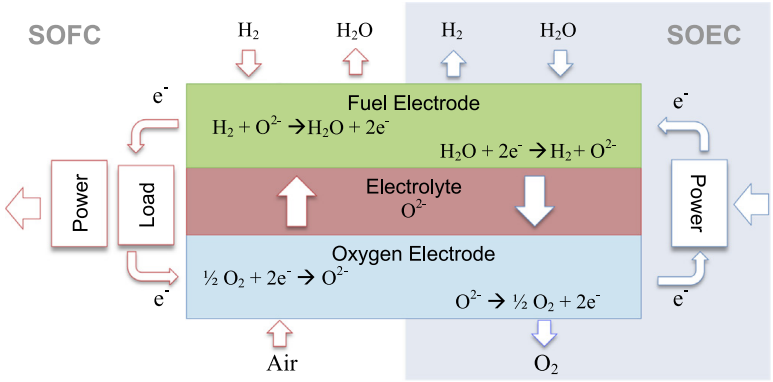

Figure 1-2: General operating principle of an SORC. Left: power generation in SOFC mode by converting hydrogen and oxygen in water. Right: power consumption in SOEC mode by converting water in hydrogen and oxygen. Adapted from [4].

1-3 Research objective

During the energy transition, SORCs could assist in gradually phasing out finite energy sources and hopefully be an alternative for natural gas-fired power plants. This requires SORCs to operate in a dynamic environment, under varying loads. To make this possible, the SORC should be kept at certain operating conditions. For example, the temperature should be kept within a certain range to ensure good performance, while not damaging the cell. Using high flow rates to prevent high temperature is not preferred, as it would result in low efficiencies. Therefore, control is needed to keep the system from breaking down, while ensuring acceptable efficiency.

The goal of this thesis is to design a power disturbance rejection controller for a large-scale SORC for daily power stabilization applications in a mixed power grid. This goal is reached by developing a dynamic model and a control strategy for a large-scale SORC. The control strategy should ensure safe operating conditions under varying load demands. Daily grid power stabilization indicates the ability to neutralize supply and demand imbalances over a day that are the result of integration of RESs in the power grid. A mixed energy grid is an energy grid consisting of both RESs and finite energy sources. An example of a mixed energy grid is shown in Figure 1-3. In this case, SORCs act as an alternative to different load following power plants, such as gas-fired power plants. A mixed energy grid is considered, because it is close to the current situation of the energy transition and shows that early introduction of SORCs is possible, as long as the technology advances enough to produce large-scale systems. Also, the possibility to use SORCs for daily grid balancing ensures its ability to solve even longer-term grid imbalances, such as seasonal variations.

To be able to meet the research objective, the following goals have to be met.

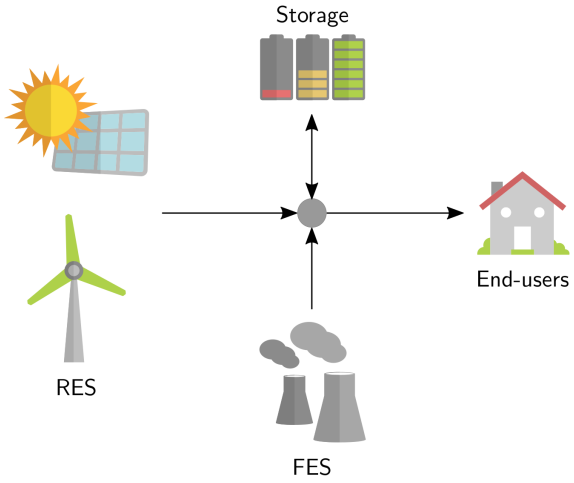

Figure 1-3: Example of a mixed power grid. Arrows indicate direction of power transfer. RES: renewable energy source, FES: finite energy source. Adapted from Freepik.com.

1. Develop a dynamic (single-cell) SORC model that accurately represents a large-scale SORC. Large-scale indicates power generation and consumption of 1 MW or more.
2. Validate the dynamic model with experimental data.
3. Set up a control goal that reflects a possible operating case for an SORC connected to a mixed power grid.
4. Analyse the open-loop system to determine its stability and controllability.
5. Design a controller that is able to guarantee safe operating conditions of the SORC. The following operating conditions are considered to be safe:
   (a) positive electrode, electrolyte, negative electrode (PEN) structure temperature: $700\,^{\circ}\text{C} < T_{PEN} < 900\,^{\circ}\text{C}$;
   (b) oxygen fraction in air channel: $\chi_{air,O_2} < 0.5$;
   (c) hydrogen fraction in fuel channel: $0.1 < \chi_{fuel,H_2} < 0.9$.

1-4 Scope of thesis

To interpret the results in this report, it is important to know the scope of this thesis. This section gives an overview of important limitations of the study.

This project only considers a theoretical study of a large-scale system, since there is no experimental setup available. Some experimental data from small-scale setups is used for validation of some parts of the model, but these setups do not represent all parts of the model.

Only the SORC itself is considered. It should be noted that an SORC alone is not enough and that auxiliary components are needed to run a system. These components are known as

the balance of plant (BOP) and are necessary to ensure suitable operating conditions of the cells. Among others, this includes heat exchangers to heat gas flows, compressors and valves to control flow rates and fuel compositions, and a condenser to be able separate water and hydrogen.

It is assumed that the SORC operates in the Dutch power grid. Therefore, power data is obtained for the Netherlands. This includes power consumption data from TenneT [5] and renewable power production from Energieopwek.nl [6]. The time period considered is January 2017 up to and including October 2019.

This study is focused on whether it is possible to use an SORC system for daily grid stabilization. It does not consider durability, cell design, costs, degradation, and efficiency. Durability and efficiency are included to some extent by the choice of reference signals for compositions and temperature. Cell design, cost and degradation effects are ignored completely. Also, possible logistical problems are not taken into account, such as storage sizing. Nonidealities, such as possible flow delays, are ignored.

1-5 Report structure

This thesis is structured in the following way. Chapter 2 presents a literature review. The first part examines the need for energy storage and different solutions, each with their own area of application. Next, modelling efforts in literature are examined. This chapter ends with an overview of literature related to control of SORCs. Next, chapter 3 describes the dynamic model of the SORC. This includes material and energy balances, and an electrochemical model. Validation of the model is discussed in chapter 4. This covers a comparison with a paper and estimation of electrochemical model parameters based on experimental data from a small stack. Further motivation of control and formulation of the disturbance rejection problem is discussed in chapter 5. Open-loop analysis of the system is presented in chapter 6. This includes examination of the stability and controllability of the SORC. Controller design is covered in chapter 7. This includes selection and performance specification of a gain-scheduling proportional-integral (PI) controller. This chapter includes simulations of the controlled SORC based on realistic power signals. The last two chapters, chapter 8 and chapter 9, discuss the conclusions and recommendations for further research.

Chapter 2

Literature Review

A literature review was conducted to get an overview of what research has been done related to modelling and control of SORCs. The goal is to get an overview of this field of study. During the review it was found that papers considering SORCs are limited. Since SORCs are a combination of an solid oxide fuel cell (SOFC) and solid oxide electrolysis cell (SOEC), literature for both was also consulted.

Before going into SORC literature, the first part of this review focusses on the more general problem of energy storage, why it is needed and what technologies are available. Next, an overview of recent modelling endeavours is given. This section considers SORC modelling, as well as SOEC and SOFC modelling, since an SORC is a combination of an SOFC and SOEC in one device. Next, a brief overview of model validation is given. After that, control of SORCs and SOFCs is discussed. SOFC control was included, because literature on control of SORCs is limited.

2-1 Energy storage

Energy storage systems are systems that are used to store energy in some form in order to be able to use it at a later time. This section gives an overview of different energy storage systems. It starts with a description of a motivation for energy storage, which is the necessity to prevent imbalances in power demand and production and to reduce peak powers, which are serious problems coming from the integration of variable RESs. After this, three possible solutions are described which could be used to counteract the problem of peak loads. The section ends with an overview of different energy storage systems, their advantages and disadvantages.

2-1-1 Peak loads, a problematic development

Literature agrees unanimously that a problem is emerging in the electricity grid. This problem is known as the occurrence of peak loads, which are short periods of time when power

consumption is high compared to the average consumption. This is problematic as it could result in power failures, higher costs due to the use of less efficient peak load stations, and unnecessary overdimensioning of power generation plants [7], [8]. Overdimensioning is the result of sizing based on these peak powers, which can be twice the power demand during off-peak periods.

The sources of these peak load are an increase in electrical energy consumption and the integration of RESs [7], [9]. The introduction of RESs does not increase the absolute peak power, but reduces the load factor, which is the ratio of the average power and the peak power [7]. This leads to a phenomenon known as the duck curve [3] where a significant dip occurs in power demanded from non-variable power plants, primarily due to the integration of solar energy. In other words, the most prominent RES solutions are not able to respond to changes in demands and their power production results in increased variations in power demand over a day [10], [11]. For example, in 2018 in the Netherlands, 73 % of renewable energy was obtained from variable RESs [12]. These increased variations are disadvantageous, as they increase the probability of power failures due to a possible imbalance between power supply and demand [11]. Furthermore, the integration of RESs results in power quality problems and seasonal fluctuations [10]. Power quality is related to the voltage and frequency of the electricity which are required to stay within certain limits and is primarily a short term problem , while seasonality is a long term problem. Nonetheless, integration of RESs is considered necessary [11] in order to reduce the use of fossil fuels and thereby the environmental impact of energy generation. In conclusion, power balancing is becoming a major concern.

2-1-2 Options for counteracting peak loads

From subsection 2-1-1, it is clear that power balancing is becoming more and more of a problem due to the integration of RESs, as unfavourable variations are introduced. Broadly speaking, there are three options when it comes to coping with this problem. These are meeting the peak loads by peak load power plants, demand side management, and energy storage. Demand side management and energy storage are peak shaving methods, which are methods in which the load curve of (base load) power generators is smoothed by reducing peak power and shifting demand to off-peak moments [7], [10]. The most extreme form of peak shaving is known as load levelling [13], in which the power generation from base load stations is kept as constant as possible. This is only possible with energy storage.

Meeting peak loads

The traditional way to deal with peak load is to use peak power plants, such as gas power plants to provide peak powers [7], [11]. This is an expensive solution, because these plants will only be used for shorts periods of times and have high maintenance costs. This makes it an inefficient solution.

Demand side management

Demand side manage is about methods to encourage end-users to shift the peak loads to off-peak periods. One way to do this is by variable pricing of energy [7]. In the ideal case,

end-users shift their power usage, because it is cheaper to consume electricity during cheap off-peak periods. The main problem with this approach is that consumers might not be willing to shift their activities.

Energy storage

Energy storage is regarded as the method with the biggest potential for peak shaving [7]. Storage systems are charged during off-peak periods and discharged during peak powers. This should result in a more stable power output, which would make it possible to obtain grids with stable and reliable RES integration [9]. Short term storage can be used to improve power quality [7], [10], [11], while long term storage can be used to smooth the power demand [8]. As a result, it is possible to run power generators at their most efficient operating points [10], [11]. Furthermore, it should be possible to reduce the cost of expensive transmission and distribution upgrades [7], [9], and should it be possible to design new power plant based on average power demand instead of peak power [7], [8], [13]. Even though energy storage is promising, most technologies are not yet commercialized, as there are still issues that require further research [7], [11]. Among others, these include optimum operation for high efficiency, sizing and economic feasibility of different energy storage solutions .

2-1-3 Energy storage technologies

Multiple technologies are researched at the moment. These technologies can be divided in five different groups based on their operating principles: mechanical, thermal, electrical, electrochemical, and chemical energy storage. Figure 2-1 gives an overview of these groups with some examples. An indication of the requirements of each application area and the position different energy storage solutions take within this plane are shown in Figure 2-2.

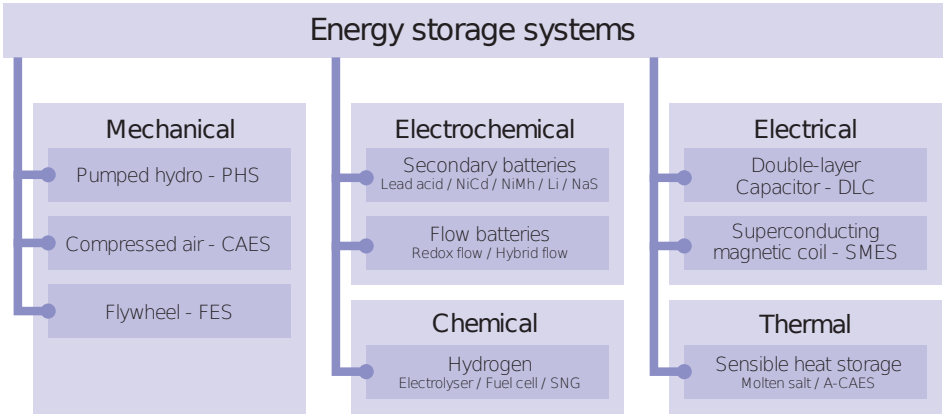

Figure 2-1: Classification of energy storage systems. Adapted from [14].

Mechanical energy storage

Mechanical storage systems store energy in the form of potential or kinetic energy. Examples are pumped hydro storage, compressed air storage, and flywheels. Pumped hydro and

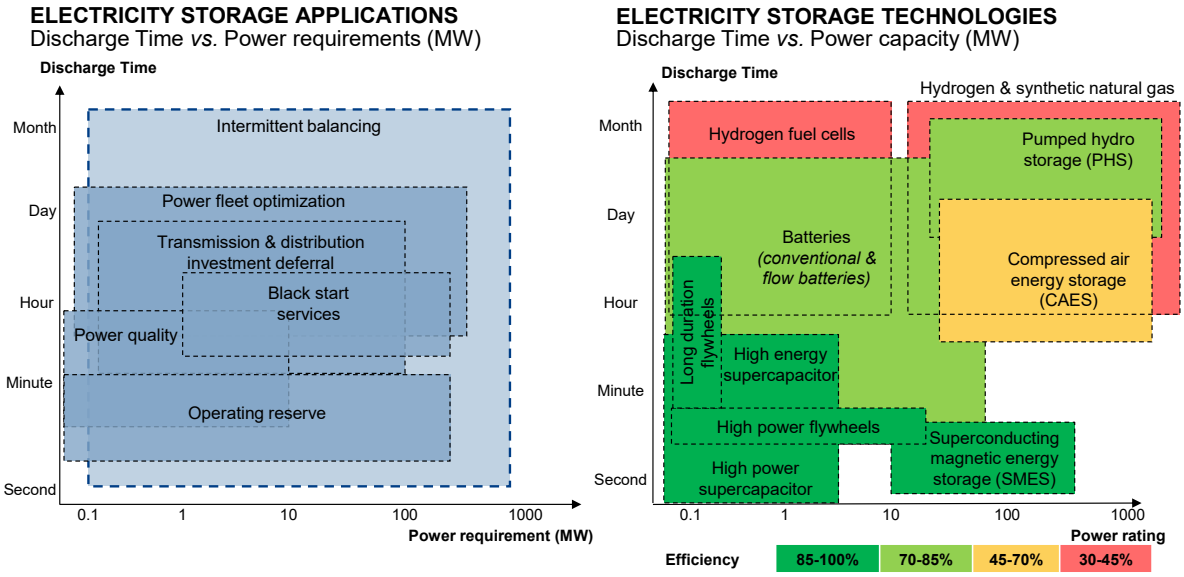

Figure 2-2: Indication of requirements for each energy storage application (left) and the position different energy storage technologies take in this plane (right). Taken from [15].

compressed air storage are large-scale energy storage systems and the most matured energy storage technologies [9], [10]. Both technologies are suitable for storage periods ranging from hours to days. Unfortunately, both have the disadvantage that certain geological conditions have to be met in order to employ them [9]–[11]. Pumped hydro requires a difference in elevation, and large amounts of water, because its energy density is low. Compressed air only works in places where gas can be stored under high pressure in gas tight containers, such as hard rock or salt caverns.

Flywheels are highly efficient, short term storage devices. They are able to react within seconds and have a high cycle life [9], [11]. Unfortunately, their self discharge rate is high [8], [9], [11], which makes them unfit for long term storage, as the energy losses would be too high.

Thermal energy storage

Thermal energy storage systems store thermal energy. An application for these methods is in the operation of steam turbines in solar thermal power plants [16, p. 126]. During normal operation, the steam turbines run on heat obtained from a solar field. Some heat is stored to be able to keep the turbines running when not enough heat is provided by the sun, for example during the night. There are three different principles on which thermal storage system can operate. These are latent, sensible, and chemical heat.

Latent heat systems use excess heat to achieve a phase change [11], which means that the temperature in these systems stays constant. As a result, its operating temperature can be low [17].

As the name implies, sensible heat uses the temperature difference of a medium to store energy. One of the popular technologies is molten salt [9], which is the technology used in

solar thermal power plants. It is cheap and has a high energy capacity [9]. However, its contents are corrosive and it operates at high temperature [9], [11].

Chemical heat is a bit different from the rest. The principle behind it is that heat is used to split a chemical compound in two parts that are stored separately. Whenever energy is needed, the two parts are brought back together and heat is released by the formation of the original chemical reactant [11]. It has the potential of high energy density, but is technically complex [17].

Electrical energy storage

Depending on the technology, energy is stored in an electrostatic field (supercapacitors) or magnetic field (superconducting magnetic energy storage). Both technologies are able to react fast, have excellent efficiency, and have a high cycle life [8], [9], [11]. This makes them excellent for short term energy storage. One of the shortcomings of supercapacitors is the self-discharge rate, which is about 5 %/d [11].

Electrochemical energy storage

This class of energy storage systems comprises batteries. They are mainly used for storage periods less than a day [7] and have excellent efficiency. However, most battery technologies do not have a high cycle life and cannot cope well with deep discharging [8]. There is a wide variety of technologies, including lead-acid, lithium-ion, and redox flow batteries. Lead-acid batteries tend to be cheaper, but are environmentally unfriendly [9], [11]. Lithium-ion, on the other hand, has a relatively good cycle life and high energy density. Unfortunately, they are expensive and could be a safety hazard [9], [10]. Redox flow batteries are batteries in which liquid electrolyte is pumped through the electrodes. This battery technology has the best cycle life, but also problems with corrosion [10].

Chemical energy storage

Chemical energy storage systems use electricity to convert some chemical in a different form. This process is reversed whenever energy needs to be supplied. An example of this is the use of electrolysers and fuel cells to convert water into hydrogen and oxygen, and vice versa. Some call it the most promising technology for long term storage [9], [11], [15], but it is still a technology in development. At the moment it is expensive and has a low round trip efficiency. It has a wide operation applicability from small-scale isolated microgrids to large-scale grid connections [8]. Furthermore, scaling is easy, as the power has no relation to the energy that can be stored.

There are multiple types of fuel cells. The main technologies are alkaline, proton exchange membrane, phosphoric acid, molten carbonate and solid oxide fuel cells, each with their own advantages and disadvantages.

Alkaline, proton exchange membrane, and phosphoric acid are low to moderate temperature fuel cells. These systems are only able to run on relatively pure hydrogen, as their platinum catalysts are susceptible to carbon monoxide and sulphur poisoning [18]. Alkaline fuel cells are

the only low temperature solutions that have the potential of using a cheaper nickel catalyst. Proton exchange membrane can operate at high power density, which makes it possible to build compact systems. Phosphoric acid cells show excellent reliability.

Molten carbonate and solid oxide cells run at high operating temperatures, which makes it possible to use cheap nickel based electrodes. Both are suitable for combined heat and power applications, and are fuel flexible, as they are able to handle hydrocarbons directly [18]. Unfortunately, molten carbonate uses a corrosive electrolyte. Solid oxide is not without disadvantages too. It is plagued by sealing issues and high costs, due to manufacturing difficulties of the ceramic electrolyte.

In terms of efficiency, proton exchange membrane and phosphoric acid are on the low side, with electrical efficiencies in the order of 40 to 50 %. Solid oxide has the best efficiency, 50 to 60 %, and alkaline and molten carbonate are somewhere in the middle, showing efficiencies in the range of 45 to 55 % [18].

Considering the operating scale of the different technologies, there is a division between the low and high temperature solutions [18]. The low temperature systems are mainly used as small-scale solutions, while the high temperature fuel cells can be employed in large-scale projects.

2-1-4 Summary

The integration of RESs comes with a major challenge: handling faster power demand changes from non-variable power sources as a result of the integration of variable energy sources. The most promising way to deal with these variations is to integrate energy storage systems which are able to store electrical energy by converting power to, for example, a chemical during off-peak periods and provide electrical power during peak periods by converting the chemical back to electricity.

Several energy storage technologies are under development, each with their own position in the energy storage market. Fuel cells and electrolyzers are expected to play an important role in large-scale long-term storage. In contrast to pumped hydro and compressed air storage, fuel cells and electrolyzers do not have strict geological requirements. Solid oxide cells are the technology with the highest potential for efficient large-scale storage. These cells run at high temperatures, but are more fuel flexible and more efficient than low temperature solutions. This makes solid oxide cells the most promising technology for counteracting variations in the power grid.

2-2 Overview of modelling in literature

This section gives an overview of modelling efforts found in literature. Several types of models can be found in literature, from single-cell models to stack models. The main idea for these models is very similar: model a single cell and assume that it is representative for a complete cell system. This does not mean that the complexity of all models is the same. The simplest models consider a completely lumped 0D model, while others consider multidimensional (1D+) models. A 0D model is a model in which spatial variations are

not taken into account. A 1D model takes into account one spatial dimension, for example variations along the length of a cell, while higher order models (1D+) include multiple spatial dimensions. 0D models are ideal from a control perspective, but the validity is questionable [19]. Higher order models could prove themselves important as they are able to capture spatial variations of, for example, the temperature.

This section discusses papers that deal with modelling of SORCs. This also includes literature focussed on SOFCs and SOECs, because literature on SORCs is limited.

2-2-1 Dynamic SORC modelling

Several attempts of developing a dynamic SORC model can be found in literature. Kazempoor and Braun [20] present a 1D hydrocarbon SORC model and focus on the validation and steady-state simulation of the SOEC region of the cell. The model used by them is an adaptation of a previously developed SOFC model [21]. The goal of the paper is to validate the cell model, so that it can be used for system-level models. Validation is done by comparing the model to steady-state experimental data of hydrocarbon and steam fuelled single-cell, button-cell, and stack setups. The results show that single-cell validated models cannot be extended directly to stack models, because of higher ohmic losses observed in stack setups. An extra correction term is added to correct for the differences between the single-cell and stack model.

In a subsequent paper, Kazempoor and Braun [22] validate steady-state cell voltage-current density (U-j) curves for the complete operating range of a single cell setup with different kinds of fuel. This paper introduces an uncommon model for the exchange current density, because the usual expressions did not provide satisfactory results. The new method is said to produce accurate results. A clever simplification is used, which assumes that the current is positive in SOFC mode and negative in SOEC mode. This simplifies modelling, because there is no need to define a discrete variable to be able to simulate both modes. Nonetheless, it is not uncommon to see the current to be defined positive in both SOFC and SOEC mode and the use of a discrete-variable to connect both modes into one SORC model, see for example [23]–[25]. Unfortunately, the dynamic model was only used for steady-states results. This was also the situation for the dynamic model paper by Wendel, Gao, Barnett, *et al.* [26].

Papers that consider dynamic mode switching of SORCs are limited. Jin and Xue [24] and Barelli, Bidini, Cinti, *et al.* [27] are two examples of papers that investigate this mode switching. For this purpose, Jin and Xue [24] use an isothermal 2D dynamic model to look into different compositions of the gas channels in SOEC and SOFC mode. A more experimental approach is taken by Barelli, Bidini, Cinti, *et al.* [27], who compare the outcomes of a dynamic model with experimental data of a six cell stack. The paper acknowledges the importance of investigating the ability of SORCs to react to variable load conditions, because of coupling with other energy sources and loads. In addition to steady-state validation, the paper shows voltage responses to current steps. Temperature variations were limited, which might be contributed to the experimental setup. The small stack was placed in a furnace. Unfortunately, the dynamic temperature data was not compared to the dynamic model. The experimental results showed that the voltage response of the system is orders faster than the temperature response. The time scale for the temperature response was in the order of 10^3 s, while the voltage reached steady-state almost immediately.

Apart from dynamic modelling, García-Camprubí, Izquierdo, and Fueyo [25] deal with electrochemical parameter fitting. This was motivated by a review on electrochemical parameter fitting literature. The conclusion of this review was that it is only vaguely described in literature, if mentioned at all. Yet, it is important, because exchange current density cannot be modelled or measured experimentally. For this purpose, a comprehensive model is introduced as well as a description of how the electrochemical parameters were fitted using experimental U-j curves of a hydrogen fuelled single-cell setup. The validity and applicability of common used parameter values was discussed. E.g., the charge transfer coefficient in the Butler-Volmer (BV) equation is often taken as 0.5, which might be inappropriate in SOEC mode. This observation was also made by Kazempoor and Braun [22]. Nonetheless, it is not unusual to select a charge transfer coefficient of 0.5 for SOEC [28], [29] or SORC [20], [30] models.

Dynamic system simulations, which include a BOP were not found, but steady-state SORC system simulations where conducted by Akikur, Saidur, Ping, *et al.* [30] and Mottaghizadeh, Santhanam, Heddrich, *et al.* [31]. Both models consisted of 0D SORC models, and 0D BOP components, such as heat exchangers (HEXs), pumps, and compressors. The system by Mottaghizadeh, Santhanam, Heddrich, *et al.* [31] uses a hydrocarbon fuel, while [30] uses hydrogen as fuel. The aim of Mottaghizadeh, Santhanam, Heddrich, *et al.* [31] is to research the feasibility of building a system for energy storage based on SORCs.

2-2-2 SOFC cell and system modelling

SOFC literature does not only consider cell models, but also efforts to provide dynamic system models. One of the more elaborated 1D cell models was developed by Colclasure, Sanandaji, Vincent, *et al.* [32]. The goal is to have a model that can be used for real-time control. The model was completely dynamic, except for the electrochemical model and turned out to be too complex for its purpose. Therefore, subspace identification was used to obtain a locally linear model. One aspect that contributes to the complexity of the model is the choice to use mass based material balances. This introduces the need to model the molar mass variations. Using a mole based material balance has an advantage in this case, because it does not include the molar mass variation [33]. A follow-up paper by Sanandaji, Vincent, Colclasure, *et al.* [34] discusses optimal control for the model.

Studies into different dynamic time scales present in SOFCs are conducted by Caisheng and Nehrir [35] and Qi, Huang, and Chuang [36]. A 0D 5 kW fuel cell stack model fuelled with hydrogen is used by Caisheng and Nehrir [35] for this purpose. The paper presents model U-j curves as well as dynamic model responses, but there is no form of validation. An equivalent circuit of the SOFC is used to compute dynamic electrical responses. The results show that dynamics associated with the electronic parts is in the order of 10^{-2} s, while the dynamics associated with the composition inside the gas channels is in the order of seconds. The thermodynamic time scale is the slowest and in the order of 100 to 1000 s. Similar time scales were mentioned by Huang, Qi, and Murshed [19], Bavarian, Soroush, Kevrekidis, *et al.* [37], and Yang, Qin, Zhang, *et al.* [38].

Qi, Huang, and Chuang [36] present a nonlinear cell-level dynamic model of a hydrogen SOFC for the purpose of dynamic simulation and control. They consider their model to be a building block for stack level models. Dynamic behaviour of voltage, current, gas consumption rates

controlled by different load and partial pressures are demonstrated through simulation. The cell is assumed to operate under isothermal conditions, which makes it possible to investigate the SOFC mass transfer dynamics on its own. The inputs to the model are a load resistance and partial pressures in the gas channels. The model outputs voltage, current, and hydrogen consumption. Validation is based on comparison of an experimental U-j curve. Just like Caisheng and Nehrir [35], it was observed that the time scales of the voltage and current dynamics are in the order of 10^{-2} s, as are diffusion dynamics.

According to Bhattacharyya, Rengaswamy, and Finnerty [39], it is important to study the transient behaviour an SOFC to be able to connect SOFCs to load-varying grids. For this purpose, a dynamic 2D model was made for the mass transfer inside the channels. The study provides a detailed dynamic model considering species material conservation in the gas flow channels and mass transport dynamics inside the porous electrodes. Not only dynamic model responses are shown, but also experimental step responses for the voltage and current were presented. The voltage and fuel flow rate were used as inputs to the setup. Initially, the diffusion model did not include Knudsen diffusion, but during the dynamic comparison it turned out to be an important factor. The setup was placed in a furnace, which resulted in (near) isothermal operation of the cell. This made it unnecessary to include an energy balance and made it possible to focus on the faster material balances. The time scale of the dynamic responses were in the order of 10^{-2} to 10^{-1} s.

A comparison of two SOFC models is presented by Iora, Aguiar, Adjiman, *et al.* [40]. This comparison was made to justify simplifications in earlier publications. The simplified model assumes constant pressure, gas stream densities, heat capacities, thermal conductivities, viscosity, and gas velocity based on inlet conditions. The results of this model are compared to the outcomes of a more complex model where these assumptions are removed. Significant differences were observed for current densities above $5\,\mathrm{kA/m^2}$.

An SOFC system comprises more than only the cell itself. Additional components, known as the BOP, are needed to operate the cell. Typical components include HEX, pumps, compressors, converters, valves, and storage tanks. In most publications, the dynamics of the BOP components are assumed to be faster than the dynamics of the SOFC. A consequence of this is that static models are used to model the BOP by most sources. Authors that include dynamic BOP models for SOFC systems do this mainly for hydrocarbon fuel cell systems, where reformer flow dynamics can have influence on the system performance. For simplicity, the reformer dynamics can be approximated by a first order system with a time constant in the order of seconds [35], [38], [41]. Dynamic HEX, reformer, and afterburner models are included in the systems of Murshed, Huang, and Nandakumar [33] and Yang, Qin, Zhang, *et al.* [38], and Adhikari and Abdelrahman [42].

Murshed, Huang, and Nandakumar [33] present a dynamic model for a fuel cell system with control applications in mind. The system consisted of a 0D dynamic hydrocarbon SOFC model, 1D dynamic HEX model, and 0D dynamic models for a reformer and an afterburner. The model is used to predict the cell voltage as well as the temperature, given a certain current. Two different 0D models were presented and compared. The first model is a completely lumped model for which no distinction is made between the different components of the cell. This model is only valid for low current densities. The second model considers 0D models for each component of the cell. Goal of the paper is to provide a model that is applicable in all operating conditions. Unfortunately, the model is somewhat limited, due to a simplification

of the electrochemical model. The activation model is approximated by the Tafel equation, which is only valid at high current densities [43].

Adhikari and Abdelrahman [42] also describe the modelling and control for an SOFC system. Their system contains a 60 W hydrocarbon SOFC. The model is 0D and the inputs of the SOFC are the gas flow rates. The inlet temperature of the channels and load current are considered as disturbance input to the model. Validation is not included, but it is mentioned that model responses were compared with model and industry data. The BOP includes a first order approximation of a blower, dynamic fuel reformer, dynamic afterburner and a static heat exchanger model.

2-2-3 SOEC modelling

Literature describing modelling of SOECs is not as present as literature on SOFCs. Udagawa, Aguiar, and Brandon [44] provide one of the first attempts to develop a 1D dynamic SOEC stack model. The model was based on a previously developed SOFC model, but was not validated in any way. Simulations showed temperature, local current density, and overpotential distribution along the cell for simulations where the current density was up to $10\,\mathrm{kA/m^2}$. The results showed that the activation overpotential is the main source of voltage drop, while the concentration overpotential remained negligible in all cases. The authors acknowledged that the concentration overpotential only has an influence at high current densities, even though it was not observed in the results.

Cai, Luna-Ortiz, Adjiman, *et al.* [45] use the same model to investigate the steady-state performance of an SOEC stack for a wide range of operating conditions. Their aim is to provide a better understanding of steady-state behaviour of an SOEC and to identify a parametric window of operating conditions that offers efficient large-scale stack operation.

A detailed 2D steady-state SOEC stack model was developed by Laurencin, Kane, Delette, *et al.* [28] to analyse the thermo-electrochemical behaviour. This model was based on a previously made SOFC model, as was the case for the SORC model by [20] and the SOEC model by [44]. Special attention was given to radiative heat transfer. It was found that radiation accounted for 73 % of the heat transfer. This contradicts the assumption made by Kazempoor, Dorer, and Ommi [21], who assumed that radiative heat transfer can be neglected.

Electrical characteristics of SOECs were studied by Ni, Leung, and Leung [29]. A steady-state electrochemical model was built for this purpose. The model was used to examine what parameters had the biggest influence on the performance of an SOEC. It turned out that electrode-supported cells provide the best performance, because of the relatively low conductivity of the electrolyte. The same benefits were observed for electrodes with high porosity and large pores.

2-2-4 Summary

Several papers consider dynamic modelling of SORCs. These models are often based on SOFC and SOEC models. Often, a discrete variable is introduced to distinguish between the two operating modes of the SORC. A more convenient method is to extent an SOFC or

SOEC model by considering the current density and power density negative in the opposing operating mode. A limited amount of literature considers mode switching. Most studies only consider the cell itself and dynamic models which included a BOP where not found

SOFC and SOEC literature was looked into due to the influence it has on SORC literature and its presence in literature compared to SORC literature. Important results from SOFC literature include the time scales of different parts of SOFCs models, which were observed to cover dynamics in the order of ms up to 1000 s. These time scales were mostly obtained from dynamic models and representative dynamic experiments are scarce. BOP models are often omitted. A small amount of papers includes first order approximations for specific setups. SOEC models were found to resemble those of SOFCs.

2-3 SORC model validation

Apart from modelling, it is also important to validate the models. Dynamic validation of an SORC is challenging. Experimental results are limited [19], [20] and often leave out detailed results for distributed variables, such as composition and temperature. Validation is often based on experimental steady-state U-j curves for single cells [24], button cells [20], [26], or small stacks consisting of a limited number of cells [27]. Small experimental setups are placed in a furnace [29] to keep the temperature of the cells approximately constant.

Unfortunately, there are publications that omit validation completely. E.g., Udagawa, Aguiar, and Brandon [44] makes an adaptation of an SOFC stack model for an SOEC stack, but does no revalidate the results. This is also the case for the model of Laurencin, Kane, Delette, *et al.* [28]. Nonetheless, the model from Udagawa, Aguiar, and Brandon [44] is used in multiple papers. See for example [45]–[47].

Validation of parts of the model is also an option. For example, Bhattacharyya, Rengaswamy, and Finnerty [39] try to validate their electrochemical and mass diffusion model. This is done by comparing steady state U-j curve and the dynamic current responses after several steps in voltage. Repeatability of the experiments was good and showed deviations of 1 % for the steady state results, and 5 % deviations for the dynamic experiments. The voltage steps were not exact step, because that was not realizable. Instead: it was more like a first order response. Steady-state validation was repeated for 700, 800, and 850 °C. One important aspect of this study is that they mention that static validation does not guarantee dynamic validation. The first version of their model did not include Knudsen diffusion, which made it impossible to get correct dynamic responses. However, adding Knudsen diffusion solved the problem.

2-4 Overview of literature on control

Literature on SORC control is limited. The need for control was mentioned by Wendel, Gao, Barnett, *et al.* [26], who called thermal management of the endothermic SOEC mode and exothermic SOFC mode in one system one of the central challenges. This section addresses control of SORCs followed by SOFC control.

2-4-1 SORC control

A first step in the direction of control literature for SORCs was given by Srikanth, Heddrich, Gupta, *et al.* [48]. This paper studied mode switching of a dynamic 1D SORC model from SOFC to SOEC mode and the influence of the rate of change of input signals on the spatial gradient of the PEN temperature. The conclusion of their study was that input signals have to changed by ramps to limit spatial temperature gradients in the PEN. However, it is not studied what the source is of the spatial temperature gradient. Instead, all input signals are changed at the same time. Therefore, it is not clear whether the temperature gradients are a result of, for example, changes in inlet temperature or compositions.

A first paper that could be considered control of the SORC temperature, is the study by Ren, Gamble, Roscoe, *et al.* [49] where the temperature of a 0D SORC model was kept constant by use of a molten bronze heat storage. The principle behind this idea is that the temperature of a substance is constant when it undergoes a phase transition from one state of matter to another. It is unclear how the bronze would be integrated into the system, but this is a very important aspect, because it determines the ability of the heat storage to keep the SORC at a constant temperature. Additionally, the paper presents a grid connection and compares control of the inverter to minimize direct current power ripples under constant power production.

One of the few studies that considers control of an SORC while it undergoes a mode switch, can be found in [50]. In contrast to Ren, Gamble, Roscoe, *et al.* [49], Botta, Romeo, Fernandes, *et al.* [50] present a more dynamic way of controlling the temperature gradient and fuel utilization of a 1D nonlinear SORC model. In this study, the current density was considered a disturbance and the air and fuel flow rate were used as input signals. It was determined through examination of the relative gain array (RGA) that decoupled control was possible. For this analysis, the nonlinear model was linearized at one unspecified operating point in SOEC and one in SOFC mode. It was found that the fuel utilization could be controlled by the fuel flow rate and that the temperature gradient could be controlled by the air flow rate. PI controllers were used to control the system. To test the controllers, an idealized situation was considered in which the current density ramped from $-6750\,\mathrm{A/m^2}$ to $3250\,\mathrm{A/m^2}$ over a period of 13.5 h.

2-4-2 Control of SOFCs

A review of dynamic modelling and control of SOFCs by Huang, Qi, and Murshed [19] showed that the main motivation for control is improvement of durability and efficiency. This results in control objectives related to prevention of fuel depletion by maintaining a constant fuel utilization or certain compositions in the gas channels, and maintaining a constant temperature which ensures good performance without damaging the cell. A common choice is to select the air flow rate to control temperature [19], [51], [52] and the fuel flow rate to control the composition of the fuel [19], [53]. Some also consider the gas flow inlet temperature to be an input that can be used to control the cell temperature [51], [54].

Apart from maintaining suitable operating conditions, another important aspect is to provide the amount of power demanded by end-users. Broadly speaking, the two ways to incorporate this are to use the SOFC to track a certain power signal or to consider a disturbance that acts

on the system. Mueller, Jabbari, and Brouwer [41] state that researching the load following capabilities of SOFC systems increases the attractiveness of SOFCs, because it would make them better suited to support the electrical grid and meet variable loads. The current tactic is to operate SOFC systems under steady state conditions, to improve durability. However, proper control could make it feasible to operate under variable load, while maintaining operating requirements. This is even more true for an SORC which should have the capability to provide a variable power.

A common approach in literature seems to adjust the current or the voltage to be able to follow a power reference signal [19], [37], [52]. However, not everyone agrees that it is possible to actively influence the power produced by an SOFC. For example, Pohjoranta, Halinen, Pennanen, *et al.* [51] consider the load current to be non-controllable, as its value is dictated from the outside and cannot be set by the SOFC itself. Therefore, they focus on providing the best possible operating conditions while undergoing current changes. This means that the current acts as a disturbance on their system. A similar approach was taken by [53].

According to Huang, Qi, and Murshed [19], simple proportional-integral-derivative (PID) controllers are enough to control SOFCs close to their nominal operating point, but more complex controllers are needed to handle constraints on the system. In [51], the effect of a current step disturbance on the cell temperature is rejected by changing the air inlet temperature. For this purpose, a PID controller is compared to a model predictive controller and it is shown that the model predictive controller does not outperform the PID controller. It should be noted that this is a simple and limited single-input single-output situation where improvement by more complex controllers is limited. Furthermore, variation of the inlet temperature only has an effect on the maximum temperature, not on the temperature distribution along the cell.

According to Chatrattanawet, Skogestad, and Arpornwichanop [53], SOFC literature is focussed on operation and design of cells and not so much on control. The goal of their paper is to present a suitable control structure design and tuning of controllers for an SOFC. Their analysis shows that two PID controllers are able to withstand step changes in current, which shows that simple PIDs also have their place in multiple-input multiple-output control of SOFCs. The first controller controls the cell temperature by manipulating the air flow rate and the second controller manipulates the fuel flow rate to control the fuel composition. The choice of input-output pairing was motivated by examination of the RGA, which was close enough to the identity matrix.

One possible limitation of most literature concerning control of SOFCs, is only considering the SOFC itself and ignoring the dynamics of the BOP, even though these components put constraints on obtainable performance. For example, Mueller, Jabbari, and Brouwer [41] and Jiang, Shen, Deng, *et al.* [54] show that it is important to consider the dynamics of the BOP. Both consider the fuel flow rate to behave as a first order system and that a time constant of less than 5 s can result in fuel depletion. Similar conclusions are drawn by [38], which examined the load following capabilities of a 5 kW SOFC system where the fuel supply system was approximated by a first order system with a time constant of 3 s.

Another important aspect is that sensor dynamics and difficulty to measure some quantities limit the obtainable performance [37]. Output temperature is measurable, but temperature throughout the cell is harder to measure. Measurement of composition is important, but also difficult and expensive [34]. State estimators might provide a solution in these cases.

2-4-3 Summary

Control of SORCs is a new field of literature, but important due to the different dynamics in SOEC and SOFC mode. Some papers look into the mode switching of SORCs, but most papers do not consider control of the SORC. One of the few studies that looks into control of SORCs does this for an ideal case where the current density rate of change is constant. This study shows that the temperature gradient and fuel utilization can be controlled by PI controllers on the air and fuel flow rate, respectively.

Literature on SOFC control focusses on improvement of durability and efficiency by considering control objectives that are related to prevention of fuel depletion, maintaining certain gas compositions, and maintaining constant cell temperatures. Literature is divided on how power or current should be treated in relation to the SOFC. Some consider the current as an input, while others consider it to be a disturbance. A common approach is to use PID controllers to control cell temperature and gas compositions. A limitation of SOFC control literature is that most studies only consider the cell itself and do not consider the dynamics of the BOP.

Chapter 3

Dynamic 0D SORC model

This chapter describes the dynamic 0D model of the planar SORC. The model describes a single cell at the center of a large stack of cells, as shown in Figure 3-1. This single cell is assumed to be representative for every cell inside the stack and consists of four parts: A fuel gas channel, air gas channel, interconnect, and PEN structure. The interconnect is used to separate the cells from each other and at the same time houses the gas channels. The PEN structure is a solid structure consisting of the electrolyte and two porous electrodes. It is the part where power is generated or consumed by the formation or consumption of steam, respectively. The cell runs on hydrogen, oxygen, and steam, which means that the only reaction taking place in the cell is given by

$$\mathrm{H_2} + \frac{1}{2}\,\mathrm{O_2} \underset{\text{SOEC}}{\overset{\text{SOFC}}{\rightleftharpoons}} \mathrm{H_2O}.$$

During SOFC mode hydrogen and oxygen are converted in steam, which makes it possible to extract electrical power from the cell. In SOEC mode electrical power has to be supplied to the cell in order to convert the steam back into hydrogen and oxygen. The reaction happens in the zone known as the triple phase boundary (TPB), which is the place where the electrolyte, gas, and catalytic electrodes are in contact [18]. It is the only place where the reaction can happen, because the electrolyte only conducts ions, while the electrodes only conduct electrons.

The chapter starts with an overview of assumptions and conventions. After that, the three parts of the model are discussed. First, material balances are formulated which describe the composition in the gas channels. Next, energy balances are used to describe the temperature of the different components of the cell. The third part of the model is the electrochemical model. This part describes the operating voltage of the cell. An overview of the model parameters is given in Appendix A.

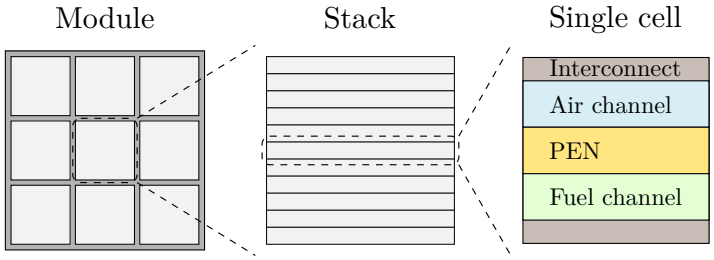

Figure 3-1: Schematic representation of where the single cell is placed inside a stack, which is placed in a large SORC module. The single cell shows the different parts of which all cells are composed.

3-1 Model assumptions and conventions

This section discusses various assumptions and modelling conventions which were applied when modelling the system.

3-1-1 Model assumptions

The following assumption were used:

Repeated cells. It is assumed that it is possible to represent the stack by one single cell at the center of a large stack of identical cells. According to Larminie and Dicks [55], the performance of one single cell can characterize the performance of a whole stack. This approach does not take into account any of the processes happening at the boundary of the system, such as heat loss to the environment. It is assumed that these effects are relatively small. This is the approach taken by most papers, see for example [44].

0D model for each part of the cell. It is assumed that it is necessary to model each individual part of the cell by its own 0D model. Murshed, Huang, and Nandakumar [33] compare two models for a planar SOFC: one where the whole cell is lumped into one model and one model where each part of the cell is represented by its own 0D model. The results in this paper show that there are no big differences between the models at low currents. However, at high current, temperature differences between the components can go up to 100 K. Since the model is 0D, it only models the output conditions of the cell. Variations along the cell are not modelled.

Constant presure and negligible pressure drop. It is assumed that the cell operates at a constant pressure and that pressure drop over the cell is negligible. This assumption is based on [40], which shows that pressure drop for a planar SOFC with a length of 40 cm is 3.6 % for the air channel and only 0.2 % for the fuel channel when operating at $5000\,\mathrm{A/m^2}$.

Ideal gas mixtures. It is assumed that the fuel and air gasses can be modelled as ideal gas mixtures. This assumption can be applied as long as the pressure is low and the temperature is high [56]. Both apply to the system, since the operating pressure is taken as 1 bar and the operating temperature is somewhere in the range of 600 to 1000 °C.

Furthermore, it is assumed that the fuel gas only consists of steam and hydrogen, and that the air channel only contains oxygen and nitrogen.

Constant heat capacities and thermal conductivities. It is assumed that the heat capacities and thermal conductivities of the gas components are constant with respect to temperature changes. However, this does not mean that they are constant as the composition of the gas mixture changes. Iora, Aguiar, Adjiman, *et al.* [40] showed that the heat capacities of the air gas changes by approximately 1 % when a planar SOFC is operating at 5000 A/m^2. For the fuel channel, the heat capacities changes around 30 %. This is probably because of the change in composition in the fuel channel, as the fuel utilization is set to 75 %. A comparison of heat capacities obtained from [57] shows that the heat capacity of steam at 800 °C is almost 40 % higher than for hydrogen. Comparing thermal conductivities of the different gasses, the differences are even bigger. The thermal conductivity of hydrogen is more than five times larger than that of hydrogen.

Constant solid mass. It is assumed that the masses of the solid interconnect and PEN structure are constant.

Quasi steady state. The processes happening inside a fuel cell appear to have a wide range of time scales. For example, the dynamics associated with the electrochemical reaction have time constants in the order of milliseconds [58], while the temperature response of the cell can have time constants as slow as 1000 s [19]. The interest of this study is in the slower dynamics of the system. Therefore, processes with time constants faster than 1 s are modelled as quasi steady state. These include the dynamics of the electrochemical reaction, diffusion through the electrodes, and dynamics related to the output voltage of the cell.

Heat addition in PEN. The TPB is the region in the PEN structure where the electrochemical reaction happens [18]. Therefore, it is assumed that all heat generated by this reaction is absorbed by the PEN structure. This approach is also used in multiple papers, see for example [33], [44].

3-1-2 Model conventions

The system is modelled using the following model conventions

Positive current SOFC, negative current SOEC. The current is defined as being positive in SOFC mode and negative in SOEC mode. Basically, this means that the system is an extended SOFC model which can also be used for SOEC operation. The reason for this approach is that there is no fundamental difference between SOEC and SOFC models. The equivalence of the SOFC and SOEC electrochemical model is shown in Appendix C. This approach makes the model less complex and make it easy to distinguish between both modes. This convention is also used by [22], [26]. Application of the common SOFC and SOEC convention that the voltage and current density are positive requires a discrete variable to be able to connect both models into one and makes it less clear what the operating mode of the cell is.

Diffusion through electrodes is accounted for via a correction term. When setting up the material balance of the gas channels, there is a choice to be made to include the diffusion in the mass balances for the gas channels [24], [32], [36], [39], [59] or to include a loss factor in the electrochemical model [21], [22], [26], [43], [45], [60]. Both approaches result in the same cell conditions, as the only difference is the place in the model where it is accounted for mass diffusion through the electrodes. The choice was made to use the approach where a correction term is used in the electrochemical model.

3-2 Material balances

Material balances are used to compute the composition inside the gas channels. This is done by combining the overall material balance and the material balances per gas component. An illustration with the flows going in and out of the system is shown in Figure 3-2, where the arrows indicate the positive flow direction. Therefore, a flow in the opposite direction has a negative value. As an example, consider the flow rate of nitrogen at the inlet of the air channel; a positive value indicates inflow of nitrogen, while a negative value indicates outflow of nitrogen via the inlet. All material balances are mole based, because the consumption rates of hydrogen, oxygen, and steam are defined as molar flows. Converting these consumption rates into mass flows would make the equations more complex than necessary.

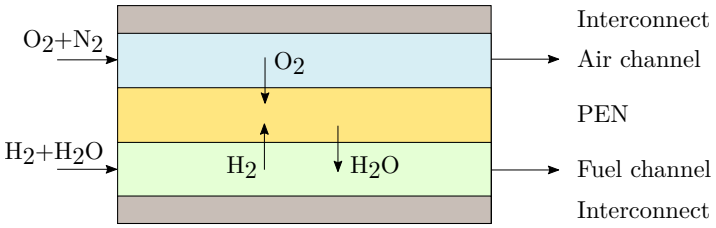

Figure 3-2: Overview of material flows. Arrows indicate positive flow direction.

The consumption rate of hydrogen, oxygen and steam are related via the reaction taking place inside the SORC,

$$\mathrm{H_2} + \frac{1}{2}\,\mathrm{O_2} \underset{\text{SOEC}}{\overset{\text{SOFC}}{\rightleftharpoons}} \mathrm{H_2O}. \tag{3-1}$$

It is clear from this reaction that the consumption rates of hydrogen R_{H_2}, oxygen R_{O_2}, and steam R_{H_2O} are related by

$$R_{H_2} = 2R_{O_2} = -R_{H_2O}. \tag{3-2}$$

The consumption rates only depend on the cell current [47], [61] and can be expressed by

$$R_{H_2} = \frac{i}{2F} = \frac{A_s j}{2F}, \tag{3-3}$$

where i is the cell current, j is the current density of the cell, A_s is the cell active area, and F is the Faraday constant.

First, the material balances for the air channel are described. After that, a description is given for the fuel channel.

3-2-1 Air channel

The overall material balance in the air channel is given by

$$\frac{\mathrm{d}n_{air}}{\mathrm{d}t} = \phi_{air,in} - \phi_{air,out} - \frac{1}{2}R_{H_2}, \tag{3-4}$$

where n_{air} is the total amount of air in the air channel, and $\phi_{air,in}$ and $\phi_{air,out}$ are the inflow and outflow rate of air, respectively. Observe that Equation (3-2) is already applied.

Defining the amount of oxygen in the air channel as $n_{air,O_2} = \chi_{air,O_2} n_{air}$, the material balance for oxygen is given by

$$\frac{\mathrm{d}\chi_{air,O_2} n_{air}}{\mathrm{d}t} = \chi_{air,O_2,in}\phi_{air,in} - \chi_{air,O_2}\phi_{air,out} - \frac{1}{2}R_{H_2}, \tag{3-5}$$

where χ_{air,O_2} is the mole fraction of oxygen inside the air channel and $\chi_{air,O_2,in}$ is the mole fraction of air in the air inlet stream.

Combining Equation (3-4) and Equation (3-5) gives

$$n_{air}\frac{\mathrm{d}\chi_{air,O_2}}{\mathrm{d}t} = (\chi_{air,O_2,in} - \chi_{air,O_2})\phi_{air,in} + \frac{1}{2}R_{H_2}(\chi_{air,O_2} - 1). \tag{3-6}$$

The amount of nitrogen in the air channel n_{air,N_2} follows directly from the mole fraction of oxygen and total amount of air inside the air channel,

$$n_{air,N_2} = (1 - \chi_{air,O_2})n_{air}.$$

This is a direct result of the assumption that the air channel gas consists only of oxygen and nitrogen

3-2-2 Fuel channel

A similar procedure is followed to find expressions for the hydrogen and steam fraction inside the fuel channel. The total material balance of the fuel channel is given by

$$\frac{\mathrm{d}n_{fuel}}{\mathrm{d}t} = \phi_{fuel,in} - \phi_{fuel,out}, \tag{3-7}$$

where n_{fuel} is the number of moles of gas inside the fuel channel, and $\phi_{fuel,in}$ and $\phi_{fuel,out}$ are the rate of inflow and outflow of matter, respectively. Note that there is no consumption rate term present in the overall fuel channel material balance. This follows directly from Equation (3-2), which indicates that the amount of hydrogen consumed/produced by the cell is equal to the amount of water vapor produced/consumed. In other words, there is no net consumption inside the fuel channel.

Defining the amount of hydrogen inside the fuel channel as $n_{fuel,H_2} = \chi_{fuel,H_2} n_{fuel}$, the material balance for hydrogen in the fuel channel is given by

$$\frac{\mathrm{d}\chi_{fuel,H_2} n_{fuel}}{\mathrm{d}t} = \chi_{fuel,H_2,in}\phi_{fuel,in} - \chi_{fuel,H_2}\phi_{fuel,out} - R_{H_2}, \tag{3-8}$$

where χ_{fuel,H_2} is the mole fraction of hydrogen inside the fuel channel and $\chi_{fuel,H_2,in}$ is the mole fraction of hydrogen in the inlet stream. Combining Equation (3-7) and Equation (3-8), it follows that

$$n_{fuel}\frac{\mathrm{d}\chi_{fuel,H_2}}{\mathrm{d}t} = (\chi_{fuel,H_2,in} - \chi_{fuel,H_2})\phi_{fuel,in} - R_{H_2}. \tag{3-9}$$

The fuel channel only contains hydrogen and steam. Therefore, the amount of water vapor in the fuel channel n_{fuel,H_2O} follows from the amount of hydrogen and total amount of fuel in the channel,

$$n_{fuel,H_2O} = (1 - \chi_{fuel,H_2})n_{fuel}.$$

3-3 Energy balances

Energy balances are used to calculate temperatures. Figure 3-3 gives an overview of all energy flows accounted for in the model. The arrows indicate positive flow direction. Flows in the opposite direction have a negative value. The energy flows are: Energy addition and removal through inflow and outflow of matter, heat addition as a result of the electrochemical reaction inside the cell, power produced by the cell, and convective and radiative heat transfer. The heat of reaction and power are accounted for in the energy balance of the PEN structure. Heat conduction inside the different parts is not taken into account, because this requires at least a 1D model of each part.

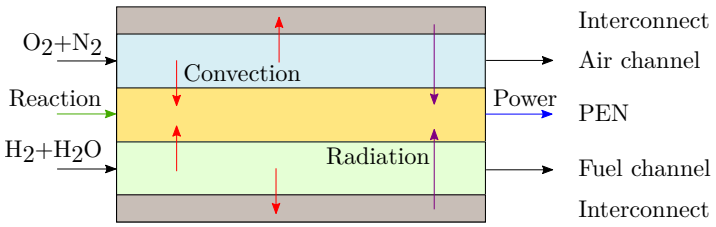

Figure 3-3: Overview of energy flows. Arrows indicate positive flow direction. Black arrows: flow of matter, green arrow: heat addition by the formation of steam in the electrochemical reaction, red arrows: convective heat transfer, purple arrows: radiative heat transfer, and blue arrow: power generated by the electrochemical reaction.

The energy balances of the PEN structure and interconnect are mass based, while the energy balances of the air and fuel channel are mole based. Mass based energy balances for the gas channels would make the equations more complex, because they should include the variation of molar mass of the gas inside them. This follows directly from considering the change of mass over time inside a gas channel and applying the ideal gas law and constant pressure assumption,

$$\frac{\mathrm{d}m}{\mathrm{d}t} = \frac{pV}{R}\left(-\frac{M}{T^2}\frac{\mathrm{d}T}{\mathrm{d}t} + \frac{1}{T}\frac{\mathrm{d}M}{\mathrm{d}t}\right),$$

where m is the mass of gas inside the channel, V is the channel volume, p is the pressure, R is the universal gas constant, M is the molar mass, and T is the temperature of the gas inside the channel. Mole based energy balances do not require the evaluation of the change of molar mass. The solid parts are expressed via mass based mass balances.

First, the energy balances for the air and fuel channel are presented. Next, the PEN structure energy balance is discussed. The last energy balance describes the temperature of the interconnect.

3-3-1 Air channel

The energy balance of the air channel is given by

$$\frac{\mathrm{d}n_{air}E_{air}}{\mathrm{d}t} = -Q^{conv}_{int,air} - Q^{conv}_{PEN,air} + \phi_{air,in}H_{air,in} - \phi_{air,out}H_{air} - \frac{1}{2}R_{H_2}H_{O_2,r}, \tag{3-10}$$

where E_{air} is the molar internal energy of air, $Q^{conv}_{int,air}$ and $Q^{conv}_{PEN,air}$ are the convective heat transfer from the air channel to the interconnect and PEN, respectively, $H_{air,in}$ and H_{air} are the molar enthalpy of air in the air inlet stream and inside the air channel, and $H_{O_2,r}$ is the molar enthalpy of the oxygen that is involved in the electrochemical reaction. The upcoming part discusses the different terms of this equation.

The molar internal energy of the ideal gas mixture air E_{air} [62] is given by

$$E_{air} = \chi_{air,O_2}E_{O_2} + (1 - \chi_{air,O_2})E_{N_2},$$

where E_{O_2} is the molar internal energy of oxygen and E_{N_2} is the molar internal energy of nitrogen. It follows that

$$\frac{\mathrm{d}E_{air}}{\mathrm{d}t} = (E_{O_2} - E_{N_2})\frac{\mathrm{d}\chi_{air,O_2}}{\mathrm{d}t} + \chi_{air,O_2}\frac{\mathrm{d}E_{O_2}}{\mathrm{d}t} + (1 - \chi_{air,O_2})\frac{\mathrm{d}E_{N_2}}{\mathrm{d}t}. \tag{3-11}$$

The molar internal energy of an ideal gas with constant molar heat capacity is given by

$$E_l = E_l^{ref} + c_{v,l}\Big(T_l - T^{ref}\Big), \quad l \in \{\mathrm{O_2}, \mathrm{N_2}\}, \tag{3-12}$$

where E_l is the molar internal energy, E_l^{ref} is a molar internal energy reference at temperature T^{ref}, and $c_{v,l}$ is the molar heat capacity at constant volume. Using the constant molar heat capacity assumption and combining Equation (3-11) and Equation (3-12),

$$\frac{\mathrm{d}E_{air}}{\mathrm{d}t} = (E_{O_2} - E_{N_2})\frac{\mathrm{d}\chi_{air,O_2}}{\mathrm{d}t} + c_{v,air}\frac{\mathrm{d}T_{air}}{\mathrm{d}t}, \tag{3-13}$$

where T_{air} is the temperature of the gas inside the air channel, $\frac{\mathrm{d}\chi_{air,O_2}}{\mathrm{d}t}$ can be obtained from Equation (3-6) and the molar heat capacity at constant volume of air $c_{v,air}$ is given by

$$c_{v,air} = \chi_{air,O_2}c_{v,O_2} + (1 - \chi_{air,O_2})c_{v,N_2},$$

where c_{v,O_2} and c_{v,N_2} are the molar heat capacities of oxygen and nitrogen, respectively.

The constant pressure assumption allows to rewrite the time derivative of the amount of air inside the channel [63] as

$$\begin{aligned}\frac{\mathrm{d}n_{air}}{\mathrm{d}t} &= -\frac{pV_{air}}{RT_{air}^2}\frac{\mathrm{d}T_{air}}{\mathrm{d}t},\\ &= -\frac{n_{air}}{T_{air}}\frac{\mathrm{d}T_{air}}{\mathrm{d}t},\end{aligned} \tag{3-14}$$

where R is the universal gas constant and V_{air} is the air channel volume.

Combining Equation (3-10), Equation (3-13), Equation (3-14), and Equation (3-4), it follows that

$$n_{air}\left(c_{v,air}+\frac{H_{air}-E_{air}}{T_{air}}\right)\frac{\mathrm{d}T_{air}}{\mathrm{d}t} = -Q^{conv}_{int,air}-Q^{conv}_{PEN,air}+\phi_{air,in}(H_{air,in}-H_{air}) - \frac{1}{2}R_{H_2}(H_{O_2,r}-H_{air})-n_{air}(E_{O_2}-E_{N_2})\frac{\mathrm{d}\chi_{air,O_2}}{\mathrm{d}t}. \tag{3-15}$$

Convective heat transfer is modelled by Newton's law of cooling. Expressions can be found in section B-1. Expressions for the different molar enthalpies are shown in section B-3.

3-3-2 Fuel channel

Formulating the energy balance of the fuel channel is very similar to the one for the air channel and is given by

$$\frac{\mathrm{d}n_{fuel}E_{fuel}}{\mathrm{d}t} = -Q^{conv}_{int,fuel}-Q^{conv}_{PEN,fuel}+\phi_{fuel,in}H_{fuel,in} - \phi_{fuel,out}H_{fuel}-R_{H_2}H_{H_2,r}+R_{H_2}H_{H_2O,r}, \tag{3-16}$$

where E_{fuel} is the molar internal energy of the fuel, $Q^{conv}_{int,fuel}$ and $Q^{conv}_{PEN,fuel}$ are convective heat transfer from fuel channel to the interconnect and PEN structure, respectively, and $H_{fuel,in}$, H_{fuel}, $H_{H_2,r}$, and $H_{H_2O,r}$ are the molar enthalpies of the fuel at the inlet of the channel, the fuel inside the channel, the hydrogen that is involved in the electrochemical reaction, and the steam from the reaction, respectively.

As for the air channel ,the derivative of the molar internal energy follows from considering

$$E_{fuel} = \chi_{fuel,H_2}E_{H_2}+(1-\chi_{fuel,H_2})E_{H_2O},$$

and is given by

$$\frac{\mathrm{d}E_{fuel}}{\mathrm{d}t} = (E_{H_2}-E_{H_2O})\frac{\mathrm{d}\chi_{fuel,H_2}}{\mathrm{d}t}+c_{v,fuel}\frac{\mathrm{d}T_{fuel}}{\mathrm{d}t}, \tag{3-17}$$

where E_{H_2} and E_{H_2O} are the molar enthalpies of hydrogen and steam, respectively, T_{fuel} is the temperature of the fuel channel, $\frac{\mathrm{d}\chi_{fuel,H_2}}{\mathrm{d}t}$ follows from Equation (3-9) and the molar heat capacity of fuel under constant volume $c_{v,fuel}$ is given by

$$c_{v,fuel} = \chi_{fuel,H_2}c_{v,H_2}+(1-\chi_{fuel,H_2})c_{v,H_2O},$$

where c_{v,H_2} and c_{v,H_2O} are the molar heat capacities of hydrogen and steam, respectively.

The time derivative of the number of moles of fuel inside the channel can be rewritten by considering an ideal gas and a constant pressure. It follows that

$$\begin{aligned}\frac{\mathrm{d}n_{fuel}}{\mathrm{d}t} &= -\frac{pV_{fuel}}{RT^2_{fuel}}\frac{\mathrm{d}T_{fuel}}{\mathrm{d}t},\\ &= -\frac{n_{fuel}}{T_{fuel}}\frac{\mathrm{d}T_{fuel}}{\mathrm{d}t},\end{aligned} \tag{3-18}$$

where V_{fuel} is the volume of the fuel channel.

Combining Equation (3-7), Equation (3-16), Equation (3-17), and Equation (3-18), it follows that

$$\begin{aligned} n_{fuel}\left(c_{v,fuel}+\frac{H_{fuel}-E_{fuel}}{T_{fuel}}\right)\frac{\mathrm{d}T_{fuel}}{\mathrm{d}t} &= -Q^{conv}_{int,fuel}-Q^{conv}_{PEN,fuel}+\phi_{fuel,in}(H_{fuel,in}-H_{fuel}) \\ &\quad + R_{H_2}(H_{H_2O,r}-H_{H_2,r}) \\ &\quad - n_{fuel}(E_{H_2}-E_{H_2O})\frac{\mathrm{d}\chi_{fuel,H_2}}{\mathrm{d}t}. \end{aligned} \tag{3-19}$$

Convective heat transfer is modelled by Newton's law of cooling. Expressions can be found in section B-1. Expressions for the different molar enthalpies are shown in section B-3.

3-3-3 PEN structure

After describing the energy balances for the gas channels, this section looks into the energy balance for the first solid part of the SORC: the PEN structure. Assuming that the heat released during the formation of water vapor is absorbed completely by the PEN, the energy balance is given by

$$\frac{\mathrm{d}m_{PEN}E^*_{PEN}}{\mathrm{d}t} = -P_{SORC}+Q^{react}+2Q^{rad}+Q^{conv}_{PEN,air}+Q^{conv}_{PEN,fuel}, \tag{3-20}$$

where m_{PEN} is the mass of the PEN, E^*_{PEN} is the specific internal energy of the PEN, P_{SORC} is the power produced by the cell, Q^{rad} is the radiative heat transfer between the PEN structure and interconnect, and Q^{react} is the heat released by the electrochemical reaction. Since the PEN is a solid structure with constant mass [62], it follows that

$$\begin{aligned} \frac{\mathrm{d}m_{PEN}E^*_{PEN}}{\mathrm{d}t} &\approx m_{PEN}\frac{\mathrm{d}H^*_{PEN}}{\mathrm{d}t}, \\ &= m_{PEN}c^*_{p,PEN}\frac{\mathrm{d}T_{PEN}}{\mathrm{d}t}, \end{aligned}$$

where H^*_{PEN} is the specific enthalpy of the PEN structure, $c^*_{p,PEN}$ is the specific heat capacity at constant pressure, and T_{PEN} is the temperature of the PEN structure. The mass of an electrode supported PEN can be approximated by

$$m_{PEN} \approx (1-\varepsilon_{el,fuel})V_{PEN}\rho_{PEN},$$

where $\varepsilon_{el,fuel}$ is the porosity of the electrode that supports the PEN, V_{PEN} is the volume of the PEN, and ρ_{PEN} is the density of the structure. This expression is valid, since the densities of the electrodes and electrolytes are roughly the same and the fuel electrode is often the thickest part of the structure, see for example [22] where the fuel electrode makes up 91 % of the PEN. The electrolyte is kept as thin as possible, because it is the part with the largest specific ohmic resistance [18].

The output power of the cell is given by

$$\begin{aligned} P_{SORC} &= iU_{cell}, \\ &= \bar{P}A_s, \end{aligned}$$

where $\bar{P}$ is the power density and U_{cell} is the cell voltage, which is obtained from the electrochemical model. The electrochemical model is covered in section 3-4.

The total heat released by the electrochemical reaction is given [28], [44], [61], [64] by

$$Q^{react} = -\Delta H_r R_{H_2}, \tag{3-21}$$

where ΔH_r is the molar enthalpy of reaction of the electrochemical reaction in the cell. An expression is given in section B-4.

Radiative heat transfer between the PEN structure and interconnect is modelled by radiation between two parallel grey bodies, as shown in section B-2. Convective heat transfer is modelled by Newton's law of cooling, for which expressions can be found in section B-1.

3-3-4 Interconnect

The last energy balance is used to describe the temperature change of the interconnect and is given by

$$\frac{\mathrm{d}m_{int}E^*_{int}}{\mathrm{d}t} = -2Q^{rad} + Q^{conv}_{int,fuel} + Q^{conv}_{int,air}, \tag{3-22}$$

where m_{int} is the mass and E^*_{int} is the specific internal energy of the interconnect. It is important to notice that the repeated cell assumption allows to only consider one interconnect in the model. Considering two interconnects with different temperatures violates the repeated cell assumption, since the interconnect is enclosed by an air and fuel channel. The choice was made to slice the interconnect in two parts for Figure 3-1, but an equivalent representation would be achieved by slicing the PEN in two parts and taking the interconnect as the middle of each unit cell. However, from a physical point of view, it makes more sense to consider the PEN structure as the center of the cell.

The interconnect is a solid with a constant mass. Therefore,

$$\frac{\mathrm{d}m_{int}E^*_{int}}{\mathrm{d}t} = m_{int}c^*_{p,int}\frac{\mathrm{d}T_{int}}{\mathrm{d}t},$$

where $c^*_{p,int}$ and T_{int} are the specific heat capacity and temperature of the interconnect, respectively. The mass of the interconnect is calculated by

$$m_{int} = V_{int}\rho_{int},$$

where V_{int} is the volume of the interconnect and ρ_{int} is its density.

Radiative heat transfer is modelled as radiation between two parallel grey surfaces and convective heat transfer is modelled using Newton's law of cooling. Expressions for these types of heat transfer are given in section B-2 and section B-1, respectively.

3-4 Electrochemical model

The electrochemical model is the last part of the model and used to relate the cell voltage and cell current. It is based on the way it is usually defined for SOFC models. It should be noted that there is no fundamental difference between the electrochemical model of an SOFC and an SOEC, as shown in Appendix C. The current density in SOFC mode is defined as positive and negative in SOEC mode.

The cell voltage of an SOFC is presented by multiple authors [19], [21], [38], [65] as

$$U_{cell} = U_{Nernst} - \eta_{ohm} - \eta_{act} - \eta_{conc}, \tag{3-23}$$

where U_{cell} is the cell voltage, U_{Nernst} is the open circuit voltage (OCV) also known as Nernst voltage or reversible voltage, η_{ohm}, η_{act}, and η_{conc} are the ohmic, activation, and concentration overpotential, respectively. These overpotentials represent different sources of losses in the system [18].

- Ohmic overpotentials are a result of ionic and electronic resistance of the electrolyte and electrodes.
- Activation overpotentials occur because of an energy barrier of the electrochemical reaction that has to be overcome.
- Concentration overpotentials originate from mass transfer through the electrodes, which results in slightly different compositions at the TPB, compared to the bulk flow.

3-4-1 Nernst equation

The Nernst equation gives an expression for the reversible cell voltage and shows how this voltage changes as a function of gas composition. It can be derived from Gibbs free energy, which represents the maximum amount of work that can be extracted from the cell.

The Nernst potential [18], [55] is given by

$$U_{Nernst} = U_0 + \frac{RT_{PEN}}{2F} \ln\left(\frac{a_{H_2}\sqrt{a_{O_2}}}{a_{H_2O}}\right),$$

where U_0 is the voltage at standard conditions, and a_{H_2}, a_{O_2} and a_{H_2O} are the activities of the chemical species. For ideal gas mixtures [18], these are given by

$$a_l = \frac{p_l}{p^0}, \quad l \in \{H_2, H_2O, O_2\},$$

where $p^0 = 1\,\text{bar}$ is the standard pressure and p_l is the partial pressure of component l . Since the pressure inside the fuel and air channel is assumed to be $p = 1\,\text{bar}$, it follows that

$$\begin{aligned} a_{H_2} &= \chi_{fuel,H_2}, \\ a_{H_2O} &= 1 - \chi_{fuel,H_2}, \\ a_{O_2} &= \chi_{air,O_2}. \end{aligned}$$

Using these expressions for the activity of the different species, it follows that

$$U_{Nernst} = U_0 + \frac{RT_{PEN}}{2F} \ln\left(\frac{\chi_{fuel,H_2}\sqrt{\chi_{air,O_2}}}{1-\chi_{fuel,H_2}}\right), \tag{3-24}$$

where U_0 is given by

$$U_0 = -\frac{\Delta g_r}{2F},$$

where Δg_r denotes the molar Gibbs free energy change of reaction on a per mole basis.

Temperature dependence of the Nernst equation can be taken into account by using a temperature dependent expression for U_0. Linear fitting of data presented in Table 2.1 of [55] for the Gibbs free energy change of reaction for the formation of water vapor, gives the following relation for U_0

$$U_0 = 1.2708 - 2.738 \times 10^{-4} T_{PEN}.$$

3-4-2 Ohmic overpotentials

Ohmic overpotentials represents resistance to electrical current flow through the electrodes and ionic flow through the electrolyte. It is proportional to the current density [22], [44],

$$\begin{aligned} \eta_{ohm} &= r_{ohm}(T_{PEN})j, \\ r_{ohm}(T_{PEN}) &= \frac{\delta_{el,air}}{\kappa_{el,air}} + \frac{\delta_{elec}}{\kappa_{elec}(T_{PEN})} + \frac{\delta_{el,fuel}}{\kappa_{el,fuel}}, \end{aligned} \tag{3-25}$$

where r_{ohm} is the specific ohmic resistance, $\delta_{el,air}$, δ_{elec} and $\delta_{el,fuel}$ are the thickness of the air electrode, electrolyte and fuel electrode, respectively, and $\kappa_{el,air}$, κ_{elec} and $\kappa_{el,fuel}$ indicate the conductivity of the air electrode, electrolyte, and fuel electrode, respectively. The ionic conductivity of a PEN structure made from YSZ is given by

$$\kappa_{elec}(T_{PEN}) = 33.4 \times 10^3 \exp\left(\frac{-10.3 \times 10^3}{T_{PEN}}\right).$$

The term related to the ionic resistance of the electrolyte is often the largest contributor and the only term for which a temperature dependence is taken into account.

3-4-3 Activation overpotentials

The activation overpotential arises from an energy barrier that restrains the electrochemical reaction from happening. It is commonly expressed by the BV equation [18], [21], [43]

$$j = j_{0,electrode}\left(\exp\left(\beta\frac{2F\eta_{act,electrode}}{RT_{PEN}}\right) - \exp\left(-(1-\beta)\frac{2F\eta_{act,electrode}}{RT_{PEN}}\right)\right),$$

where $j_{0,electrode}$ is the exchange current density which represents the rate at which the forward and backward reaction in Equation (3-1) happen when the current density is $0\,\mathrm{A/m^2}$, and β is a symmetry factor that expresses how the forward and backward reaction in a cell are affected by a change in overpotential. For most reactions and materials, it ranges from 0.2 to

0.5 [18]. An often used value is $\beta = 0.5$ [26], [29], [38], [65], which makes it possible to rewrite the implicit expression into the following explicit expression,

$$\eta_{act,electrode} = \frac{RT_{PEN}}{F} \sinh^{-1}\left(\frac{j}{2j_{0,electrode}}\right).$$

Accounting for both air and fuel side, gives

$$\eta_{act} = \frac{RT_{PEN}}{F}\left(\sinh^{-1}\left(\frac{j}{2j_{0,fuel}}\right) + \sinh^{-1}\left(\frac{j}{2j_{0,air}}\right)\right), \tag{3-26}$$

where $j_{0,fuel}$ and $j_{0,air}$ are the exchange current densities for the fuel and air electrode, respectively. A common choice [22] is to take

$$j_{0,fuel} = \gamma_{fuel}\left(\frac{p_{H_2}}{p_{amb}}\right)^{\alpha_1}\left(\frac{p_{H_2O}}{p_{amb}}\right)^{\alpha_2} \exp\left(-\frac{E_{act,fuel}}{RT_{PEN}}\right),$$
$$j_{0,air} = \gamma_{air}\left(\frac{p_{O_2}}{p_{amb}}\right)^{\alpha_3} \exp\left(-\frac{E_{act,air}}{RT_{PEN}}\right),$$

where $E_{act,air}$ and $E_{act,fuel}$ represent activation energies, and γ_{air}, γ_{fuel}, α_1, α_2, and α_3 act as fitting parameters. Using the fact that $p_{amb} = p = 1\,\text{bar}$, these expressions can be rewritten to

$$j_{0,fuel} = \gamma_{fuel}{\chi_{fuel,H_2}}^{\alpha_1}(1-\chi_{fuel,H_2})^{\alpha_2} \exp\left(-\frac{E_{act,fuel}}{RT_{PEN}}\right),$$
$$j_{0,air} = \gamma_{air}{\chi_{air,O_2}}^{\alpha_3} \exp\left(-\frac{E_{act,air}}{RT_{PEN}}\right).$$

The benefit of these expressions is that they are widely used. However, they might underestimate the activation overpotential when current and temperature are high [22]. A different model is proposed by Kazempoor and Braun [22], but since this model is used less often it might be harder to find parameters for this model.

3-4-4 Concentration overpotentials

The concentration overpotential represents losses due to concentration differences between bulk and at reaction side near the electrolyte. These differences in concentration are a result of mass transfer in which matter is transported through the electrodes from and to the reaction site. It follows from considering the difference in Nernst potential due to the difference in concentration,

$$\eta_{conc} = U_{Nernst} - U_{Nernst,TPB},$$

where $U_{Nernst,TPB}$ is the Nernst voltage based on the fuel and air compositions at the TPB. Applying Equation (3-24), it follows that

$$\eta_{conc} = \frac{RT_{PEN}}{2F} \ln\left(\frac{\chi_{fuel,H_2}(1-\chi_{fuel,H_2,TPB})\sqrt{\chi_{air,O_2}}}{\chi_{fuel,H_2,TPB}(1-\chi_{fuel,H_2})\sqrt{\chi_{air,O_2,TPB}}}\right), \tag{3-27}$$

where the mole fractions $\chi_{air,O_2,TPB}$ and $\chi_{fuel,H_2,TPB}$ follow from Fick's law of diffusion [22], [43], [45], [66].

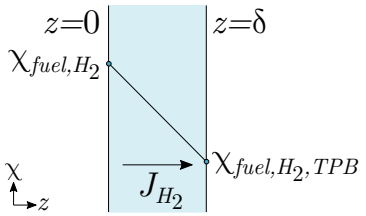

Figure 3-4: Schematic overview of concentration gradient of hydrogen through fuel electrode. z represents the distance through the medium, δ is the thickness of the electrode, χ_{fuel,H_2} is the mole fraction in the bulk, and $\chi_{fuel,H_2,TPB}$ is the mole fraction at the TPB, J_{H_2} is the diffusion flux of hydrogen through the medium.

A simplified overview of the diffusion of hydrogen through the fuel electrode is shown in Figure 3-4. Diffusion inside the channels themselves is not taken into account.

The diffusion in the fuel electrode is modelled as equimolar counter diffusion [43], [67], which means that the diffusion flux of hydrogen J_{H_2} is equal to the diffusion flux of steam J_{H_2O}, but in opposite direction. Therefore,

$$J_{H_2} = -J_{H_2O},$$

and the diffusion flux is given by Fick's law

$$J_{H_2} = -D_{eff,fuel}\frac{\mathrm{d}c_{H_2}}{\mathrm{d}z}, \tag{3-28}$$

where $D_{eff,fuel}$ is the effective diffusivity, c_{H_2} is the hydrogen concentration, and z is the distance through the electrode. Fick's law describes the system at steady-state conditions. This means that the flux of hydrogen has to be equal to the hydrogen production

$$J_{H_2} = \frac{j}{2F}. \tag{3-29}$$

Since ideal gasses are considered, it is also true that

$$\mathrm{d}c_{H_2} = \frac{1}{RT_{PEN}}\,\mathrm{d}p_{H_2}\,. \tag{3-30}$$

The partial pressure of hydrogen is defined as

$$p_{H_2} = \chi_{fuel,H_2}p. \tag{3-31}$$

Combining Equation (3-28), Equation (3-29), Equation (3-30), and Equation (3-31) gives the following expression for the mole fraction of hydrogen at the TPB

$$\chi_{fuel,H_2,TPB} = \chi_{fuel,H_2} - \frac{RT_{PEN}\delta_{el,fuel}j}{2FD_{eff,fuel}p}. \tag{3-32}$$

Expressions for the effective diffusivity are shown in section B-5. It considers both molecular and Knudsen diffusion, which both have to be considered. This follows from calculating the Knudsen number, which is given by

$$N_{Kn} = \frac{\lambda}{2\bar{r}},$$

where λ is the mean free path for a gas molecule in the porous electrode and $\bar{r}$ is the mean pore radius of the electrode. It is necessary to consider both types of diffusion if this number is between 0.01 and 10 [68]. Smaller numbers make it possible to neglect Knudsen diffusion and only consider molecular diffusion, while numbers larger than 10 allow ignoring molecular diffusion.

An approximation for the mean free path can be obtained from [56]

$$\lambda = \frac{1}{4\sqrt{2}\pi\rho_n r_{mol}^2},$$

where ρ_n is the number of molecules per m^3 and r_{mol} is the radius of the molecule. As a rule of thumb, $r_{mol} \approx 1.0 \cdot 10^{-10}$ m [56]. The number density can be calculated from the ideal gas law as

$$\rho_n = \frac{\frac{n}{V}}{N_A},$$
$$\frac{n}{V} = \frac{p}{RT},$$

where $N_A = 6.022 \cdot 10^{23}$/mol is the Avogadro number. Assuming an operating temperature of 800 °C, it follows that the mean free path in the gas is $8.34 \cdot 10^{-7}$ m, which means that both molecular and Knudsen diffusion have to be taken into account for pore diameters between 0.0834 and 83.4 µm. Kazempoor and Braun [22] and Chan, Khor, and Xia [43] report a pore diameter of the electrodes of 1 µm, which shows that both Knudsen and molecular diffusion are important for fuel cells.

Diffusion in the air electrode is modelled as unimolecular diffusion [43], [67]. Thus,

$$N_{O_2} = -D_{eff,O_2}\frac{\mathrm{d}c_{O_2}}{\mathrm{d}z} + \chi_{air,O_2}N_{O_2}, \tag{3-33}$$

where N_{O_2} is the molar flux of oxygen, D_{eff,O_2} is the effective diffusivity, and c_{O_2} is the concentration of oxygen.

Similar conditions hold for the air channel as for the fuel channel. Production of oxygen is equal to the diffusion flux of oxygen J_{O_2},

$$J_{O_2} = \frac{j}{4F}. \tag{3-34}$$

It follows from the ideal gas law that

$$\mathrm{d}c_{O_2} = \frac{1}{RT_{PEN}}\,\mathrm{d}p_{O_2}\,. \tag{3-35}$$

The partial pressure of oxygen is defined as

$$p_{O_2} = \chi_{air,O_2}p. \tag{3-36}$$

Combining Equation (3-33), Equation (3-34), Equation (3-35), and Equation (3-36) it follows that the molar fraction of oxygen at the TPB is given by

$$\chi_{air,O_2,TPB} = 1 - (1 - \chi_{air,O_2})\exp\left(\frac{RT_{PEN}\delta_{el,air}j}{4FD_{eff,O_2}p}\right), \tag{3-37}$$

where the effective diffusion coefficient is described in section B-5 and considers both molecular and Knudsen diffusion.

3-5 Conclusion

A dynamic 0D SORC model was developed. The model describes one single cell, which is assumed to represent the performance of a complete stack. Dynamic material balances were used to describe the gas composition in the fuel and gas channels. The temperature of the gas channels, PEN structure, and interconnect were modelled with dynamic energy balances. The relation between the current density and the cell voltage is described by static relations, because this part of model is much faster than the other components of the model. Time constants for the electrochemical model are in the order of milliseconds, while the material and energy balances are in the order of seconds and minutes. A summary of the dynamic equations can be found in section 5-4. An overview of parameter values is given in Appendix A.

Chapter 4

SORC model validation

A model is of little use if it is unknown how well it describes the system of interest. Therefore, it is important to validate the model from chapter 3. Validation is done by comparing cell voltage-current density (U-j) curve results from the 0D model with experimental and modelling data from [22] and a set of experimental data obtained from the French Alternative Energies and Atomic Energy Commission (CEA) as part of the Balance project[1]. Comparison of U-j curves makes it possible to validate the electrochemical model and, to a lesser extent, the steady-state material balances. The only parts of a U-j curve where the effects of the material balances can be observed are at the current densities limits where the SORC starts to run out of fuel. This is the region where the concentration overpotential starts to show its effects in the form of a sharp rise in voltage when running as SOEC and sharp decline in voltage when operated as SOFC. This sudden change only occurs when fuel concentrations are low. Therefore, if the model shows an increased change in voltage at the same time as observed in data from literature, this is an indication of correct material balances. Suitable data was not found in literature for validation of the energy balances.

Goodness of fit of the 0D model with respect to the datasets is quantified by the normalized root mean squared error (NRMSE) and mean absolute percentage error (MAPE). Normalization for the NRMSE is based on the range of values of the original data. Therefore, the NRMSE is defined by

$$NRMSE = \frac{\sqrt{\frac{1}{\mathcal{N}_U}\sum_{l=1}^{\mathcal{N}_U}\left(U_{cell,l} - U_{cell,l}^{ref}\right)^2}}{U_{cell,max}^{ref} - U_{cell,min}^{ref}} \cdot 100\,\%, \tag{4-1}$$

where U_{cell} represents the estimated cell voltage, U_{cell}^{ref} is the actual value obtained from data, $U_{cell,max}^{ref} - U_{cell,min}^{ref}$ is the range of the actual data, and $\mathcal{N}_U$ is the total number of data points in the dataset.

[1] https://www.balance-project.org/

The MAPE is defined as

$$MAPE = \frac{1}{\mathcal{N}_U} \sum_{l=1}^{\mathcal{N}_U} \left| \frac{U_{cell,l} - U_{cell,l}^{ref}}{U_{cell,l}^{ref}} \right| \cdot 100\,\%. \tag{4-2}$$

First, the model is compared to single-cell U-j curve data taken from [22]. Next, the data supplied by CEA is used to estimate parameter values for the activation electrochemical model. This data comes from a small stack consisting of 25 cells instead of a single-cell experiment. Therefore, this dataset could be seen as an attempt to bridge single-cell testing and system level testing. The chapter ends with a conclusion.

4-1 Validation based on experimental and modelling data from a single-cell SORC

A 1D dynamic model of a fuel electrode supported internal reforming SORC is presented by Kazempoor and Braun [22] along with experimental results. The model consists of an electrochemical model, material balances, energy balances, and momentum balances for a single channel of a $5 \times 5\,\text{cm}$ single cell with an active area of $4 \times 4\,\text{cm}$. The results in the paper are obtained by assuming that the interconnect temperature is fixed and equal to the inlet temperature of the gasses, while the temperature of other parts are allowed to vary. The reason for such an isothermal assumption is that the experimental setup consisted of only one cell. Such a cell is not able to operate on its own, because it would lose too much heat. Therefore, the experimental setup is placed in a furnace to counteract these effects. The result is that the temperature of the experimental setup is close to the temperature inside the furnace. Unfortunately, the only useful data presented in the paper are a U-j curve and thermoneutral voltage for an SORC operating on a 50 mol % H_2/50 mol % H_2O fuel mixture at an operating temperature of 850 °C.

Model parameters are taken the same as the ones presented in the paper as much as possible. Unfortunately, some parameters were not given in the publication and the activation model is different from the one described in section 3-4. The parameters that were not mentioned in the paper were taken from publications referred to in [22] and are shown in Table 4-1, including the sources for these values. The parameters for the activation model were taken from a previous paper describing the same model, but only applied to the SOEC part of the model, [20]. Values for the density and specific heat capacity of the PEN structure were not found in any of the papers referred to. Therefore, these values were taken from [61]. It should be mentioned that values for the density and specific heat capacity of the interconnect are not included in this table. These parameters have no influence on the model, since it is assumed that the interconnect operates at a constant temperature.

It is assumed that the flow rates mentioned in the paper are defined at standard temperature and pressure (STP) conditions, which is assumed to be 0 °C and 1 bar. This definition is mentioned by Calvert [69] as being the definition of the STP used by the International Union of Pure and Applied Chemistry (IUPAC). Another assumption had to be made for the number of channels. There is no mention of the number of channels, but a previous paper by the same authors mentions that the interconnect ribs are assumed to have the same thickness as the

interconnect [21]. Applying this assumption results in approximately 18 gas channels per side.

The following sections describe the comparison of the model with the data in the paper and possible sources for the differences between the 0D model and the data from the paper.

Table 4-1: Assumed values for missing parameter values in [22].

Parameter	Value
Number of channels	18*
Emissivity of interconnect ϵ_{int}	0.8†
Emissivity of PEN ϵ_{PEN}	0.1†
Nusselt air channel Nu_{air}	4†
Nusselt fuel channel Nu_{fuel}	4†
Density PEN ρ_{PEN} [kg/m^3]	$6.6 \cdot 10^3$‡
Specific heat capacity PEN $c^*_{p,PEN}$ [J/(kg K)]	$0.4 \cdot 10^3$‡
OCV at STP U_0 [V]	$1.2723 - 2.7645 \cdot 10^{-4} T_{PEN}$¶
Activation energy air electrode $E_{act,air}$ [J/mol]	$110 \cdot 10^3$§
Activation energy fuel electrode $E_{act,fuel}$ [J/mol]	$100 \cdot 10^3$§
Exponent α_1	0.5§
Exponent α_2	0.1§
Exponent α_3	0.5§
Pre-exponential factor γ_{air} [A/m^2]	$7 \cdot 10^8$§
Pre-exponential factor γ_{fuel} [A/m^2]	$5.5 \cdot 10^8$§

* Based on modelling approach in [21] where rib thickness was taken the same as the interconnect thickness.
† Value taken form [21]
‡ Value taken from [61]
¶ Value taken from [70]. This value was also used in [20].
§ Value taken from [20]

4-1-1 Comparison of voltage-current curves

A comparison of the U-j curve of the model and experimental data from the paper and the results from the model described in chapter 3 is shown in Figure 4-1. The model shows good agreement with the SOEC part of the data, but the SOFC part shows some departure from the curve presented in the paper, especially at high current densities. The NRMSE for the model is 6.68 %, while the MAPE is 3.7 %. A good fit for the SOEC part of the model was to be expected, since the parameters taken for the activation model were taken from a previous paper which only considered the SOEC part of the SORC operating range. The next section discusses possible sources of error.

The paper does not provide any data regarding the temperature of the cell component as a function of the current density. It does mention a thermoneutral voltage, which might give a little bit of insight in the correctness of the energy balance. Figure 4-2 shows the PEN temperature as a function of the cell voltage. It is found that the thermoneutral voltage of the model is 1.285 V, as shown in Figure 4-2. The thermoneutral voltage mentioned in the paper is 1.288 V at 850 °C. The prediction by the model is close to this value, which

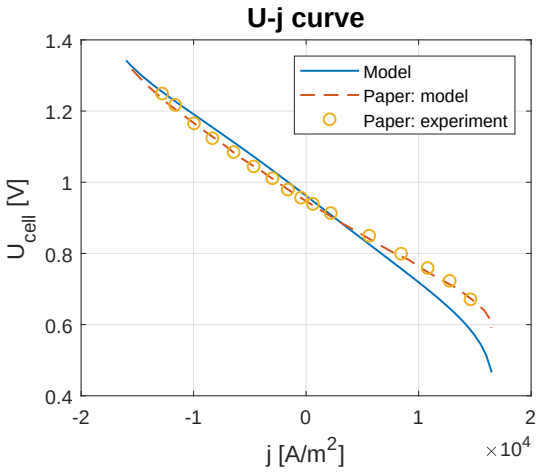

Figure 4-1: U-j curves for the 0D model (blue line) compared to model (dashed red line) and experimental data (yellow circles) from [22].

might be an indication that the energy balance produces comparable results to the one in the paper. The difference of 0.003 V could arise from a difference in the enthalpy of reaction. Unfortunately, the enthalpy of reaction is not listed in the paper.

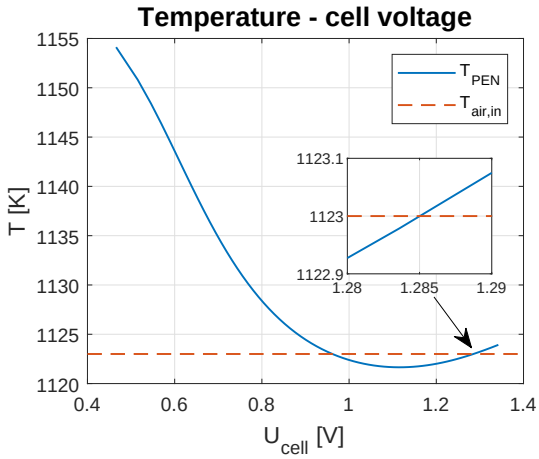

Figure 4-2: PEN structure temperature as a function of cell voltage for the 0D model. T_{PEN}: PEN temperature, $T_{air,in}$: air inlet temperature.

4-1-2 Differences between developed model and data from paper

The difference between the U-j curves could have multiple sources, including

- Different activation overpotential model,
- Slightly different expressions for the ohmic and concentration overpotential,
- Different values for densities and specific heat capacities of PEN structure,

- The paper describes a 1D model instead of 0D, which results in more complex energy and material balances.

First, the difference in activation model is investigated by implementing the activation model discussed in the paper in the 0D model. Next, differences in the ohmic and concentration overpotential are discussed. The last part discusses the difference in model dimension.

Different expressions for the activation model

The first difference between the model presented in chapter 3 and the model presented in [22] is a different activation overpotential model. The paper uses an uncommon representation. Apart from that, the paper is not completely clear on which temperature it uses as a reference temperature for the expressions in this part of the model, both 750 and 850 °C are mentioned in the model calibration part of the paper. Figure 4-3 shows the model response for both reference temperatures, from which it can be concluded that the correct reference temperature is probably 750 °C. The NRMSE and MAPE for this model are reduced to 2.59 and 1.06 %, respectively.

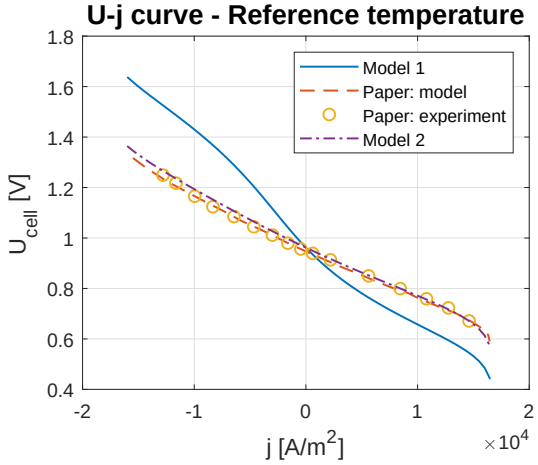

Figure 4-3: U-j curves for the 0D model with the activation model presented in [22], but with different reference temperatures for the activation overpotential model. Model 1: 850 °C, Model 2: 750 °C. Steam partial pressure expressed in Pa. Paper: model: model data from the paper, Paper: experiment: experimental data from the paper.

Unfortunately, this is not the only point with lack of clarity. The expression for the exchange current density is not clear, because units seem to be mixed up in this equation. The expression for the exchange current density of the fuel electrode $J_{0,FE}$ is given by,

$$J_{0,FE} = J^*_{H_2} \frac{\left(\frac{p_{H_2}}{p^*_{H_2}}\right)^{\frac{\alpha_{a,FE}}{2}} (P_{H_2O})^{1-\frac{\alpha_{a,FE}}{2}}}{1+\left(\frac{p_{H_2}}{p^*_{H_2}}\right)^{0.5}}, \tag{4-3}$$

where p_{H_2} is the partial pressure of hydrogen in atm, P_{H_2O} is the partial pressure of steam, $\alpha_{a,FE}$ is a charge transfer coefficient, and expressions for $J^*_{H_2}$ and $p^*_{H_2}$ are given by the paper

itself. It is mentioned that all lower case partial pressures are in atm. The steam partial pressure P_{H_2O} is shown with a capital letter, which make it look as if this partial pressure should be expressed in Pa. This approach gives a reasonable fit as shown in Figure 4-3. However, this expression produces unrealistic values for the activation potential of the fuel electrode, as shown in Figure 4-4, where model 2, the model with the steam partial pressure in Pa, shows unrealistic small values when compared to the activation overpotential of the air electrode. Implementing the model with the assumption that the steam partial pressure is given in atm (model 3), shows more realistic values for the activation overpotential. However, this model is a worse fit of the U-j curve, as shown in Figure 4-5. It can be concluded that the expression with the partial pressure in atm is probably the correct expression, although the expression with Pa is probably used, since it shows a better agreement with the data from the paper.

The difference in activation overpotential model has a big influence on the U-j curve of the model. It is likely that this is the main contributor to the differences between the 0D model and the paper.

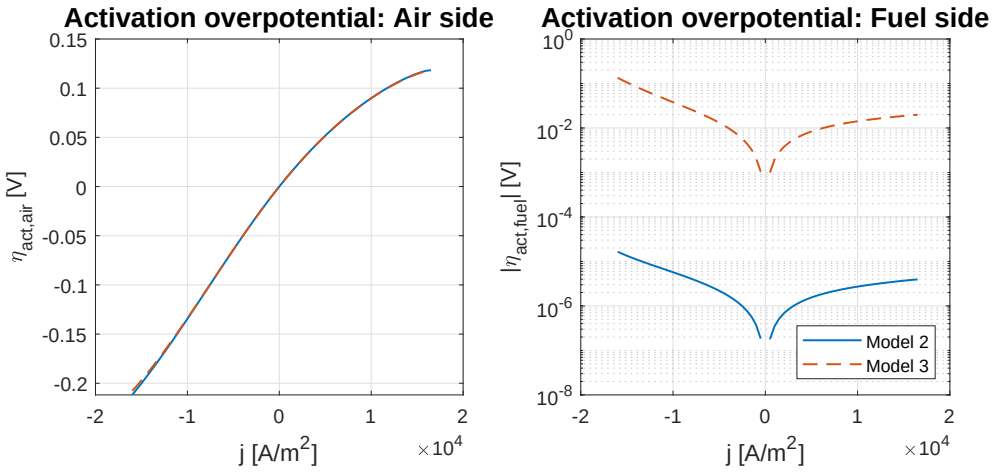

Figure 4-4: Activation overpotentials for the fuel and air electrode for the 0D model with the activation model presented in [22]. Model 2: Partial pressure of steam in Equation (4-3) in Pa, Model 3: Partial pressure of steam in atm. The activation overpotential of the fuel electrode shows the absolute value, but is negative in the SOEC region.

Differences in ohmic and concentration overpotential

The ohmic overpotential presented in the paper does not only consider the resistance of the PEN, but also includes a term for the interconnect. It is unlikely that this term has a big influence on the U-j curve, because the electrolyte is the largest contributor to the ohmic overpotential, to which more than 99.5 % can be attributed. The resistance of the interconnect would contribute less than 0.1 % to the ohmic resistance.

A similar principle holds for the concentration overpotential. Its contribution to the overpotentials is less than 10 % in the current density range $-15 \cdot 10^3$ to $11 \cdot 10^3\,\mathrm{A^2/m}$. This corresponds to less than 2 % of the cell voltage. The concentration overpotential is only important when the system starts to run out of fuel. The expressions in the paper are more

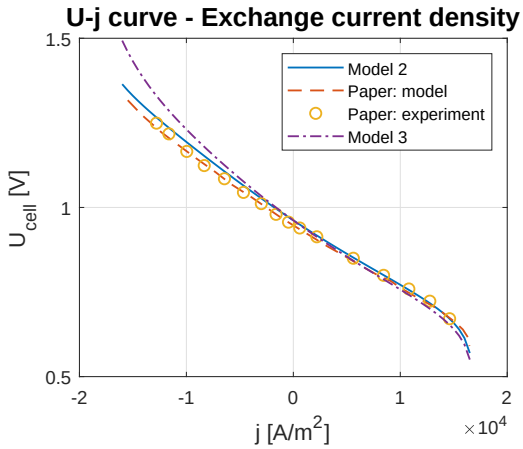

Figure 4-5: U-j curves for the 0D model with the activation model presented in [22], but with different expressions for the exchange current density of the fuel electrode. Model 2: steam partial pressure in Pa, Model 3: steam partial pressure in atm. Paper: model: model data from the paper, Paper: experiment: experimental data from the paper.

elaborate than the ones in the developed model and should result in a slightly larger concentration overpotential. Considering the fact that its contribution is small, it is not expected that implementation of the concentration overpotential presented in the paper would make a big difference.

The differences between the model and the paper are not attributed to the differences in the ohmic and concentration overpotential, due to their small contributions to the cell voltage.

Different values for PEN structure properties

Another source of error might be incorrect values for the density and specific heat capacity of the PEN structure. To test the influence of these terms, the model was run without taking into account the energy balance. If big differences are visible in the U-j curves, this means that the model might be sensitive to changes in the density and specific heat capacity. Variations in these parameters leads to different temperatures inside the system. The comparison between the model with isothermal interconnect and a completely isothermal model is shown in Figure 4-6. The differences are hardly noticeable. It is probable that this source does not contribute much to the error between the model and the paper.

Different dimensions of model

The last reason for the differences between the model and the paper might be that the model in the paper is a 1D model, while the developed model is 0D. The small differences between the 0D model with the activation model presented in [22] and the U-j curves in the paper do not justify the full implementation of the 1D model presented in the paper.

The 1D material balances would probably give comparable results, as both the model from the paper and the developed model seem to run out of fuel around $15 \cdot 10^3\ \mathrm{A}^2/\mathrm{m}$. Also, since the interconnect is assumed to be isothermal, it is expected that the temperature variations

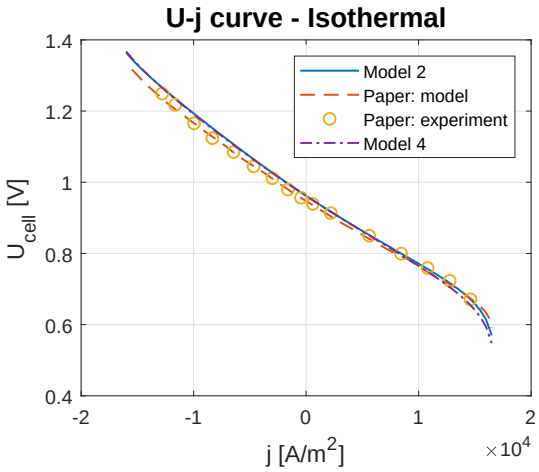

Figure 4-6: U-j curves for the 0D model with the activation model presented in [22], but with different energy balances. Model 2: isothermal interconnect, Model 4: completely isothermal model. Paper: model: model data from the paper, Paper: experiment: experimental data from the paper.

along the cell length are small, which means that differences in the energy balances should not result in large differences.

4-2 Parameter estimation based on experimental small stack SORC data from CEA

A dataset consisting of U-j curves for a small stack was supplied by CEA. The data is obtained from a small stack consisting of 25 fuel electrode supported cells with an active area of $10 \times 10\,\text{cm}$ operating at 700, 750 and 800 °C. The specifications of the stack are shown in Table 4-2. Because of the small size of the stack, it is assumed that the system runs at isothermal conditions. This means that energy balances are not taken into account. It was discussed in section 4-1 that this assumption has minor consequences for the outcome of the model.

This section describes parameter estimation for the parameters of the activation overpotential model such that the U-j curve of the model corresponds with the experimental data obtained from CEA. It was shown in section 4-1 that the parameters of the activation model are important. Furthermore, the activation model parameters are often treated as fitting parameters, because it is not possible to measure them [25]. First, the model is slightly adjusted such that the model is able to process the nitrogen present in the fuel channel during SOFC operation. After that, the approach for estimating the parameters is discussed. Next, it was noticed that there was something peculiar about the datasets; the model runs out of fuel faster than the experimental setup in SOFC mode. This is discussed after which the section ends with the results obtained from estimating the parameters for the activation overpotential model.

Table 4-2: Specifications of the SORC stack at CEA.

Parameter	Value
Number of cells	25
Single cell active area [mm^2]	100×100
Stack dimensions [mm^3]	$205 \times 205 \times 123.5$
Fuel electrode material	Ni-YSZ
Fuel electrode thickness [µm]	345–368
Air electrode material	LSC-CGO and LSC
Air electrode thickness [µm]	40
Electrolyte material	YSZ
Electrolyte thickness [µm]	5–6
Interconnect material	AISI441
Interconnect thickness [mm]	0.2
End plate thickness [mm]	10
Operating pressure [atm]	1
Fuel flow rate [$Nml/(min\,cm^2)$]	7.38
Air flow rate [$Nml/(min\,cm^2)$]	11
Fuel inlet composition in SOEC mode [$H_2/H_2O/N_2$ mol %]	10/90/0
Fuel inlet composition in SOFC mode [$H_2/H_2O/N_2$ mol %]	50/0/50
Air composition	Air*

* Assumed to be 79 % N_2 / 21 % O_2.

4-2-1 Model adaptation to include nitrogen in the fuel channel

Introduction of nitrogen in the fuel channel makes it necessary to make two small alterations of the model to be able to compare the U-j curve of the model with the given data. The model described in chapter 3 does not allow nitrogen in the fuel channel. This can easily be fixed by adding a material balance for the nitrogen and adding nitrogen to the diffusion model of the fuel channel used for computing the concentration overpotential. The new set of material balances is given by

$$\begin{aligned} n_{fuel}\frac{\mathrm{d}\chi_{fuel,H_2}}{\mathrm{d}t} &= (\chi_{fuel,H_2,in} - \chi_{fuel,H_2})\phi_{fuel,in} - R_{H_2}, \\ n_{fuel}\frac{\mathrm{d}\chi_{fuel,N_2}}{\mathrm{d}t} &= (\chi_{fuel,N_2,in} - \chi_{fuel,N_2})\phi_{fuel,in}, \\ n_{fuel,H_2O} &= (1 - \chi_{fuel,H_2} - \chi_{fuel,N_2})n_{fuel}, \end{aligned} \tag{4-4}$$

where χ_{fuel,N_2} is the mole fraction of nitrogen in the fuel channel. Only the steady-state versions are needed for parameter estimation, because the U-j curves are given for steady-state conditions. It follows that

$$\begin{aligned} \chi_{fuel,H_2} &= \chi_{fuel,H_2,in} - \frac{R_{H_2}}{\phi_{fuel,in}}, \\ \chi_{fuel,N_2} &= \chi_{fuel,N_2,in}, \\ n_{fuel,H_2O} &= (1 - \chi_{fuel,H_2} - \chi_{fuel,N_2})n_{fuel}. \end{aligned} \tag{4-5}$$

The second adaptation is to include nitrogen in the diffusion model used for the calculation of the concentration overpotential. According to Kazempoor, Dorer, and Ommi [21], this can be done by considering the following expression for the molecular diffusion coefficient

$$D_l = \frac{1 - \chi_l}{\sum\limits_{\substack{q=1 \\ q \neq l}}^{\mathcal{N}_C} \frac{\chi_q}{D_{l-q}}}, \quad l \in \{H_2, H_2O\}, q \in \{\text{all components present in the gas}\}, \tag{4-6}$$

where D_l is the effective binary diffusion coefficient for component l, χ_l is the fraction of component l in the gas channel, D_{l-q} is the binary diffusion coefficient, and $\mathcal{N}_C$ represents the total number of components present in the gas. Strictly, this expression is only valid if $\chi_l \ll 1$ [71], but this approach was used successfully by Kazempoor and Braun [22], who applied it to systems with hydrogen and steam fractions over 45 %.

4-2-2 Activation overpotential model parameter estimation problem

The activation overpotential parameters were estimated using nonlinear least squares with a trust-region algorithm, because it is able to handle bounds on parameter values [72]. The problem can be formulated as

$$\begin{aligned} \min_X \quad & \left\| U_{cell}(X) - U_{cell}^{ref} \right\|_2^2, \\ \text{s.t.} \quad & X_{min} \leq X \leq X_{max}, \end{aligned}$$

where X is the vector with activation overpotential parameters that need to be estimated, X_{min} represents minimal values and X_{max} represents maximum values for the parameters. The vector X is given by

$$X = \begin{bmatrix} \gamma_{air}, & \gamma_{fuel}, & \alpha_1, & \alpha_2, & \alpha_3, & E_{act,air}, & E_{act,fuel} \end{bmatrix}^T.$$

The elements γ_{air}, γ_{fuel}, $E_{act,air}$, and $E_{act,fuel}$ were only limited by a lower limit of 0. Based on [22], exponents α_1, α_2, and α_3 were given lower limits of 0.1, 0.1, and 0.25, respectively, and upper limits of 1, 1, and 0.5, respectively.

Three datasets are available. Therefore, each dataset is used to estimate different parts of the model. The estimation procedure was

- Estimate the pre-exponential factors γ_{air} and γ_{fuel} from the experimental data at 750 °C
- Estimate the activation energies of the electrodes $E_{act,air}$ and $E_{act,fuel}$ from the experimental data at 800 °C
- Estimate the exponents α_1, α_2, and α_3 from the experimental data at 700 °C

A downside of this approach is that all data is used for parameter estimation, which makes it impossible to appropriately validate the model.

4-2-3 Initial parameters and model fit

The initial set of parameters was taken from [20] and are shown in Table 4-3, next to the final parameter values. The remainder of parameters is taken as shown in Appendix A. Figure 4-7 shows the initial U-j curves obtained from the model next to the experimental curves from CEA and the initial NRMSE and MAPE values are shown in Table 4-4. These curves show two serious issues with the dataset. First, the cell voltages of the model and data in SOFC mode near $j = 0\,\mathrm{A/m^2}$ are not the same while they should be. Close to this point, the cell voltage should be close to the Nernst potential, irrespective of the used overpotential models. The fact that this is not the case for the tests at 700 and 800 °C suggests that the fuel inlet compositions were different for these tests. The absence of a clear peak in cell voltage indicates that the fuel inlet contained steam.

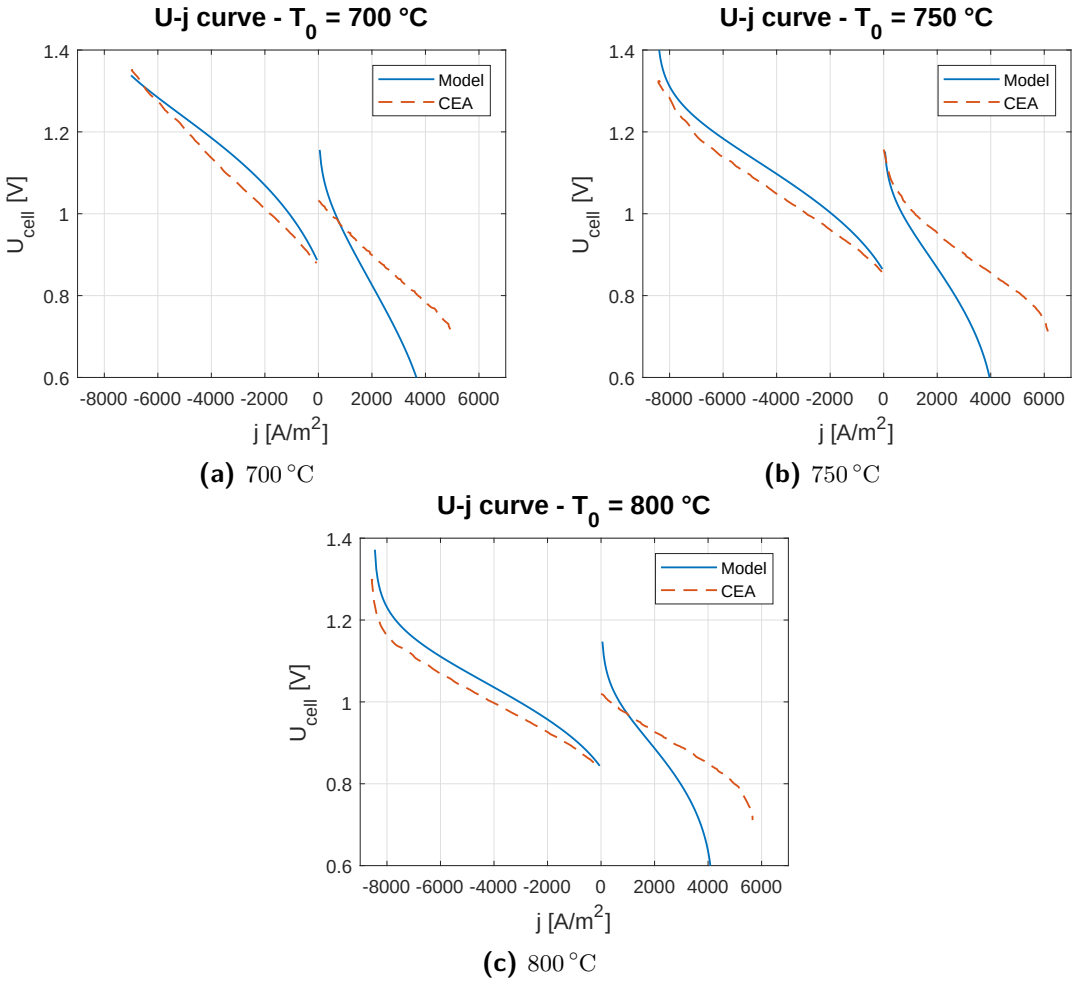

(a) 700 °C **(b)** 750 °C

(c) 800 °C

Figure 4-7: U-j curves of experimental data at multiple operating temperatures from CEA (dashed red lines) compared to U-j curves obtained from the 0D model (blue line) with initial activation overpotential parameters obtained from [20].

Secondly, the model seems to show signs of fuel depletion around $4000\,\mathrm{A/m^2}$, while the ex-

periments were run up to 6000 A/m^2. A quick calculation shows that

$$\begin{aligned} \phi_{H_2,in} &= R_{H_2}, \\ \rightarrow j_{max} &= \frac{2F\chi_{fuel,H_2,in}\phi_{fuel,in}}{A_s}, \\ &\approx 4.87 \cdot 10^3 \, A/m^2, \end{aligned}$$

where $\phi_{H_2,in}$ is the inlet flow rate of hydrogen in the fuel channel and j_{max} is the maximum current density at which the model is able to run, not taking into account concentration overpotentials. Therefore, given the data by CEA, the cell should not be able to run at current densities higher than $4.87 \cdot 10^3 \, A/m^2$. The actual current density at which the system is still able to run should be lower, because the concentrations at the TPB are lower than in the bulk in SOFC mode. The fact that the system ran at higher current densities suggests that the hydrogen fraction in the fuel or the fuel flow rate was higher than reported.

4-2-4 Parameter estimation results

The estimated values of the activation overpotential parameters are shown in Table 4-3. The pre-exponential factors and exponents α_1 and α_3 changed the most, while the rest of the parameters barely changed from their initial guesses. NRMSE and MAPE values for the estimated activation model are shown in the middle two columns of Table 4-4. Improvement is observed for all experiments, which can also be observed from Figure 4-8, where the updated U-j curves are shown next to the experimental ones. The fit is especially good in the SOEC region at 750 and 800 °C. However, the fit in the SOFC region is bad for reasons explained in subsection 4-2-3. To fix this, it was assumed that the experimental setup ran at different fuel inlet compositions, because a different fuel composition can explain both deviations from the experimental data. It was found via manual manipulation of the inlet compositions that better results were obtained when using 0.9 H_2/0.0 H_2O/0.1 N_2 as SOFC inlet compositions at 750 °C and 0.85 H_2/0.15 H_2O/0.0 N_2 at 700 °C and 800 °C, as shown in Figure 4-9. The inlet compositions were manipulated such that the voltage at 0 A/m^2 of the model and the data were close to each other, as well as that the model ran out of hydrogen around the same current density as observed from the experimental data.

The NRMSE and MAPE for the model with different compositions than mentioned by CEA are shown in the last two columns of Table 4-4. The fit between the model and the experiment was considered good enough and no new estimation attempts were carried out.

Table 4-3: Activation overpotential parameter values for the experimental data obtained from CEA.

Parameter	Initial value*	Estimated value
Pre-exponential factor γ_{air} [A/m^2]	$7 \cdot 10^8$	$28.3 \cdot 10^8$
Pre-exponential factor γ_{fuel} [A/m^2]	$5.5 \cdot 10^8$	$13.3 \cdot 10^8$
Activation energy air electrode $E_{act,air}$ [kJ/mol]	110	107
Activation energy fuel electrode $E_{act,fuel}$ [kJ/mol]	100	105
Exponent α_1	0.5	0.1
Exponent α_2	0.1	0.1
Exponent α_3	0.5	0.25

* Initial values were taken from [20]

Table 4-4: Quality of fit of the activation model for the data from CEA for the initial parameter set, estimated parameter set, and estimated parameter set with different fuel inlet composition than reported by CEA (Fuel composition columns). The NRMSE and MAPE are both given as percentage (%).

	Initial parameters		Estimated parameters		Fuel composition	
Experiment	NRMSE	MAPE	NRMSE	MAPE	NRMSE	MAPE
700 °C	15.15	6.77	7.74	3.02	4.95	2.07
750 °C	18.03	6.49	8.28	2.65	3.07	1.23
800 °C	16.20	5.23	7.98	1.82	1.75	0.63

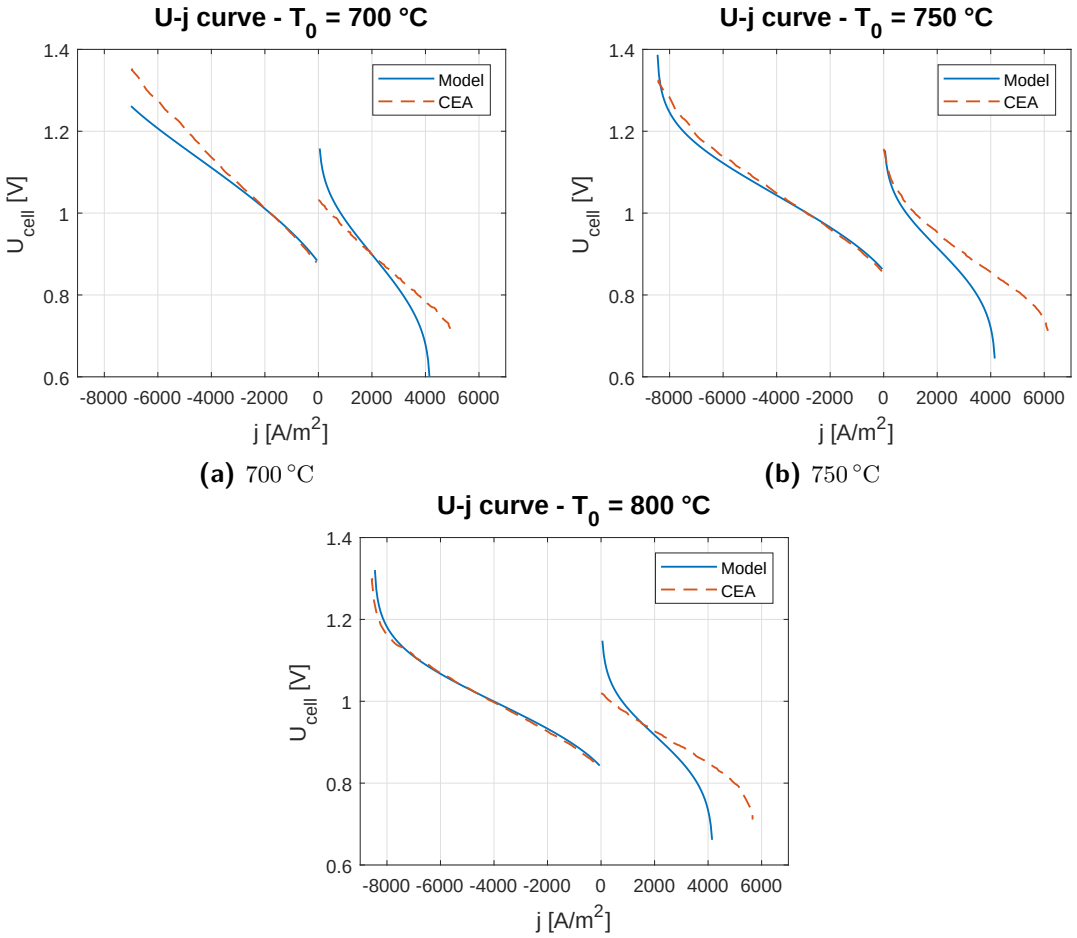

(a) 700 °C **(b)** 750 °C

(c) 800 °C

Figure 4-8: U-j curves of experimental data at multiple temperatures from CEA (dashed red line) compared to U-j curves obtained from the 0D model (blue line) with estimated activation overpotential parameters.

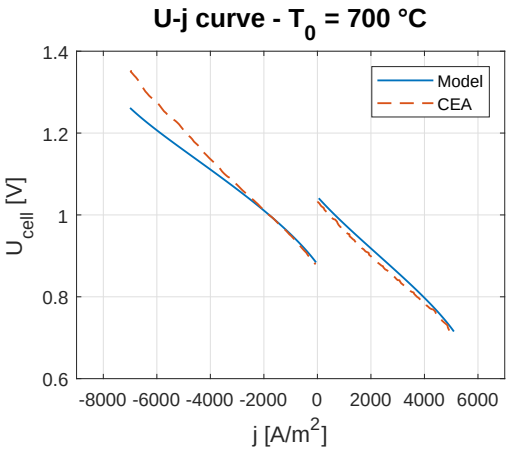

(a) 700 °C, SOFC inlet composition: 0.85 H_2/0.15 H_2O/0.0 N_2

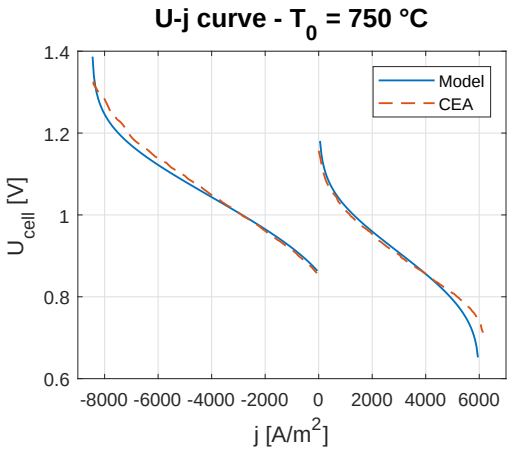

(b) 750 °C, SOFC inlet composition: 0.9 H_2/0.0 H_2O/0.1 N_2

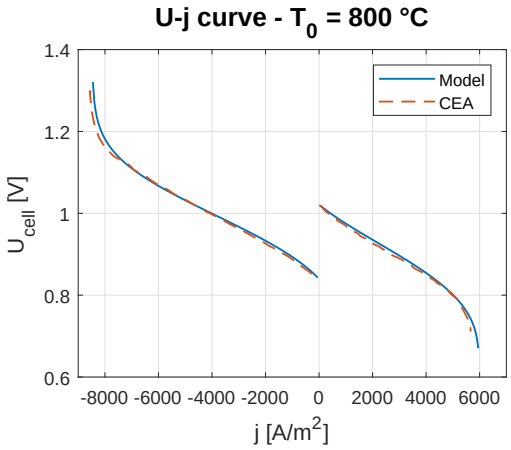

(c) 800 °C, SOFC inlet composition: 0.85 H_2/0.15 H_2O/0.0 N_2

Figure 4-9: U-j curves of experimental data at multiple operating temperatures from CEA (dashed red line) compared to U-j curves obtained from the 0D model (blue line) with estimated activation overpotential parameters, but with different fuel inlet compositions in SOFC mode than stated by CEA.

4-3 Conclusion

This chapter discussed validation of the 0D SORC model described in chapter 3. Validation was only possible based on steady-state U-j curves. This made it possible to validate the electrochemical model and to some extent the material balances.

The first part of the chapter discussed validation of the electrochemical model by comparing the model with data presented in [22]. The model showed decent agreement, especially in SOEC mode. It turned out that the NRMSE was 6.68 %, while the MAPE was 3.7 %. A different activation model was the primary source of the difference between the paper and the model. Implementing the activation model presented in the paper reduced the NRMSE and MAPE to 2.59 and 1.06 %, respectively. Comparison of the U-j curves also gave an idea about the correctness of the material balances. This followed from the current density at which the concentration overpotential started to become noticeable. This only happens at extreme current densities when the system starts to run out of fuel. The model showed this effect around the same current density value as in the paper, which is an indication that the material balance of the fuel channel gives correct values at steady-state.

The second part of the chapter discussed estimation of the activation overpotential parameters based on experimental data of a 25 cell stack from CEA. The estimated model showed great agreement at high temperatures (800 °C), with NRMSE and MAPE values as low as 1.75 and 0.63 %, respectively. At lower temperatures of 700 °C the model shows deviations from the SOEC part of the experimental data. This also showed by the quality of fit values with an NRMSE of 4.95 % and an MAPE of 2.07 %.

Chapter 5

Control problem formulation

The SORC should run in a dynamic environment, connected to the Dutch power grid. However, in order to be able to do this, some conditions have to be guaranteed to be sure that the cells do not break down. This chapter starts with a motivation for control of an SORC and gives an overview of important limitations. After that, the control goal is defined, which is motivated by the grid connection of the SORC. Next, the selection of input and outputs signals is discussed. This part also include a short introduction to disturbance signal and an overview of reference signals. After that, a nonlinear state-space model is presented followed by a summary of the important dynamic equations from chapter 3. After that, a general block diagram representation is given of the controlled SORC. The chapter ends with a small recap of the chapter.

5-1 Motivation for control

The goal of control is to prevent the SORC from breaking down and ensuring that the balance of plant (BOP) power consumption is not higher than needed to keep the system running under fluctuating grid demands. Without control, the operating conditions of the SORC might vary unfavourably as its operating power changes due to variations in grid demands. Uncontrolled fluctuations are a problem, because they can result in inefficient or even damaging operating conditions [37]. Next, an overview of important limitations on parts of the SORC and their cause is presented.

Temperature of the cell. High operating temperatures are preferred, because it results in higher conductivity of the electrolyte. However, cell materials are only able to withstand temperature up to a certain level. Literature mentions several suitable operating ranges. The widest feasible range found for SORCs is 600 to 1000 °C [20], where low temperature ranges are less harsh on the cell materials, while higher temperatures give better performance due to better conductivity of the electrolyte. Typical operating ranges are in the range of 700 to 900 °C for both SOFC [28] and SOEC [73].

Spatial temperature gradients along the cell. Some more elaborate studies consider a limit on the temperature gradient throughout the cell to limit internal stresses. For example, a maximum gradient of 15 K/cm is considered in [22]. It is only possible to enforce such a constraint if the model is at least 1D. It is not possible to formulate spatial gradients as time derivatives, because the spatial gradient and time derivative of the temperature are not directly linked to each other. For example, It is possible to have a time derivative of zero, while the spatial gradient is in the order of 25 K/cm as a result of relative low constant flow rates under constant operating power.

Fuel utilization. Limitations on the fuel utilization have two purposes. First, a lower limit ensures that the BOP does not consume more power than needed, which reduces the amount of fuel wasted. However, fuel utilization also has to be limited by some maximum, since high utilization factors can lead to fuel depletion, which could result in degradation of the cell [41], [44]. Typical utilizations are in the range of 40 to 80 % [73]. A lower limit on the fuel utilization is also meaningful in case unused fuel is recycled. As an example, consider the SORC system with BOP shown in Figure 5-1 where all unused fuel is recycled. The BOP contains all the auxiliary components that are needed to operate the SORC, such as pumps and heaters. In this case, it is important to try to keep the utilization high in order to prevent high energy consumption of the BOP. The unused fuel needs to be cooled down in order to store water and hydrogen in separate tanks. However, before entering the cell, it is necessary to heat up the inlet streams. Therefore, low fuel utilization, which is a result of relative high flow rate, results in unnecessary high energy consumption of the condenser and evaporator.

Maximum amount of oxygen in the air channel. A maximum could be imposed on the oxygen fraction in the air channel to prevent corrosion of metallic components. A maximum of 50 % is proposed in [74].

Based on the foregoing, the following operating conditions are considered safe:

- PEN structure temperature: $700\,^{\circ}\text{C} < T_{PEN} < 900\,^{\circ}\text{C}$;
- oxygen fraction in air channel: $\chi_{air,O_2} < 0.5$;
- hydrogen fraction in fuel channel: $0.1 < \chi_{fuel,H_2} < 0.9$.

Spatial gradients are not considered, because the 0D model does not allow to evaluate them. The SORC is actively controlled on the PEN temperature and the hydrogen fraction in the fuel channel. The hydrogen fraction in the fuel channel is linked to the fuel utilization. The maximum allowable oxygen fraction in the air channel is not expected to be a problem, because high flow rates are expected to be required to cool the cell. See for example Figure 6-1 where it is shown that the variations in the oxygen fraction over the operating points stay between 0.2 and 0.3.

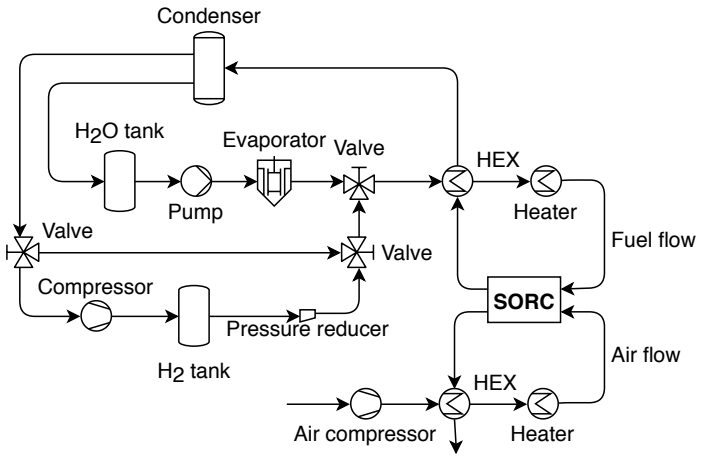

Figure 5-1: Schematic of a possible SORC system including BOP components. HEX: heat exchanger.

5-2 Control goal: power disturbance rejection

A simplified overview of an SORC system connected to a power grid consisting of power producers and consumers is shown in Figure 5-2. A distinction is made between RESs and other energy sources, because most renewable energy sources are variable [12], while it is assumed that other energy sources, such as coal power plants, prefer a constant energy demand. This means that SORCs act as peak load managing devices to limit variations in demand from base load power plants.

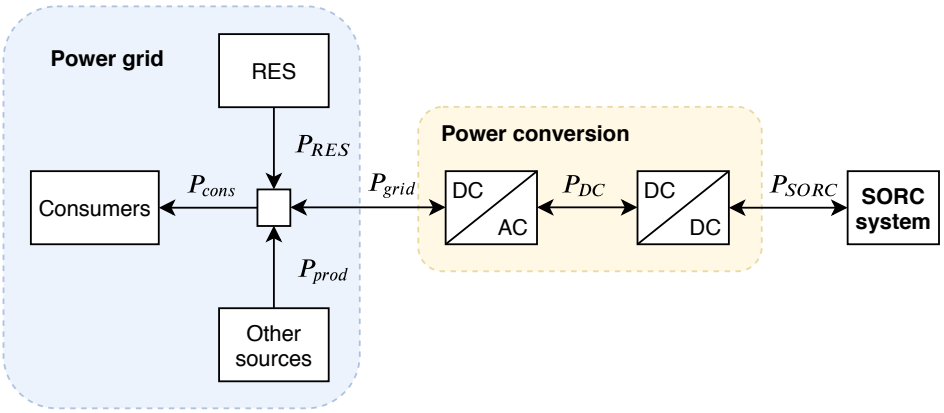

Figure 5-2: Simplified representation of an SORC system connected to a power grid consisting of power producers and consumers. P_{cons}: power consumption, P_{RES}: power produced by variable RESs. P_{prod}: power produced by non-variable power plants, P_{grid}: power demanded by the grid in order to guarantee constant P_{grid}, P_{DC}: Power demanded by the grid at a fixed direct current voltage, P_{SORC}: Power from the SORC system.

It is assumed that the power conversion units operate on their own control which tries to match input and output power of the power conversion part as good as possible. In other words, the power conversion part tries to match the grid power with the power from the

SORC. Therefore, there is no control over the power produced or consumed by the SORC. The operating power of the SORC is dictated by the grid in order to guarantee constant power production from other (non-renewable) energy sources.

Additionally, it is assumed that power conversion components are faster than the time scale of interest. See, for example, [75] where new voltage levels of converters are attained in the order of 0.01 s. This makes it possible to model the power conversion stage by the following static relations

$$\begin{aligned} P_{SORC} &= P_{DC}, \\ U_{cell} &= d_{conv} U_{DC}, \end{aligned}$$

where P_{SORC} represents the power of the SORC at voltage U_{cell}, P_{DC} is the power at a fixed direct current voltage U_{DC}, and d_{conv} is the duty cycle of the converter. The duty cycle is varied by the controller of the converter in order to ensure that input and output power of the converter are equal. This idealization does not take into account voltage ripples which are a result of switching of electronic switches in the converter [55].

Control goal

The approach described in this section results in the following control goal: Drive errors in PEN temperature and hydrogen composition in the fuel channel introduced by a power disturbance to zero twice as fast as the open-loop response of the SORC.

The requirement for closed-loop responses twice as fast as the open-loop was chosen to have a fast responding system, while not enforcing excessive input efforts. Unfortunately, it is unknown what input efforts the system can process. Consideration of dynamics of BOP components would show what performance is obtainable.

The error signal is defined as the difference between the reference and the output signal. The reference signal r is given by

$$r = \begin{bmatrix} r_{T_{PEN}}, & r_{\chi_{fuel,H_2}} \end{bmatrix}^T.$$

The PEN temperature reference signal $r_{T_{PEN}}$ and reference signal for the hydrogen fraction in the fuel channel $r_{\chi_{fuel,H_2}}$ are given by Equation (5-2) and Equation (5-5), respectively. The output signal is given by

$$y = \begin{bmatrix} T_{PEN}, & \chi_{fuel,H_2} \end{bmatrix}^T.$$

From the reference and output signal, it follows that the error signal e is defined as

$$\begin{aligned} e &= r - y, \\ &= \begin{bmatrix} e_{T_{PEN}}, & e_{\chi_{fuel,H_2}} \end{bmatrix}^T, \end{aligned}$$

where $e_{T_{PEN}}$ indicates the error in PEN temperature and $e_{\chi_{fuel,H_2}}$ is the hydrogen fraction error in the fuel channel.

5-3 Selection of input and output signals

An overview of signals associated with the SORC is shown in Figure 5-3. Symbol descriptions are provided in Table 5-1. Not all signals going into the SORC are suitable candidates for input signal and not all signals going out of the SORC are outputs of interest. This section discusses which signals are chosen as inputs, outputs, and disturbance of the SORC, as well as the specification of reference signals.

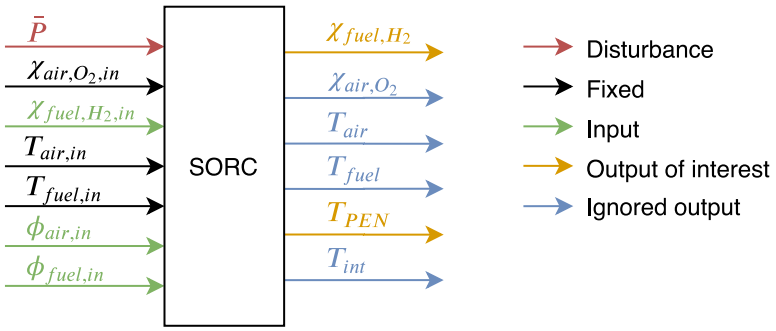

Figure 5-3: Overview of signals associated with the SORC. Descriptions of the symbols can be found in Table 5-1.

Table 5-1: Description of symbols used in Figure 5-3.

Symbol	Description
$\bar{P}$	Power density
T_{air}	Air channel temperature
$T_{air,in}$	Air inlet temperature
T_{fuel}	Fuel channel temperature
$T_{fuel,in}$	Fuel inlet temperature
T_{int}	Interconnect temperature
T_{PEN}	PEN temperature
$\phi_{air,in}$	Air inlet flow rate
$\phi_{fuel,in}$	Fuel inlet flow rate
χ_{air,O_2}	Oxygen fraction in air channel
$\chi_{air,O_2,in}$	Oxygen fraction in air inlet stream
χ_{fuel,H_2}	Hydrogen fraction in fuel channel
$\chi_{fuel,H_2,in}$	Hydrogen fraction in fuel inlet stream

5-3-1 Input signals

No information was found about the dynamics of the input signals due to BOP dynamics. It is assumed that air inlet flow rate $\phi_{air,in}$, fuel inlet flow rate $\phi_{fuel,in}$, and fuel inlet flow composition $\chi_{fuel,H_2,in}$ can be influenced fast enough by valves, pumps, and compressors such that these signals can be used as inputs to the system. Ambient air is used in the system, which means that there is no control over the mole fraction of oxygen in the air inlet $\chi_{air,O_2,in}$. It is assumed that air only consists of nitrogen and oxygen in the composition 79 % N_2 and

21 % O_2, as these are the main components of air [62]. Temperature of the air inlet flow $T_{air,in}$ and fuel inlet flow $T_{fuel,in}$ are taken constant, because it is not known how fast they can be changed, as the timescales of the BOP components are unknown. Both air and fuel gas inlet temperature are fixed at $T_{air,in} = T_{fuel,in} = 750\,^{\circ}\text{C}$.

5-3-2 Output signals

It was already mentioned in section 5-1 that the outputs of interest are the PEN structure temperature T_{PEN} and the hydrogen fraction in the fuel outlet χ_{fuel,H_2}. The oxygen fraction in the air channel χ_{air,O_2} is not controlled as it is expected that the air inlet flow rate $\phi_{air,in}$ is high enough without explicitly controlling the air flow rate, because relatively high air flow rates are expected to keep the cell at its desired temperature.

5-3-3 Disturbance signal

The power density demand from the grid $\bar{P}$ is considered a disturbance on the system. It was already mentioned in section 5-2 that there is no control over the power produced by the SORC, but that a certain power signal is enforced on the system. Therefore, the grid power acts as a disturbance signal on the system. The grid power demand signal is such that the SORC counteracts on the fluctuations that are a result of variations in consumer demand and renewable energy production.

The choice was made to consider power production and consumption curves for the Netherlands in 2017, 2018, and 2019 up to and including October 2019. Figure 5-4 shows power consumption and renewable generation on two days, one in winter and one in summer. Data for power consumption was obtained from TenneT [5], and data for power production by renewable sources was obtained from Energieopwek.nl [6]. The renewable power consists of the variable renewable energy sources solar and wind power. It can be observed that during the summer, the main source of renewable energy is solar energy, while energy from wind is dominant during the winter. Average net power signals for four months throughout the year are shown in Figure 5-5. Additional average net power signals for January 2017 to October 2019 can be found in section E-1. These power curves are the basis for the disturbance signal of the system. Net power P_{net} is defined as

$$P_{net} = P_{cons} - P_{RES}, \tag{5-1}$$

where P_{cons} is the power consumption of the Netherlands and P_{RES} is the power production by wind and solar energy.

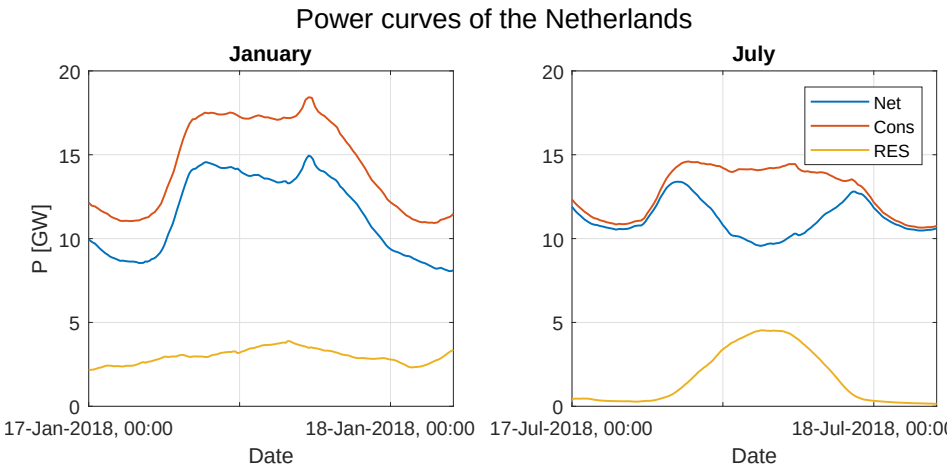

Figure 5-4: Power curves for two days in 2018 in the Netherlands. RES: power produced by renewable energy sources wind and solar obtained from [6], Cons: power consumption obtained from [5], Net: power production from other sources.

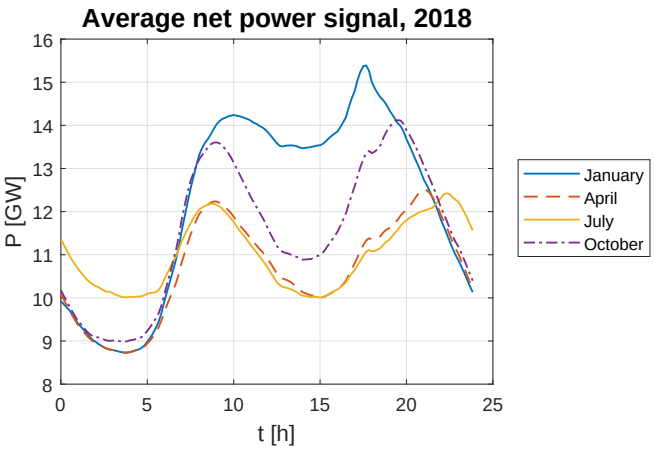

Figure 5-5: Average daily net power curves from the Netherlands for different months throughout 2018.

5-3-4 Reference signals

Reference signals are needed for temperature and fuel composition. These reference signals depend on current density j instead of operating power of the cell. This might look like an odd choice, but the current density is proportional to the hydrogen consumption R_{H_2}, as shown by Equation (3-3). Moreover, the heat production due to the electrochemical reaction Q^{react}, which directly influences the PEN temperature, is also directly influenced by the current density, which can be observed from Equation (3-21).

In an ideal case the temperature of the PEN structure would be constant. However, as described in section 5-3, it is not known how fast the gas flow inlet temperature can be changed and are considered to be constant. Furthermore, changes in air flow rate have different effects in SOFC and SOEC mode. This is a result of the SOFC being exothermic and the SOEC being endothermic. As a result, an increase in air flow rate has a cooling effect on an SOFC and a heating effect on an SOEC. This combination of effects motivates the need for a temperature reference that is a function of current density and for which the temperature in SOEC and SOFC mode is different. Additionaly, the current density is used to indicate the operating mode of the SORC. Negative current density indicates SOEC mode and positive current density indicates SOFC mode. Based on the earlier mentioned common range of 700 to 900 °C and gas inlet temperature of 750 °C, a possible choice for the PEN temperature reference $r_{T_{PEN}}$ is

$$r_{T_{PEN}} = \begin{cases} T_{SOEC} = 700\,^{\circ}\mathrm{C} & \text{if } j < 0\,\mathrm{A/m^2} \\ T_0 = 750\,^{\circ}\mathrm{C} & \text{if } j = 0\,\mathrm{A/m^2} \\ T_{SOFC} = 820\,^{\circ}\mathrm{C} & \text{if } j > 0\,\mathrm{A/m^2} \end{cases},$$

where T_{SOEC}, T_0, and T_{SOFC} are the reference temperatures in SOEC mode, at $P_{net} = 0$, and in SOFC mode, respectively. The temperature difference over the cell was chosen larger in SOFC mode than in SOEC mode, because the SOFC is strongly exothermic and allowing a larger temperature difference over the cell might conserve power usage by the BOP as it results in lower air flow rates. This reference signal cannot be applied to the system, as it gives rise to sharp changes when the current density is close to $0\,\mathrm{A/m^2}$. Therefore, it is approximated by a hyperbolic tangent function, shown in Figure 5-6,

$$r_{T_{PEN}}(j) = \mathcal{A}_1 \tanh(\mathcal{B}_1 j + \mathcal{D}_1) + \mathcal{C}_1, \tag{5-2}$$

where

$$\begin{aligned} \mathcal{A}_1 &= \frac{T_{SOFC} - T_{SOEC}}{2}, \\ \mathcal{B}_1 &= \frac{2}{\Delta j}, \\ \mathcal{C}_1 &= \frac{T_{SOFC} + T_{SOEC}}{2}, \\ \mathcal{D}_1 &= \tanh^{-1}\left(\frac{T_0 - \mathcal{C}_1}{\mathcal{A}_1}\right), \end{aligned} \tag{5-3}$$

where Δj represents the transition zone from T_{SOEC} to T_{SOFC}, which was set to $4000\,\mathrm{A/m^2}$. A derivation of these terms can be found in Appendix D.

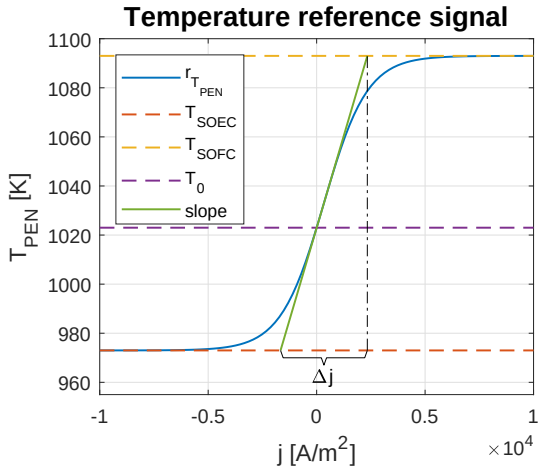

Figure 5-6: Hyperbolic tangent temperature reference function. $r_{T_{PEN}}$: reference signal of the PEN temperature, T_{SOEC}, T_{SOFC}, and T_0: ideal reference temperature in SOEC mode, SOFC mode, and when there is no current extracted from the system, respectively, Δj: transition zone for the reference signal, slope: slope of the reference signal.

A similar situation is true for the composition reference signals. In SOFC mode water is produced from hydrogen and oxygen, while in SOEC mode hydrogen and oxygen are produced from water. This makes it impossible to have the same reference signals in SOFC and SOEC mode. Ideal references of the inlet composition of the fuel channel $r_{\chi_{fuel,H_2,in}}$ and outlet composition of the fuel channel $r_{\chi_{fuel,H_2}}$ can be taken as

$$r_{\chi_{fuel,H_2,in}} \begin{cases} 0.1 & \text{if } j < 0\,\mathrm{A/m^2} \\ 0.5 & \text{if } j = 0\,\mathrm{A/m^2} \\ 0.9 & \text{if } j > 0\,\mathrm{A/m^2} \end{cases},$$

$$r_{\chi_{fuel,H_2}} \begin{cases} 0.82 & \text{if } j < 0\,\mathrm{A/m^2} \\ 0.5 & \text{if } j = 0\,\mathrm{A/m^2} \\ 0.18 & \text{if } j > 0\,\mathrm{A/m^2} \end{cases},$$

where a small amount of the non-reacting species is kept in the gas flows in both cases to prevent degradation [22]. The ideal compositions at the outlet of the fuel channel are based on a fuel utilization FU of 80 %. In case of an SOFC $\left(j > 0\,\mathrm{A/m^2}\right)$ operating at steady state conditions, it follows from Equation (3-9) and the following expression for the fuel utilization

$$FU = \frac{R_{H_2}}{\phi_{H_2,in}},$$

that

$$\chi_{fuel,H_2} = (1 - FU)\chi_{fuel,H_2,in}.$$

The same idea holds for SOEC, but in this case steam is consumed instead of hydrogen. As in Equation (5-2), the composition reference signals can be approximated by a smooth

hyperbolic tangent,

$$r_{\chi_{fuel,H_2,in}}(j) = \mathcal{A}_2 \tanh(\mathcal{B}_2 j + \mathcal{D}_2) + \mathcal{D}_2, \tag{5-4}$$
$$r_{\chi_{fuel,H_2}}(j) = \mathcal{A}_3 \tanh(\mathcal{B}_3 j + \mathcal{D}_3) + \mathcal{C}_3, \tag{5-5}$$

with similar expressions as in Equation (5-3).

5-4 Nonlinear state-space representation of an SORC

It is possible to formulate a state-space representation based on the model presented in chapter 3 and the choice of input, disturbance, and output signals described in section 5-3. First, the state-space representation is presented. Thereafter, a short recap is given of the dynamic equations fully describing the state of the system.

The nonlinear state-space representation is given by

$$\begin{aligned} \dot{x} &= f_1(x, u, \chi_{fuel,H_2,in}, d), \\ y &= g_1(x), \end{aligned}$$

where the state vector x, input vector u, disturbance signal d, and output vector y are given by

$$\begin{aligned} x &= \begin{bmatrix} \chi_{air,O_2}, & \chi_{fuel,H_2}, & T_{air}, & T_{fuel}, & T_{PEN}, & T_{int} \end{bmatrix}^T, \\ u &= \begin{bmatrix} \phi_{air,in}, & \phi_{air,out} \end{bmatrix}^T, \\ d &= \bar{P}, \\ y &= \begin{bmatrix} T_{PEN}, & \chi_{fuel,H_2}, \end{bmatrix}^T. \end{aligned}$$

The dynamic equations consist of material and energy balances and describe gas compositions and temperatures of SORC components. A summary of the dynamic equations is given.

Material balances

The Material balances for the air and fuel channel are

$$\begin{aligned} n_{air} \frac{\mathrm{d}\chi_{air,O_2}}{\mathrm{d}t} &= (\chi_{air,O_2,in} - \chi_{air,O_2})\phi_{air,in} + \frac{1}{2} R_{H_2}(\chi_{air,O_2} - 1), \\ n_{fuel} \frac{\mathrm{d}\chi_{fuel,H_2}}{\mathrm{d}t} &= (\chi_{fuel,H_2,in} - \chi_{fuel,H_2})\phi_{fuel,in} - R_{H_2}. \end{aligned}$$

Energy balances

The energy balances for the single cell are given by

$$n_{air}\left(c_{v,air}+\frac{H_{air}-E_{air}}{T_{air}}\right)\frac{\mathrm{d}T_{air}}{\mathrm{d}t} = -Q^{conv}_{int,air}-Q^{conv}_{PEN,air}+\phi_{air,in}(H_{air,in}-H_{air}) - \frac{1}{2}R_{H_2}(H_{O_2,r}-H_{air})-n_{air}(E_{O_2}-E_{N_2})\frac{\mathrm{d}\chi_{air,O_2}}{\mathrm{d}t},$$

$$n_{fuel}\left(c_{v,fuel}+\frac{H_{fuel}-E_{fuel}}{T_{fuel}}\right)\frac{\mathrm{d}T_{fuel}}{\mathrm{d}t} = -Q^{conv}_{int,fuel}-Q^{conv}_{PEN,fuel}+\phi_{fuel,in}(H_{fuel,in}-H_{fuel}) + R_{H_2}(H_{H_2O,r}-H_{H_2,r}) - n_{fuel}(E_{H_2}-E_{H_2O})\frac{\mathrm{d}\chi_{fuel,H_2}}{\mathrm{d}t},$$

$$m_{PEN}c^{*}_{p,PEN}\frac{\mathrm{d}T_{PEN}}{\mathrm{d}t} = -P_{SORC}+Q^{react}+2Q^{rad}+Q^{conv}_{PEN,air}+Q^{conv}_{PEN,fuel},$$

$$m_{int}c^{*}_{p,int}\frac{\mathrm{d}T_{int}}{\mathrm{d}t} = -2Q^{rad}+Q^{conv}_{int,fuel}+Q^{conv}_{int,air}.$$

5-5 Control stucture

A simple block diagram representing the control system of the SORC is shown in Figure 5-7. Dependency of the reference signals on the current density is not shown in this figure. A feedback controller is used to influence the PEN temperature T_{PEN} and fuel hydrogen fraction χ_{fuel,H_2} with the air flow rate $\phi_{air,in}$ and fuel flow rate $\phi_{fuel,in}$. This is a common approach, see for example [50] where a similar approach is taken. A difference between the approach by Botta, Romeo, Fernandes, *et al.* [50] and the approach in this study, is that they consider a constant fuel inlet composition, while in this study the fuel inlet composition varies as a function of the current density. The relation between the current density and the hydrogen fraction in the fuel inlet is given by Equation (5-4). This static relation between the current density and hydrogen fraction in the fuel inlet motivated the use of a feedforward controller which sets the inlet composition of the fuel channel based on the current density.

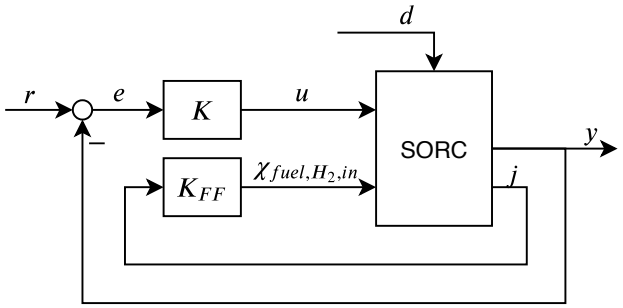

Figure 5-7: Block diagram of the SORC control system. K: feedback fuel and air flow rate controller, K_{FF}: feedforward fuel flow inlet composition controller.

5-6 Conclusion

Important motivations for control of an SORC are efficiency and preventing damage to the cell arising from PEN temperature and gas composition variations which are the result of a power disturbance. The SORC is connected to a grid via power converters, which means that there is not control over the power produced by the SORC. This approach resulted in a control goal where errors in PEN temperature and fuel composition as a result of the power disturbance need to be driven to zero. The first step in solving this problem was to select suitable input, output, and reference signals. Hydrogen fraction in the fuel inlet, and fuel and air flow rate were selected as inputs. Outputs for the cell consist of the hydrogen fraction in the fuel channel and the PEN temperature. Reference signals were specified for the PEN temperature, and fuel inlet and outlet composition. A hyperbolic tangent function was used to ensure smooth reference functions as the current density of the system changes. This should prevent sudden big changes as the system goes from SOFC to SOEC or vice versa. Based on the choice of inputs and outputs, a nonlinear state-space representation was given by

$$\begin{aligned} \dot{x} &= f_1(x, u, d), \\ y &= g_1(x). \end{aligned}$$

A block diagram representing the control system was shown in Figure 5-7. This block diagram is the basis for controller design, which is treated in chapter 7.

Chapter 6

Open-loop analysis

Before designing a controller for the system, it is useful to know the open-loop characteristics of the system. This allows for better controller selection and design. The open-loop analysis presented in this chapter covers stability and controllability of a linear model based on the nonlinear model and analysis of the nonlinear model itself.

The first section describes determination of operating point around which the nonlinear model operates. 39 operating points were determined for the power density range from -7000 to $7000\,\mathrm{W/m^2}$. These operating points are used to linearize the system is the second section. Next, it is shown that the system is locally asymptotically stable and an estimate of the region of attraction of the nonlinear system is given. Thereafter, it is shown that all linear models are functionally controllable, which indicates that all output signals of the system can be controlled independently. This section also examines input-output pairing via the relative gain array (RGA), which gives an indication of level of interaction between different inputs and outputs. Furthermore, sensitivity of outputs of the nonlinear model to the inputs and disturbance is examined. The chapter ends with a conclusion in which the outcomes of the chapter are summarized.

6-1 Determination of operating points

Before linearizing the system, it is necessary to determine its operating points. An operating point is determined by the following quantities:

- power density $\bar{P}$;
- current density j;
- temperature of
  - PEN structure T_{PEN};
  - interconnect T_{int};

  - fuel channel T_{fuel};
  - air channel T_{air};
  - fuel inlet flow $T_{fuel,in}$;
  - air inlet flow $T_{air,in}$;
- the following variables related to compositions of gasses:
  - hydrogen fraction in the fuel channel χ_{fuel,H_2};
  - hydrogen fraction in the fuel inlet flow $\chi_{fuel,H_2,in}$;
  - oxygen fraction in the air channel χ_{air,O_2};
  - oxygen fraction in the air inlet flow $\chi_{air,O_2,in}$;
- fuel inlet flow rate $\phi_{fuel,in}$;
- air inlet flow rate $\phi_{air,in}$.

It was explained in section 5-3 that the air and fuel inlet flow temperature are taken constant, as well as the oxygen fraction in the air inlet flow. It was also explained that the reference signals for the PEN temperature, hydrogen fraction in the fuel channel and hydrogen fraction in the fuel inlet flow are made depended only on the current density. This leaves a system of eight unknowns and seven equations. It was already mentioned that the system has to operate over a certain power density range. Therefore, the power density is the last variable that is fixed in order to determine an operating point. The operating points were determined for 39 equidistant operating power densities in the range of -7000 to $7000\,\mathrm{W/m^2}$. The choice for 39 operating points was motivated by the fact that different dynamics were expected in each mode due to the exothermic hydrogen consuming SOFC mode and the endothermic hydrogen producing SOEC mode. Therefore, at least one operating point had to be defined in each mode. It was unclear which operating power would be the most suitable, because the SORC has to be able to operate over a range of powers. Therefore, the choice was made to consider multiple operating points in each mode. This way, the differences in dynamics in each mode were also considered. It was unclear what operating powers would best represent the different dynamics throughout each mode and the decision was made to consider equidistant operating powers. The results were considered good enough and no refinement was done of the chosen operating powers.

The system that needs to be solved consists of the state vector derivative and an expression to balance the output power of the cell. The nonlinear equation for the state vector derivative is given by

$$\dot{x} = f_1(x, u, d),$$

and the output power of the cell is given by

$$A_s d = P_{SORC} = i U_{cell},$$

where U_{cell} follows from the electrochemical model described in section 3-4. Operating points x_{eq}, u_{eq} and i_{eq} follow from solving

$$f_2(x_{eq}, u_{eq}, d_{eq}) = \begin{bmatrix} f_1(x_{eq}, u_{eq}, d_{eq}) \\ A_s d_{eq} - i_{eq} U_{cell,eq} \end{bmatrix} = \begin{bmatrix} 0 \\ 0 \end{bmatrix}, \tag{6-1}$$

where the subscript eq indicates equilibrium conditions.

The material balances are easy enough to solve by hand. From section 3-2 it follows that

$$\chi_{air,O_2} = \frac{\frac{1}{2}R_{H_2} - \chi_{air,O_2,in}\phi_{air,in}}{\frac{1}{2}R_{H_2} - \phi_{air,in}},$$
$$\phi_{fuel,in} = \frac{R_{H_2}}{\chi_{fuel,H_2,in} - \chi_{fuel,H_2}}.$$

The energy balances can be simplified by realizing that χ_{air,O_2} and χ_{fuel,H_2} are at equilibrium after solving the material balances. Therefore, the parts in the energy balances that depend on the material balances vanish. The remaining system is too complex to solve by hand and is solved numerically using the `fsolve` function in Matlab [76], which uses a trust-region dogleg algorithm. This algorithm was designed to solve nonlinear equations [72].

The operating points were calculated one at a time, starting from $0\,\mathrm{W/m^2}$ and increasing to $7000\,\mathrm{W/m^2}$ for the SOFC region and decreasing to $-7000\,\mathrm{W/m^2}$ for the SOEC region. The initial guess for each operating point was taken as the solution of the previously solved operating point. The reasoning behind this approach being that the variable values at the previous operating point are expected to be close enough to the variable values at the current operating point. This makes the previous operating point a good initial guess for the current operating point.

Figure 6-1 gives an overview of the results from determining the operating points and shows the values of the seven variables that needed to be determined at every operating point. In contrast to the hydrogen fraction in the fuel channel, the oxygen fraction in the air channel stays close to the oxygen fraction in the inlet flow. This is a consequence of the relatively high air flow rate that is needed to keep the cell at temperature, especially when operating as SOFC. The air flow rate is the lowest when the cell operates close to $-7000\,\mathrm{W/m^2}$, which results in a relatively high oxygen content in the air channel. This is because the cell starts to become less endothermic after a certain point, as shown in Figure 6-4b. If the magnitude of SOEC power density becomes big enough, the cell becomes exothermic. Attention is needed for the air and fuel flow rate at $\bar{P} = 0\,\mathrm{W/m^2}$. At this operating point, fuel and air flow are not required, because the cell is turned off at this operating point. Therefore, the air and fuel flow rate are equal to $0\,\mathrm{mol/s}$ at $\bar{P} = 0\,\mathrm{W/m^2}$.

The results also show that the temperature difference between the different parts of the cell increases as the power density increases, which is due to the SOFC being highly exothermic.

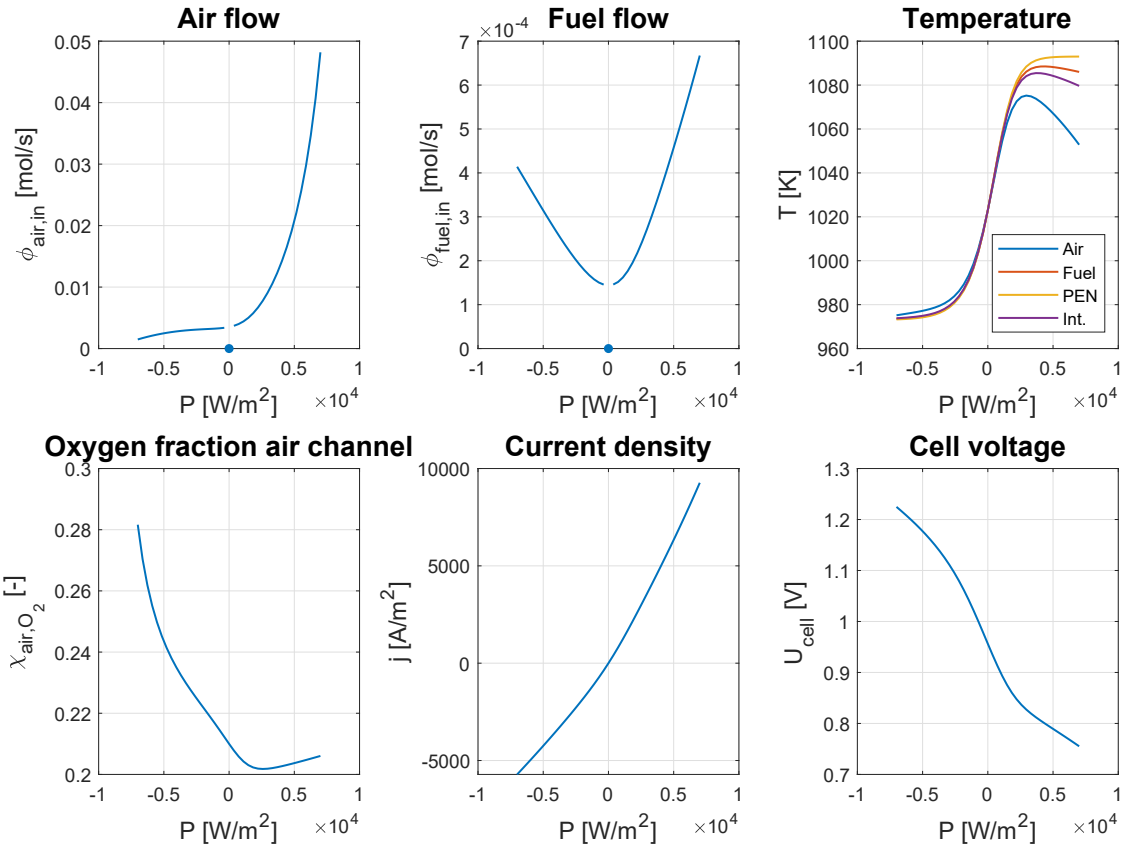

Figure 6-1: Operating point values of several quantities. Air: air channel, Fuel: fuel channel, PEN: PEN structure, Int.: interconnect. P indicates power density. Air and fuel flow rate are $0\,\mathrm{mol/s}$ at $\bar{P} = 0\,\mathrm{W/m^2}$, because the SORC is turned off at this operating point.

6-2 Linearization of the nonlinear SORC model

The nonlinear system is numerically linearized. An illustration indicating which part of the model is linearized and what the linearized model looks like is shown in Figure 6-2. The linear response to the inputs is represented by G and the response to the disturbance is represented by G_d.

For a general nonlinear system

$$\begin{aligned} \dot{x} &= f_1(x, u, d), \\ y &= g_1(x, u, d), \end{aligned}$$

the Jacobian linearization is given by

$$\begin{aligned} \dot{x} &= \underbrace{\frac{\partial f_1}{\partial x}}_{A}(x - x_{eq}) + \underbrace{\frac{\partial f_1}{\partial u}}_{B}(u - u_{eq}) + \underbrace{\frac{\partial f_1}{\partial d}}_{B_d}(d - d_{eq}), \\ y &= \underbrace{\frac{\partial g_1}{\partial x}}_{C}(x - x_{eq}) + \underbrace{\frac{\partial g_1}{\partial u}}_{D}(u - u_{eq}) + \underbrace{\frac{\partial g_1}{\partial d}}_{D_d}(d - d_{eq}). \end{aligned} \tag{6-2}$$

Numerical approximations are obtained by use of the Matlab function `linearize` [77]. Based on this general linearization, the transfer functions G and G_d are obtained from

$$G(s) = C(sI - A)^{-1}B + D, \tag{6-3}$$

$$G_d(s) = D_d(sI - A)^{-1}B_d + D_d, \tag{6-4}$$

where I is the identity matrix.

Figure 6-3 shows Bode diagrams of several individual responses of the linearized systems at -7000, -4790, -2580, -370, 370, 2580, 4790 and 7000 $\mathrm{W/m^2}$. It includes the responses to the inputs as well as the responses to the disturbance. A couple of things can be noticed from these responses.

- The response from the air flow rate $\phi_{air,in}$ to the PEN temperature T_{PEN} behaves like a second order system, with different gains and pole locations at each operating point.
- The PEN temperature T_{PEN} reacts oppositely to changes in the air flow $\phi_{air,in}$ when operating as SOFC or SOEC. This can be explained by the exothermic nature of the

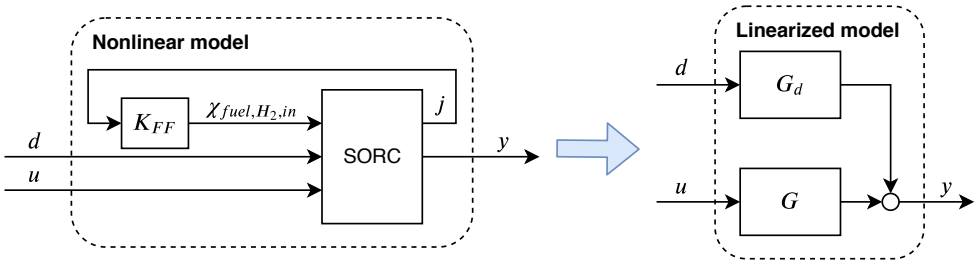

Figure 6-2: Illustration of linearization of the nonlinear model.

SOFC and the endothermic nature of the SOEC. Because of this, air acts as a cooling medium for an SOFC, while it acts as heating medium for an SOEC. Therefore, increasing the air flow rate results in a lower temperature when operating as SOFC and in a higher temperature when operating as SOEC.

- The response from the fuel flow rate $\phi_{fuel,in}$ to the fuel channel composition χ_{fuel,H_2} behaves like a first order system. The only differences between the operating points are the gain and pole location of the linearized approximation.
- A change in fuel flow $\phi_{fuel,in}$ has a different effect in SOFC and SOEC mode. Reason for this is the fact that an SOFC uses hydrogen, while an SOEC produces it. Therefore, increasing the fuel flow rate results in a higher hydrogen fraction in SOFC mode, while it results in a lower hydrogen fraction for an SOEC.
- The air flow $\phi_{air,in}$ has a limited influence on the fuel composition χ_{fuel,H_2}. A change in air flow rate results in small changes in the fuel composition.
- Fuel flow rate $\phi_{fuel,in}$ and air flow rate $\phi_{air,in}$ both have a significant influence on PEN temperature T_{PEN}.
- The response from the power density disturbance $\bar{P}$ to the fuel composition χ_{fuel,H_2} behaves as a first order system. An increase in power density results in an increase of hydrogen fraction in both modes. This increase in hydrogen fraction can be explained by an increase in current density which is a result of the increase in power density, as shown in Figure 6-4a. The hydrogen production is directly affected by the current density. In SOFC mode, an increase in current density results in a higher hydrogen consumption, while in SOEC mode it results in a decrease in production. Therefore, an increase in current density results in an increase of hydrogen fraction in the fuel channel. Note that an increase in power or current density in SOEC mode refers to the absolute power density becoming smaller, for example, an increase from -5000 to $-4000\,\mathrm{A/m^2}$.
- The PEN temperature T_{PEN} response to changes in power density $\bar{P}$ shows that the SOEC does not always react the same way to a change in power density. For some operating points in the SOEC region, an increase in power density leads to an increase in temperature, while in other operating points it leads to a temperature decrease. Reason for this is that in a certain power density region the system gets more endothermic as power density increases, while it becomes less endothermic in other regions, as can be observed from Figure 6-4b. This figure shows the PEN temperature as a function of the power density, which shows that if power density becomes low enough, the system becomes exothermic in SOEC mode.

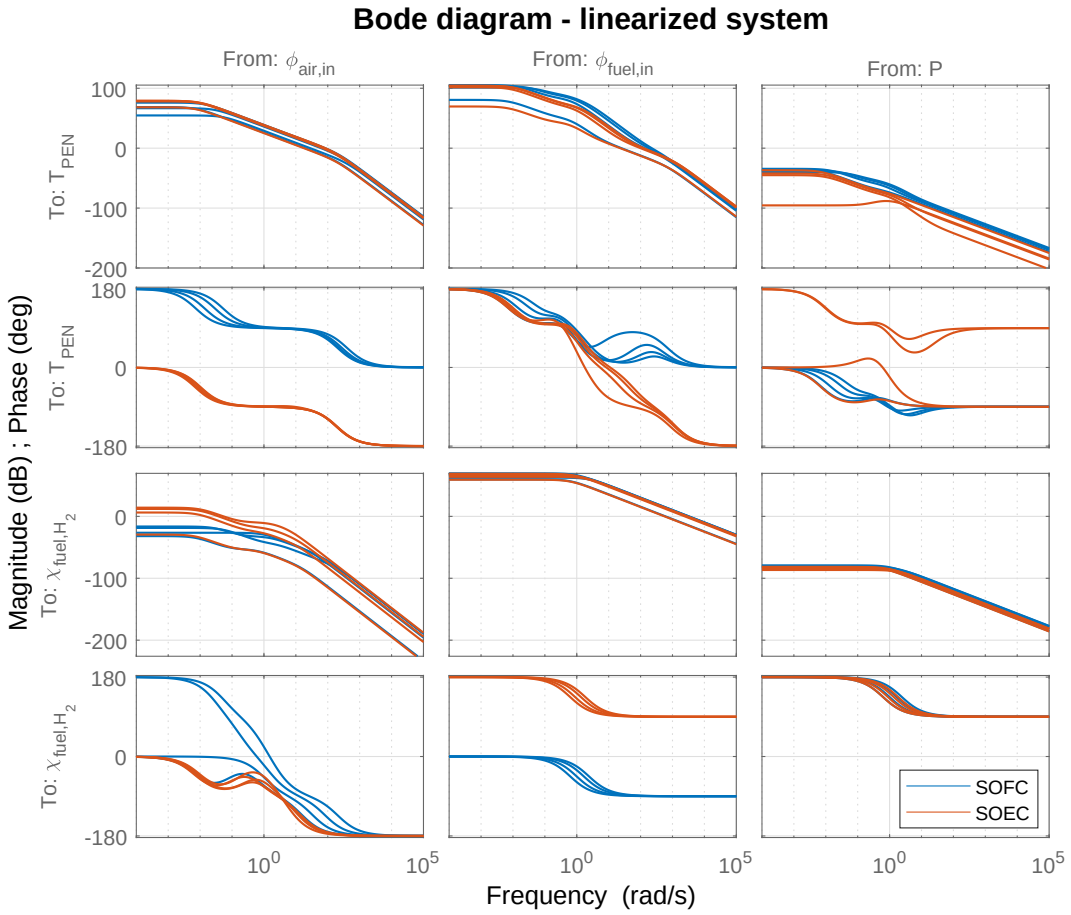

Figure 6-3: Bode diagrams for the linearized system at 8 operating points over the range -7000 to $7000\,\mathrm{W/m^2}$. Included operating points: -7000, -4790, -2580, -370, 370, 2580, 4790 and $7000\,\mathrm{W/m^2}$. It includes the bode diagrams from the inputs ($\phi_{air,in}$, $\phi_{fuel,in}$) and the disturbance (P indicating power density) to the outputs (T_{PEN}, χ_{fuel,H_2}).

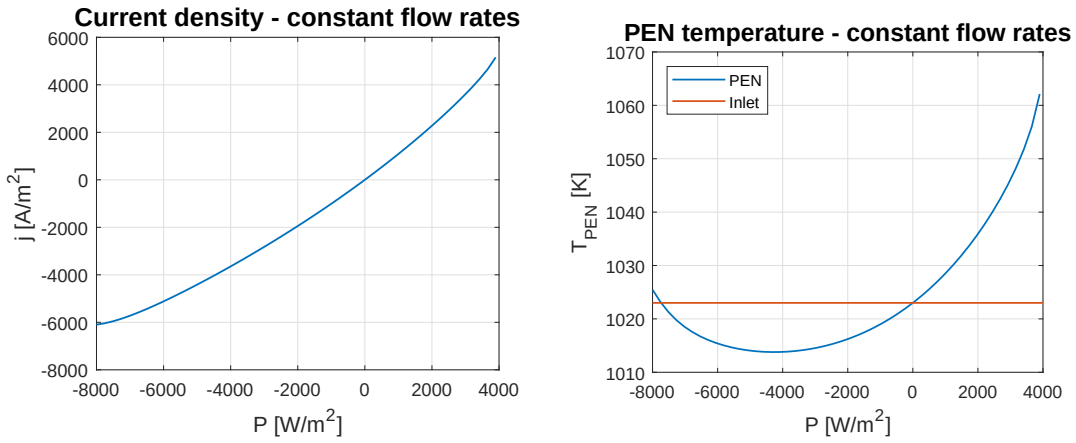

(a) Current density

(b) PEN temperature. Inlet: inlet temperature

Figure 6-4: Current density and PEN temperature as function of power density. Fuel and air flow rates, and inlet compositions were kept constant to only show the influence of changes in power density. P indicates power density.

6-3 Stability of the SORC

This section discusses stability of the SORC. First, it is shown that each linearized system at each operating point is asymptotically stable. After that, an estimate is given for the region of attraction of the nonlinear system.

6-3-1 Asymptotic stability of linearized system

A linear system is asymptotically stable if and only if all poles are in the open left-hand plane, which is the same as all poles having a negative real part. Figure 6-5 shows the range of real parts of the poles of each linearized system G at each operating point. All poles are in the open left-hand plane, which indicates that the collection of linear systems is asymptotically stable.

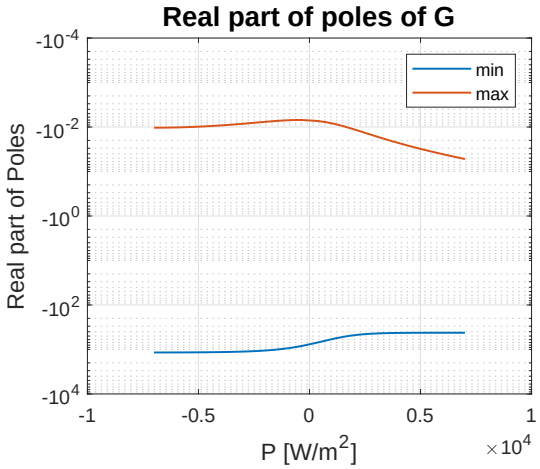

Figure 6-5: Minimum (min) and maximum (max) real parts of poles of the linearized model G as a function of power density. P indicates power density.

6-3-2 Region of attraction of the nonlinear system

A theorem known as Lyapunov's indirect method says that, if the equilibrium of a linearized system is asymptotically stable, then that equilibrium is a locally asymptotically stable equilibrium of the nonlinear system [78]. It was shown in subsection 6-3-1 that all linearized systems are asymptotically stable. Therefore, the nonlinear system is locally asymptotically stable around its operating points. However, this theorem says nothing about the region of attraction, which is the region for which trajectories of the nonlinear sytem return to the equilibrium point. A simulation is used to give an estimate for the region of attraction of the nonlinear system. This was done using the following procedure,

1. Estimate the region of attraction of each individual state in the nonlinear system at each operating point by repeating the following procedure for each individual state.

(a) Pick a guess for the maximum allowable deviation of a single state Δx_l. As an example, consider the oxygen fraction in the air channel χ_{air,O_2}. It is not possible for the oxygen fraction to be smaller than 0, which means that a value slightly smaller than the oxygen fraction in the air channel is a sensible candidate for the maximum allowable deviation.

(b) Take a random initial condition $\tilde{x}_l \in \Big[x_{eq,l} - \Delta x_l, \quad x_{eq,l} + \Delta x_l\Big]$, where $x_{eq,l}$ indicates the value of state l at a certain equilibrium point.

(c) Simulate the system with initial state $\tilde{x}_l$.

(d) If the simulated system does not return to its original equilibrium, take a slightly smaller deviation Δx_l and retry.

(e) If the simulated system returns to its original equilibrium, take a new random point $\tilde{x}_l \in \Big[x_{eq,l} - \Delta x_l, \quad x_{eq,l} + \Delta x_l\Big]$ and simulate the system again. Repeat this $\mathscr{N}$ times. After $\mathscr{N}$ consecutive successful attempts, it can be concluded that the range from which $\tilde{x}_l$ was selected is an estimate for the region of attraction for a single state.

2. Use the estimated region of attraction of each individual state to find an estimate for the region of attraction of the state vector at each operating point. This is done by applying the following procedure.

(a) Define a six dimensional ellipsoid that describes possible perturbed initial state vectors based on the estimates for the region of attraction of each individual state.

(b) Take a random point $\tilde{x}$ on this ellipsoid. This was done by picking a random point on the surface of a six dimensional ball, for which method 2 of [79] was used. The idea is to generate six independent values of the standard normal distribution and to scale these values such that distance to the origin is 1. Next, the point on the surface of the ball is scaled to put it on the ellipsoid. It is enough to consider points on the ellipsoid, because it encloses all possible initial states inside the ellipsoid. Therefore, any possible unstable trajectory based on an initial state vector inside the ellipsoid has to pass through the surface of the ellipsoid.

(c) Simulate the nonlinear system with the initial state $\tilde{x}$.

(d) If the system does not return to its original equilibrium, take a slightly smaller ellipsoid and retry.

(e) If the system returns to its original equilibrium, take a new random point $\tilde{x}$ on the ellipsoid and simulate the nonlinear system. Repeat this $\mathscr{N}$ times. After $\mathscr{N}$ consecutive succesful attempts, it can be concluded that the ellipsoid is an estimate for the region of attraction of the nonlinear system.

The ellipsoid describing an estimate of the region of attraction based on $\mathscr{N} = 1000$ simulations per operating point is based on the values shown in Figure 6-6, where the maximum temperature deviation was limited to 200 K. A couple of things stand out in this figure.

- The region of attraction of the gas compositions seems to be limited by the mole fraction inside the gas channels, when compared to Figure 6-1 and the description of the hydrogen fraction reference in section 5-3. This can be explained by the fact that the composition cannot be smaller than 0 or larger than 1.

- Temperature deviations of the PEN structure are more severe than temperature deviations of the interconnect or the channels. This can be explained by the relatively large heat capacity of the PEN $\left(m_{PEN}c^*_{p,PEN}\right)$, compared to the other components. The heat capacity of the gas channels (nc_v) is the lowest and temperature deviations in these parts have the smallest effect on the system. The heat capacity of the PEN structure is at least $1.7 \cdot 10^3$ times larger than the heat capacity of the gas channels and 1.5 times larger than the heat capacity of the interconnect.

- The SOEC region is able to handle much larger temperature deviations than the SOFC region. This is a result of the fact that low temperatures have more severe effects in SOFC mode than in SOEC mode. A simulation that does not return to it equilibrium point is shown in Figure 6-7. The initial PEN temperature T_{PEN} is taken 100 K under its equilibrium value at an operating power density of $\bar{P} = 4.8 \cdot 10^3\,\mathrm{W/m^2}$. According to Figure 6-6, this simulation should not succeed. Reason for this is the fact that the low PEN temperature results in a low cell voltage U_{cell}, because of higher electrochemical losses. This, combined with the fixed operating power, results in a high current density j and thus a higher hydrogen consumption. The system runs out of hydrogen, since the fuel inlet flow $\phi_{air,in}$ is not sufficient to overcome the hydrogen depletion and the PEN structure temperature T_{PEN} does not return to its equilibrium fast enough. It should be mentioned that operating temperatures higher than the equilibrium temperature are no issue.

It has to be mentioned that the estimated region of attraction is somewhat conservative. Maximum deviations in composition are limited by the fraction of chemical species in the gas channels and the maximum deviation in PEN temperature is limited by a lower limit in SOFC mode. Asymmetrical deviations, where temperature and composition are allowed to deviate further in the non-limiting direction, might result in a larger region of attraction. It should also be noted that only 1000 random initial state vectors were simulated. There may be non-simulated points on the ellipsoid that may not return to the equilibrium point.

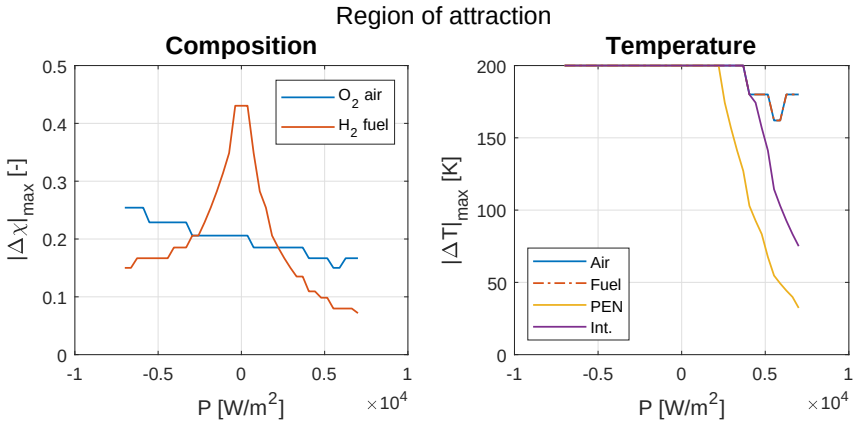

Figure 6-6: Visualisation of the region of attraction by the maximum allowable range of each individual state. Temperature deviations were limited to 200 K. O_2 air: oxygen fraction in air channel, H_2 fuel: hydrogen fraction in fuel channel, Air: air channel, Fuel: fuel channel, PEN: PEN structure, Int.: interconnect. P indicates power density.

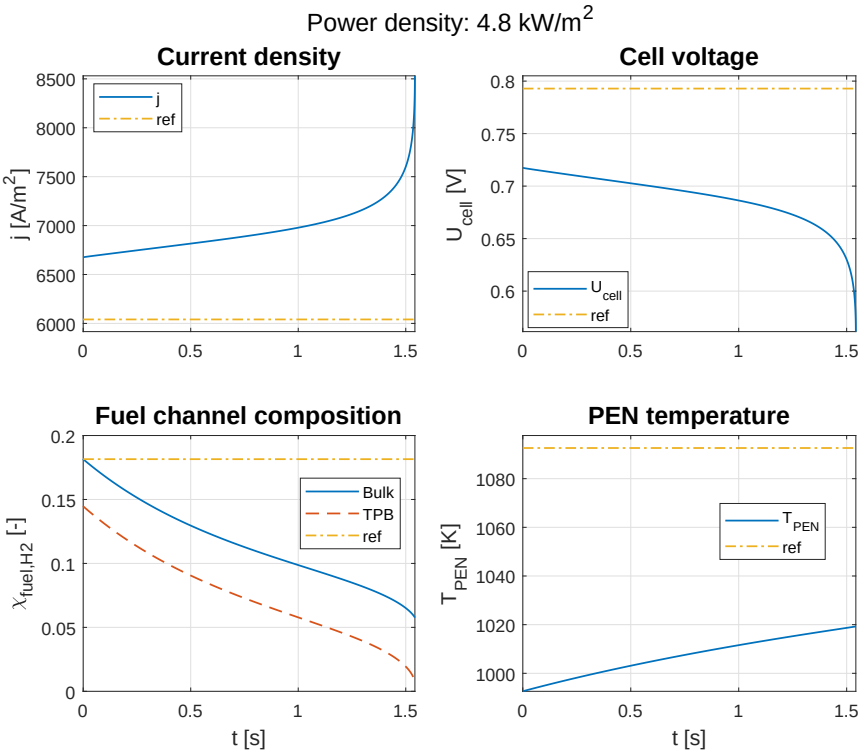

Figure 6-7: SOFC simulation where the initial PEN temperature is taken $100\,\mathrm{K}$ lower than its temperature at the equilibrium point. ref: reference value at equilibrium, Bulk: value in the fuel channel, TPB: value at the TPB.

6-4 Controllability of the SORC

This section examines controllability of the SORC. This is done by checking the functional controllability of the the system and computing the RGA of the linearized system for each operating point. Sensitivity of the outputs of the nonlinear system to the input and disturbance signals is also investigated by numerical simulation.

6-4-1 Functional controllability - singular values

A system is said to be functionally controllable if all outputs of the system can be controlled independently [80]. This is the same as the system $G(s)$ having full row rank, which can be checked by examining the singular values of the system. The system is functional controllable if

$$\underline{\sigma}(G(\mathrm{i}\omega)) > 0, \forall \omega,$$

where $\underline{\sigma}(G(\mathrm{i}\omega))$ is the smallest singular value of the plant G at frequency ω. A plot of the range of singular values of the dynamic system is shown in Figure 6-8. Only four different curves are shown for each mode. The included operating points are at -7000, -4790, -2580, -370, 370, 2580, 4790 and $7000\,\mathrm{W/m^2}$ and reflect the complete range of singular values of all operating points. The remaining operating points showed similar responses. The figure shows that all singular values are larger than 0, which means that the linearized systems are functionally controllable.

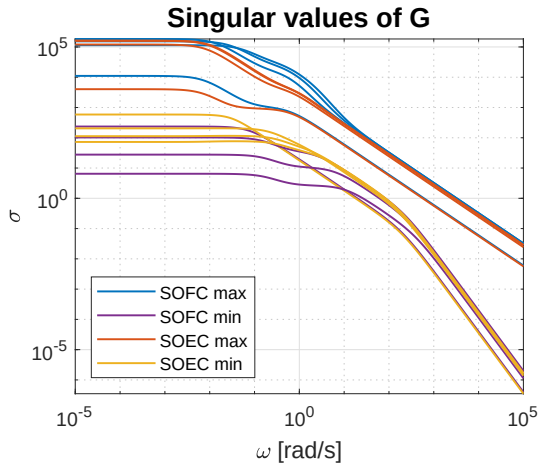

Figure 6-8: Singular values of the linearized system G for 8 operating points over the range -7000 to $7000\,\mathrm{W/m^2}$. Included operating points: -7000, -4790, -2580, -370, 370, 2580, 4790 and $7000\,\mathrm{W/m^2}$. SOFC max: maximum singular value at an operating point in the SOFC region, SOFC min: minimum singular value at an operating point in the SOFC region, SOEC max: maximum singular value at an operating point in the SOEC region, SOEC min: minimum singular value at an operating point in the SOEC region.

6-4-2 Measure for interaction - relative gain array (RGA)

The RGA can be used for pairing input and output signals, because it gives an indication of the level of interaction between different inputs and outputs. Inputs and outputs should be

paired based on the elements of tha RGA close to 1 around the crossover frequency [80].

The RGA of a non-singular square complex matrix $\mathcal{A}$ is defined as

$$RGA(\mathcal{A}) = \mathcal{A} \odot \left(\mathcal{A}^{-1}\right)^T,$$

where $\odot$ indicates element-wise multiplication, also known as the Hadamard product. Figure 6-9 shows element $RGA(G)_{11}$. This entry defines the complete RGA, since it is has size 2×2 and its rows and columns sum up to 1. The RGA is close to the identity matrix at each operating point for every frequency. Therefore, it should be possible to control the system with two independent controllers: One controller for the temperature based on the air flow rate and one controller for the fuel channel composition based on the fuel flow rate.

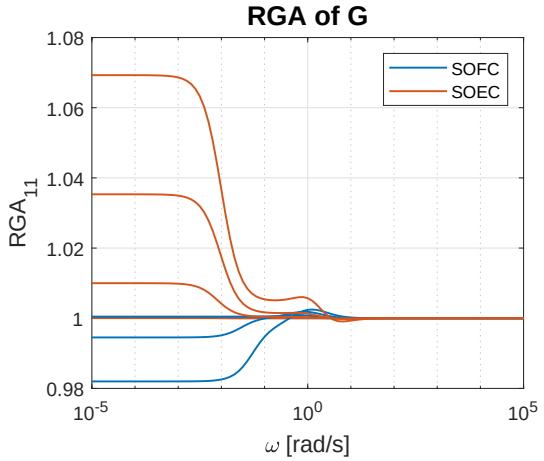

Figure 6-9: RGA element 1,1 for the linearized system G for 8 operating points. Included operating points: -7000, -4790, -2580, -370, 370, 2580, 4790 and $7000\,\mathrm{W/m^2}$.

6-4-3 Sensitivity of outputs of the nonlinear system

Figure 6-10 shows the sensitivity of outputs to changes in inputs and the disturbance around the operating points of the nonlinear system. At each operating point, the input signals and disturbance were perturbed by a small positive and negative amount. The fuel flow rate $\phi_{fuel,in}$ was perturbed by $\pm 2.5 \cdot 10^{-6}\,\mathrm{mol/s}$, the air flow rate $\phi_{air,in}$ was perturbed by $\pm 2.5 \cdot 10^{-5}\,\mathrm{mol/s}$, and the power density disturbance $\bar{P}$ was perturbed by $\pm 25\,\mathrm{W/m^2}$. The gradient was approximated using central differences based on the results of these simulations, which shows the sensitivity of the outputs to changes in the inputs. From this figure, it can be concluded that the fuel flow has significant influence on the temperature and fuel channel composition, while the air flow only has a significant influence on the temperature. This confirms the results obtained from the RGA that the fuel and air flow rate can be used for control of the fuel channel composition and temperature, respectively.

Figure 6-10 also shows that the system has a low sensitivity to the inputs around $\bar{P} = 0\,\mathrm{W/m^2}$. Sensitivity of the disturbance at $\bar{P} = 0\,\mathrm{W/m^2}$ could not be determined, because there are no gas flows at this operating point, as shown in Figure 6-1. Consequently, a change in power results in fuel depletion at this point.

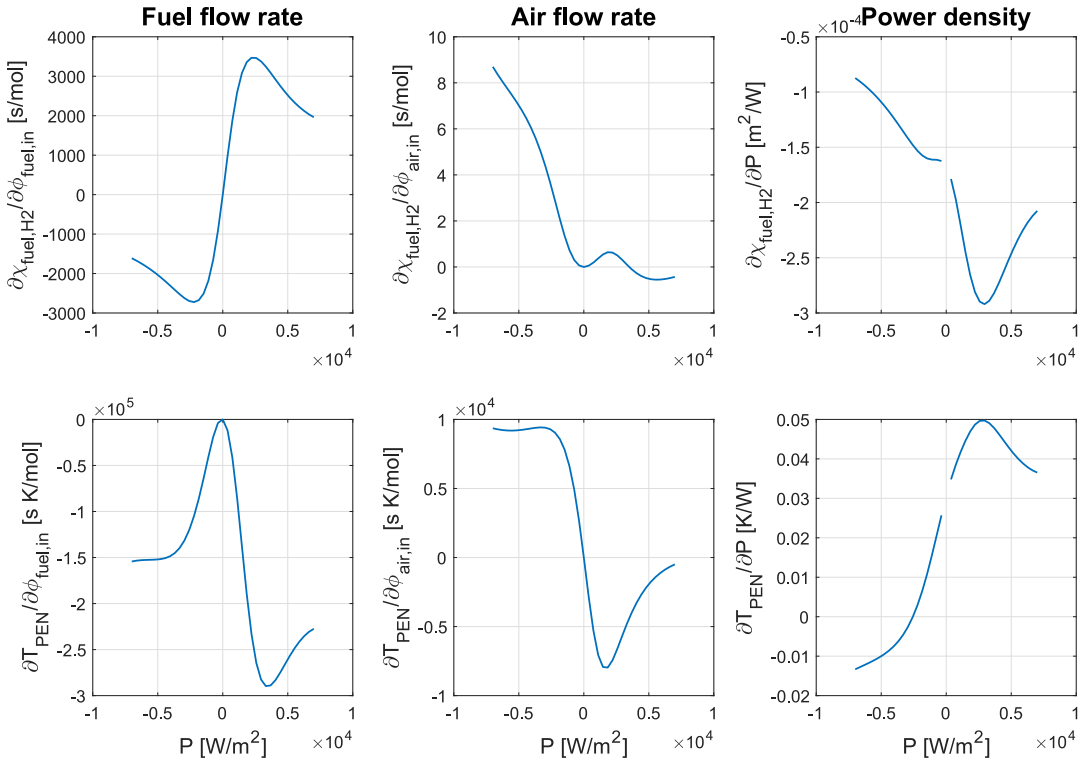

Figure 6-10: Sensitivity of outputs (T_{PEN}, χ_{fuel,H_2}) of nonlinear model to changes in inputs ($\phi_{fuel,in}$, $\phi_{air,in}$) and disturbance (P, which indicates power density). Sensitivity to the power density disturbance at $\bar{P} = 0\,\mathrm{W/m^2}$ could not be determined, because there is no air and fuel flow at this operating point (see Figure 6-1).

6-5 Conclusion

A collection of linear models was obtained by linearization of the nonlinear model at 39 operating points over the power density range -7000 to $7000\,\mathrm{W/m^2}$. It was shown that the linearized models are asymptotically stable and functional controllable. The RGA element 1,1 of each linearized model was between 0.98 and 1.08, which showed that it is possible to control the temperature with the air flow rate and the fuel channel composition with the fuel flow rate.

Analysis of the nonlinear model gave an estimate for the region of attraction for which the nonlinear model is asymptotically stable. The region of attraction is limited by the amount of chemical species present in the gas channels and a lower limit on component temperatures. The nonlinear model was also used to show that the fuel channel composition is primarily influenced by the fuel flow rate, while the temperature was influenced significantly by both air and fuel flow rate. This is another indication that the fuel flow rate can be used for controlling the fuel channel composition, while the air flow rate can be used for temperature control.

Chapter 7

Controller design and simulation

After analyzing the open-loop characteristics of the SORC model, it is possible to select, design, and test controllers for it. This chapter describes the development of two proportional-integral (PI) controllers. Both controllers are obtained from an $\mathcal{H}_\infty$ optimization with different weighting matrices representing the required performance of the controllers. Performance requirements are based on average net power signals. This was done by first characterizing the power signals by power spectral density (PSD) estimates, as described in the first section. Next, the choice for gain-scheduling $\mathcal{H}_\infty$ tuned PI controllers is motivated based on the control goal and results from chapter 6. The performance specification of the controllers is discussed in section 7-3. This includes scaling of the system to represent allowed deviations and the selection of weighting filters to ensure performance. Next, the controllers obtained from the controller synthesis are presented. This includes smoothing of the PI controller parameter functions, because gain scheduling requires smooth parameter functions with respect to the scheduling variable. After controller synthesis, the controllers are applied to the nonlinear system and simulations are done. For the first set of simulations, the disturbance signal is based on the average net power curves. The second set of simulation considers actual daily power signals. The chapter ends with a conclusion.

7-1 Characterization of disturbance signal

Average net power signals were introduced in subsection 5-3-3 as the basis for the power disturbance signals. This section looks into the PSD as a means of characterizing the dynamics of the power disturbance applied on the SORC. The objective is to see if certain frequencies dominate the signal and what bandwidth is required for the closed-loop system to be able to reject the power disturbance. The first step to characterize the power disturbance is to detrend the power data. Next, the PSD is estimated using a modified periodogram method.

7-1-1 Detrending of net power curves

A figure with average daily net power signals was shown in Figure 5-5 for four different months throughout 2018 in the Netherlands. These signals need to be detrended to be able to get meaningful estimates of the PSD of these signals. Not doing so would result in a peak at $f = 0\,\text{Hz}$. A vertical shift seems enough to detrend the April and July signal. However, January and October show a bell-like or low frequency sine wave shape. This bell is most noticeable in the January data. Therefore, these signals are detrended by fitting and subtracting a shifted sine wave $\tilde{P}$,

$$\tilde{P} = \mathcal{A}\sin\left(\mathcal{B}t + \mathcal{C}\right) + P_{mean}, \tag{7-1}$$

where P_{mean} is the mean value of the power signal P, and $\mathcal{A}$, $\mathcal{B}$ and $\mathcal{C}$ are fitting parameters related to the amplitude, frequency and phase shift of the fitted sine wave. The upper limit of the frequency $\mathcal{B}$ was set to $2.4 \cdot 10^{-5}\pi\text{rad/s}$, which corresponds to approximately one cycle per day. This was done to preserve the two cycles per day characteristic in the PSD estimates of the detrended power signals. The last step in detrending the power curves is to apply an additional vertical shift to ensure that the mean value of the detrended power signals is 0. The detrended power signals are shown in Figure 7-1. Detrended power signals for January 2017 to October 2019 can be found in section E-2.

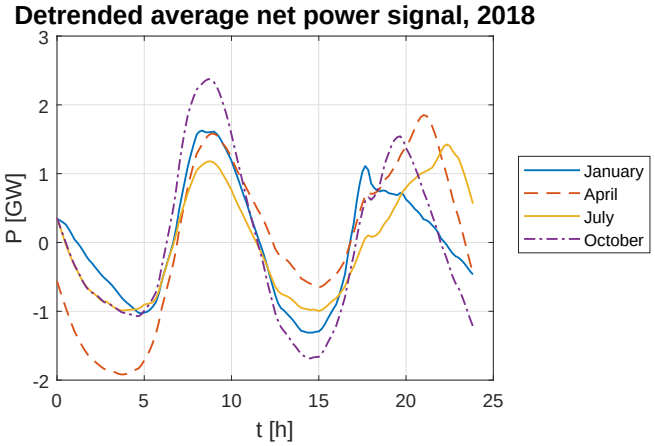

Figure 7-1: Detrended average net power signals for several months in 2018. April and July are detrended by a vertical shift, and January and October are detrended by fitting a shifted low frequency sine wave.

7-1-2 PSD estimate of the detrended net power curves

The PSD is estimated using the modified periodogram with a Hamming window with a window length of 144. Reason for this window length is that all detrended power curves show approximately two sine cycles per day, resulting in a frequency of

$$\begin{aligned} f_{exp} &= \frac{1}{\Delta t}, \\ &= \frac{1}{12 \cdot 3600}, \\ &\approx 2.31 \cdot 10^{-5}\,\text{Hz}, \end{aligned}$$

where f_{exp} is the frequency at which a peak in the PSD is expected, and Δt is the period of the signal. There is one data sample every 10 min, resulting in 144 data points and a sample frequency of $f_s = \frac{1}{600}$Hz. The frequency resolution follows from

$$f_{res} = \frac{f_s}{N_{DFT}},$$

where N_{DFT} is the number of points used in the discrete Fourier transform (DFT) for the PSD estimate. Therefore, taking N_{DFT} as a multiple of

$$\frac{f_s}{f_{exp}} = 72,$$

ensures that the frequency f_{exp} is included.

Estimates of the PSD of January, April, July, and October are shown in Figure 7-2, including the expected peak frequency. PSD estimates for January 2017 to October 2019 can be found in section E-3. As expected, there is a peak in each PSD estimate at f_{exp}. A different window or more DFT points showed comparable PSD estimates. Welch's method is considered inadequate, because of the small number of data points compared to the number of points required to capture the expected peak frequency. This method divides the data into several segments and takes the average PSD estimate of these segments as an estimate of the PSD. More information on PSD estimation can be found in [81].

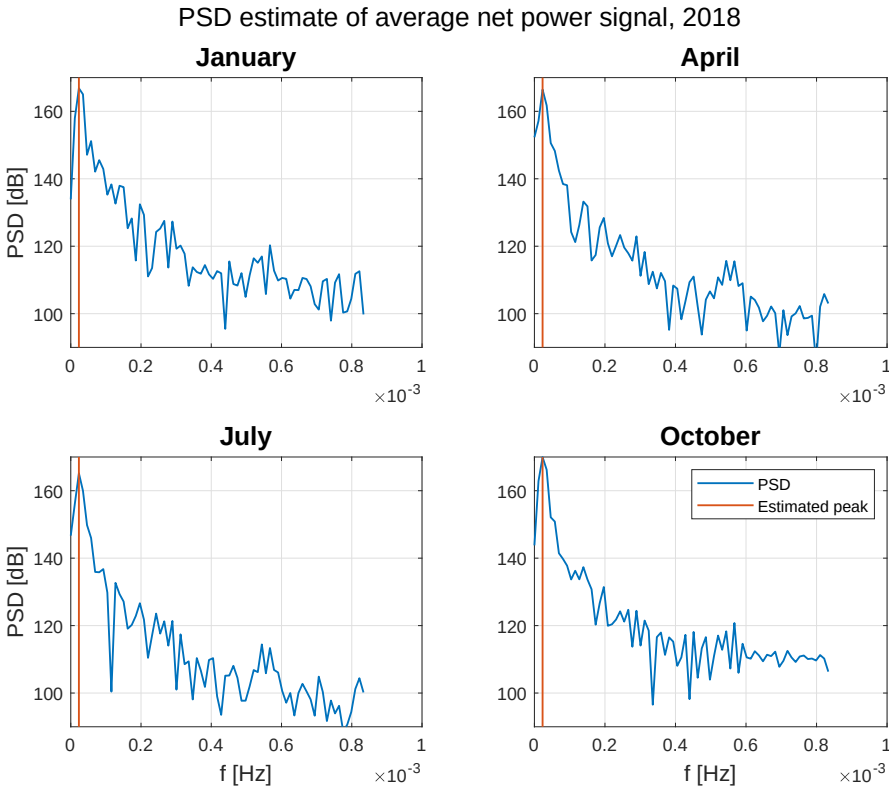

Figure 7-2: PSD estimates using the periodogram with Hamming filter and 144 DFT points. Estimated peak: expected peak frequency at $f_{exp} = 2.31 \cdot 10^{-5}$ Hz.

7-2 Motivation for gain-scheduling $\mathcal{H}_\infty$ tuned PI controllers

The open-loop analysis in section 6-4 showed that the RGA of G is close to the identity matrix at each frequency for all operating points along the operating range of -7000 to $7000\,\mathrm{W/m^2}$. This indicates that it is possible to decouple the system and use two single-input single-output controllers to control the PEN temperature T_{PEN} and fuel channel composition χ_{fuel,H_2} separately. This approach was further justified by examination of the sensitivity of the outputs of the nonlinear system. It was shown that the air flow rate $\phi_{air,in}$ and fuel flow rate $\phi_{fuel,in}$ have a substantial influence on the PEN temperature, but the composition of the fuel channel is primarily influenced by the fuel flow rate. This indicates that it is possible to control the fuel channel composition with the fuel flow rate, while the air flow rate controls the temperature of the PEN.

Furthermore, it was shown that the response from air flow rate to PEN temperature behaves like a second order system, with poles around $1 \cdot 10^{-2}\,\mathrm{rad/s}$ and $1 \cdot 10^{2}\,\mathrm{rad/s}$. It is not expected that the crossover frequency of the temperature response has to be near the fastest pole. Therefore, a PI controller should be able to provide adequate control. The fuel composition response from the fuel flow rate was shown to behave as a first order system with a pole around $1\,\mathrm{rad/s}$. A PI controller is considered adequate. Both PI controllers are of the form

$$K(s) = K_p + \frac{K_i}{s}, \tag{7-2}$$

where K_p is the proportional gain and K_i is the integral gain of controller K.

Open-loop analysis revealed that it is impossible to use a non-varying controller to control the SORC. This is a consequence of the different responses to changes in fuel and air flow rate in SOFC and SOEC mode, as explained in subsection 5-3-4. This makes it necessary to design a controller with variable parameters, such as a gain-scheduling controller. A gain-scheduling controller changes controller parameters based on the value of a scheduling variable which represents different operating conditions. Basically, it consists of a look-up table for the controller parameters based on the values of the scheduling variables [82]. This method allows for quick responses to changing operating conditions. However, it is an open-loop method, which means that there is no correction of incorrect scheduling. This makes it important to select the right scheduling variable. Another disadvantage is that it can only be applied if the dynamics of the system and disturbance are known accurately. One important aspect of the scheduled controller is that the controller parameter functions should be smooth function of the scheduling variable[83], because frequent and rapid changes may lead to instabilities. In other words, $K_p = K_p(X)$ and $K_i = K_i(X)$ are smooth functions of the scheduling variable X.

There are two important guidelines for selection of the scheduling variable [84]:

- The scheduling variable should be able to capture the nonlinearities of the nonlinear model for which a controller is designed.
- The scheduling variable should vary slowly compared to the dynamics of the controlled system. This preserves stability of the system.

The common approach [85], which was also followed in this thesis, is to select several operating points which cover the range of dynamics of the system. This was already done in section 6-2. Next, controllers are designed for each operating point. The last step is to schedule the controller parameters based on the scheduling variable. The power density signal $\bar{P}$ is taken as the scheduling variable.

The PI controllers are tuned using an $\mathcal{H}_\infty$ method with a fixed controller structure with the help of the `hinfstruct` function in Matlab [86]. The $\mathcal{H}_\infty$ norm of a proper linear stable system $G(s)$ is given by

$$\|G(s)\|_\infty = \max_\omega \bar{\sigma}(G(\mathrm{i}\omega)),$$

where $\bar{\sigma}(G(\mathrm{i}\omega))$ represents the maximum singular value of G at frequency ω. This norm is the peak of the magnitude of the transfer function $G(s)$. $\mathcal{H}_\infty$ design methods aim to keep the maximum peaks below a certain bound [80]. These methods can be used to guarantee certain performance by introducing weights. Therefore, by choosing suitable weights, $\mathcal{H}_\infty$ optimization can be used to synthesize a controller that rejects disturbances up to a certain frequency. If this frequency is higher than the highest frequency that characterizes the power disturbance signal, then the power disturbance gets rejected by the controller obtained from $\mathcal{H}_\infty$ optimization.

7-3 Performance specification for controllers

Locally, the nonlinear model can be represented by the following linear model.

$$\begin{aligned} y &= \underbrace{(I+GK)^{-1}GK}_{\mathcal{T}}\, r + \underbrace{(I+GK)}_{\mathcal{S}}\, G_d d, \\ e &= \mathcal{S}r - \mathcal{S}G_d d, \\ u &= K\mathcal{S}r - K\mathcal{S}G_d d, \end{aligned}$$

where I is the identity matrix, G is the linear plant model, G_d is the linear disturbance model, and $\mathcal{S}$ and $\mathcal{T}$ represent the sensitivity and complementary sensitivity function, respectively. This representation shows that there are multiple ways to specify performance requirements. Options include,

- Shape $\mathcal{T}$ to guarantee tracking of the reference signals. It is also useful when noise attenuation is important, but that is not considered in this report.
- Shape $\mathcal{S}$ for disturbance rejection. Using the error signal instead of the output signal, it is possible to simultaneously shape for reference tracking.
- Shape $K\mathcal{S}$ to limit the size and bandwidth of the controller.

Shaping of all three functions at the same time is said to be difficult [80]. The choice was made to shape $\mathcal{S}$ and $K\mathcal{S}$, because the goal of the controller is to reject a power disturbance coming from the grid. Furthermore, it also ensures that the system can follow the reference signals. Shaping $K\mathcal{S}$ ensures that the controller is limited. A block diagram representing the $\hat{\mathcal{S}}/\hat{K}\hat{\mathcal{S}}$ mixed sensitivity optimization problem is shown in Figure 7-3. The circumflexes

(ˆ) in this diagram indicate scaled objects and signals. Scaling is used to express allowed or expected variations in certain signals. W_p and W_u are weighting filters used to specify the desired performance of the system. The remainder of this section describes the selection of scaling and weighting matrices.

The exogenous signals Ψ_1 and Ψ_2 are used for controller synthesis and given by

$$\begin{aligned}\Psi &= \begin{bmatrix}\Psi_1 \\ \Psi_2\end{bmatrix}, \\ &= \begin{bmatrix}W_u\hat{K}\hat{\mathcal{S}} & W_u\hat{K}\hat{\mathcal{S}}\hat{G}_d \\ W_p\hat{\mathcal{S}} & W_p\hat{\mathcal{S}}\hat{G}_d\end{bmatrix}\begin{bmatrix}\hat{r} \\ \hat{d}\end{bmatrix}.\end{aligned}$$

The $\mathcal{H}_\infty$ controller minimizes

$$\left\|\begin{bmatrix}W_u\hat{K}\hat{\mathcal{S}} & W_u\hat{K}\hat{\mathcal{S}}\hat{G}_d \\ W_p\hat{\mathcal{S}} & W_p\hat{\mathcal{S}}\hat{G}_d\end{bmatrix}\right\|_\infty,$$

subject to the control structure

$$\hat{K} = \begin{bmatrix}\hat{K}_{p,TPEN} + \frac{\hat{K}_{i,TPEN}}{s} & 0 \\ 0 & \hat{K}_{p,\chi_{fuel,H_2}} + \frac{\hat{K}_{i,\chi_{fuel,H_2}}}{s}\end{bmatrix}.$$

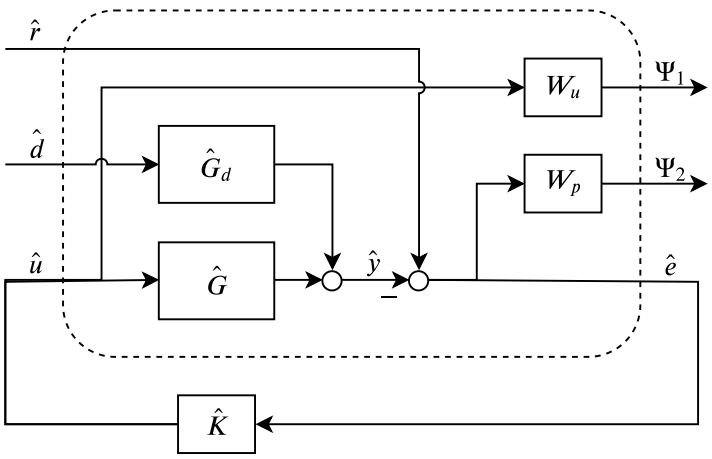

Figure 7-3: Block diagram representation of the $\hat{\mathcal{S}}/\hat{K}\hat{\mathcal{S}}$ mixed sensitivity optimization.

7-3-1 Scaling based on maximum expected or allowed signal values

Signals are scaled using constant diagonal matrices which represent the maximum expected or allowed values of each signal. Scaling of the disturbance d, error e, output y, reference r, and input u signals is given by

$$\begin{aligned}d &= \theta_d\hat{d}, \\ e &= \theta_e\hat{e}, \\ y &= \theta_e\hat{y}, \\ r &= \theta_e\hat{r}, \\ u &= \theta_u\hat{u},\end{aligned}$$

where θ_d, θ_e, and θ_u are diagonal matrices representing the largest allowed or expected changes in d, e, and u, respectively, and $\hat{Y}$ represents the scaled version of $Y \in \{d, e, y, r, u\}$. It follows that

$$\hat{G} = {\theta_e}^{-1} G \theta_u,$$
$$\hat{G}_d = {\theta_e}^{-1} G_d \theta_d,$$
$$\hat{K} = {\theta_u}^{-1} K \theta_e,$$

where $\hat{G}$, $\hat{G}_d$, and $\hat{K}$ represent scaled version of the plant model, disturbance model, and controller, respectively.

Selection of scaling matrices

θ_d indicates the largest expected change in the disturbance. The maximum absolute power density time derivative present in the scaled average net power density signal from January 2017 up to and including October 2019 as a function of operating power density is shown in Figure 7-4. All power signal were scaled such that the power density of each signal was between -7000 and $7000\,\mathrm{W/m^2}$. Based on this figure, it is sufficient to select

$$\theta_d = 2.$$

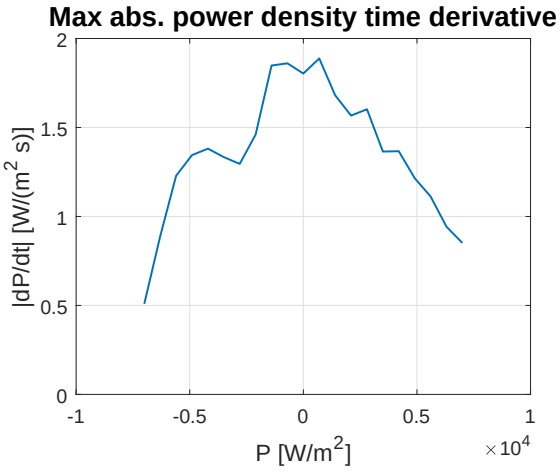

Figure 7-4: Maximum absolute power density time derivatives present in the scaled average net power density signals from January 2017 up to and including October 2019.

θ_e indicates the largest allowed errors on the PEN temperature T_{PEN} and fuel channel composition χ_{fuel,H_2}. A possible choice is

$$\theta_e = \begin{bmatrix} 5 & 0 \\ 0 & 0.05 \end{bmatrix},$$

which means that an error of 5 K in temperature and 5 pp in hydrogen fraction in the fuel channel are considered acceptable. According to Stiller, Thorud, Bolland, *et al.* [87], a constant

PEN temperature reduces the thermal fatigue, but no number was provided for acceptable temperature fluctuations. A limit on the hydrogen fraction error in the fuel channel ensures that the SORC does not run out of fuel. Based on the region of attraction, the chosen maximum allowed errors should ensure that the system stays within its stability region. This should ensure that the system stays close to its operating points.

θ_u indicates the largest allowed input change. Selecting suitable values is not straightforward. Possible choices include:

- Base the maximum allowed air flow change on a maximum allowable air ratio. The air ratio is the ratio between the oxygen inflow rate and the amount of oxygen produced (SOEC) or consumed (SOFC). For example, Cai, Adjiman, and Brandon [47] mention that air ratios between 0.4 and 14 are preferred when operating an SOEC. This range ensures that the oxygen fraction stays below 0.5, while it is said to keep the air compressor power within acceptable limits.
- Allow the flow rates to deviate by a percentage of the equilibrium flow rate.
- Consider a constant maximum flow rate deviation.

Figure 7-5 shows the equilibrium air flow rate as a function of the power density next to the air flow rate for an air ratio of 14. This shows that it is not possible to use the first approach to define the allowed air flow range based on an air ratio of 14. The air flow rate is often higher than 14 to be able to cool the cell in SOFC mode.

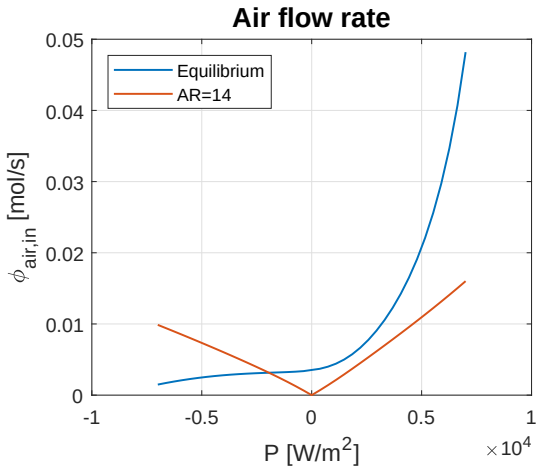

Figure 7-5: Comparison of equilibrium air flow rate as a function of power density and the air flow rate corresponding to an air ratio of 14. Equilibrium: equilibrium air flow rate, AR=14: air flow rate corresponding to an air ratio of 14.

The second option, to allow the flow rates to deviate by a percentage of the flow rate at equilibrium would result in large differences in allowed flow rate ranges over the operating point. This is especially true for the air flow rate, where the equilibrium flow rate at $7000\,\mathrm{W/m^2}$ is 32 times as high as the flow rate at $-7000\,\mathrm{W/m^2}$. For the fuel flow rate, the highest equilibrium flow rate was 4.5 times higher than the lower equilibrium flow rate.

The taken approach was based on the third option. Flow rates are allowed to change by a fixed amount, unless this results in negative flow rates. In the case of possible negative flow rate, the allowed change was set equal to the equilibrium flow rate. The allowed change in air flow rate $\phi_{air,in}$ is given by

$$\theta_{u,air} = \min(0.005, \phi_{air,in,eq}),$$

where $\phi_{air,in,eq}$ indicates the equilibrium flow rate at the operating point under consideration. Introduction of this nonlinearity does not result in more complicated controller synthesis, because controllers are synthesized at each individual operating point. The only effect this nonlinear expression has, is that it can result in different maximum allowed air flow rate changes at operating points. The fuel flow rate $\phi_{fuel,in}$ is allowed to vary by $1.0 \cdot 10^{-4}$ mol/s. Therefore,

$$\theta_u = \begin{bmatrix} \theta_{u,air} & 0 \\ 0 & 1.0 \cdot 10^{-4} \end{bmatrix}.$$

The allowed flow rate ranges as a function of power density are shown in Figure 7-6

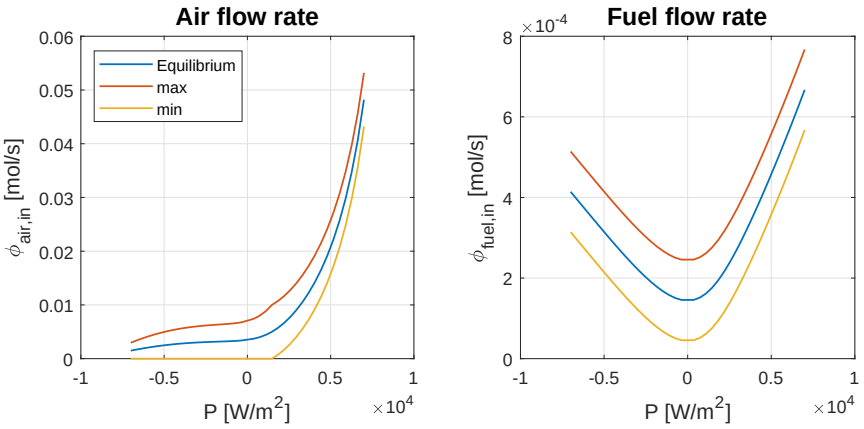

Figure 7-6: Allowed flow rate ranges as a function of power density. Left: air flow, right: fuel flow. Equilibrium: flow rate at equilibrium, min: minimum allowed flow rate, max: maximum allowed flow rate.

7-3-2 Choice of weighting filters

Two common options for weighting filters for a scaled system [80] are

Option 1: Tune controllers based on a desired closed-loop bandwidth of the system.

- W_p: Low pass filter with crossover frequency equal to that of the desired closed-loop bandwidth,

$$W_{p,l} = \frac{\frac{s}{\mathcal{A}_l} + \omega_{B,l}}{s + \omega_{B,l}\mathcal{B}_l}, \quad \mathcal{A}_l \approx 2, \mathcal{B}_l \ll 1, l \in y.$$

- W_u: Identity matrix or high pass filter with frequency approximately the closed-loop bandwidth

$$W_{u,l} = \frac{s}{s + \omega_{B,l}}, \quad l \in u.$$

Option 2: Use disturbance information to tune controllers.

- W_p: Low pass filter with bandwidth equal to that of the disturbance.
- W_u: High pass filter with crossover frequency approximately the desired closed-loop bandwidth

The main difference between the methods is the choice to use disturbance information to select the performance weights or not. This makes the second method attractive, as it uses more available information. However, if the disturbance is slow compared to the closed-loop bandwidths that can be obtained with the system, this approach results in lousy tuned controllers. The first method does not use information about the disturbance, unless the closed-loop bandwidths are selected with this information in mind.

Determination of weighting filter bandwidths

Depending on the chosen weighting filters, it is necessary to define a bandwidth that represents the dynamics of the disturbance or a desired closed-loop bandwidth. Based on the PSD estimates presented in subsection 7-1-2, a disturbance bandwidth of

$$\omega_{B,d} = 1 \cdot 10^{-3}\,\text{rad/s},$$

should make it possible to withstand power disturbances from the grid.

The desired closed-loop bandwidth can be based on settling times of open-loop system. Figure 7-7 shows the settling times of the step response of the linearized models. The settling time for the response from fuel flow rate to hydrogen content of the fuel channel ranges from 1.9 to 7.5 s and the settling time of the temperature as a result of a change in air flow rate ranges from 85 to 670 s. These wide ranges of settling times motivated the choice to select different desired closed-loop bandwidths for each operating point. The closed-loop time constant is selected twice the open-loop time constant at each operating point. The desired closed-loop frequency follows from

$$\omega_B = \frac{2}{\tau},$$

where the time constant τ is approximated by

$$\tau = \frac{t_{ss}}{4.6},$$

where t_{ss} is the open-loop settling time of the system at an operating point.

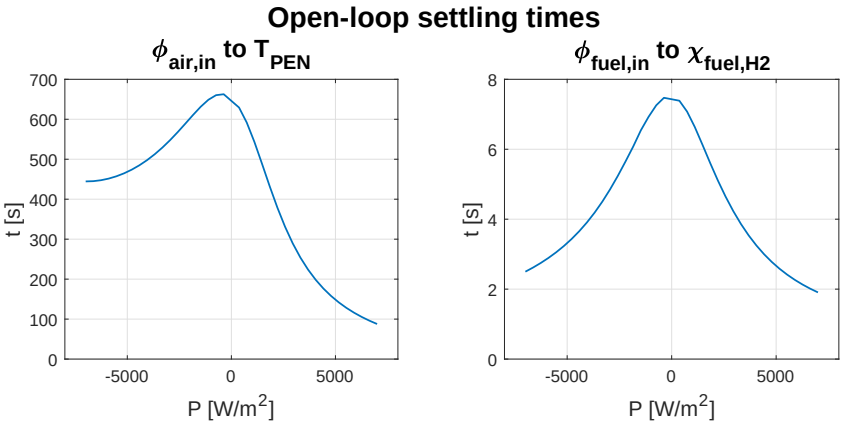

Figure 7-7: Open-loop settling times of the linearized models. Left: air inlet flow rate to PEN temperature, right: fuel inlet flow rate to hydrogen fraction in the fuel channel.

7-4 Controller synthesis

This section describes the synthesis of two controllers. The first controller is based on the disturbance signal, presented as option 2 in subsection 7-3-2. The second controller, option 1 controller, is based solely on the desired closed-loop bandwidths. This section also shows how the controller parameter functions are smoothed to make them suitable for the gain-scheduling controller.

7-4-1 Option 2: W_p based on disturbance, W_u based on desired closed-loop bandwidth

The first controller was based on option 2 in subsection 7-3-2, because it provides a convenient way to include information about the disturbance signal in controller synthesis. The choice of the scaling matrices is as described in subsection 7-3-1. The controller designed in this subsection is called the option 2 controller.

The controller parameter functions of the PI controller are shown in Figure 7-8 alongside a smoothed version of these parameter functions. The tuned controller parameter functions were not smooth close to $\bar{P} = 0\,\mathrm{W/m^2}$, which violated the requirement that the controller parameter functions must be smooth functions of the scheduling variable. Therefore, functions were fitted to approximate the controller parameter functions. An overview of the fitted controller parameter functions is shown in Table 7-1.

The temperature controller parameter functions $K_{p,T_{PEN}}$ and $K_{i,T_{PEN}}$ were approximated by an exponential function of the form

$$f_{fit} = \mathcal{A}\exp\left(\mathcal{B}\bar{P}\right) - \mathcal{A}.$$

This expression guarantees that the origin is included and that no sign changes occur when $\bar{P} \neq 0\,\mathrm{W/m^2}$. Both requirements have to be met, because the signs of the controller parameter functions are different for SOEC and SOFC, but do not change in these modes. Different parameter signs would result in controllers that operate in the opposite direction of what they

are supposed to do, such as increasing a flow rate when it should be decreased. The choice of an exponential function has no physical motivation. Several functions were tested and the exponential function showed the best fit in this case. The same motivation applies to the fits of other parameter functions. It is important to point out again that the parameter functions have to be smooth for gain scheduling. Therefore, certain functions that provide a better fit for the parameter functions were not considered. As an example, consider some function which incorporates the expression $\frac{1}{\bar{P}}$. This function might provide a better fit, but is not a smooth function, which makes it unsuitable for gain scheduling.

The controller parameter functions of the fuel composition controller $K_{p,\chi_{fuel,H_2}}$ and $K_{i,\chi_{fuel,H_2}}$ were approximated by the linear function

$$f_{fit} = \mathcal{A}\bar{P}.$$

An additional distinction was made between SOEC and SOFC mode for the K_p of the fuel composition controller, by considering a different function parameter value for both modes. This approach showed a better fit than considering one linear function for the complete power density range.

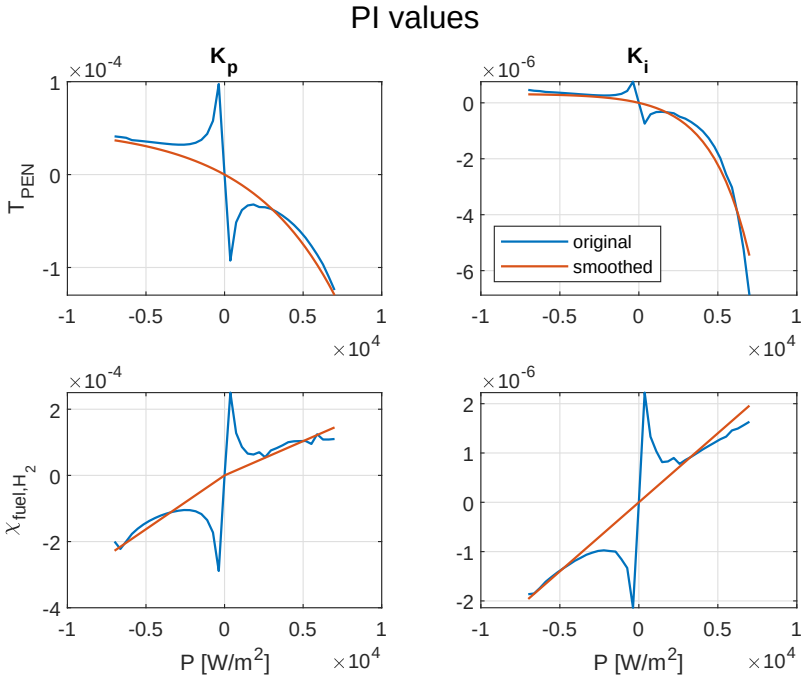

Figure 7-8: PI controller parameter values corresponding to the option 2 controller based on the power disturbance characteristics. Original: parameter values obtained from the $\hat{\mathcal{S}}/\hat{K}\hat{\mathcal{S}}$ mixed sensitivity optimization problem, smoothed: controller parameter functions fitted on the original controller values to fulfil gain-scheduling guidelines. Function values are presented in Table 7-1.

Figure 7-9 shows $W_p\hat{\mathcal{S}}$, $W_p\hat{\mathcal{S}}\hat{G}_d$, $W_u\hat{K}\hat{\mathcal{S}}$, and $W_p\hat{K}\hat{\mathcal{S}}\hat{G}_d$ for the tuned linear system at selected operating point, as well as for the linear system with smoothed controller parameter functions. The selected operating points were at -4100, -700, 400 and $1500\,\mathrm{W/m^2}$ and were selected because they show the effects of smoothing controller parameter functions. Operating points

Table 7-1: Fitted controller parameter functions for the option 2 controller based on power disturbance characteristics.

Controller	Parameter	Function	Function parameter value
Temperature	$K_{p,T_{PEN}}$	$\mathcal{A}\exp\left(\mathcal{B}\bar{P}\right) - \mathcal{A}$	$\mathcal{A} = -5.16 \cdot 10^{-5}$
			$\mathcal{B} = 1.80 \cdot 10^{-4}$
	$K_{i,T_{PEN}}$	$\mathcal{A}\exp\left(\mathcal{B}\bar{P}\right) - \mathcal{A}$	$\mathcal{A} = -3.21 \cdot 10^{-7}$
			$\mathcal{B} = 4.13 \cdot 10^{-4}$
Composition	$K_{p,\chi_{fuel,H_2}}$, SOEC	$\mathcal{A}\bar{P}$	$\mathcal{A} = 3.25 \cdot 10^{-8}$
	$K_{p,\chi_{fuel,H_2}}$, SOFC	$\mathcal{A}\bar{P}$	$\mathcal{A} = 2.07 \cdot 10^{-8}$
	$K_{i,\chi_{fuel,H_2}}$	$\mathcal{A}\bar{P}$	$\mathcal{A} = 2.80 \cdot 10^{-10}$

at higher absolute power densities showed smaller differences between the responses of the original and smoothed controllers, because the smoothed controller parameter functions are closer to the unsmoothed ones far from $\bar{P} = 0$. Furthermore, the closer the operating point is to $\bar{P} = 0$, the worse the smoothed responses meet the requirements set by W_p. This was to be expected, since the smoothed controller parameter functions are closer to 0 than the unsmoothed controller parameter functions, which means there is hardly any control close to $\bar{P} = 0$ for the controller with the smoothed parameter functions. This effect is clear in the $W_p\hat{\mathcal{S}}$ as well as in the $W_p\hat{\mathcal{S}}\hat{G}_d$ response. Disturbances close to $\bar{P} = 0$ have a relatively large influence on the system.

The $\hat{K}\hat{\mathcal{S}}$ responses show that a PI controller is not enough to lift $\hat{K}\hat{\mathcal{S}}$ such that it follows the prescribed filter W_u^{-1}. The response of $\hat{K}\hat{\mathcal{S}}$ is flat for most of the frequencies.

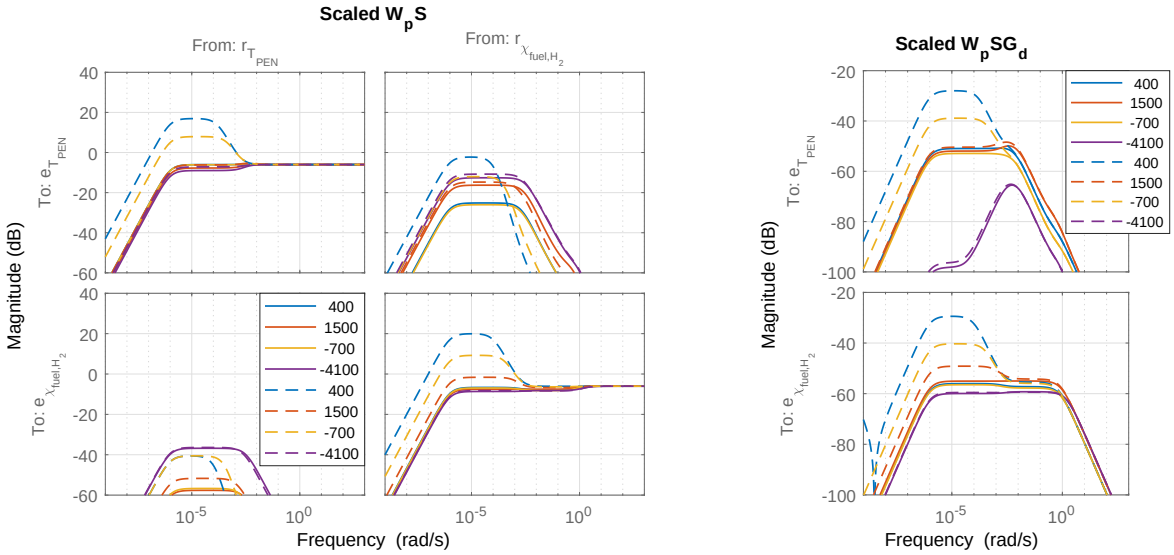

(a) $W_p\hat{\mathcal{S}}$

(b) $W_p\hat{\mathcal{S}}\hat{G}_d$

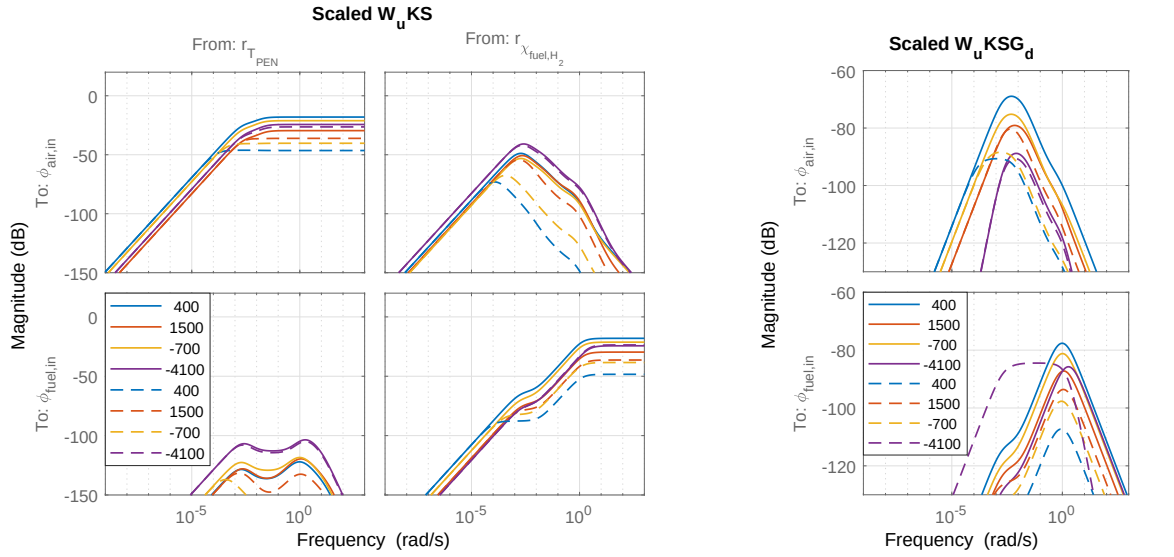

(c) $W_u\hat{K}\hat{\mathcal{S}}$

(d) $W_p\hat{K}\hat{\mathcal{S}}\hat{G}_d$

Figure 7-9: Bode magnitude plots for $W_p\hat{\mathcal{S}}$, $W_p\hat{\mathcal{S}}\hat{G}_d$, $W_u\hat{K}\hat{\mathcal{S}}$, and $W_p\hat{K}\hat{\mathcal{S}}\hat{G}_d$ for the option 2 controller based on power disturbance characteristics. Solid lines: systems with the original controller parameter functions obtained from the $\hat{\mathcal{S}}/\hat{K}\hat{\mathcal{S}}$ mixed sensitivity optimization problem, dashed lines: systems with fitted controller parameter functions as presented in Table 7-1. The numbers in the legend indicate the power density in $\mathrm{W/m^2}$ at the operating points included in the figure.

7-4-2 Option 1: W_p and W_u based on desired closed-loop bandwidth

A controller was also synthesized for weighting filter selection option 1 from subsection 7-3-2 where W_u was taken as the identity matrix instead of a high pass filter. A high pass filter should not yield an improvement over this approach, because it is likely that a PI controller will not be able to meet the requirements set by s high pass W_u. This follows from subsection 7-4-1, which showed that a PI controller was not able to lift the $\hat{K}\hat{\mathcal{S}}$ function enough to closely follow weighting filter W_u. The controller synthesized in this section is called the option 1 controller.

Figure 7-10 presents the original and smoothed controller parameter functions. The temperature controller parameter functions $K_{p,T_{PEN}}$ and $K_{i,T_{PEN}}$, and $K_{p,\chi_{fuel,H_2}}$ of the composition controller are approximated by

$$f_{fit} = \mathcal{A}\exp\left(\mathcal{B}\bar{P}\right) - \mathcal{A}.$$

The parameter function $K_{i,\chi_{fuel,H_2}}$ of the composition controller is approximated by two exponentials of the same form: one for SOEC, one for SOFC. The values of the fitted functions can be found in Table 7-2. The smoothed controller parameters functions $K_{p,T_{PEN}}$, $K_{i,T_{PEN}}$, and $K_{p,\chi_{fuel,H_2}}$ of controller option 1 are 8 to 25 times larger than the controller parameter functions of controller option 2. Smoothed controller parameter function $K_{i,\chi_{fuel,H_2}}$ is even 250 to $3.2 \cdot 10^4$ times higher for controller option 1 compared to controller option 2.

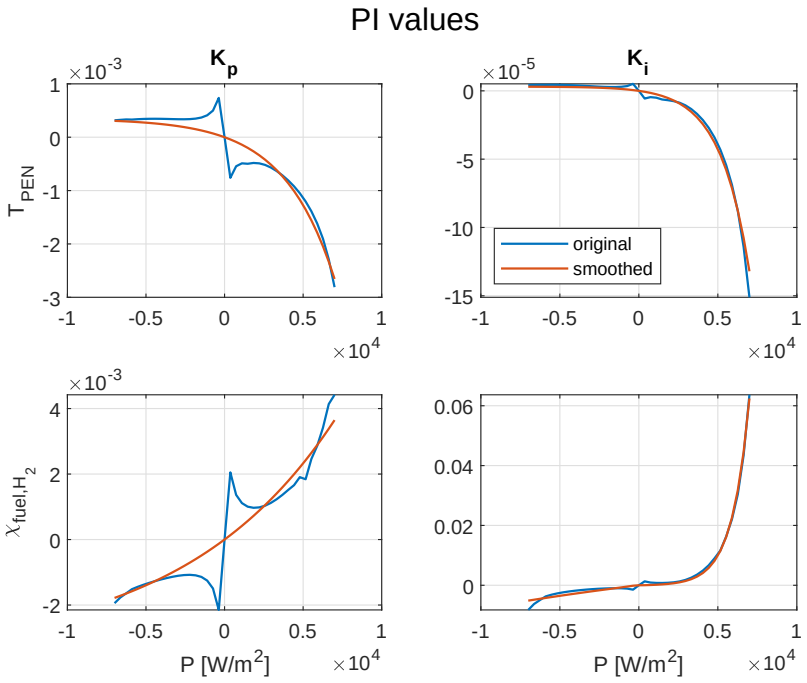

Figure 7-10: PI controller parameter values corresponding to the option 1 controller based on desired closed-loop bandwidth. Original: parameter values obtained from the $\hat{\mathcal{S}}/\hat{K}\hat{\mathcal{S}}$ mixed sensitivity optimization problem, smoothed: controller parameter functions fitted on the original controller values to fulfil gain-scheduling guidelines. Function values are presented in Table 7-2.

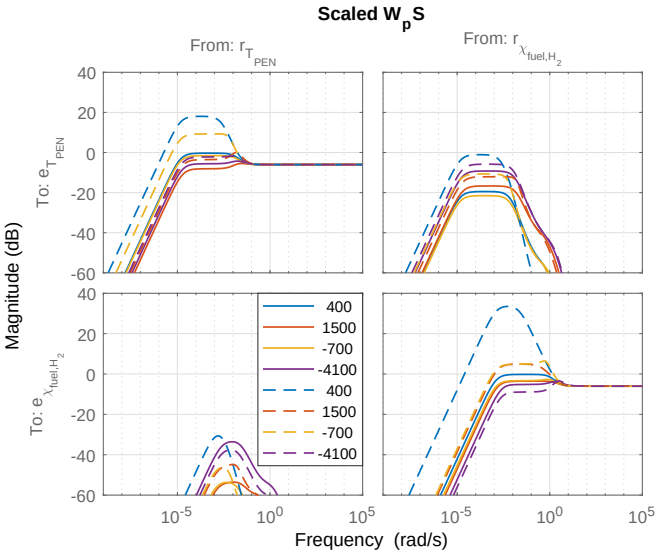

(a) $W_p\hat{\mathcal{S}}$

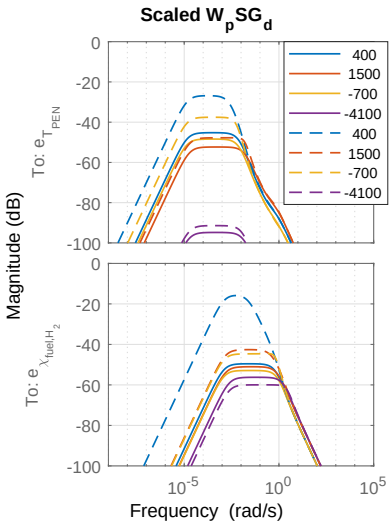

(b) $W_p\hat{\mathcal{S}}\hat{G}_d$

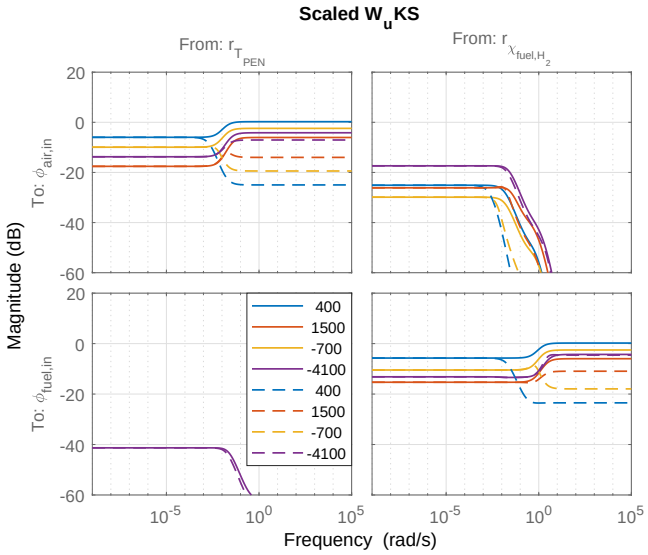

(c) $W_u\hat{K}\hat{\mathcal{S}}$

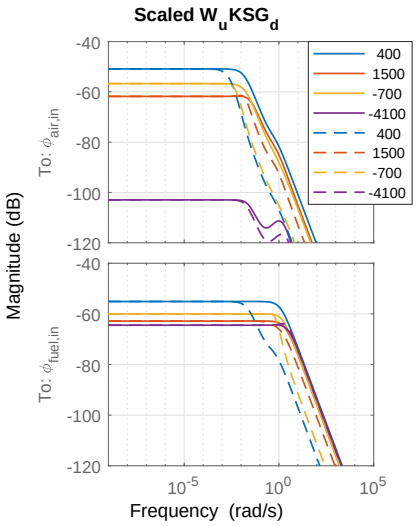

(d) $W_p\hat{K}\hat{\mathcal{S}}\hat{G}_d$

Figure 7-11: Bode magnitude plots for $W_p\hat{\mathcal{S}}$, $W_p\hat{\mathcal{S}}\hat{G}_d$, $W_u\hat{K}\hat{\mathcal{S}}$, and $W_p\hat{K}\hat{\mathcal{S}}\hat{G}_d$ for the option 1 controller based on power disturbance characteristics. Solid lines: systems with the original controller parameter functions obtained from the $\hat{\mathcal{S}}/\hat{K}\hat{\mathcal{S}}$ mixed sensitivity optimization problem, dashed lines: systems with fitted controller parameter functions as presented in Table 7-2. The numbers in the legend indicate the power density in $\mathrm{W/m^2}$ at the operating points included in the figure.

Table 7-2: Fitted controller parameter functions for the option 1 controller based on desired closed-loop bandwidths.

Controller	Parameter	Function	Function parameter value
Temperature	$K_{p,T_{PEN}}$	$\mathcal{A}\exp\left(\mathcal{B}\bar{P}\right)-\mathcal{A}$	$\mathcal{A}=-3.46\cdot10^{-4}$ $\mathcal{B}=3.09\cdot10^{-4}$
	$K_{i,T_{PEN}}$	$\mathcal{A}\exp\left(\mathcal{B}\bar{P}\right)-\mathcal{A}$	$\mathcal{A}=-3.07\cdot10^{-6}$ $\mathcal{B}=5.40\cdot10^{-4}$
Composition	$K_{p,\chi_{fuel,H_2}}$	$\mathcal{A}\exp\left(\mathcal{B}\bar{P}\right)-\mathcal{A}$	$\mathcal{A}=3.49\cdot10^{-3}$ $\mathcal{B}=1.02\cdot10^{-4}$
	$K_{i,\chi_{fuel,H_2}}$, SOEC	$\mathcal{A}\exp\left(\mathcal{B}\bar{P}\right)-\mathcal{A}$	$\mathcal{A}=-1.70\cdot10^{-2}$ $\mathcal{B}=-3.78\cdot10^{-5}$
	$K_{i,\chi_{fuel,H_2}}$, SOFC	$\mathcal{A}\exp\left(\mathcal{B}\bar{P}\right)-\mathcal{A}$	$\mathcal{A}=1.03\cdot10^{-4}$ $\mathcal{B}=9.16\cdot10^{-4}$

Responses of $W_p\hat{\mathcal{S}}$, $W_p\hat{\mathcal{S}}\hat{G}_d$, $W_u\hat{K}\hat{\mathcal{S}}$, and $W_p\hat{K}\hat{\mathcal{S}}\hat{G}_d$ are shown in Figure 7-11 for selected operating points. This figure includes the responses for the unsmoothed and the smoothed controller. As for systems with the option 2 controller, there is virtually no control when the power density is close to $\bar{P}=0$. This expresses itself by relative large responses of $W_p\hat{\mathcal{S}}$ and $W_p\hat{\mathcal{S}}\hat{G}_d$ at operating points close to $\bar{P}=0$. The responses of $W_u\hat{K}\hat{\mathcal{S}}$ shows that all controlled systems meet the requirements set by the weighting filter W_u.

7-5 Simulation of the controlled nonlinear system

This section puts the smoothed gain-scheduling PI controllers to the test by implementing them in the nonlinear SORC model. Two different simulations were done. First, scaled and shifted versions of the average net power signals are used to see if the controlled system is able to withstand the disturbances the controllers were designed for. Next, simulations are run for certain days that exhibit large variations over relatively short periods of time. A comparison of the nonlinear system controlled by smoothed controllers and unsmoothed controllers can be found in section G-1. The results from this comparison show that unsmoothed controllers are more aggressive than smoothed controllers when the power density is close to zero. The more aggressive temperature control can result in situations where the SORC is overflown with oxygen or runs out of oxygen, which is detrimental to the SORC. Additionally, section G-2 evaluates the PEN temperature time derivative of the simulations presented in this section.

In all cases, the controller performance is quantified by the trapezoidal approximation of the integral of squared error (ISE),

$$\begin{aligned} ISE &= \int e^2(t)\,\mathrm{d}t\,, \\ &\approx \sum_{l=2}^{\mathcal{N}_e} \frac{e^2(t_{l-1})+e^2(t_l)}{2}\Delta t_l, \end{aligned}$$

where e is the error signal as defined in section 5-4 and $\mathcal{N}_e$ is the number of data points. The ISE was chosen instead of the integral of absolute error, because it puts a higher penalty on

large errors compared to small errors. Some simulations did not succeed, for example because the SORC ran out of hydrogen. No ISE value were assigned in these cases.

The reference signals for the simulations were defined in subsection 5-3-4.

Each power signal is scaled such that it covers the complete operating range of the SORC, which is -7000 to $7000\,\mathrm{W/m^2}$. The initial conditions and flow rates are obtained from the operating point closest to the power density at the start of the simulation. Reason for this approach was that the interest of this study lies within dynamic operation of an SORC, not the start-up of the system. The output power density signal of the SORC is given by

$$\bar{P} = -\hat{P}_{net},$$

where $\hat{P}_{net}$ indicates the scaled net power, such that it represents a power density in the range of -7000 to $7000\,\mathrm{W/m^2}$. The net power P_{net} is defined as Equation (5-1). This output power signal ensures that the SORC counteracts the power variations in the grid, resulting in a constant power demand from non-variable power sources.

7-5-1 Average net power signal as disturbance

Simulations were conducted for disturbance signals based on the average net power signal of January 2018 and July 2018. All simulations were done with controllers with smoothed parameter functions. The performance of the controlled system is summarized in Table 7-3. Option 1 controller shows lower peak values and ISE values than controller option 2, which indicates better performance for controller option 1.

The simulation for the power density signal of January 2018 is shown in Figure 7-12 together with the corresponding PEN temperature reference and hydrogen fraction in the fuel channel reference. Controller option 1 is more capable to follow the prescribed references. This is also clear from Figure 7-13, where the inputs and error signals are plotted. The system controlled by controller option 2 exceeds the temperature boundaries two times and fails at three instances to keep the fuel channel composition within its boundaries. Controller option 1 fails once to keep the PEN temperature within its boundaries, but has no problem keeping the hydrogen fraction close to its reference value. As expected, both controllers show relatively large deviations when the power density is close to $\bar{P} = 0$. It should be noted that this is no problem, as the temperature and hydrogen fraction are close to the inlet conditions, which makes it possible to sustain larger deviations. The input signals show that flow rates stay within their limits.

Additional data is shown in Figure 7-14. This figure does not show significant differences between controller option 1 and controller option 2. As mentioned in section 5-1, the oxygen fraction in the air channel stays within 0.2 and 0.3 as a result of the relatively high air flow rate needed to cool or heat the SORC. No additional oxygen fraction controller is needed in this case.

Figure 7-15 shows simulation results for the average net power density of July 2018. Controller option 2 shows larger deviations than controller option 1. Controller option 1 seems to keep the system within a reasonable operating range. Figure 7-16 shows that this is the case for most of the simulation. Controller option 1 has no problem keeping the fuel channel composition around its reference signal, but the temperature error signal shows that the nonlinear system

exceeds the 5 K limit twice. As before, this is when the system transitions from SOFC to SOEC, or vice versa, and should not result in problems when running the system.

The cell voltage, shown in Figure 7-17, shows larger voltage variations for controller option 2 than for controller option 1. These variations are not as visible in the current density response. As for the previous simulation, the oxygen fraction in the air channel stays close to the oxygen fraction in the inlet air flow.

Additional performance data for the smoothed and unsmoothed controllers based on average net power density disturbance signals from January 2017 to October 2019 can be found in Appendix F.

Table 7-3: Controller performance measures for the controlled nonlinear SORC system disturbed by scaled average net power signal. ISE: integral of squared error. Max. abs. error: maximum absolute error. ISE values were not assigned for failed simulations.

				Max. abs. error	
Month	Controller	ISE T_{PEN} [K^2]	ISE χ_{fuel,H_2} [-]	T_{PEN} [K]	χ_{fuel,H_2} [pp]
January 2018	Option 1	$1.31 \cdot 10^6$	$1.37 \cdot 10^{-4}$	5.34	$4.28 \cdot 10^{-2}$
	Option 2	$2.23 \cdot 10^8$	$7.97 \cdot 10^3$	8.02	10.7
July 2018	Option 1	$8.10 \cdot 10^5$	$9.94 \cdot 10^{-3}$	7.63	$7.12 \cdot 10^{-2}$
	Option 2	$3.70 \cdot 10^8$	$1.42 \cdot 10^3$	11.1	14.0

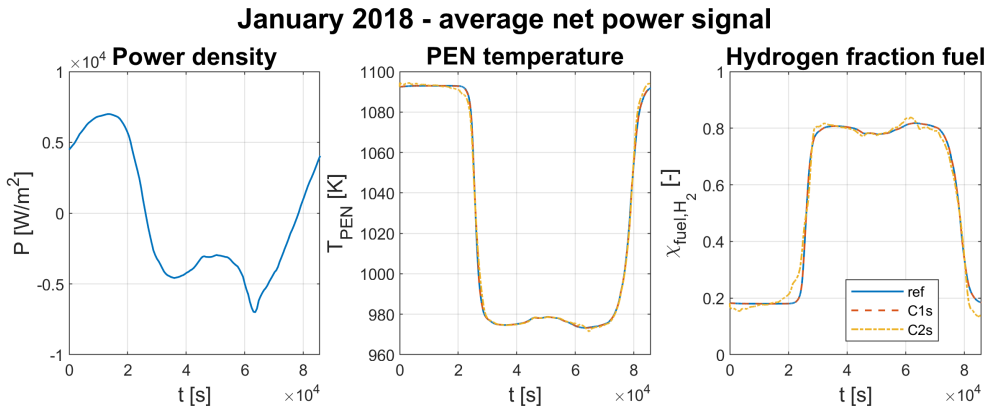

Figure 7-12: Output (center and right) of dynamic simulation of the controlled nonlinear system with the average net power density signal of January 2018 as disturbance signal (left). ref: reference signal, C1s: controller option 1 with smoothed parameter functions, C2s: controller option 2 with smoothed parameter functions, Hydrogen fraction fuel: Hydrogen fraction in fuel channel.

7-5-2 Daily power signals as disturbance

One of the consequences of considering an average power signal is that it reduces the variations that might be present in the original data. This subsection considers the net power signals of 10 December 2017 and 18 June 2019, since both power signals contained unusual variations

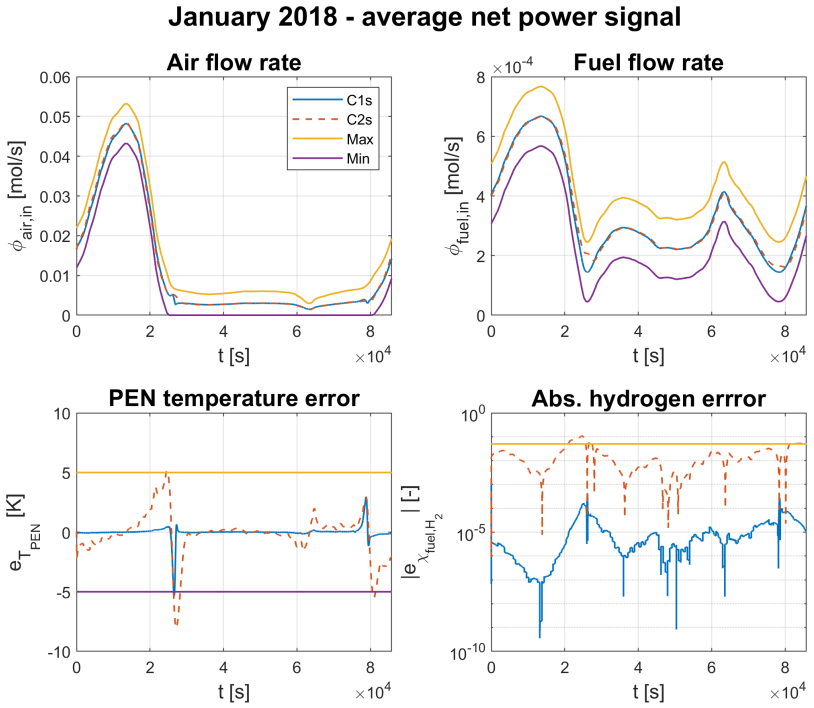

Figure 7-13: Input signals (top) and error signals (bottom) of the dynamic simulation of the controlled nonlinear system with the average net power density signal of January 2018 as disturbance signal. C1s: controller option 1 with smoothed parameter functions, C2s: controller option 2 with smoothed parameter functions, Max: maximum allowed input and error value as set by the scaling matrices θ_u and θ_e, respectively, Min: minimum allowed input and error value as set by the scaling matrices θ_u and θ_e, respectively, Abs. hydrogen error: absolute hydrogen fraction in the fuel channel error.

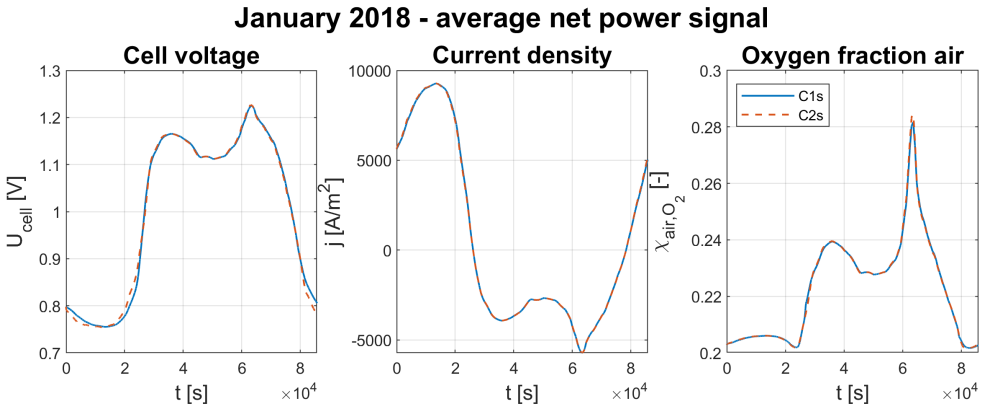

Figure 7-14: Additional outputs of the dynamic simulation of the controlled nonlinear system with the average net power density signal of January 2018 as disturbance signal. C1s: controller option 1 with smoothed parameter functions, C2s: controller option 2 with smoothed parameter functions, Oxygen fraction air: oxygen fraction in air channel.

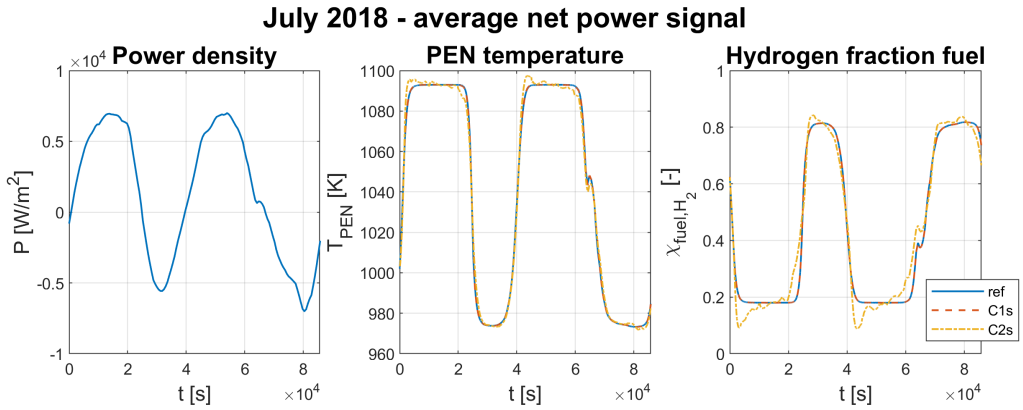

Figure 7-15: Output (center and right) of dynamic simulation of the controlled nonlinear system with the average net power density signal of July 2018 as disturbance signal (left). ref: reference signal, C1s: controller option 1 with smoothed parameter functions, C2s: controller option 2 with smoothed parameter functions, Hydrogen fraction fuel: Hydrogen fraction in fuel channel.

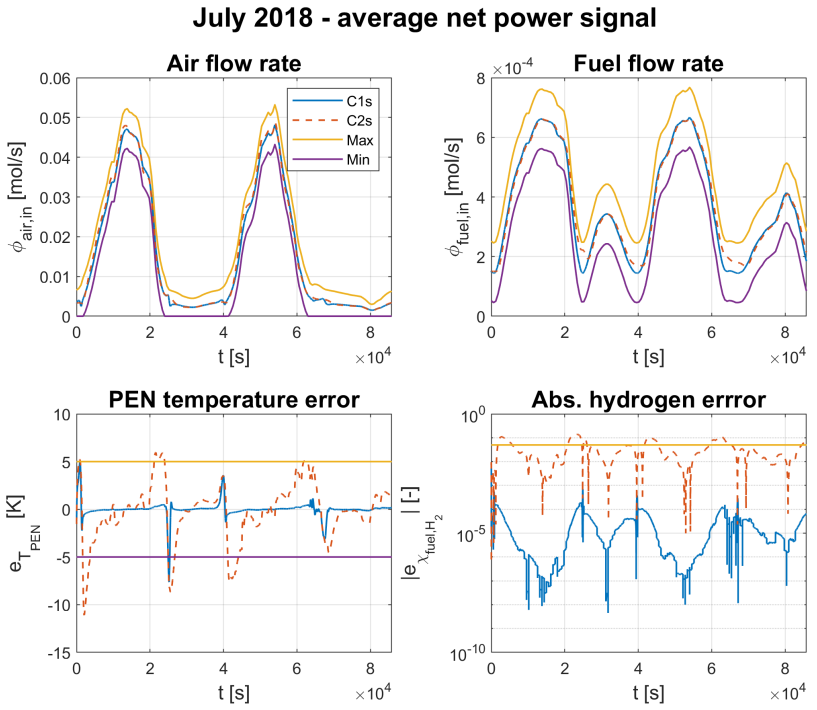

Figure 7-16: Input signals (top) and error signals (bottom) of the dynamic simulation of the controlled nonlinear system with the average net power density signal of July 2018 as disturbance signal. C1s: controller option 1 with smoothed parameter functions, C2s: controller option 2 with smoothed parameter functions, Max: maximum allowed input and error value as set by the scaling matrices θ_u and θ_e, respectively, Min: minimum allowed input and error value as set by the scaling matrices θ_u and θ_e, respectively, Abs. hydrogen error: absolute hydrogen fraction in the fuel channel error.

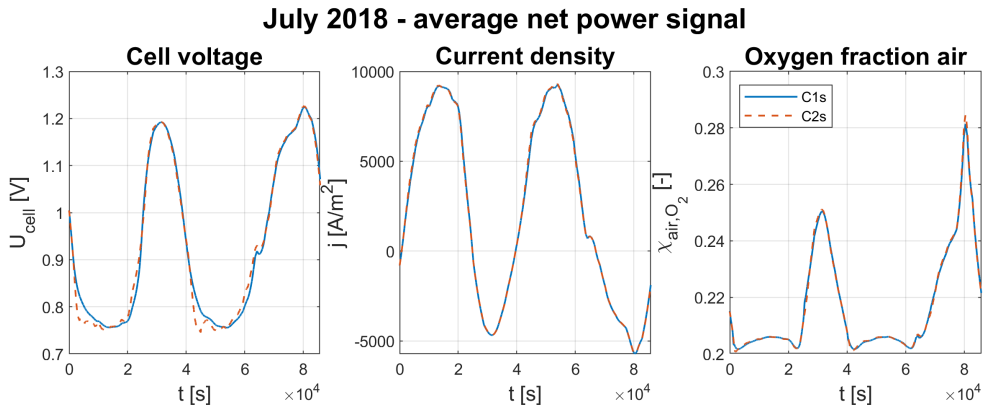

Figure 7-17: Additional outputs of the dynamic simulation of the controlled nonlinear system with the average net power density signal of July 2018 as disturbance signal. C1s: controller option 1 with smoothed parameter functions, C2s: controller option 2 with smoothed parameter functions, Oxygen fraction air: oxygen fraction in air channel.

over a day. The performance of the controllers is summarized in Table 7-4. Again, controller option 1 shows better performance than option 2. The results also show that controller option 2 is not always able to complete the simulation. This is a result of the system running out of hydrogen.

First, the power signal of 10 December 2017 was applied to the controlled system. The results are shown in Figure 7-18, Figure 7-19, and Figure 7-20. The power signal shows unusual large variations in SOEC mode between $6 \cdot 10^4$ and $7 \cdot 10^4$ s, showing four changes in the order of $300\,\mathrm{W/(m^2\,min)}$. These changes result in relatively fast changes in the reference signals. Both controllers are able to complete the simulations, but the performances of the controllers is different. Controller option 1 is able to follow the fuel composition reference. The temperature error exceeds 5 K once as a result of a fast change in temperature reference. The variations in cell voltage and current density are relatively large. This is unpreventable, because of the large power density change. As before, the oxygen fraction stays within 0.19 and 0.29. Controller option 2 violates the PEN temperature error bound of 5 K five times and the hydrogen fraction bound of 5 pp six times as a result steep power changes. The performance of controller option 2 are considered to be unsatisfactory.

The simulation for 18 June 2019 is shown in Figure 7-21, Figure 7-22, and Figure 7-23. The power density signal of this day shows two changes in the order of $300\,\mathrm{W/(m^2\,min)}$ in SOFC mode. Only controller option 1 was able to complete the simulations. Option 2 controller failed, because it ran out of hydrogen. This was the result of a voltage drop accompanied by a current density increase, which is proportional to the hydrogen consumption. The controller was not able to respond fast enough and failed to provide enough hydrogen. Controller option 1 keeps the system within its bounds at all times, only showing relatively large temperature deviations when switching from one operating mode to another.

Table 7-4: Controller performance measures for the controlled nonlinear SORC system disturbed by scaled net power signal. ISE: integral of squared error. Max. abs. error: maximum absolute error. ISE values were not assigned for failed simulations.

				Max. abs. error	
Date	Controller	ISE T_{PEN} [K^2]	ISE χ_{fuel,H_2} [-]	T_{PEN} [K]	χ_{fuel,H_2} [pp]
10 December 2017	Option 1	$9.03 \cdot 10^5$	$2.79 \cdot 10^{-3}$	5.63	0.108
	Option 2	$2.58 \cdot 10^7$	$3.79 \cdot 10^4$	26.8	16.6
18 June 2019	Option 1	$2.12 \cdot 10^7$	$3.98 \cdot 10^{-3}$	4.57	$8.28 \cdot 10^{-2}$
	Option 2	–	–	20.2	20.3

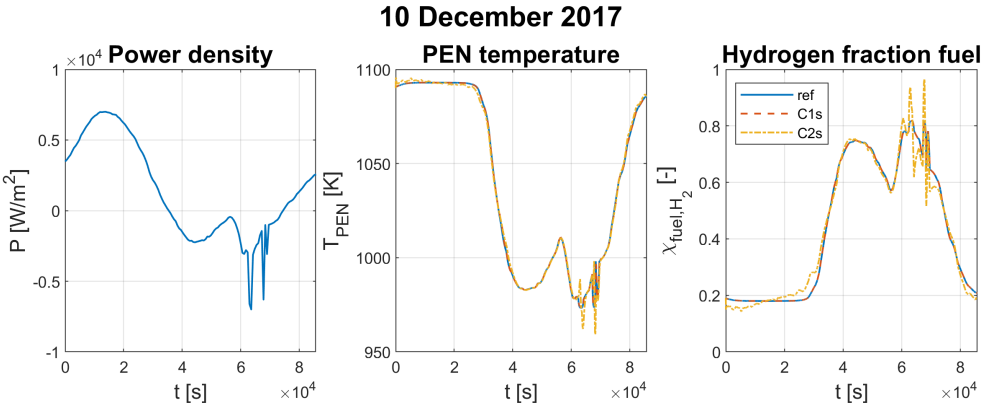

Figure 7-18: Output (center and right) of dynamic simulation of the controlled nonlinear system with the net power density signal of 10 December 2017 as disturbance signal (left). ref: reference signal, C1s: controller option 1 with smoothed parameter functions, C2s: controller option 2 with smoothed parameter functions, Hydrogen fraction fuel: Hydrogen fraction in fuel channel.

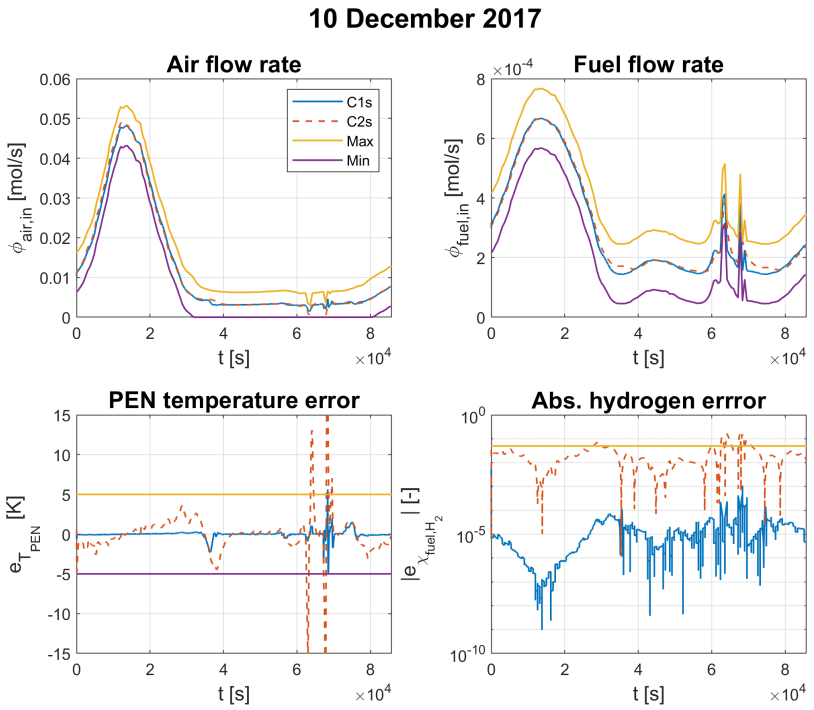

Figure 7-19: Input signals (top) and error signals (bottom) of the dynamic simulation of the controlled nonlinear system with the net power density signal of 10 December 2017 as disturbance signal. C1s: controller option 1 with smoothed parameter functions, C2s: controller option 2 with smoothed parameter functions, Max: maximum allowed input and error value as set by the scaling matrices θ_u and θ_e, respectively, Min: minimum allowed input and error value as set by the scaling matrices θ_u and θ_e, respectively, Abs. hydrogen error: absolute hydrogen fraction in the fuel channel error.

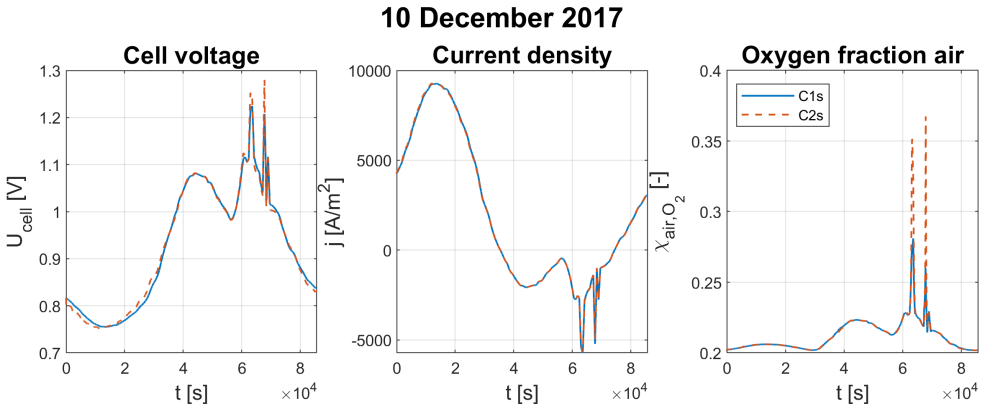

Figure 7-20: Additional outputs of the dynamic simulation of the controlled nonlinear system with the net power density signal of 10 December 2017 as disturbance signal. C1s: controller option 1 with smoothed parameter functions, C2s: controller option 2 with smoothed parameter functions, Oxygen fraction air: oxygen fraction in air channel.

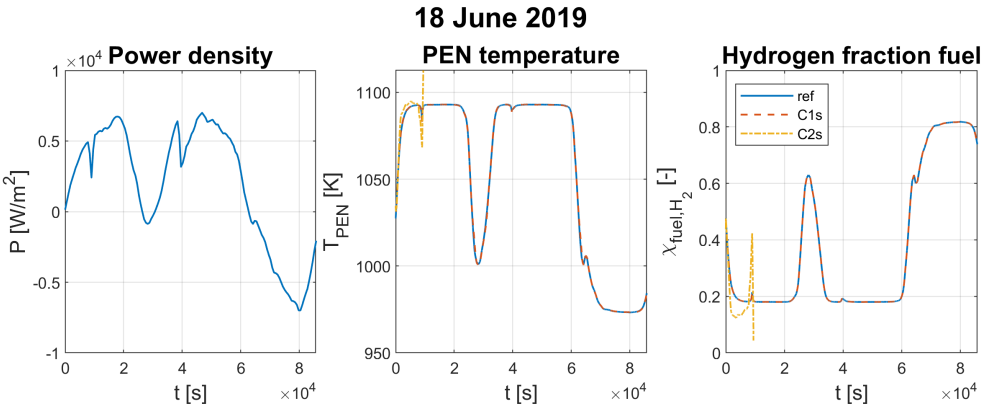

Figure 7-21: Output (center and right) of dynamic simulation of the controlled nonlinear system with the net power density signal of 18 June 2019 as disturbance signal (left). ref: reference signal, C1s: controller option 1 with smoothed parameter functions, C2s: controller option 2 with smoothed parameter functions, Hydrogen fraction fuel: Hydrogen fraction in fuel channel. Controller C2s was unable to complete the simulation, because the SORC ran out of hydrogen.

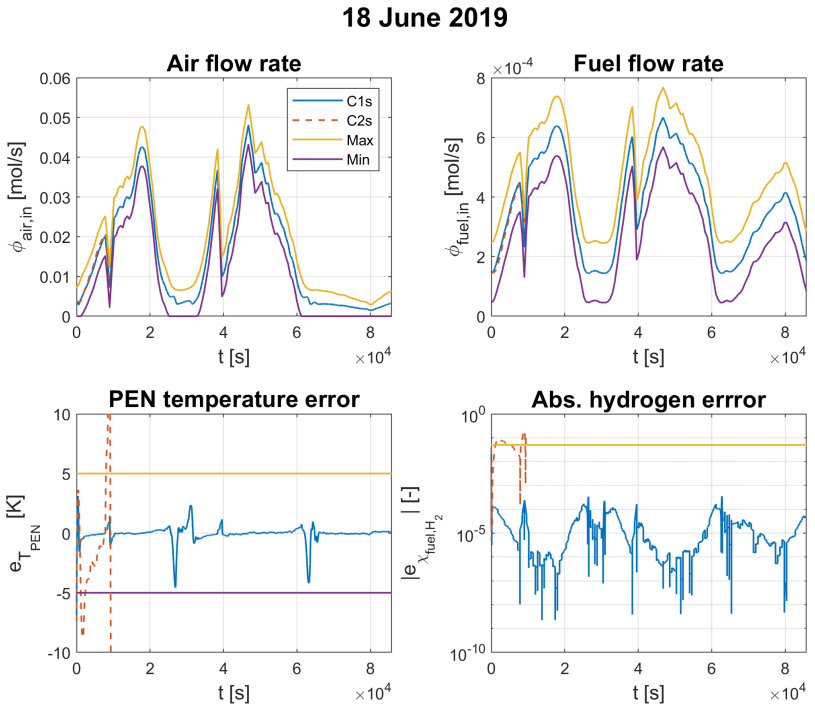

Figure 7-22: Input signals (top) and error signals (bottom) of the dynamic simulation of the controlled nonlinear system with the net power density signal of 18 June 2019 as disturbance signal. C1s: controller option 1 with smoothed parameter functions, C2s: controller option 2 with smoothed parameter functions, Max: maximum allowed input and error value as set by the scaling matrices θ_u and θ_e, respectively, Min: minimum allowed input and error value as set by the scaling matrices θ_u and θ_e, respectively, Abs. hydrogen error: absolute hydrogen fraction in the fuel channel error. Controller C2s was unable to complete the simulation, because the SORC ran out of hydrogen (see Figure 7-21).

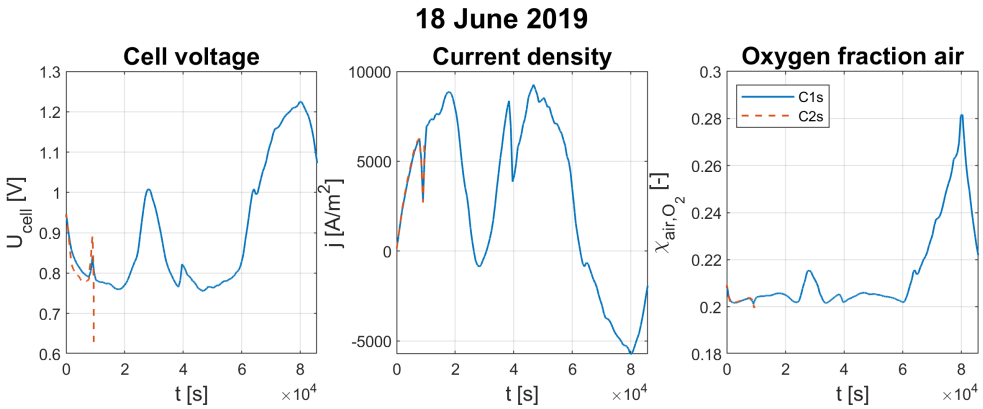

Figure 7-23: Additional outputs of the dynamic simulation of the controlled nonlinear system with the net power density signal of 18 June 2019 as disturbance signal. C1s: controller option 1 with smoothed parameter functions, C2s: controller option 2 with smoothed parameter functions, Oxygen fraction air: oxygen fraction in air channel. Controller C2s was unable to complete the simulation, because the SORC ran out of hydrogen (see Figure 7-21).

7-6 Conclusion

Two gain-scheduling PI controllers were designed using $\mathcal{H}_\infty$ optimization for the purpose of rejecting power disturbances coming from the power grid. Controller option 1 was based on the desired closed-loop bandwidth, while controller option 2 also used characteristic information about the power disturbance. The PI controller based solely on the closed-loop bandwidth showed better performance than the controller which also used information about the power disturbance signal.

Controller option 2 showed relatively large errors in temperature and fuel channel composition and exceeded the error limits of 5 K in PEN temperature and 5 pp in hydrogen fraction in the fuel channel more often than controller option 1. There were also instances where controller option 2 was unable to complete a simulation, due to the hydrogen controller being too slow to prevent fuel depletion.

Controller option 1 had no problems following the hydrogen fraction reference and the largest observed error was 0.108 pp. This controller was also able to follow the temperature reference within 5 K at most instances. The temperature error limit was exceeded when the power density signal showed variations in the order of 300 $\mathrm{W/m^2}$ in SOEC mode and twice when transitioning from one operating mode to another. The largest observed temperature error during transitioning from SOEC to SOFC, or vice versa, was 7.63 K. This error is acceptable, taking into account that the reference signal was chosen in such a way that the temperature reference is close to the inlet temperature when the power density is close to 0 $\mathrm{W/m^2}$.

Control of the oxygen fraction in the air channel was not necessary for the simulations shown in this chapter, because there were no simulations where the oxygen fraction in the air channel exceeded 0.5. However, stricter temperature control, possibly combined with a faster varying reference signal, could result in situations where oxygen fraction control is necessary. Reason for this is the fact that the temperature controller uses the air flow rate, but does not consider the oxygen levels in the air channel.

Chapter 8

Conclusions

The objective of this thesis was the following: design a power disturbance rejection controller for a large-scale solid oxide reversible cell (SORC) for daily power stabilization applications in a mixed power grid. Power stabilization refers to the ability to reduce the effects of time-based variations in the demand for electricity coming from controllable energy sources as a result of the growing integration of variable renewable energy sources (RESs). The reason for reducing these variations lies in the inability of base load power plants to deal with large and fast power variations. SORCs are one of the most promising technologies to deal with these variations by converting hydrogen to electricity during peak hours and converting electricity to hydrogen when electricity demand is low. The objective was met by developing a dynamic single-cell SORC model and a control strategy for a case where the SORC operates in a mixed electrical power grid.

A 0D dynamic SORC model was developed based on solid oxide fuel cell (SOFC) models from literature. The SORC model is an extended SOFC model, where positive power/current indicates fuel cell mode and negative power/current indicates electrolyzer mode. Reason for this approach was that an SORC is a combination of an SOFC and an solid oxide electrolysis cell (SOEC), and that there are no differences between the (electrochemical) models of these types of cells. Therefore, this approach makes it possible to have one continuous model that is able to describe both operating modes.

Validation of the model was done by comparing static cell voltage-current density (U-j) curves of a single cell experiment with the developed model. This made it possible to validate the electrochemical model and to some extent steady-state expressions of the material balances. Next, electrochemical model parameters were estimated from experimental data of a small stack setup.

The control goal was formulated as driving errors in positive electrode, electrolyte, negative electrode (PEN) temperature and hydrogen composition in the fuel channel introduced by a power disturbance to zero twice as fast as the open-loop response of the SORC. This control goal was motivated by the envisioned operation of SORCs as load shifting devices in the electrical power grid.

Open-loop analysis of the model showed that the system is stable and can be decoupled. The air flow rate only has noticeable influence on the PEN temperature, while the fuel flow rate influences both the PEN temperature and fuel composition. This was confirmed by calculation of the relative gain array (RGA) of the plant model G, which showed that RGA element 1,1 was between 0.98 and 1.08.

A sensitivity analysis of the outputs to changes in input signals showed that input changes have different effects in SOFC and SOEC mode. These differences are explained by the exothermic, hydrogen consuming nature of the SOFC and the endothermic, hydrogen producing nature of the SOEC. In SOFC mode, an increase in air flow rate results in a lower temperature and an increase in fuel flow rate results in a higher hydrogen fraction in the fuel channel. In SOEC mode, an increased air flow rate leads to higher temperatures and an increase in fuel flow rate results in a lower hydrogen fraction in the fuel channel. It was also shown that input changes have smaller effects when the SORC operates at power densities close to $0\,\mathrm{W/m^2}$.

Based on the results of the open-loop analysis, it was concluded that two gain-scheduling proportional-integral (PI) controllers were sufficient to control the SORC. Gain scheduling was necessary due to the different nature of the SOFC and SOEC. The power density disturbance was chosen as scheduling variable. The first PI controller controlled the PEN temperature by manipulating the air flow rate. The second controller used the fuel flow rate to control the hydrogen fraction in the fuel channel.

Controller parameter functions were obtained from solving an $\mathcal{H}_\infty$ optimization problem based on the sensitivity function $\mathcal{S}$ and the product of controller and sensitivity function $K\mathcal{S}$. The gain-scheduling approach made it necessary to smooth the controller parameter functions, which left the system with virtually no control when operated at power densities close to $0\,\mathrm{W/m^2}$. This situation did not result in critical situations, provided that the reference signals were shaped in such a way that the PEN temperature is close to the inlet temperature and the hydrogen fraction is close to 0.5 when operating in this region.

Two method were considered and compared for the selection of performance weighting filters for the optimization problem. The first method was based on the desired closed-loop bandwidth, while the second method used the bandwidth of the disturbance signal. The first method showed to be superior to the second method, because obtainable closed-loop bandwidths were faster than the bandwidth of the disturbance. Therefore, the controllers obtained from the first method are tuned tighter than the controllers of the second method. Controller 2 ran the risk of running out of hydrogen and had troubles following the temperature reference. Controller 1 was able to keep the hydrogen fraction in the fuel channel within 0.11 pp of the reference signal. Transitions from SOFC to SOEC mode, or vice versa, were the only moments when the temperature error occasionally exceeded the 5 K error limit for controller 1. Therefore, it was shown that a decoupled controller consisting of two PI controllers based on the desired closed-loop bandwidths was capable of controlling the SORC when subjected to a power disturbance coming from a mixed power grid. This makes it possible to use SORCs for daily grid power stabilization applications.

It should be mentioned that the power disturbance signal used in this study contained one measurement every ten minutes. Faster power variations were not considered and the system response to faster variations is unknown. If necessary, SORCs can be coupled with fast responding energy storage solutions, such as supercapacitors, to filter fast power variations in the power grid.

Chapter 9

Recommendations

The research conducted for this thesis is not complete. Many challenges lie ahead before implementation of SORCs is possible in the power grid. This chapter presents ideas for improvement and further research.

9-1 Higher order model for simulation of local variations

The model presented in this thesis is a 0D model. A limitation of such a model is that it does not capture local variations, while these local variations can have serious implications. For example, hot spots in the cells could damage the cell, but are not captured by the model, because this requires at least a 1D model.

Higher order models might not be necessary for controller design, but they make it possible to better judge the performance of controllers that were designed using simpler models by applying them on a higher order model. This way, simulation of a controlled higher order model gives an indication of performance of controllers in a practical setup. This is important, since a representative setup is not available. Such simulations could show if and when the developed controller has undesired effects on the system, such as the occurrence of hot spots. Subsequently, it could motivate the purposefulness of development of more complex controllers for SORCs.

9-2 Representative dynamic experimental data for dynamic validation

At the moment, only the electrochemical model is validated under steady-state conditions. However, this does not guarantee that the dynamic model correctly represents de dynamics of an SORC. Therefore, representative dynamic experimental data is needed to further validate the model. Representative data is considered to be data that represents the conditions under

which a real system would operate. This means that, ideally, the data should come from a stand-alone SORC that is heated and cooled by gas flows instead of placed in a furnace that tries to keep the temperature constant.

9-3 Inclusion of balance of plant components

balance of plant (BOP) components were not considered, but are an important part of an SORC system, because they put a limit on obtainable performance. Most literature that considers a BOP, assumes that the BOP is fast enough to change flow rates and inlet temperatures immediately. However, there seems no research aimed at BOPs where it is checked if this is the case. Some papers consider a (partially) dynamic BOP, and assume a certain time constant or base it on a small-scale experimental setup. At the same time, literature shows that BOP dynamics are important. For example, flow rates of several seconds can have serious implications. Yet, the dynamics of large-scale BOP systems are unknown. Therefore, research into BOP dynamics is important.

Another important aspect ignored in this thesis, is that the BOP does not operate for free, but needs power to run. This means that in SOEC mode, the effective power available for hydrogen production is lower than the oversupply of power by the grid. In SOFC mode, the system also needs to produce the power used by the BOP, which lowers the effective power output. Therefore, efficient dynamic operation of the BOP is necessary to ensure good efficiency.

9-4 Optimization of weighting and scaling matrices

No optimization of weighting and scaling matrices was conducted. However, this might result in better closed-loop responses. A comparison of different approaches of weighting and scaling selection could show what approach results in the best performance. One approach might be to consider variable matrices based on the operating region, comparable to the selection of the desired closed-loop bandwidth of the SORC as described in subsection 7-3-2.

9-5 Consideration of sensor dynamics

Another important aspect is the inclusion of sensor dynamics. At the moment, it was assumed that every necessary measurement was available. However, this is probably not the case in practice. Sensors can be expensive and difficult to implement. Therefore, implementation of an observer might be necessary to end up with an economically feasible system in the long run.

9-6 Transition from endothermic to exothermic SOEC conditions

Research needs to be done on the dynamic transition from endothermic to exothermic conditions in SOEC mode. When SOEC power consumption increases, there is a point known

as the thermoneutral point where the SOEC goes from an endothermic to an exothermic system. The power density at which this transition occurs depends on the operating temperature: Higher operating temperature result in higher power density at which this transition happens, because of lower losses compared to low operating temperatures. Therefore, the lower the operating temperature, the more important this transition becomes. It is comparable to the transition from SOEC to SOFC, except that the power and current density at which this transition happens is less fixed. The power density range in this thesis was chosen such that this point was avoided. However, a different operating temperature might result in a situation where this transition is essential to guarantee a feasible operating range. Therefore, a controller needs to be developed which makes it possible to handle this transition.

9-7 Dynamic reference signals to reduce wasted fuel during mode transitions

The current implementation of reference signals is not optimal, because it results in relative high amount of wasted fuel when operating close to the zero power density point due to the fixed reference signals. Motivation for this approach was that it results in less critical conditions when close to the zero power point. This is beneficial from a durability point of view, but disadvantageous for the efficiency of the system. During a slow transition, this leaves the system running at inefficient conditions for a long period of time. Therefore, more dynamic reference signals based on the rate of change of operating power and the proximity to the zero power point could improve the system performance.

9-8 Power scaling based on zero net hydrogen production

The operating power density range of -7000 to $7000\,\mathrm{W/m^2}$ is probably suboptimal and results in a system that is not able to run as a closed system that does not require refilling of tanks at some point. The choice for this range was based on the endothermic region of the SOEC and the fact that a wider SOFC range makes little sense in such a case. Reason for this is the fact that an SOFC uses more hydrogen at a certain power density magnitude than an SOEC produces at the same power density magnitude. Therefore, a skewed power density range is expected to perform better in terms of net hydrogen production. A suggestion for power density signal scaling is to scale it such that net hydrogen production over a certain time window is zero. Net hydrogen production refers to the difference in hydrogen production in SOEC mode and hydrogen consumption in SOFC mode.

Appendix A

List of stack specification and parameter values of 0D model

This appendix gives an overview of the stack specifications of the 25 cell stack of the French Alternative Energies and Atomic Energy Commission (CEA) in Table A-1 and all parameter values used for simulation of the SORC. Physical constants and operating conditions are shown in Table A-2 and Table A-3, respectively. Cell properties are shown in Table A-4 and gas properties are shown in Table A-5.

A-1 CEA stack specifications

Table A-1: Specifications of the SORC stack at CEA.

Parameter	Value	Unit
Number of cells	25	
Single cell active area	100×100	mm^2
Stack dimensions	$205 \times 205 \times 123.5$	mm^3
Fuel electrode material	Ni-YSZ	
Fuel electrode thickness	345–368	µm
Air electrode material	LSC-CGO and LSC	
Air electrode thickness	40	µm
Electrolyte material	YSZ	
Electrolyte thickness	5–6	µm
Interconnect material	AISI441	
Interconnect thickness	0.2	mm
End plate thickness	10	mm
Operating pressure	1	atm

Continued on next page.

Table A-1 – Continued from previous page.

Parameter	Value	Unit
Operating temperature	700–850	°C
Nominal fuel flow rate	7.38	$\mathrm{Nml/(min\,cm^2)}$
Nominal air flow rate	11	$\mathrm{Nml/(min\,cm^2)}$
Fuel inlet composition in SOEC mode	10/90/0	$\mathrm{H_2/H_2O/N_2}$ mol %
Fuel inlet composition in SOFC mode	50/0/50	$\mathrm{H_2/H_2O/N_2}$ mol %
Air composition	Air*	

* Assumed to be 79 % $\mathrm{N_2}$ / 21 % $\mathrm{O_2}$.

A-2 Physical constants

Table A-2: Overview of physical constants.

Symbol	Constant name	Value	Unit	Source
F	Faraday constant	96485	$\mathrm{s\,A/mol}$	[18]
R	Universal gas constant	8.314	$\mathrm{J/(K\,mol)}$	[18]
σ_{sb}	Stefan-Boltzmann constant	$5.670 \cdot 10^{-8}$	$\mathrm{W/(m^2\,K^4)}$	[61]

A-3 Operating conditions of the SORC

Table A-3: Overview of operating conditions of the SORC.

Symbol	Parameter name	Value	Unit
p	Pressure	$1 \cdot 10^5$	Pa
$T_{air,in}$	Air inlet stream temperature	750	°C
$T_{fuel,in}$	Fuel inlet stream temperature	750	°C
$\chi_{air,O_2,in}$	Oxygen fraction in air inlet stream	0.21	

A-4 Cell properties

Table A-4: Overview of cell properties.

Symbol	Parameter name	Value	Unit	Source
b	Cell height	$2 \cdot 10^{-3}$	m	CEA*
$c^*_{p,int}$	Specific heat capacity interconnect	$0.5 \cdot 10^3$	$\mathrm{J/(kg\,K)}$	[44]
$c^*_{p,PEN}$	Specific heat capacity PEN	$0.5 \cdot 10^3$	$\mathrm{J/(kg\,K)}$	[44]

Continued on next page.

Table A-4 – Continued from previous page.

Symbol	Parameter name	Value	Unit	Source
$E_{act,air}$	Activation energy air electrode	$107 \cdot 10^3$	J/mol	
$E_{act,fuel}$	Activation energy fuel electrode	$105 \cdot 10^3$	J/mol	
L	Cell length	0.1	m	CEA
Nu_{air}	Nusselt number air channel	4		[21]
Nu_{fuel}	Nusselt number fuel channel	4		[21]
$\bar{r}_{air}$	Mean pore radius air electrode	$0.5 \cdot 10^{-6}$	m	[22]
$\bar{r}_{fuel}$	Mean pore radius fuel electrode	$0.5 \cdot 10^{-6}$	m	[22]
U_0	Reversible OCV at STP	$1.2708 - 2.738 \cdot 10^{-4}\,\mathrm{T_{PEN}}$	V	[55]†
w	Cell width	0.1	m	CEA
α_1	Exponent	0.1		
α_2	Exponent	0.1		
α_3	Exponent	0.25		
γ_{air}	Pre-exponential factor	$28.3 \cdot 10^8$	$\mathrm{A/m^2}$	
γ_{fuel}	Pre-exponential factor	$13.3 \cdot 10^8$	$\mathrm{A/m^2}$	
$\varepsilon_{el,air}$	Porosity air electrode	0.3		[22]
$\varepsilon_{el,fuel}$	Porosity fuel electrode	0.3		[22]
ϵ_{int}	Emissivity interconnect	0.1		[21]
ϵ_{PEN}	Emissivity PEN	0.8		[21]
$\xi_{el,air}$	Tortuosity air electrode	3		[22]
$\xi_{el,fuel}$	Tortuosity fuel electrode	3		[22]
ρ_{int}	Density interconnect	$7.7 \cdot 10^3$	$\mathrm{kg/m^3}$	[88]
ρ_{PEN}	Density PEN	$5.9 \cdot 10^3$	$\mathrm{kg/m^3}$	[44]
$\kappa_{el,air}$	Specific conductivity air electrode	$8.4 \cdot 10^3$	$1/(\Omega\,\mathrm{m})$	[22], [44]
κ_{elec}	Specific conductivity electrolyte	$33.4 \cdot 10^3 \exp\left(-\frac{10.3e3}{T_{PEN}}\right)$	$1/(\Omega\,\mathrm{m})$	[22], [44]
$\kappa_{el,fuel}$	Specific conductivity fuel electrode	$80 \cdot 10^3$	$1/(\Omega\,\mathrm{m})$	[22], [44]
$\delta_{el,air}$	Air electrode thickness	$40 \cdot 10^{-6}$	m	CEA
δ_{elec}	Electrolyte thickness	$5.5 \cdot 10^{-6}$	m	CEA
$\delta_{el,fuel}$	Fuel electrode thickness	$356.5 \cdot 10^{-6}$	m	CEA
δ_{int}	Interconnect thickness	$0.2 \cdot 10^{-3}$	m	CEA

* Calculated from stack dimensions.
† Linear interpolation of table 2.1 in [55].

A-5 Gas properties

Molar heat capacity at constant volume of a gas l can be calculated by

$$c_{v,l} = c_{p,l} - R.$$

Table A-5: Overview of gas properties.

Symbol	Parameter name	Value	Unit	Source
c_{p,H_2}	Molar heat capacity H_2 at 750 °C	30.30	J/(mol K)	[57]
c_{p,H_2O}	Molar heat capacity H_2O at 750 °C	41.58	J/(mol K)	[57]
c_{p,N_2}	Molar heat capacity N_2 at 750 °C	32.83	J/(mol K)	[57]
c_{p,O_2}	Molar heat capacity O_2 at 750 °C	34.98	J/(mol K)	[57]
E_{H_2}	Molar internal energy H_2 at 750 °C	$20.80 \cdot 10^3$	J/mol	[57]
E_{H_2O}	Molar internal energy H_2O at 750 °C	$64.34 \cdot 10^3$	J/mol	[57]
E_{N_2}	Molar internal energy N_2 at 750 °C	$22.38 \cdot 10^3$	J/mol	[57]
E_{O_2}	Molar internal energy O_2 at 750 °C	$23.68 \cdot 10^3$	J/mol	[57]
H_{H_2}	Molar enthalpy H_2 at 750 °C	$29.31 \cdot 10^3$	J/mol	[57]
H_{H_2O}	Molar enthalpy H_2O at 750 °C	$72.85 \cdot 10^3$	J/mol	[57]
H_{N_2}	Molar enthalpy N_2 at 750 °C	$30.89 \cdot 10^3$	J/mol	[57]
H_{O_2}	Molar enthalpy O_2 at 750 °C	$32.19 \cdot 10^3$	J/mol	[57]
$H_{H_2}(298)$	Molar enthalpy H_2 at 25 °C	$7.922 \cdot 10^3$	J/mol	[57]
$H_{H_2O}(298)$	Molar enthalpy H_2O at 25 °C	$45.25 \cdot 10^3$	J/mol	[57]
$H_{N_2}(298)$	Molar enthalpy N_2 at 25 °C	$8.690 \cdot 10^3$	J/mol	[57]
$H_{O_2}(298)$	Molar enthalpy O_2 at 25 °C	$8.668 \cdot 10^3$	J/mol	[57]
k_{H_2}	Thermal conductivity H_2 at 750 °C	0.5364	W/(m K)	[57]
k_{H_2O}	Thermal conductivity H_2O at 750 °C	0.1003	W/(m K)	[57]
k_{N_2}	Thermal conductivity N_2 at 750 °C	0.0672	W/(m K)	[57]
k_{O_2}	Thermal conductivity O_2 at 750 °C	0.0812	W/(m K)	[57]
M_{H_2}	Molar weight H_2	2.016	kg/mol	[62]
M_{H_2O}	Molar weight H_2O	18.016	kg/mol	[62]
M_{N_2}	Molar weight N_2	28	kg/mol	[62]
M_{O_2}	Molar weight O_2	32	kg/mol	[62]

Continued on next page.

Table A-5 – Continued from previous page.

Symbol	Parameter name	Value	Unit	Source
$\Delta H_{f,H_2}$	Enthalpy of formation H_2 at 25 °C	0	J/mol	[62]
$\Delta H_{f,H_2O}$	Enthalpy of formation H_2O at 25 °C	$-241.83 \cdot 10^3$	J/mol	[57], [62]
$\Delta H_{f,O_2}$	Enthalpy of formation O_2 at 25 °C	0	J/mol	[62]
$\sum \nu_{H_2}$	Special atomic diffusion volume H_2	7.07		[89]
$\sum \nu_{H_2O}$	Special atomic diffusion volume H_2O	12.7		[89]
$\sum \nu_{N_2}$	Special atomic diffusion volume N_2	17.9		[89]
$\sum \nu_{O_2}$	Special atomic diffusion volume O_2	16.6		[89]

Appendix B

Additional equations

This appendix provides additional equations for the dynamic model described in chapter 3. It contains expressions for convective heat transfer, radiative heat transfer, molar enthalpies, enthalpy of reaction, and diffusion coefficients.

B-1 Convective heat transfer

The convective heat transfer terms $Q^{conv}$are given by Newton's law of cooling,

$$\begin{aligned} Q^{conv}_{int,air} &= A_s h_{air}(T_{air} - T_{int}), \\ Q^{conv}_{PEN,air} &= A_s h_{air}(T_{air} - T_{PEN}), \\ Q^{conv}_{int,fuel} &= A_s h_{fuel}(T_{fuel} - T_{int}), \\ Q^{conv}_{PEN,fuel} &= A_s h_{fuel}(T_{fuel} - T_{PEN}), \end{aligned}$$

where A_s is the cell active surface area of the PEN, and h_{air} and h_{fuel} are the heat transfer coefficients for the air and fuel channel, respectively. Standard expressions for the heat transfer coefficients [61], [65], [90] are given by

$$\begin{aligned} h_{air} &= \frac{k_{air} Nu_{air}}{d_{h,air}}, \\ k_{air} &= \chi_{air,O_2} k_{O_2} + (1 - \chi_{air,O_2}) k_{N_2}, \\ d_{h,air} &= \frac{2 b_{air} w_{air}}{b_{air} + w_{air}}, \end{aligned}$$

where k_{air}, k_{O_2} and k_{N_2} are the thermal conductivity of air, oxygen and nitrogen, respectively, Nu_{air} is the Nusselt number of the air channel, $d_{h,air}$ is the hydrodynamic diameter, w_{air} is the width of the channel, and b_{air} is the height of the air channel.

$$
\begin{aligned}
h_{fuel} &= \frac{k_{fuel} Nu_{fuel}}{d_{h,fuel}}, \\
k_{fuel} &= \chi_{fuel,H_2} k_{H_2} + (1 - \chi_{fuel,H_2}) k_{H_2O}, \\
d_{h,fuel} &= \frac{2 b_{fuel} w_{fuel}}{b_{fuel} + w_{fuel}},
\end{aligned}
$$

where k_{fuel}, k_{H_2} and k_{H_2O} are the thermal conductivity of fuel, hydrogen and steam, respectively, Nu_{fuel} is the Nusselt number of the fuel channel, $d_{h,fuel}$ is the hydrodynamic diameter, w_{fuel} is the width of the channel, and b_{fuel} is the height of the fuel channel.

B-2 Radiative heat transfer

Radiative heat transfer between the PEN structure and interconnect is modelled as radiation between two grey surfaces and given by

$$
Q^{rad} = \frac{\sigma_{sb} A_s}{R_{rad}} \Big(T_{int}^4 - T_{PEN}^4 \Big),
$$

where σ_{sb} is the Stefan–Boltzmann constant, and R_{rad} for two parallel grey surfaces [44], [90] is given by

$$
R_{rad} = \frac{1}{\epsilon_{PEN}} + \frac{1}{\epsilon_{int}} - 1,
$$

where ϵ_{PEN} and ϵ_{int} are the emissivity of the PEN and interconnect, respectively.

B-3 Molar enthalpies

The molar enthalpy of the ideal gas mixture air H_{air} [62] is given by

$$
\begin{aligned}
H_{air} &= \chi_{air,O_2} H_{O_2} + (1 - \chi_{air,O_2}) H_{N_2}, \\
H_{O_2} &= H_{O_2}^{ref} + c_{p,O_2} \Big(T_{air} - T_{air}^{ref} \Big), \\
H_{N_2} &= H_{N_2}^{ref} + c_{p,N_2} \Big(T_{air} - T_{air}^{ref} \Big),
\end{aligned}
$$

where H_{O_2} and H_{N_2} are the molar enthalpies of oxygen and nitrogen, respectively, and c_{p,O_2} and c_{p,N_2} are molar heat capacities under constant pressure.

Similar expressions are used for the ideal gas mixture fuel.

$$
\begin{aligned}
H_{fuel} &= \chi_{fuel,H_2} H_{H_2} + (1 - \chi_{fuel,H_2}) H_{H_2O}, \\
H_{H_2} &= H_{H_2}^{ref} + c_{p,H_2} \Big(T_{fuel} - T_{fuel}^{ref} \Big), \\
H_{H_2O} &= H_{H_2O}^{ref} + c_{p,H_2O} \Big(T_{fuel} - T_{fuel}^{ref} \Big),
\end{aligned}
$$

where H_{H_2} and H_{H_2O} are the molar enthalpies of hydrogen and steam, respectively, and c_{p,H_2} and c_{p,H_2O} are molar heat capacities under constant pressure.

The molar enthalpies for the amount of oxygen, hydrogen, and steam consumed/produced by the electrochemical reaction are given by

$$H_{O_2,r} = H_{O_2}^{ref} + \begin{cases} c_{p,O_2}\Big(T_{PEN} - T_{O_2}^{ref}\Big) & \text{if } j \leq 0 \\ c_{p,O_2}\Big(T_{air} - T_{O_2}^{ref}\Big) & \text{if } j > 0 \end{cases},$$

$$H_{H_2,r} = H_{H_2}^{ref} + \begin{cases} c_{p,H_2}\Big(T_{PEN} - T_{H_2}^{ref}\Big) & \text{if } j \leq 0 \\ c_{p,H_2}\Big(T_{fuel} - T_{H_2}^{ref}\Big) & \text{if } j > 0 \end{cases},$$

$$H_{H_2O,r} = H_{H_2O}^{ref} + \begin{cases} c_{p,H_2O}\Big(T_{fuel} - T_{H_2O}^{ref}\Big) & \text{if } j \leq 0 \\ c_{p,O_2}\Big(T_{PEN} - T_{H_2O}^{ref}\Big) & \text{if } j > 0 \end{cases}.$$

Introducing the discrete variable Γ

$$\Gamma = \begin{cases} 0 & \text{if } j \leq 0 \\ 1 & \text{if } j > 0 \end{cases},$$

and defining

$$T^{ref} = T_{O_2}^{ref} = T_{H_2}^{ref} = T_{H_2O}^{ref},$$

it is possible to rewrite

$$H_{O_2,r} = H_{O_2}^{ref} + \Gamma c_{p,O_2}(T_{air} - T_{PEN}) + c_{p,O_2}\Big(T_{PEN} - T^{ref}\Big),$$
$$H_{H_2,r} = H_{H_2}^{ref} + \Gamma c_{p,H_2}(T_{fuel} - T_{PEN}) + c_{p,H_2}\Big(T_{PEN} - T^{ref}\Big),$$
$$H_{H_2O,r} = H_{H_2O}^{ref} + \Gamma c_{p,H_2O}(T_{PEN} - T_{fuel}) + c_{p,H_2O}\Big(T_{fuel} - T^{ref}\Big).$$

B-4 Enthalpy of reaction

The enthalpy of reaction ΔH_r of the electrochemical reaction in the cell is given by [62]

$$\begin{aligned}\Delta H_r &= -\Delta H_{f,H_2} - \frac{1}{2}\Delta H_{f,O_2} + \Delta H_{f,H_2O}, \\ &= -\Big(\Delta H_{f,H_2}^0 + \Delta H_{H_2}\Big) - \frac{1}{2}\Big(\Delta H_{f,O_2}^0 + \Delta H_{O_2}\Big) + \Big(\Delta H_{f,H_2O}^0 + \Delta H_{H_2O}\Big),\end{aligned}$$

where $\Delta H_{f,H_2}$, $\Delta H_{f,O_2}$ and $\Delta H_{f,H_2O}$ are the enthalpies of formation of hydrogen, oxygen, and steam, respectively, $\Delta H_{f,H_2}^0$, $\Delta H_{f,O_2}^0$ and $\Delta H_{f,H_2O}^0$ are the enthalpies of formation at 298 K and 1 atm, and ΔH_{H_2}, ΔH_{O_2} and ΔH_{H_2O} are the differences in enthalpy between standard conditions and the state of interest.The enthalpies of formation are given by [57], [62]

$$\Delta H_{f,H_2}^0 = \Delta H_{f,O_2}^0 = 0,$$
$$\Delta H_{f,H_2O}^0 = -241.83\,\text{kJ/mol}.$$

The enthalpies that describe the deviation from the reference point are given by [62]

$$\begin{aligned}\Delta H_l &= H_l(T) - H_l(298), \\ &= H_l^{ref} + c_{p,l}\Big(T - T^{ref}\Big) - H_l(298), \quad l \in \{H_2, H_2O, O_2\},\end{aligned}$$

where H_l^{ref} is the molar enthalpy reference of component l at the reference temperature of the SORC.

B-5 Diffusion coefficients

Diffusion coefficients follow from considering molecular and Knudsen diffusion. The effective diffusivity is given by [43], [61]

$$\begin{aligned} D_{eff,fuel} &= \chi_{fuel,H_2} D_{eff,H_2} + (1 - \chi_{fuel,H_2}) D_{eff,H_2O}, \\ \frac{1}{D_{eff,H_2}} &= \frac{\xi_{el,fuel}}{\varepsilon_{el,fuel}} \left(\frac{1}{D_{k,H_2}} + \frac{1}{D_{H_2-H_2O}} \right), \\ \frac{1}{D_{eff,H_2O}} &= \frac{\xi_{el,fuel}}{\varepsilon_{el,fuel}} \left(\frac{1}{D_{k,H_2O}} + \frac{1}{D_{H_2-H_2O}} \right). \end{aligned}$$

In these equations, D_{eff,H_2} and D_{eff,H_2O} represent the effective diffusivity of hydrogen and water vapor, respectively, $\xi_{el,fuel}$ is the tortuosity of the fuel electrode, D_{k,H_2} and D_{k,H_2O} are the Knudsen diffusion coefficients for hydrogen and steam, respectively, and $D_{H_2-H_2O}$ is the binary molecular diffusion coefficient of hydrogen and water vapor.

For straight and round pores, the Knudsen diffusion coefficient is given by [43], [71]

$$D_{k,l} = 97.0 \bar{r} \sqrt{\frac{T_{PEN}}{M_l}}, \quad l \in \{H_2, H_2O, O_2, N_2\}, \tag{B-1}$$

where $\bar{r}$ is the average pore radius of the electrode, and l is component of interest, for example, $l = H_2$ for hydrogen.

The binary ordinary diffusion coefficient can be obtained from Fuller's equation, which is considered to be more accurate than a coefficient obtained via Chapman-Enskog theory [28], [60], [61], [89], [91]

$$D_{H_2-H_2O} = \frac{3.203 \times 10^{-4} {T_{PEN}}^{1.75} \sqrt{\frac{1}{M_{H_2}} + \frac{1}{M_{H_2O}}}}{p\Big(\big(\sum \nu_{H_2}\big)^{\frac{1}{3}} + \big(\sum \nu_{H_2O}\big)^{\frac{1}{3}} \Big)^2}.$$

Values for the special atomic diffusion volumes of hydrogen $\sum \nu_{H_2}$ and steam $\sum \nu_{H_2O}$ are given in Table 1 of [89].

The effective diffusion coefficient of air is defined in a similar way,

$$\frac{1}{D_{eff,O_2}} = \frac{\xi_{el,air}}{\varepsilon_{el,air}} \left(\frac{1}{D_{O_2-N_2}} + \frac{1}{D_{k,O_2}} \right),$$

where Fuller's equation is used for the ordinary diffusion coefficient

$$D_{O_2-N_2} = \frac{3.203 \times 10^{-4} {T_{PEN}}^{1.75} \sqrt{\frac{1}{M_{O_2}} + \frac{1}{M_{N_2}}}}{p\Big(\big(\sum \nu_{O_2}\big)^{\frac{1}{3}} + \big(\sum \nu_{N_2}\big)^{\frac{1}{3}} \Big)^2},$$

where $\sum \nu_{O_2}$ and $\sum \nu_{N_2}$ are the special atomic diffusion volume of oxygen and nitrogen, respectively. Both are obtained from Table 1 of [89].

Appendix C

Proof of equivalence of electrochemical model

Often in SOFC and SOEC papers, the current is defined as positive, which gives seemingly different expressions for the cell voltage. This gives the illusion that the electrochemical models for SOFCs and SOECs are different. However, this is not the case, as is shown in this appendix. Given the same parameters, SOFC and SOEC electrochemical models are interchangeable.

Considering the convention of positive current for fuel cells, the cell voltage is given by:

$$U_{cell,f}(j_f) = U_{Nernst,f}(j_f) - \eta_{ohm,f}(j_f) - \eta_{act,f}(j_f) - \eta_{conc,f}(j_f), \tag{C-1}$$

where the subscript f indicates fuel cell mode.

Now, if instead the convention is followed where the current is positive for electrolysers, the cell voltage is given by:

$$U_{cell,e}(j_e) = U_{Nernst,e}(j_e) + \eta_{ohm,e}(j_e) + \eta_{act,e}(j_e) + \eta_{conc,e}(j_e), \tag{C-2}$$

where the subscript e indicates electrolyser mode and the current density for the electrolyser follows from

$$j_e = -j_f.$$

To show that these representations are the same, it is necessary to show that

$$U_{cell,e}(-j) = U_{cell,f}(j), \tag{C-3}$$

which is equal to showing:

$$U_{Nernst,e}(-j) = U_{Nernst,f}(j), \tag{C-4}$$
$$\eta_{ohm,e}(-j) = -\eta_{ohm,f}(j), \tag{C-5}$$
$$\eta_{act,e}(-j) = -\eta_{act,f}(j), \tag{C-6}$$
$$\eta_{conc,e}(-j) = -\eta_{conc,f}(j). \tag{C-7}$$

C-1 Nernst equation

The definition of the Nernst potential only depends on the reaction in the cell. Furthermore, it is independent of current density and given by the following expression for both modes

$$U_{Nernst} = U_0 + \frac{RT_{PEN}}{2F} \ln\left(\frac{a_{H_2}\sqrt{a_{O_2}}}{a_{H_2O}}\right).$$

Therefore,

$$U_{Nernst} = U_{Nernst,e}(-j) = U_{Nernst,f}(j),$$

which means that Equation (C-4) is true.

C-2 Ohmic overpotentials

The ohmic overpotential of an SOFC and SOEC have a very similar definition. For a Fuel cell it is given by:

$$\eta_{ohm,f}(j_f) = r_{ohm} j_f.$$

For an electrolyser, it follows that:

$$\eta_{ohm,e}(j_e) = r_{ohm} j_e.$$

Inserting $j_e = -j$, it follows that

$$\begin{aligned}\eta_{ohm,e}(-j) &= -r_{ohm} j, \\ &= -\eta_{ohm,f}(j),\end{aligned}$$

which shows that Equation (C-5) is correct.

C-3 Activation overpotentials

The activation overpotential is given by

$$\eta_{act} = \eta_{act,fuel} + \eta_{act,air},$$

where $\eta_{act,fuel}$ and $\eta_{act,air}$ represent the activation overpotential for the fuel and air electrode, respectively.

For SOFC, the activation overpotential for a single electrode is given by

$$\eta_{act,el,f}(j_f) = \frac{RT_{PEN}}{F} \sinh^{-1}\left(\frac{j_f}{2j_{0,electrode}}\right),$$

where the subscript $el \in \{fuel, air\}$ indicates a single electrode.

The activation overpotential for SOEC electrode is given by the same expression,

$$\eta_{act,el,e}(j_e) = \frac{RT_{PEN}}{F} \sinh^{-1}\left(\frac{j_e}{2j_{0,electrode}}\right).$$

Inserting $j_e = -j$, it follows that

$$\eta_{act,el,e}(-j) = \frac{RT_{PEN}}{F} \sinh^{-1}\left(\frac{-j}{2j_{0,electrode}}\right).$$

The inverse hyperbolic sine ($\sinh^{-1}$) is an odd function. Therefore,

$$\begin{aligned}\eta_{act,el,e}(-j) &= -\frac{RT_{PEN}}{F} \sinh^{-1}\left(\frac{j}{2j_{0,electrode}}\right),\\ &= -\eta_{act,el,f}(j),\end{aligned}$$

which shows that Equation (C-6) holds.

C-4 Concentration overpotentials

The last part considers the concentration overpotential. For an SOFC, this is given by

$$\begin{aligned}\eta_{conc,f} &= U_{Nernst} - U_{Nernst,TPB,f}(j_f),\\ &= \frac{RT_{PEN}}{2F} \ln\left(\frac{\chi_{fuel,H_2}(1-\chi_{fuel,H_2,TPB,f}(j_f))\sqrt{\chi_{air,O_2}}}{\chi_{fuel,H_2,TPB,f}(j_f)(1-\chi_{fuel,H_2})\sqrt{\chi_{air,O_2,TPB,f}(j_f)}}\right),\end{aligned}$$

For an SOEC, the concentration overpotential follows from

$$\begin{aligned}\eta_{conc,e} &= U_{Nernst,TPB,e}(j_e) - U_{Nernst},\\ &= \frac{RT_{PEN}}{2F} \ln\left(\frac{\chi_{fuel,H_2,TPB,f}(j_e)(1-\chi_{fuel,H_2})\sqrt{\chi_{air,O_2,TPB,f}(j_e)}}{\chi_{fuel,H_2}(1-\chi_{fuel,H_2,TPB,f}(j_e))\sqrt{\chi_{air,O_2}}}\right),\end{aligned}$$

Now, if

$$\chi_{fuel,H_2,TPB,e}(-j) = \chi_{fuel,H_2,TPB,f}(j), \tag{C-8}$$

$$\chi_{air,O_2,TPB,e}(-j) = \chi_{air,O_2,TPB,f}(j), \tag{C-9}$$

it follows that

$$\eta_{conc,e}(-j) = -\eta_{conc,f}(j).$$

C-4-1 Fuel channel side

For the fuel side, consider the situations as shown in Figure C-1 and model the diffusion in the fuel electrode as equimolar diffusion. In other words,

$$J_{H_2} = -J_{H_2O}.$$

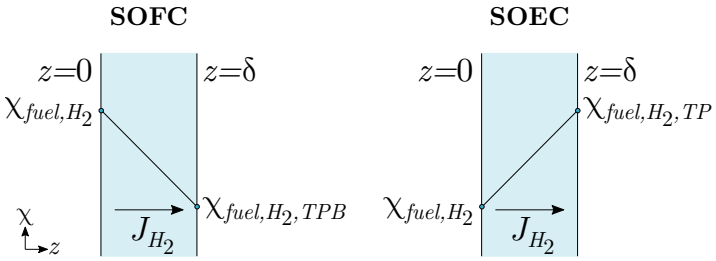

Figure C-1: Schematic overview of concentration gradient of hydrogen through fuel electrode in SOFC and SOEC mode. z represents the distance through the electrode, δ is the thickness of the electrode, χ_{fuel,H_2} is the mole fraction in the bulk, and $\chi_{fuel,H_2,TPB}$ is the mole fraction at the TPB. J_{H_2} is the diffusion flux of hydrogen through the medium.

SOFC

For the SOFC, the diffusion flux is given by

$$J_{H_2} = -D_{eff,fuel}\frac{\mathrm{d}c_{H_2}}{\mathrm{d}z}.$$

From the ideal gas law, it follows that

$$\mathrm{d}c_{H_2} = \frac{p}{RT_{PEN}}\,\mathrm{d}\chi_{fuel,H_2}\,.$$

Also, the molar flux of hydrogen is equal to

$$J_{H_2} = \frac{j_f}{2F}.$$

Doing the maths, it follows that:

$$\chi_{fuel,H_2,TPB,f}(j_f) = \chi_{fuel,H_2} - \underbrace{\frac{RT_{PEN}\delta_{el,fuel}}{2FD_{eff,fuel}p}}_{\mathcal{A}}\,j_f.$$

SOEC

Now consider the SOEC. There are two options in redefining the diffusion through the electrode.

1. Redefine J_{H_2} as
$$J_{H_2} = -\frac{j_e}{2F}.$$
2. Reverse the direction of J_{H_2}, which changes the differential equation to
$$J_{H_2} = D_{eff,fuel}\frac{\mathrm{d}c_{H_2}}{\mathrm{d}z}.$$

The approach shown in Figure C-1 uses the first approach. Of course, the second approach gives the same results.

Again, doing the maths gives:

$$\chi_{fuel,H_2,TPB,e}(j_e) = \chi_{fuel,H_2} + \mathcal{A}j_e.$$

Inserting $j_e = -j$, it follows that

$$\begin{aligned}\chi_{fuel,H_2,TPB,e}(-j) &= \chi_{fuel,H_2} - \mathcal{A}j, \\ &= \chi_{fuel,H_2,TPB,f}(j),\end{aligned}$$

which shows Equation (C-8).

C-4-2 Air channel side

Next, the diffusion through the air electrode is given by unimolecular diffusion.

SOFC

It follows for the SOFC that

$$N_{O_2} = \chi_{air,O_2} N_{O_2} - D_{eff,O_2} \frac{\mathrm{d}c_{O_2}}{\mathrm{d}z},$$

where the molar flux of oxygen is given by

$$N_{O_2} = \frac{j_f}{2F},$$

and from the ideal gas law

$$\mathrm{d}c_{O_2} = \frac{p}{RT_{PEN}} \mathrm{d}\chi_{air,O_2}\,.$$

Doing the maths, it follows that

$$\chi_{air,O_2,TPB,f}(j_f) = 1 - (1 - \chi_{air,O_2}) \exp\left(\underbrace{\frac{RT_{PEN}\delta_{el,air}}{4FD_{eff,O_2}p}}_{\mathcal{B}} j_f \right).$$

SOEC

Again, the two same options apply as for the fuel electrode. Using the first option, it follows that

$$N_{O_2} = -\frac{j_e}{2F}.$$

Doing the maths, it is found that

$$\chi_{air,O_2,TPB,e}(j_e) = 1 - (1 - \chi_{fuel,H_2}) \exp(-\mathcal{B}j_e).$$

Inserting $j_e = -j$, it follows that

$$\begin{aligned}\chi_{air,O_2,TPB,e}(-j) &= 1 - (1 - \chi_{fuel,H_2}) \exp(\mathcal{B}j), \\ &= \chi_{air,O_2,TPB,f}(j),\end{aligned}$$

which shows Equation (C-9).

Therefore, Equation (C-7) is also true.

C-5 conclusion

This appendix showed that Equation (C-4), Equation (C-5), Equation (C-6), and Equation (C-7). From this, it can be concluded that Equation (C-3) is true, which shows the equivalence of Equation (C-1) and Equation (C-2). Therefore, there is no difference in the representation of the cell voltage for a fuel cell or an electrolyser.

Appendix D

Derivation of reference signals terms

Assume that a reference signal r is given by

$$r(j) = \mathcal{A}\tanh(\mathcal{B}j + \mathcal{D}) + \mathcal{C}, \tag{D-1}$$

where $\mathcal{A}$ represents the amplitude, $\mathcal{B}$ is the maximum slope, $\mathcal{C}$ is the vertical shift, and $\mathcal{D}$ is the phase shift of a hyperbolic tangent function. This function is used to approximate and smooth the ideal reference signal

$$r = \begin{cases} r_{SOEC} & \text{if } j \ll 0\,\mathrm{A/m^2} \\ r_0 & \text{if } j = 0\,\mathrm{A/m^2} \\ r_{SOFC} & \text{if } j \gg 0\,\mathrm{A/m^2} \end{cases}.$$

As an example, take the reference signal for the PEN temperate, shown in Figure D-1.

$\mathcal{A}$ represents the amplitude of the hyperbolic tangent function and is given by

$$\mathcal{A} = \frac{r_{SOFC} - r_{SOEC}}{2}.$$

$\mathcal{B}$ represents the maximum slope of the reference function, which is attained when the argument of the hyperbolic tangent is 0,

$$\begin{aligned} \mathcal{B}j + \mathcal{D} &= 0, \\ j &= -\frac{\mathcal{D}}{\mathcal{B}}. \end{aligned}$$

An expression for $\mathcal{B}$ follows from

$$\begin{aligned} \frac{\mathrm{d}r}{\mathrm{d}j} &= \frac{\mathcal{A}\mathcal{B}}{\cosh^2(\mathcal{B}j + \mathcal{D})}, \\ \left.\frac{\mathrm{d}r}{\mathrm{d}j}\right|_{j=-\frac{\mathcal{D}}{\mathcal{B}}} &= \mathcal{A}\mathcal{B}. \end{aligned} \tag{D-2}$$

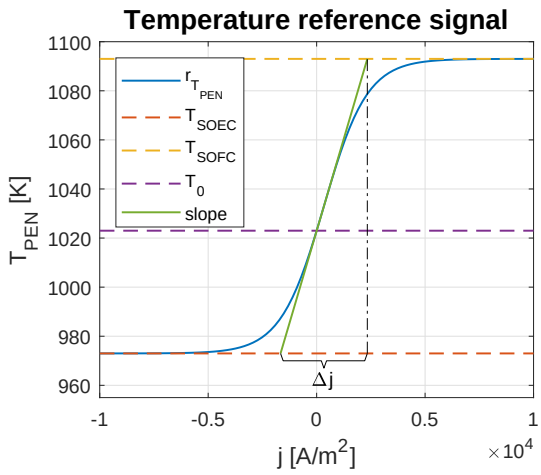

Figure D-1: Example of hyperbolic tangent temperature reference function. $r_{T_{PEN}}$: reference signal of the PEN temperature, T_{SOEC}, T_{SOFC}, and T_0: ideal reference temperature in SOEC mode, SOFC mode, and when there is no current extracted from the system, respectively, Δj: transition zone for the reference signal, slope: slope of the reference signal.

The maximum slope is also related to the transition zone Δj and the amplitude $\mathcal{A}$ by

$$\left.\frac{\mathrm{d}r}{\mathrm{d}j}\right|_{j=-\frac{\mathcal{D}}{\mathcal{B}}} = \frac{2\mathcal{A}}{\Delta j}. \tag{D-3}$$

It follows from combining Equation (D-2) and Equation (D-3) that,

$$\mathcal{B} = \frac{2}{\Delta j}.$$

The vertical shift $\mathcal{C}$ follows from

$$\mathcal{C} = \frac{r_{SOFC} + r_{SOEC}}{2}.$$

The phase shift $\mathcal{D}$ follows from considering the reference value at $j = 0$,

$$\begin{aligned} r(0) &= r_0, \\ &= \mathcal{A}\tanh(\mathcal{D}) + \mathcal{C}, \\ \rightarrow \mathcal{D} &= \tanh^{-1}\left(\frac{r_0 - \mathcal{C}}{\mathcal{A}}\right). \end{aligned}$$

Appendix E

Additional average net power data

Average daily power signals per month for January 2017 up to and including October 2019 from the Netherlands are presented in this appendix. First, average power signals are shown. This includes consumption and renewable production from wind and solar, and net power demand from non-variable energy sources. After that, the net power signals are detrended using a low frequency sine wave. The last part of the appendix shows the power spectral density (PSD) estimates for the detrended net power signal.

E-1 Average power signals from January 2017 to October 2019

Power consumption data is obtained from TenneT [5] and renewable power production is obtained from Energieopwek.nl [6]. The net power demand for non-variable energy sources is given by

$$P_{net} = P_{cons} - P_{RES}.$$

The power signals are shown in Figure E-1, Figure E-2, and Figure E-3.

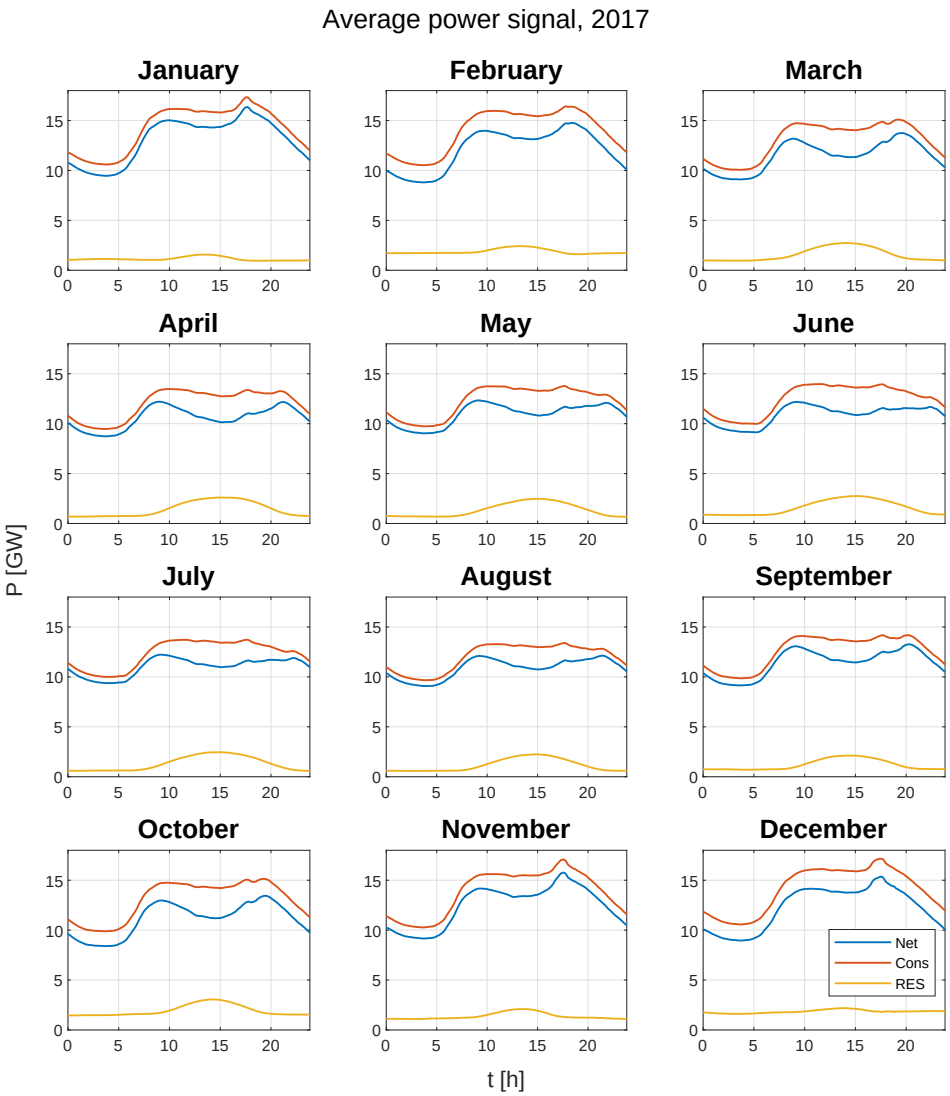

Figure E-1: Average daily power signals for 2017. RES: power produced by by renewable energy sources wind and solar obtained from [6], Cons: power consumption obtained from [5], Net: power production from other sources.

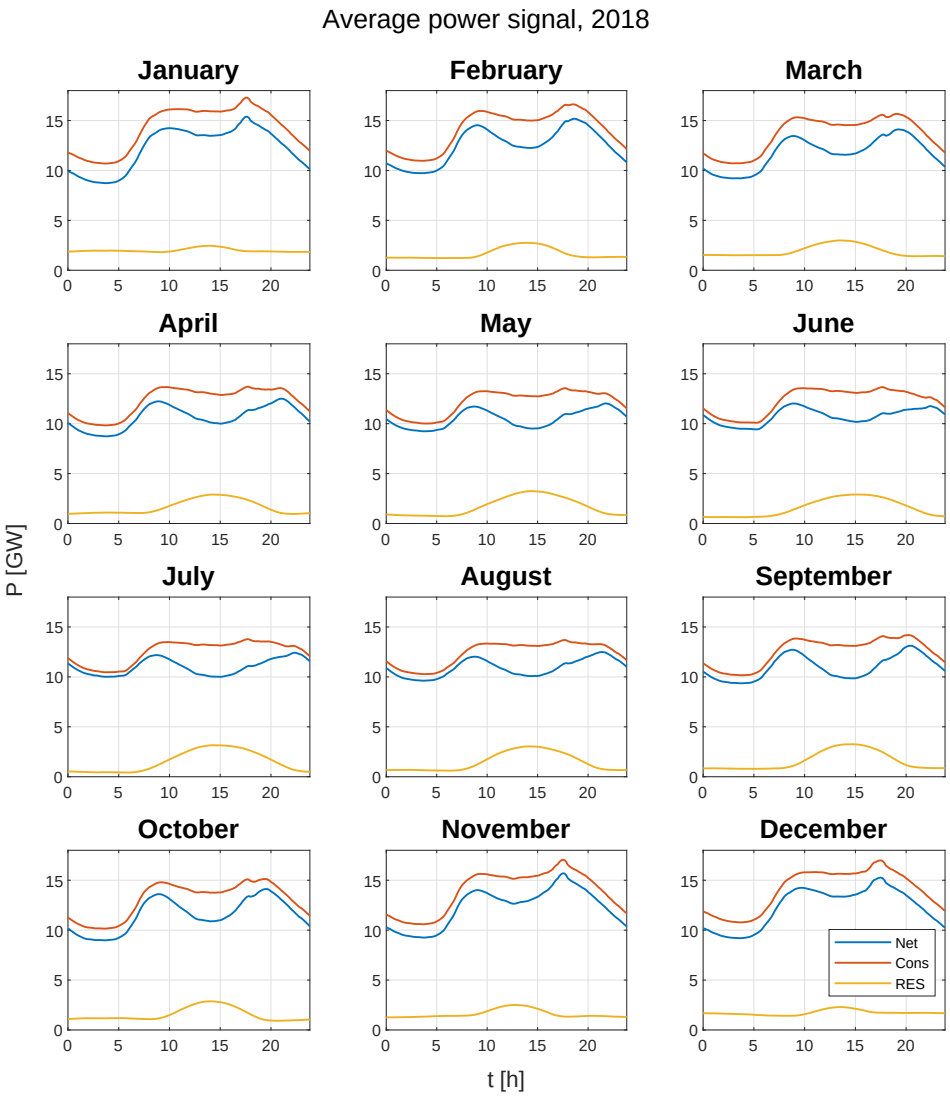

Figure E-2: Average daily power signals for 2018. RES: power produced by by renewable energy sources wind and solar obtained from [6], Cons: power consumption obtained from [5], Net: power production from other sources.

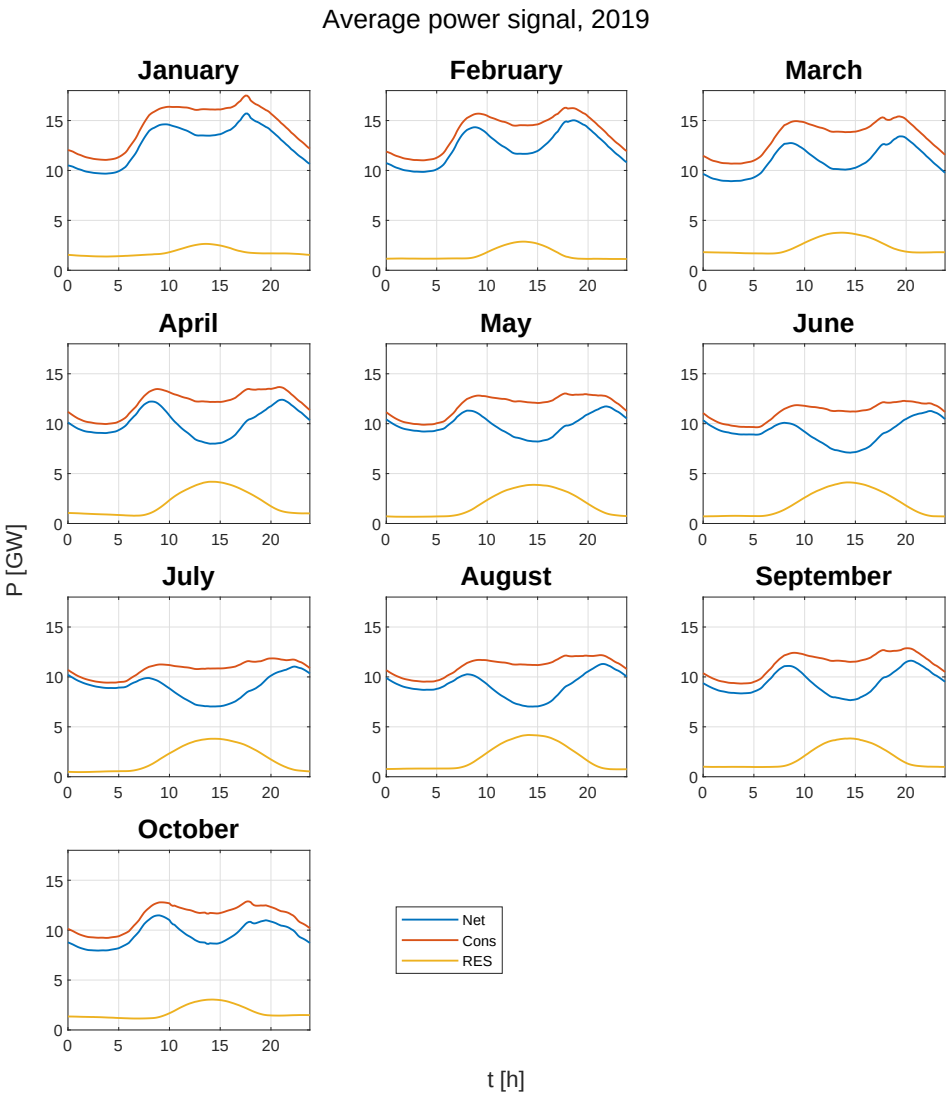

Figure E-3: Average daily power signals for 2019. RES: power produced by by renewable energy sources wind and solar obtained from [6], Cons: power consumption obtained from [5], Net: power production from other sources.

E-2 Detrended net power signals from January 2017 to October 2019

Most of the net power signals are detrended using

$$\tilde{P} = \mathcal{A}\sin(\mathcal{B}t + \mathcal{C}) + P_{mean},$$

where P_{mean} is the mean value of the power signal P, and $\mathcal{A}$, $\mathcal{B}$ and $\mathcal{C}$ are fitting parameters. After detrending, an additional vertical shift is performed to ensure that the mean value of the detrended net power signal is is zero. A small portion of the data did not require detrending by this low frequency sine, but only needed a vertical shift. This was especially true for 2018. The detrended power signals are shown in Figure E-4, Figure E-5, and Figure E-6.

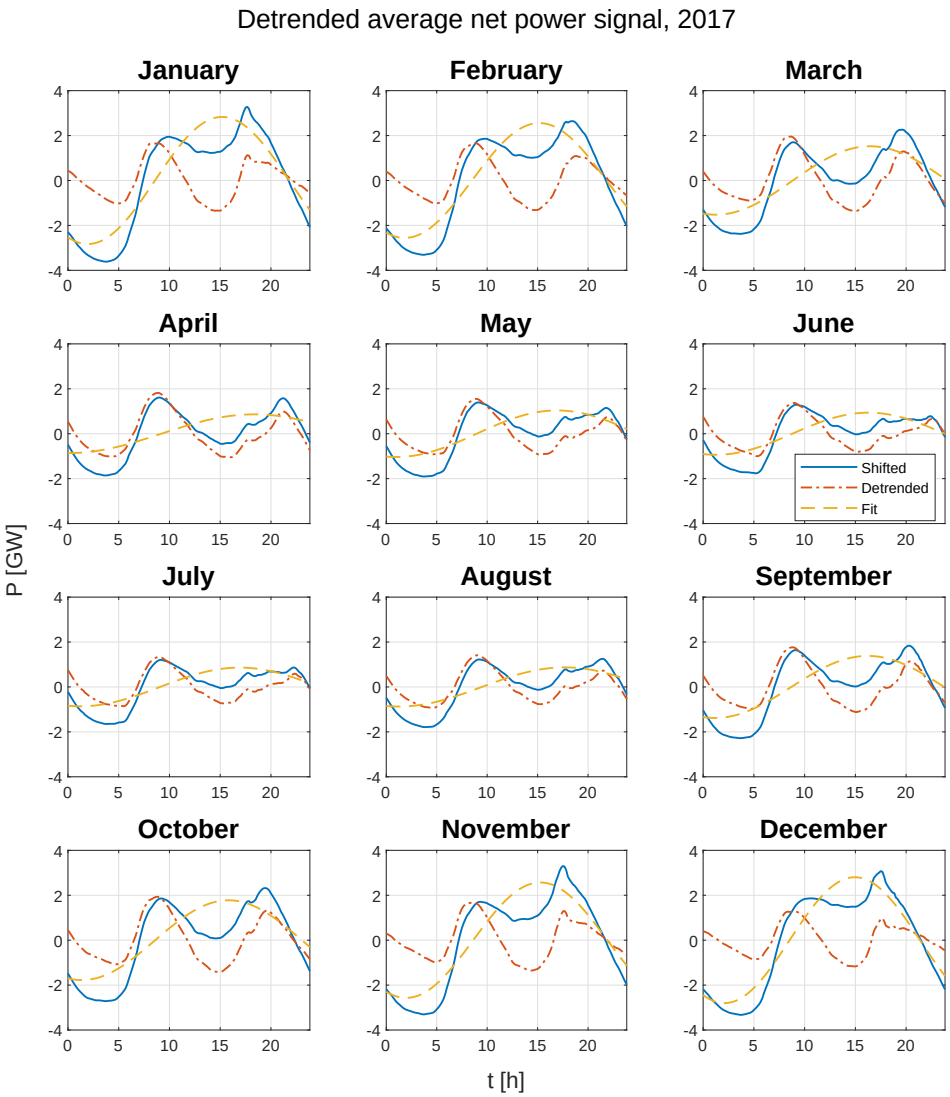

Figure E-4: Detrending of net power signal for 2017. Shifted: shifted net power curve, Fit: low frequency sine wave fit of shifted net power signal, Detrended: shifted net power signal detrended by the sine wave fit and additional vertical shift to ensure that the mean of the signal is 0. In case only the shifted signal is shown (blue line), the detrended signal is equal to the shifted signal.

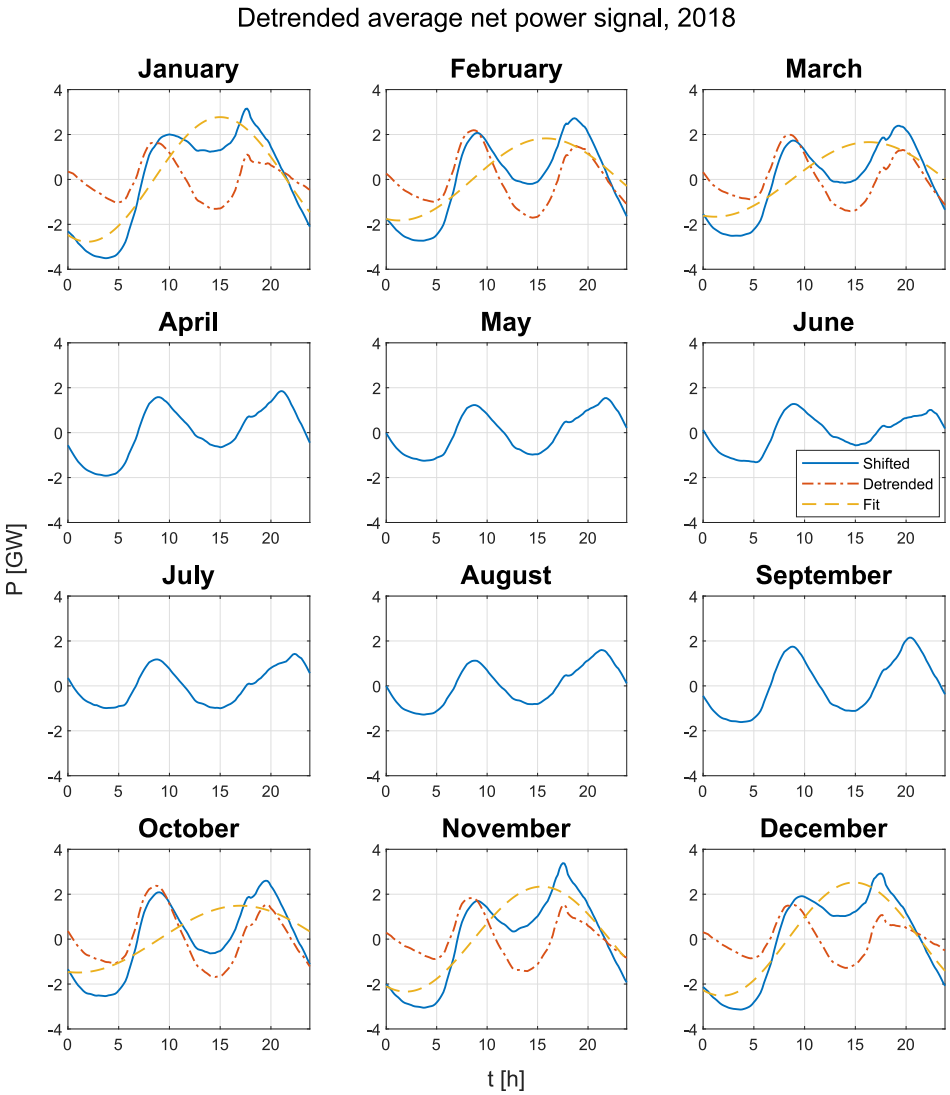

Figure E-5: Detrending of net power signal for 2018. Shifted: shifted net power curve, Fit: low frequency sine wave fit of shifted net power signal, Detrended: shifted net power signal detrended by the sine wave fit and additional vertical shift to ensure that the mean of the signal is 0. In case only the shifted signal is shown (blue line), the detrended signal is equal to the shifted signal.

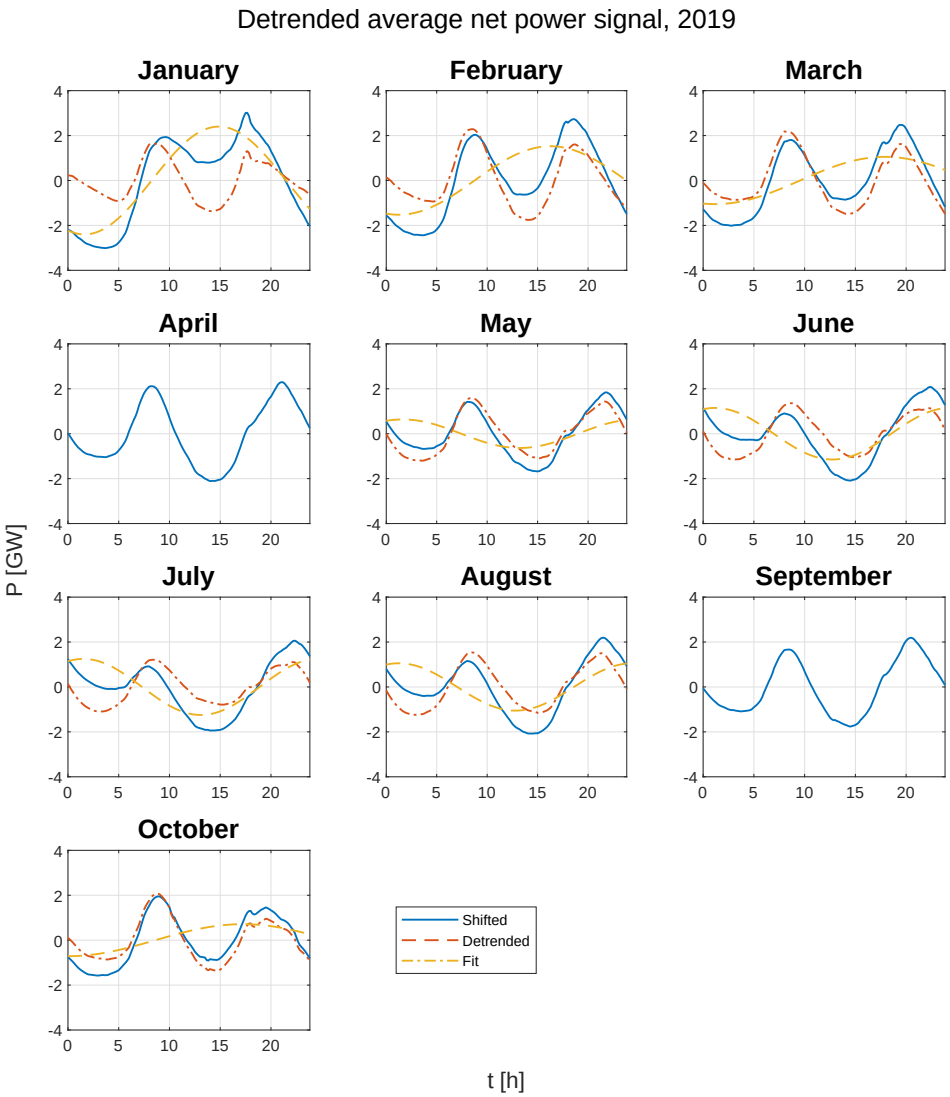

Figure E-6: Detrending of net power signal for 2019. Shifted: shifted net power curve, Fit: low frequency sine wave fit of shifted net power signal, Detrended: shifted net power signal detrended by the sine wave fit and additional vertical shift to ensure that the mean of the signal is 0. In case only the shifted signal is shown (blue line), the detrended signal is equal to the shifted signal.

E-3 PSD estimates for detrended net power signals from January 2017 to October 2019

PSD estimates using a periodogram with Hamming window based on 144 discrete Fourier transform (DFT) points are shown in Figure E-7, Figure E-8, and Figure E-9. The detrended power signals show roughly two sine wave cycles a day. Therefore, a peak in the PSDs is expected around

$$f_{exp} \approx 2.31 \cdot 10^{-5}\,\text{Hz}.$$

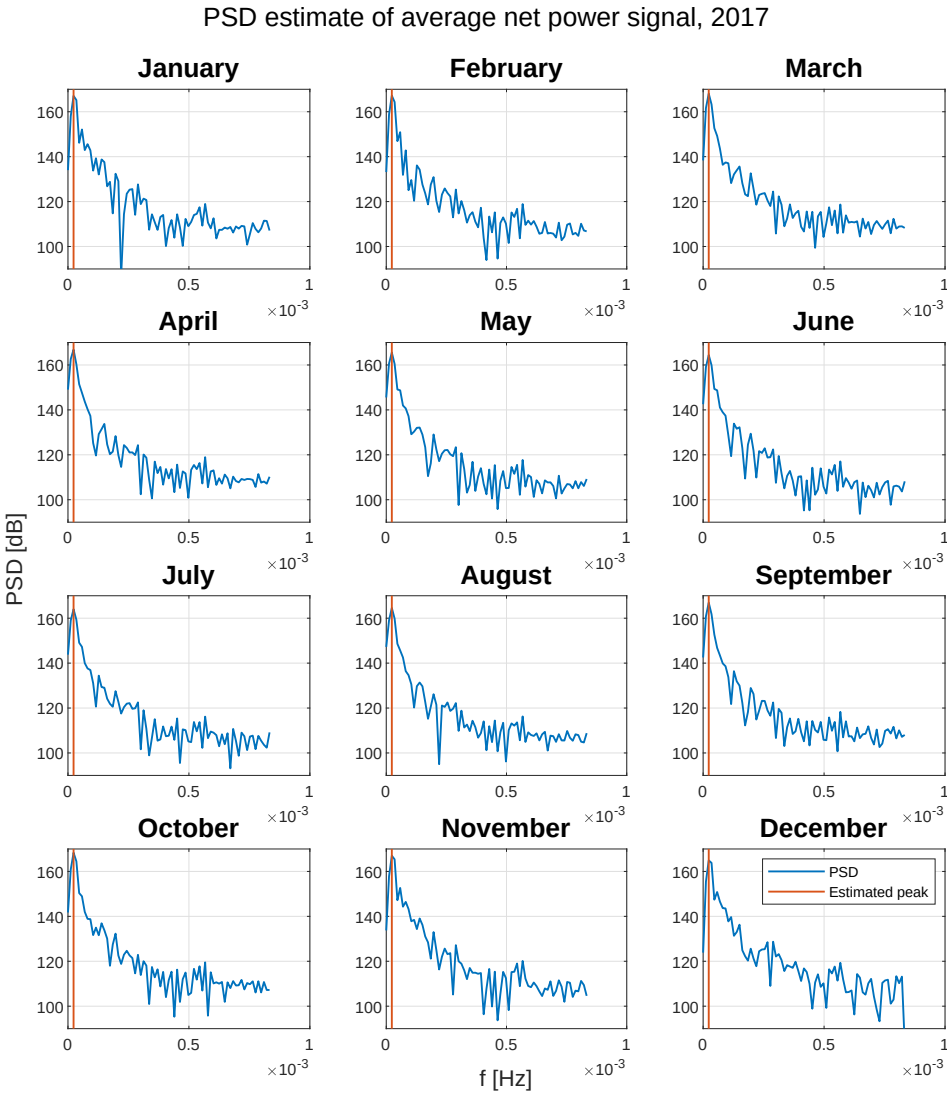

Figure E-7: PSD estimates for 2017 using a periodogram with Hamming filter and 144 DFT points. Estimated peak: expected peak at $f_{exp} = 2.31 \cdot 10^{-5}\,\text{Hz}$.

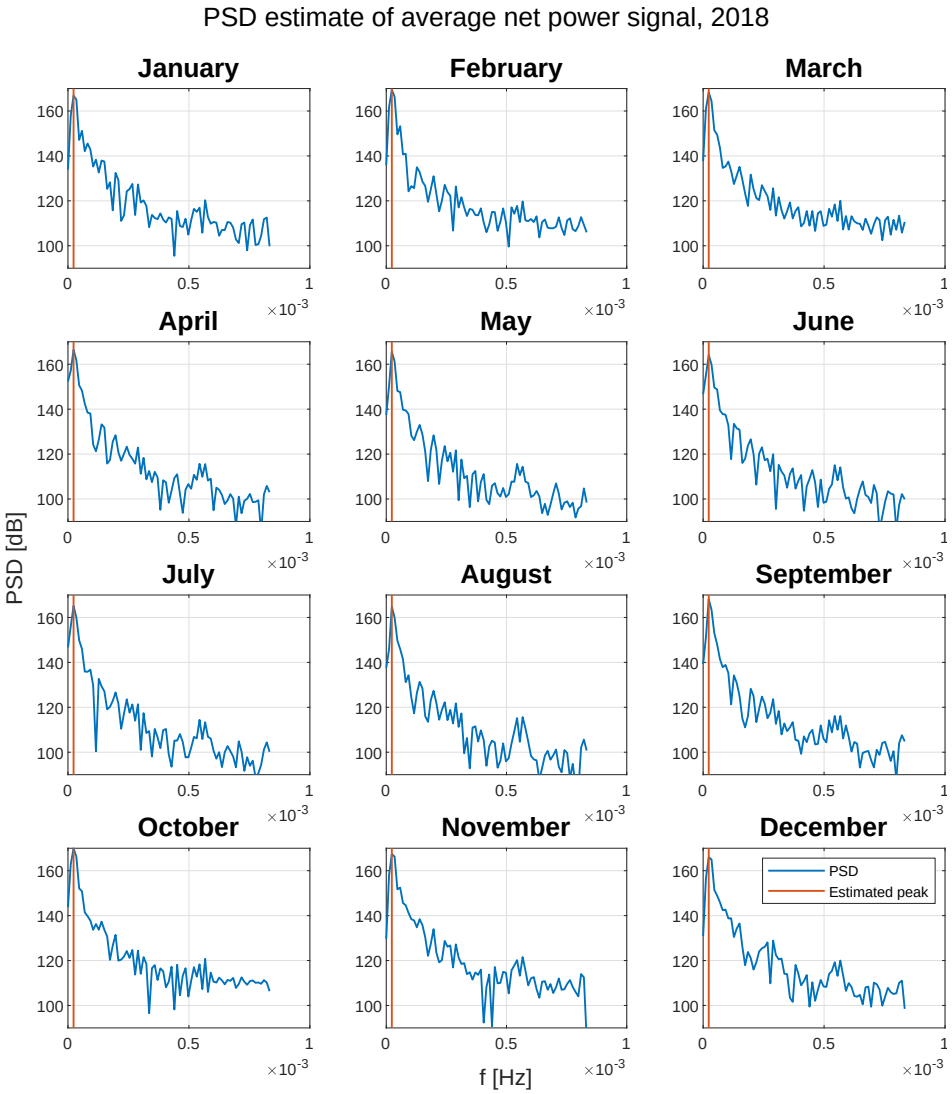

Figure E-8: PSD estimates for 2018 using a periodogram with Hamming filter and 144 DFT points. Estimated peak: expected peak at $f_{exp} = 2.31 \cdot 10^{-5}$ Hz.

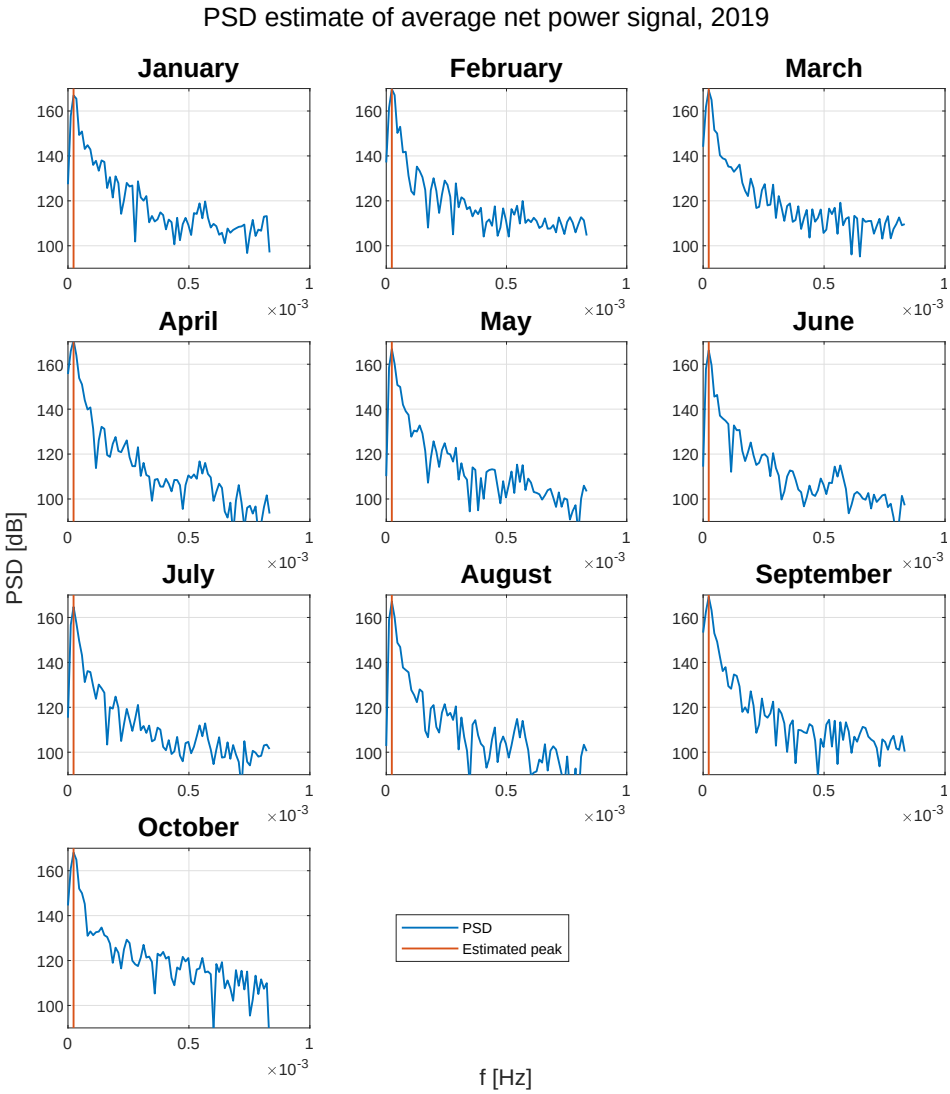

Figure E-9: PSD estimates for 2019 using a periodogram with Hamming filter and 144 DFT points. Estimated peak: expected peak at $f_{exp} = 2.31 \cdot 10^{-5}$ Hz.

Appendix F

Controller performance measures - average net power signals

Controller performance measures for the controlled nonlinear system where average net power signals are used as disturbance signal are shown in Table F-1 for smoothed controller option 1, Table F-2 for original unsmoothed controller option 1, Table F-3 for smoothed controller option 2, and Table F-4 for original unsmoothed controller option 2. Original unsmoothed controller refers to the proportional-integral (PI) controller parameter functions obtained from the $\hat{\mathcal{S}}/\hat{K}\hat{\mathcal{S}}$ mixed sensitivity optimization problem described in chapter 7 and smoothed controller refers to the controllers for which the parameters of the original unsmoothed controller were approximated by smooth functions. The average net power signals span January 2017 to October 2019. It is clear from the tables that smoothed controller option 1 keeps the system closest to its reference signals. The hydrogen composition error of this controller does not exceed 0.1 pp and the maximum temperature error is 7.97 K.

The integral of squared error (ISE) values corresponding to the different controllers are visualized in Figure F-1. This figure shows that the ISE values for smoothed controller option 1 is often multiple orders smaller than for the smoothed and original unsmoothed controller 2. Original unsmoothed controller option 1 is able to outperform smoothed controller option 1 at multiple occasions. However, this controller also failed to complete 7 out of 34 simulations. Two of these simulations failed because the SORC ran out of oxygen, as shown Figure F-3.

The maximum absolute error in PEN temperature and hydrogen fraction in the fuel channel is shown in Figure F-2. Both types of controller option 1 outperform any of controller option 2. The option 2 composition controllers fail in most simulations to keep the hydrogen fraction within 10 pp of the reference value.

Table F-1: Controller performance measures for smoothed controller option 1 applied to the controlled nonlinear SORC system disturbed by scaled net power signal. ISE: integral of squared error. Max. abs. error: maximum absolute error. ISE values were not assigned for failed simulations.

			Max. abs. error	
Date	ISE T_{PEN} [K^2]	ISE χ_{fuel,H_2} [-]	T_{PEN} [K]	χ_{fuel,H_2} [pp]
January 2017	$1.24 \cdot 10^6$	$3.02 \cdot 10^{-4}$	5.36	$4.34 \cdot 10^{-2}$
February 2017	$1.53 \cdot 10^6$	$9.73 \cdot 10^{-6}$	6.21	$5.04 \cdot 10^{-2}$
March 2017	$6.76 \cdot 10^6$	$1.93 \cdot 10^{-4}$	6.80	$6.08 \cdot 10^{-2}$
April 2017	$4.29 \cdot 10^6$	$3.59 \cdot 10^{-3}$	7.31	$6.48 \cdot 10^{-2}$
May 2017	$9.03 \cdot 10^6$	$3.24 \cdot 10^{-3}$	7.06	$7.44 \cdot 10^{-2}$
June 2017	$1.48 \cdot 10^7$	$1.47 \cdot 10^{-3}$	7.23	$6.42 \cdot 10^{-2}$
July 2017	$5.14 \cdot 10^6$	$3.49 \cdot 10^{-2}$	7.97	$9.04 \cdot 10^{-2}$
August 2017	$3.87 \cdot 10^6$	$1.39 \cdot 10^{-2}$	6.17	$5.22 \cdot 10^{-2}$
September 2017	$1.13 \cdot 10^6$	$9.33 \cdot 10^{-4}$	6.85	$6.09 \cdot 10^{-2}$
October 2017	$1.72 \cdot 10^6$	$1.60 \cdot 10^{-4}$	6.70	$6.50 \cdot 10^{-2}$
November 2017	$1.46 \cdot 10^6$	$1.36 \cdot 10^{-4}$	5.42	$4.29 \cdot 10^{-2}$
December 2017	$1.44 \cdot 10^6$	$3.71 \cdot 10^{-6}$	4.77	$3.91 \cdot 10^{-2}$
January 2018	$1.31 \cdot 10^6$	$1.37 \cdot 10^{-4}$	5.34	$4.28 \cdot 10^{-2}$
February 2018	$2.25 \cdot 10^6$	$1.09 \cdot 10^{-5}$	6.68	$6.23 \cdot 10^{-2}$
March 2018	$3.41 \cdot 10^5$	$9.64 \cdot 10^{-4}$	6.48	$5.71 \cdot 10^{-2}$
April 2018	$3.75 \cdot 10^6$	$3.14 \cdot 10^{-3}$	6.90	$6.16 \cdot 10^{-2}$
May 2018	$2.15 \cdot 10^7$	$6.16 \cdot 10^{-5}$	7.28	$6.95 \cdot 10^{-2}$
June 2018	$2.67 \cdot 10^6$	$1.51 \cdot 10^{-3}$	7.84	$7.89 \cdot 10^{-2}$
July 2018	$8.10 \cdot 10^5$	$9.94 \cdot 10^{-3}$	7.63	$7.12 \cdot 10^{-2}$
August 2018	$8.36 \cdot 10^6$	$8.80 \cdot 10^{-3}$	5.85	$5.86 \cdot 10^{-2}$
September 2018	$4.11 \cdot 10^6$	$1.38 \cdot 10^{-3}$	6.82	$5.90 \cdot 10^{-2}$
October 2018	$2.18 \cdot 10^6$	$1.56 \cdot 10^{-3}$	7.29	$6.66 \cdot 10^{-2}$
November 2018	$2.40 \cdot 10^6$	$1.00 \cdot 10^{-5}$	5.40	$4.67 \cdot 10^{-2}$
December 2018	$1.23 \cdot 10^6$	$3.69 \cdot 10^{-5}$	5.16	$4.10 \cdot 10^{-2}$
January 2019	$1.34 \cdot 10^6$	$6.81 \cdot 10^{-5}$	5.47	$4.34 \cdot 10^{-2}$
February 2019	$3.74 \cdot 10^6$	$3.11 \cdot 10^{-4}$	6.97	$6.20 \cdot 10^{-2}$
March 2019	$2.79 \cdot 10^6$	$6.85 \cdot 10^{-4}$	6.31	$4.99 \cdot 10^{-2}$
April 2019	$2.06 \cdot 10^7$	$3.00 \cdot 10^{-6}$	4.99	$4.42 \cdot 10^{-2}$
May 2019	$5.48 \cdot 10^5$	$3.91 \cdot 10^{-3}$	4.48	$3.55 \cdot 10^{-2}$
June 2019	$1.99 \cdot 10^6$	$5.77 \cdot 10^{-4}$	3.06	$3.10 \cdot 10^{-2}$
July 2019	$1.88 \cdot 10^6$	$7.28 \cdot 10^{-4}$	3.64	$3.09 \cdot 10^{-2}$
August 2019	$2.18 \cdot 10^6$	$3.05 \cdot 10^{-3}$	3.55	$3.87 \cdot 10^{-2}$
September 2019	$1.90 \cdot 10^6$	$1.26 \cdot 10^{-2}$	5.05	$4.38 \cdot 10^{-2}$
October 2019	$2.03 \cdot 10^6$	$1.33 \cdot 10^{-3}$	6.18	$5.82 \cdot 10^{-2}$

Table F-2: Controller performance measures for original unsmoothed controller option 1 applied to the controlled nonlinear SORC system disturbed by scaled net power signal. ISE: integral of squared error. Max. abs. error: maximum absolute error. ISE values were not assigned for failed simulations.

			Max. abs. error	
Date	ISE T_{PEN} [K^2]	ISE χ_{fuel,H_2} [-]	T_{PEN} [K]	χ_{fuel,H_2} [pp]
January 2017	$1.10 \cdot 10^4$	$3.06 \cdot 10^{-5}$	3.89	$4.22 \cdot 10^{-2}$
February 2017	$8.00 \cdot 10^2$	$2.75 \cdot 10^{-5}$	4.43	$4.88 \cdot 10^{-2}$
March 2017	$1.79 \cdot 10^4$	$2.90 \cdot 10^{-8}$	5.08	$5.88 \cdot 10^{-2}$
April 2017	-	-	5.47	$6.39 \cdot 10^{-2}$
May 2017	$3.65 \cdot 10^5$	$2.51 \cdot 10^{-5}$	5.46	$7.17 \cdot 10^{-2}$
June 2017	$1.77 \cdot 10^6$	$1.02 \cdot 10^{-3}$	5.10	$5.90 \cdot 10^{-2}$
July 2017	-	-	7.82	0.171
August 2017	$3.03 \cdot 10^4$	$2.68 \cdot 10^{-4}$	4.37	$4.99 \cdot 10^{-2}$
September 2017	$2.43 \cdot 10^4$	$4.58 \cdot 10^{-4}$	5.09	$5.90 \cdot 10^{-2}$
October 2017	$1.17 \cdot 10^4$	$1.82 \cdot 10^{-5}$	5.34	$6.28 \cdot 10^{-2}$
November 2017	$6.58 \cdot 10^2$	$1.21 \cdot 10^{-5}$	3.86	$4.11 \cdot 10^{-2}$
December 2017	$6.26 \cdot 10^3$	$4.29 \cdot 10^{-5}$	3.53	$3.80 \cdot 10^{-2}$
January 2018	$2.42 \cdot 10^3$	$1.37 \cdot 10^{-6}$	3.90	$4.16 \cdot 10^{-2}$
February 2018	$1.15 \cdot 10^4$	$5.83 \cdot 10^{-5}$	5.18	$6.03 \cdot 10^{-2}$
March 2018	$1.36 \cdot 10^5$	$3.95 \cdot 10^{-5}$	4.84	$5.53 \cdot 10^{-2}$
April 2018	$5.17 \cdot 10^4$	$2.18 \cdot 10^{-4}$	5.18	$6.05 \cdot 10^{-2}$
May 2018	-	-	5.62	$6.71 \cdot 10^{-2}$
June 2018	-	-	6.17	$7.59 \cdot 10^{-2}$
July 2018	-	-	5.73	$6.87 \cdot 10^{-2}$
August 2018	$2.37 \cdot 10^3$	$1.10 \cdot 10^{-5}$	4.64	$5.67 \cdot 10^{-2}$
September 2018	$2.48 \cdot 10^4$	$3.51 \cdot 10^{-5}$	5.06	$5.73 \cdot 10^{-2}$
October 2018	-	-	5.45	$6.44 \cdot 10^{-2}$
November 2018	85.5	$1.23 \cdot 10^{-5}$	3.87	$4.54 \cdot 10^{-2}$
December 2018	$1.15 \cdot 10^3$	$1.21 \cdot 10^{-5}$	3.79	$3.99 \cdot 10^{-2}$
January 2019	$2.31 \cdot 10^3$	$2.16 \cdot 10^{-7}$	3.93	$4.19 \cdot 10^{-2}$
February 2019	$2.52 \cdot 10^4$	$1.76 \cdot 10^{-5}$	5.19	$6.06 \cdot 10^{-2}$
March 2019	$3.77 \cdot 10^4$	$4.06 \cdot 10^{-8}$	4.38	$4.84 \cdot 10^{-2}$
April 2019	$1.81 \cdot 10^6$	$7.75 \cdot 10^{-4}$	3.62	$3.87 \cdot 10^{-2}$
May 2019	$1.10 \cdot 10^5$	$2.28 \cdot 10^{-4}$	3.26	$3.31 \cdot 10^{-2}$
June 2019	$1.78 \cdot 10^3$	$8.06 \cdot 10^{-6}$	2.67	$2.65 \cdot 10^{-2}$
July 2019	$1.72 \cdot 10^3$	$5.78 \cdot 10^{-5}$	2.75	$2.65 \cdot 10^{-2}$
August 2019	$1.47 \cdot 10^4$	$1.38 \cdot 10^{-4}$	3.19	$3.29 \cdot 10^{-2}$
September 2019	$1.94 \cdot 10^5$	$2.02 \cdot 10^{-4}$	3.76	$4.15 \cdot 10^{-2}$
October 2019	-	-	4.70	0.343

Table F-3: Controller performance measures for smoothed controller option 2 applied to the controlled nonlinear SORC system disturbed by scaled net power signal. ISE: integral of squared error. Max. abs. error: maximum absolute error. ISE values were not assigned for failed simulations.

			Max. abs. error	
Date	ISE T_{PEN} [K^2]	ISE χ_{fuel,H_2} [-]	T_{PEN} [K]	χ_{fuel,H_2} [pp]
January 2017	$2.01 \cdot 10^8$	$5.59 \cdot 10^3$	7.93	11.2
February 2017	$2.77 \cdot 10^8$	$1.07 \cdot 10^4$	8.60	11.4
March 2017	$2.28 \cdot 10^8$	$5.17 \cdot 10^3$	8.18	12.1
April 2017	$3.91 \cdot 10^8$	$1.22 \cdot 10^4$	9.08	12.3
May 2017	$2.55 \cdot 10^8$	$5.37 \cdot 10^4$	9.60	13.2
June 2017	$3.89 \cdot 10^8$	$6.87 \cdot 10^4$	9.96	14.2
July 2017	$3.81 \cdot 10^8$	$5.96 \cdot 10^4$	10.1	13.7
August 2017	$2.15 \cdot 10^8$	$3.70 \cdot 10^4$	9.04	10.7
September 2017	$1.24 \cdot 10^8$	$3.66 \cdot 10^3$	8.37	12.8
October 2017	$2.19 \cdot 10^8$	$9.74 \cdot 10^3$	9.04	12.2
November 2017	$2.42 \cdot 10^8$	$8.56 \cdot 10^3$	7.98	11.2
December 2017	$2.56 \cdot 10^8$	$1.43 \cdot 10^4$	7.39	11.4
January 2018	$2.23 \cdot 10^8$	$7.97 \cdot 10^3$	8.02	10.7
February 2018	$4.08 \cdot 10^8$	$1.27 \cdot 10^3$	8.72	11.6
March 2018	$1.93 \cdot 10^8$	$1.26 \cdot 10^3$	8.00	12.1
April 2018	$3.97 \cdot 10^8$	$1.56 \cdot 10^3$	8.40	11.3
May 2018	$9.07 \cdot 10^8$	$6.43 \cdot 10^4$	9.05	13.1
June 2018	$9.67 \cdot 10^8$	$4.22 \cdot 10^4$	10.7	14.1
July 2018	$3.70 \cdot 10^8$	$1.42 \cdot 10^3$	11.1	14.0
August 2018	$7.77 \cdot 10^8$	$3.38 \cdot 10^4$	9.32	11.5
September 2018	$6.00 \cdot 10^8$	$1.40 \cdot 10^4$	8.71	13.1
October 2018	$5.21 \cdot 10^8$	$4.13 \cdot 10^3$	8.97	12.4
November 2018	$3.13 \cdot 10^8$	$2.60 \cdot 10^4$	7.88	11.0
December 2018	$2.40 \cdot 10^8$	$9.47 \cdot 10^3$	7.81	10.1
January 2019	$2.24 \cdot 10^8$	$8.60 \cdot 10^3$	8.30	10.7
February 2019	$5.97 \cdot 10^8$	$9.66 \cdot 10^3$	8.64	11.9
March 2019	$4.91 \cdot 10^8$	$2.65 \cdot 10^3$	8.59	12.3
April 2019	$1.02 \cdot 10^9$	$6.18 \cdot 10^4$	7.80	11.9
May 2019	$3.38 \cdot 10^8$	$1.16 \cdot 10^3$	7.55	11.5
June 2019	$5.96 \cdot 10^8$	$1.79 \cdot 10^{-2}$	6.30	10.7
July 2019	$2.98 \cdot 10^8$	$1.21 \cdot 10^4$	6.73	9.20
August 2019	$6.59 \cdot 10^8$	$2.95 \cdot 10^3$	6.74	11.1
September 2019	$6.53 \cdot 10^8$	$5.66 \cdot 10^4$	7.92	11.6
October 2019	$5.60 \cdot 10^8$	$1.39 \cdot 10^4$	9.26	13.2

Table F-4: Controller performance measures for original unsmoothed controller option 2 applied to the controlled nonlinear SORC system disturbed by scaled net power signal. ISE: integral of squared error. Max. abs. error: maximum absolute error. ISE values were not assigned for failed simulations.

			Max. abs. error	
Date	ISE T_{PEN} [K^2]	ISE χ_{fuel,H_2} [-]	T_{PEN} [K]	χ_{fuel,H_2} [pp]
January 2017	$1.34 \cdot 10^7$	$1.73 \cdot 10^3$	6.20	8.88
February 2017	$5.56 \cdot 10^7$	0.454	5.97	9.76
March 2017	$2.47 \cdot 10^7$	$1.07 \cdot 10^3$	7.64	11.3
April 2017	$1.91 \cdot 10^7$	21.4	9.14	12.0
May 2017	$4.72 \cdot 10^7$	$7.78 \cdot 10^2$	8.14	11.6
June 2017	$1.33 \cdot 10^8$	$2.13 \cdot 10^3$	8.56	12.2
July 2017	$1.38 \cdot 10^8$	$1.34 \cdot 10^3$	8.33	12.0
August 2017	$2.95 \cdot 10^7$	$3.55 \cdot 10^2$	7.90	9.17
September 2017	$6.52 \cdot 10^6$	$1.76 \cdot 10^3$	7.30	11.7
October 2017	$2.62 \cdot 10^7$	$8.23 \cdot 10^2$	6.83	11.0
November 2017	$1.82 \cdot 10^7$	$1.64 \cdot 10^3$	6.11	9.27
December 2017	$4.53 \cdot 10^7$	91.1	6.61	9.04
January 2018	$2.39 \cdot 10^7$	$7.10 \cdot 10^2$	5.83	8.38
February 2018	$3.23 \cdot 10^7$	$2.51 \cdot 10^2$	6.63	10.7
March 2018	$6.40 \cdot 10^6$	$2.08 \cdot 10^3$	7.60	11.2
April 2018	$2.37 \cdot 10^7$	$2.76 \cdot 10^2$	7.50	10.7
May 2018	$1.64 \cdot 10^8$	$1.09 \cdot 10^3$	9.07	12.1
June 2018	$1.57 \cdot 10^8$	$1.02 \cdot 10^3$	9.29	13.3
July 2018	$1.26 \cdot 10^8$	$2.11 \cdot 10^3$	8.85	12.9
August 2018	$9.32 \cdot 10^7$	$2.03 \cdot 10^2$	9.40	9.84
September 2018	$7.45 \cdot 10^7$	84.8	7.82	12.2
October 2018	$3.64 \cdot 10^7$	$1.53 \cdot 10^3$	7.03	11.2
November 2018	$3.42 \cdot 10^7$	$1.44 \cdot 10^2$	5.78	9.19
December 2018	$3.33 \cdot 10^7$	$1.71 \cdot 10^2$	5.49	8.14
January 2019	$2.81 \cdot 10^7$	$4.70 \cdot 10^2$	5.79	8.76
February 2019	$7.40 \cdot 10^7$	$1.97 \cdot 10^2$	7.02	11.0
March 2019	$6.16 \cdot 10^7$	$7.45 \cdot 10^2$	7.55	11.3
April 2019	$1.50 \cdot 10^8$	$1.11 \cdot 10^3$	6.92	10.6
May 2019	$3.43 \cdot 10^7$	$5.15 \cdot 10^2$	6.82	10.8
June 2019	$1.94 \cdot 10^7$	$9.27 \cdot 10^2$	6.16	9.50
July 2019	$8.97 \cdot 10^6$	$2.49 \cdot 10^3$	5.74	8.39
August 2019	$3.32 \cdot 10^7$	$6.08 \cdot 10^2$	6.25	9.57
September 2019	$4.95 \cdot 10^7$	$4.89 \cdot 10^2$	6.95	10.3
October 2019	$1.37 \cdot 10^8$	$8.43 \cdot 10^2$	8.33	11.7

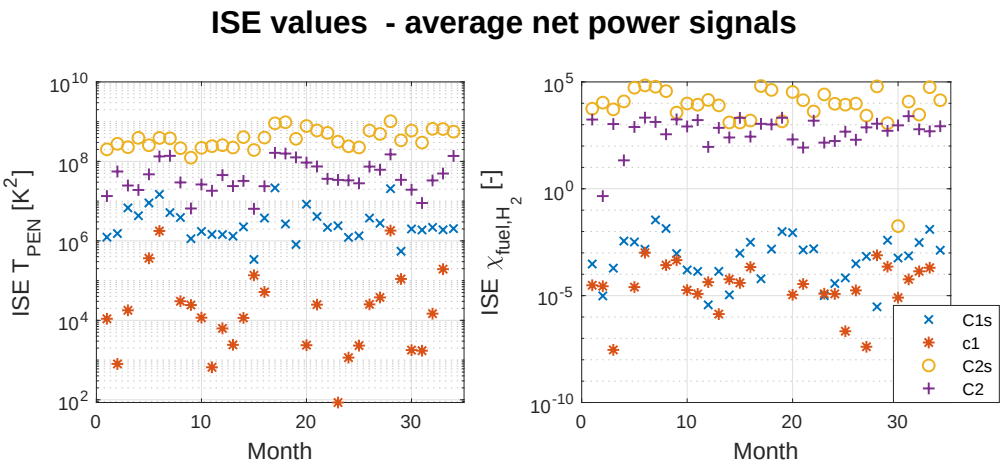

Figure F-1: Comparison of ISE performance measure for smoothed controller option 1 (C1s), original unsmoothed controller option 1 (C1), controller option 2 (C2s), and original unsmoothed controller option 2 (C2). Month spans January 2017 (month 1) to October 2019 (month 34).

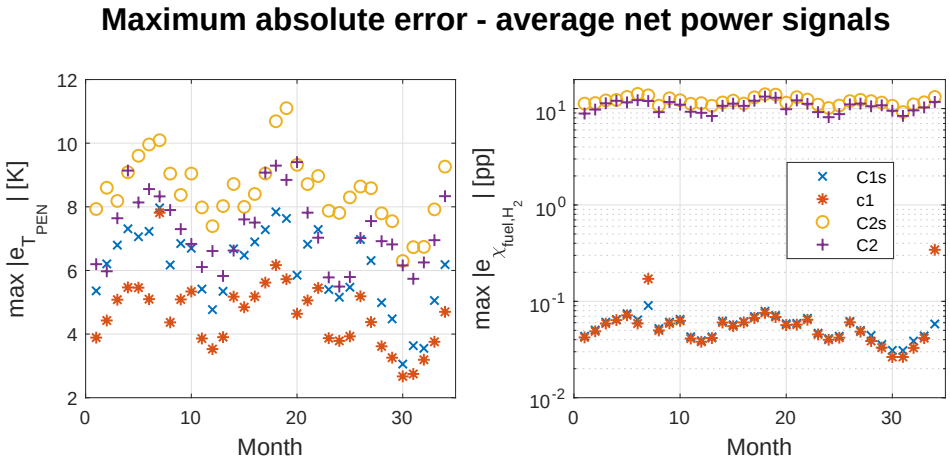

Figure F-2: Comparison of maximum absolute error for smoothed controller option 1 (C1s), original unsmoothed controller option 1 (C1), controller option 2 (C2s), and original unsmoothed controller option 2 (C2). Month spans January 2017 (month 1) to October 2019 (month 34).

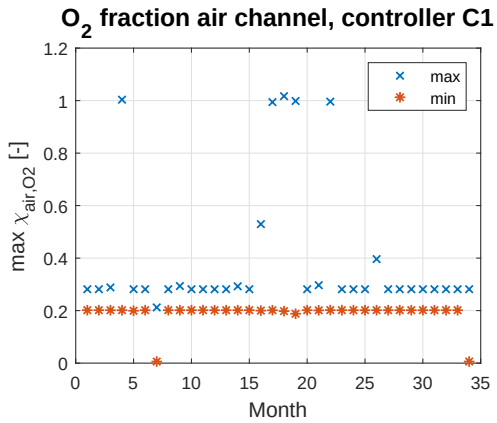

Figure F-3: Maximum (max) and minimum (min) oxygen fractions in the air channel during dynamic simulations for original unsmoothed controller option 1 (C1). Month spans January 2017 (month 1) to October 2019 (month 34).

Appendix G

Additional results of the controlled SORC

This appendix provides additional results of the controlled SORC. First, the importance of smooth controller parameter functions is shown by comparing simulations where the control parameter functions are unsmoothed with simulations where the control parameter functions are smoothed. The second set of results shows the temperature time derivative for the simulations in section 7-5.

G-1 Importance of smooth controller parameter functions

The controller parameter functions were smoothed in section 7-4 to meet the gain-scheduling control recommendation that the controller parameter functions should be smooth functions of the scheduling variable. This section shows that using unsmoothed controller parameter functions can be harmful to the SORC.

Figure G-1 shows a selection of results of simulations for smoothed and unsmoothed controller option 1 where the average net power signal of July 2018 is the basis for the disturbance signal. The moment the system enters the endothermic SOEC mode, the air flow controller quickly reduces the air flow rate in an attempt to cool the cell. This results in an overflow of oxygen in the air channel and the controller is no longer able to operate the SORC. This shows that the air flow controller of unsmoothed controller option 1 is too aggressive around $\bar{P} = 0$. A steep change from SOEC to SOFC can result in a similar situation where the controller desperately tries to heat the cell, which results in oxygen depletion.

The same story holds for controller 2 as for controller 1, as shown in Figure G-2. This figure shows that unsmoothed controller option 2 also runs the risk of overflowing the SORC with oxygen when the system experiences large PEN temperature errors.

Smoothing of the controller parameter functions is a way of enforcing less aggressive control around $\bar{P} = 0$ and results in a controller that is more likely to be able to complete the

simulation. This approach results in larger errors around $\bar{P} = 0$. However, this should not be a problem if the reference signals are chosen such that the system does not operate in critical conditions in this region. Non-critical conditions are conditions where relatively large errors do not result in a damaged system. As an example, consider a hydrogen composition around 0.15 and around 0.5 in SOFC mode. In the first case, a change of 0.1 has serious consequences as the cell might run out of hydrogen. In the latter case, the system is still far from hydrogen depletion and it is unlikely that the system will be damaged.

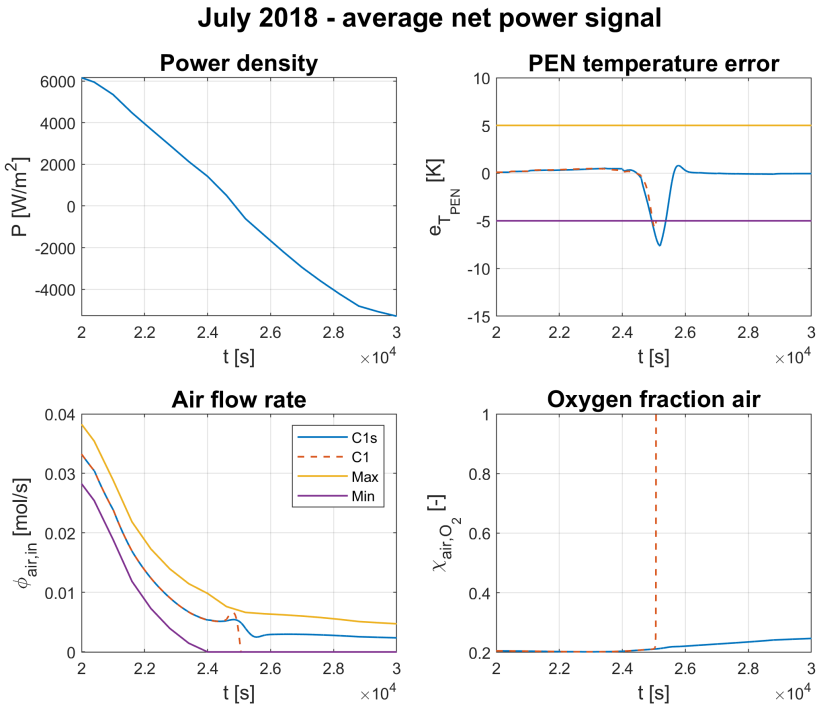

Figure G-1: Selected results of a dynamic simulation of the controlled nonlinear system with the average net power density signal of July 2018 as a disturbance signal. Legend does not apply to the power density plot. C1s: controller option 1 with smoothed parameter functions, C1: controller option 1 with unsmoothed parameter functions, Max: maximum allowed input and error value as set by the scaling matrices θ_u and θ_e, respectively, Min: minimum allowed input and error value as set by the scaling matrices θ_u and θ_e, respectively, Oxygen fraction air: oxygen fraction in the air channel. Controller C1 was unable to complete the simulation, because the SORC was overflown with oxygen.

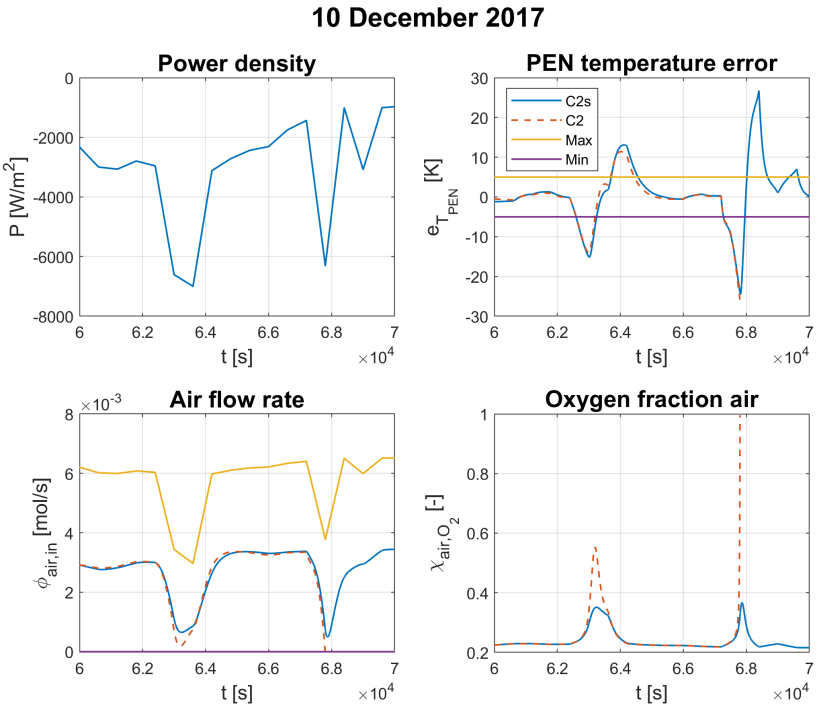

Figure G-2: Selected results of a dynamic simulation of the controlled nonlinear system with the average net power density signal of 10 December 2017 as a disturbance signal. Legend does not apply to the power density plot. C2s: controller option 2 with smoothed parameter functions, C2: controller option 2 with unsmoothed parameter functions, Max: maximum allowed input and error value as set by the scaling matrices θ_u and θ_e, respectively, Min: minimum allowed input and error value as set by the scaling matrices θ_u and θ_e, respectively, Oxygen fraction air: oxygen fraction in the air channel. Controller C2 was unable to complete the simulation, because the SORC was overflown with oxygen.

G-2 PEN temperature time derivative

The PEN temperature time derivative for the simulations in chapter 7 are shown in Figure G-3. The largest absolute PEN temperature time derivatives are observed when the SORC switches from one mode to another.

For smoothed controller option 1, the maximum absolute PEN temperature time derivative was 0.17 K/s. This time derivative was observed during the start of the simulation on 10 December 2017. Therefore, the relatively large derivative was a result of an initial deviation from the reference signal.

The maximum absolute PEN temperature time derivative observed for smoothed controller option 2 is 0.23 K/s, during the start of the simulation of 10 December 2017. The simulation on 18 June 2019 was excluded, because the SORC ran out of hydrogen during this simulation. The peak value during the 18 June 2019 simulation was 1.6 K/s.

It should be noted that it is unknown what temperature time derivative the SORC can handle. Most literature does not consider a limit on it. Srikanth, Heddrich, Gupta, *et al.* [48] claims that the absolute PEN temperature time derivative must be smaller than 0.25 K/s for their electrolyte supported cell with an electrolyte thickness of 90 µm, cell length of 9.0 cm and cell width of 14.2 cm.

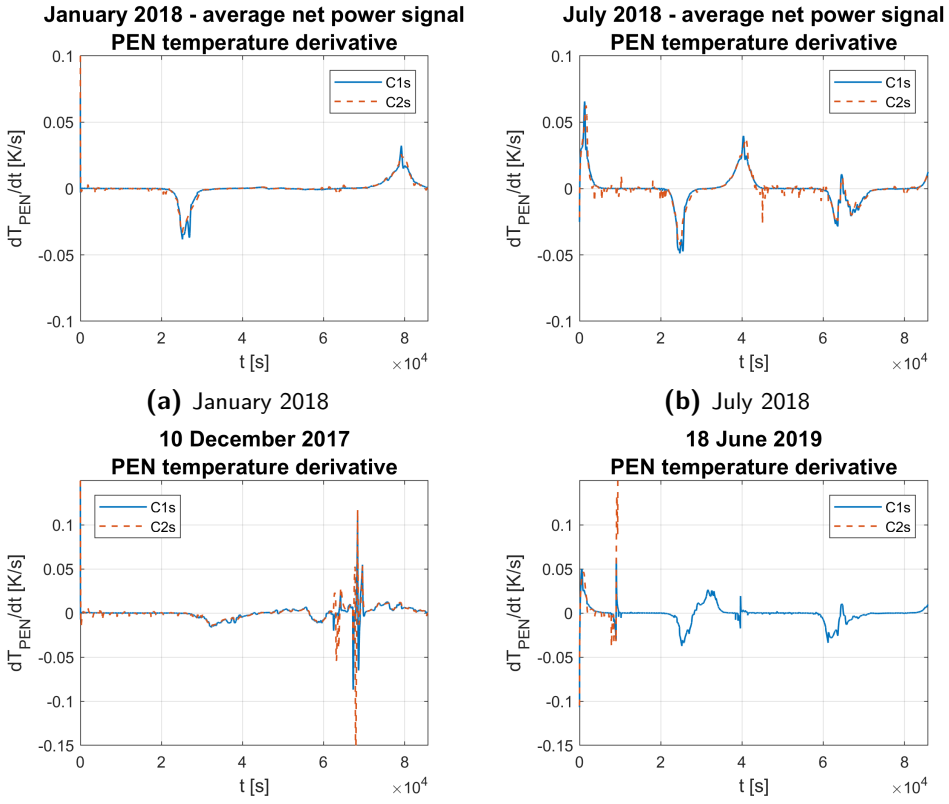

(a) January 2018 **(b)** July 2018

(c) 10 December 2017 **(d)** 18 June 2019

Figure G-3: PEN temperature time derivative for the simulations in chapter 7. C1s: controller option 1 with smoothed parameter functions, C2s: controller option 2 with smoothed parameter functions. The simulation with C2s on 18 June 2019 did not complete, because the SORC ran out of hydrogen (see Figure 7-21).

Bibliography

[1] Climate Action Tracker. "EU - Country Summary, 19 september 2019." ClimateActionTracker.org. https://climateactiontracker.org/countries/eu/ (accessed Nov. 5, 2019).

[2] QIC. "Technology Disruptions Affecting Infrastructure (Part 1)." QIC.com.au. https://www.qic.com.au/knowledge-centre/technology-disruptions-affecting-infrastructure-20160414 (accessed Jun. 15, 2019).

[3] "What the duck curve tells us about managing a green grid," California ISO, Folsom, CA, USA, Nov. 2016. [Online]. Available: http://www.caiso.com/Documents/FlexibleResourcesHelpRenewables_FastFacts.pdf.

[4] S. Y. Gómez and D. Hotza, "Current developments in reversible solid oxide fuel cells," *Renewable Sustainable Energy Rev.*, vol. 61, pp. 155–174, Aug. 2016, doi: 10.1016/j.rser.2016.03.005.

[5] TenneT. "Load." TenneT.eu. https://www.tennet.eu/electricity-market/data-dashboard/load/ (accessed Feb. 28, 2019).

[6] Energieopwek.nl. "Energie akkoord." Energieopwek.nl. https://energieopwek.nl/ (accessed Mar. 1, 2019).

[7] M. Uddin, M. F. Romlie, M. F. Abdullah, S. Abd Halim, A. H. Abu Bakar, and T. Chia Kwang, "A review on peak load shaving strategies," *Renewable Sustainable Energy Rev.*, vol. 82, pp. 3323–3332, Feb. 2018, doi: 10.1016/j.rser.2017.10.056.

[8] H. Ibrahim, A. Ilinca, and J. Perron, "Energy storage systems—characteristics and comparisons," *Renewable Sustainable Energy Rev.*, vol. 12, no. 5, pp. 1221–1250, Jun. 2008, doi: 10.1016/j.rser.2007.01.023.

[9] L. Yao, B. Yang, H. Cui, J. Zhuang, J. Ye, and J. Xue, "Challenges and progresses of energy storage technology and its application in power systems," *J. Mod. Power Syst. Clean Energy*, vol. 4, no. 4, pp. 519–528, Oct. 2016, doi: 10.1007/s40565-016-0248-x.

[10] G. L. Kyriakopoulos and G. Arabatzis, "Electrical energy storage systems in electricity generation: energy policies, innovative technologies, and regulatory regimes," *Renewable Sustainable Energy Rev.*, vol. 56, pp. 1044–1067, Apr. 2016, doi: 10.1016/j.rser.2015.12.046.

[11] M. Aneke and M. Wang, "Energy storage technologies and real life applications – a state of the art review," *Appl. Energy*, vol. 179, pp. 350–377, Oct. 2016, doi: 10.1016/j.apenergy.2016.06.097.

[12] A. Meurink, G. Muller, and R. Segers, "Hernieuwbare energie in Nederlands," Centraal Bureau voor de Statistiek, Den Haag, The Netherlands, Sep. 2019. [Online]. Available: https://www.cbs.nl/nl-nl/publicatie/2019/40/hernieuwbare-energie-in-nederland-2018.

[13] H. Chen, T. N. Cong, W. Yang, C. Tan, Y. Li, and Y. Ding, "Progress in electrical energy storage system: a critical review," *Prog. Nat. Sci.*, vol. 19, no. 3, pp. 291–312, Mar. 2009, doi: 10.1016/j.pnsc.2008.07.014.

[14] Electrical Energy Storage project team, "Electrical energy storage," International Electrotechnical Commission, Geneva, Switzerland, 2011. [Online]. Available: https://www.iec.ch/whitepaper/energystorage/.

[15] B. Decourt and R. Debarre, "Leading the energy transition factbook - electricity storage," SBC Energy Institute, The Hague, The Netherlands, Sep. 2013. [Online]. Available: https://www.cpuc.ca.gov/WorkArea/DownloadAsset.aspx?id=3170.

[16] F. Díaz-González, A. Sumper, and O. Gomis-Bellmunt, *Energy Storage in Power Systems*, 1st ed. Chichester, U.K.: Wiley, 2016.

[17] T. Kousksou, P. Bruel, A. Jamil, T. El Rhafiki, and Y. Zeraouli, "Energy storage: applications and challenges," *Sol. Energy Mater. Sol. Cells*, vol. 120, pp. 59–80, Jan. 2014, doi: 10.1016/j.solmat.2013.08.015.

[18] R. O'hayre, S.-W. Cha, W. G. Colella, and F. B. Prinz, *Fuel Cell Fundamentals*, 3rd ed. Hoboken, NJ, USA: Wiley, 2016.

[19] B. Huang, Y. Qi, and M. Murshed, "Solid oxide fuel cell: Perspective of dynamic modeling and control," *J. Process Control*, vol. 21, no. 10, pp. 1426–1437, 2011, doi: 10.1016/j.jprocont.2011.06.017.

[20] P. Kazempoor and R. J. Braun, "Model validation and performance analysis of regenerative solid oxide cells: Electrolytic operation," *Int. J. Hydrogen Energy*, vol. 39, no. 6, pp. 2669–2684, Feb. 2014, doi: 10.1016/j.ijhydene.2013.12.010.

[21] P. Kazempoor, V. Dorer, and F. Ommi, "Modelling and performance evaluation of solid oxide fuel cell for building integrated co- and polygeneration," *Fuel Cells*, vol. 10, no. 6, pp. 1074–1094, Dec. 2010, doi: 10.1002/fuce.200900082.

[22] P. Kazempoor and R. J. Braun, "Model validation and performance analysis of regenerative solid oxide cells for energy storage applications: Reversible operation," *Int. J. Hydrogen Energy*, vol. 39, no. 11, pp. 5955–5971, Apr. 2014, doi: 10.1016/j.ijhydene.2014.01.186.

[23] Y. Luo, Y. Shi, Y. Zheng, Z. Gang, and N. Cai, "Mutual information for evaluating renewable power penetration impacts in a distributed generation system," *Energy*, vol. 141, pp. 290–303, Dec. 2017, doi: 10.1016/j.energy.2017.09.033.

[24] X. Jin and X. Xue, "Mathematical modeling analysis of regenerative solid oxide fuel cells in switching mode conditions," *J. Power Sources*, vol. 195, no. 19, pp. 6652–6658, 2010, doi: 10.1016/j.jpowsour.2010.04.018.

[25] M. García-Camprubí, S. Izquierdo, and N. Fueyo, "Challenges in the electrochemical modelling of solid oxide fuel and electrolyser cells," *Renewable Sustainable Energy Rev.*, vol. 33, pp. 701–718, May 2014, doi: 10.1016/j.rser.2014.02.034.

[26] C. H. Wendel, Z. Gao, S. A. Barnett, and R. J. Braun, "Modeling and experimental performance of an intermediate temperature reversible solid oxide cell for high-efficiency, distributed-scale electrical energy storage," *J. Power Sources*, vol. 283, pp. 329–342, Jun. 2015, doi: 10.1016/j.jpowsour.2015.02.113.

[27] L. Barelli, G. Bidini, G. Cinti, and A. Ottaviano, "Study of SOFC-SOE transition on a RSOFC stack," *Int. J. Hydrogen Energy*, vol. 42, no. 41, pp. 26 037–26 047, Oct. 2017, doi: 10.1016/j.ijhydene.2017.08.159.

[28] J. Laurencin, D. Kane, G. Delette, J. Deseure, and F. Lefebvre-Joud, "Modelling of solid oxide steam electrolyser: Impact of the operating conditions on hydrogen production," *J. Power Sources*, vol. 196, no. 4, pp. 2080–2093, Feb. 2011, doi: 10.1016/j.jpowsour.2010.09.054.

[29] M. Ni, M. K. H. Leung, and D. Y. C. Leung, "Parametric study of solid oxide steam electrolyzer for hydrogen production," *Int. J. Hydrogen Energy*, vol. 32, no. 13, pp. 2305–2313, Sep. 2007, doi: 10.1016/j.ijhydene.2007.03.001.

[30] R. K. Akikur, R. Saidur, H. W. Ping, and K. R. Ullah, "Performance analysis of a co-generation system using solar energy and SOFC technology," *Energy Convers. Manage.*, vol. 79, pp. 415–430, Mar. 2014, doi: 10.1016/j.enconman.2013.12.036.

[31] P. Mottaghizadeh, S. Santhanam, M. P. Heddrich, K. A. Friedrich, and F. Rinaldi, "Process modeling of a reversible solid oxide cell (r-SOC) energy storage system utilizing commercially available SOC reactor," *Energy Convers. Manage.*, vol. 142, pp. 477–493, Jun. 2017, doi: 10.1016/j.enconman.2017.03.010.

[32] A. M. Colclasure, B. M. Sanandaji, T. L. Vincent, and R. J. Kee, "Modeling and control of tubular solid-oxide fuel cell systems. I: Physical models and linear model reduction," *J. Power Sources*, vol. 196, no. 1, pp. 196–207, Jan. 2011, doi: 10.1016/j.jpowsour.2010.06.074.

[33] A. K. M. M. Murshed, B. Huang, and K. Nandakumar, "Control relevant modeling of planer solid oxide fuel cell system," *J. Power Sources*, vol. 163, no. 2, pp. 830–845, Jan. 2007, doi: 10.1016/j.jpowsour.2006.09.080.

[34] B. M. Sanandaji, T. L. Vincent, A. M. Colclasure, and R. J. Kee, "Modeling and control of tubular solid-oxide fuel cell systems: II. Nonlinear model reduction and model predictive control," *J. Power Sources*, vol. 196, no. 1, pp. 208–217, 2011, doi: 10.1016/j.jpowsour.2010.06.075.

[35] W. Caisheng and M. H. Nehrir, "A physically based dynamic model for solid oxide fuel cells," *IEEE Trans. Energy Convers.*, vol. 22, no. 4, pp. 887–897, Dec. 2007, doi: 10.1109/tec.2007.895468.

[36] Y. Qi, B. Huang, and K. T. Chuang, "Dynamic modeling of solid oxide fuel cell: The effect of diffusion and inherent impedance," *J. Power Sources*, vol. 150, pp. 32–47, Oct. 2005, doi: 10.1016/j.jpowsour.2005.02.080.

[37] M. Bavarian, M. Soroush, I. G. Kevrekidis, and J. B. Benziger, "Mathematical modeling, steady-state and dynamic behavior, and control of fuel cells: A review," *Ind. Eng. Chem. Res.*, vol. 49, no. 17, pp. 7922–7950, 2010, doi: 10.1021/ie100032c.

[38] J. Yang, S. Qin, W. Zhang, T. Ding, B. Zhou, X. Li, and L. Jian, "Improving the load-following capability of a solid oxide fuel cell system through the use of time delay control," *Int. J. Hydrogen Energy*, vol. 42, no. 2, pp. 1221–1236, 2017, doi: 10.1016/j.ijhydene.2016.10.107.

[39] D. Bhattacharyya, R. Rengaswamy, and C. Finnerty, "Dynamic modeling and validation studies of a tubular solid oxide fuel cell," *Chem. Eng. Sci.*, vol. 64, no. 9, pp. 2158–2172, May 2009, doi: 10.1016/j.ces.2008.12.040.

[40] P. Iora, P. Aguiar, C. S. Adjiman, and N. P. Brandon, "Comparison of two IT DIR-SOFC models: Impact of variable thermodynamic, physical, and flow properties. Steady-state and dynamic analysis," *Chem. Eng. Sci.*, vol. 60, no. 11, pp. 2963–2975, Jun. 2005, doi: 10.1016/j.ces.2005.01.007.

[41] F. Mueller, F. Jabbari, and J. Brouwer, "On the intrinsic transient capability and limitations of solid oxide fuel cell systems," *J. Power Sources*, vol. 187, no. 2, pp. 452–460, 2009, doi: 10.1016/j.jpowsour.2008.11.057.

[42] P. Adhikari and M. Abdelrahman, "Modeling, control, and integration of a portable solid oxide fuel cell system," *J. Fuel Cell Sci. Technol.*, vol. 9, no. 1, pp. 011010–011010–14, Feb. 2012, doi: 10.1115/1.4005386.

[43] S. H. Chan, K. A. Khor, and Z. T. Xia, "A complete polarization model of a solid oxide fuel cell and its sensitivity to the change of cell component thickness," *J. Power Sources*, vol. 93, no. 1-2, pp. 130–140, Feb. 2001, doi: 10.1016/s0378-7753(00)00556-5.

[44] J. Udagawa, P. Aguiar, and N. Brandon, "Hydrogen production through steam electrolysis: Model-based steady state performance of a cathode-supported intermediate temperature solid oxide electrolysis cell," *J. Power Sources*, vol. 166, no. 1, pp. 127–136, Mar. 2007, doi: 10.1016/j.jpowsour.2006.12.081.

[45] Q. Cai, E. Luna-Ortiz, C. S. Adjiman, and N. P. Brandon, "The effects of operating conditions on the performance of a solid oxide steam electrolyser: A model-based study," *Fuel Cells*, vol. 10, no. 6, pp. 1114–1128, Dec. 2010, doi: 10.1002/fuce.200900211.

[46] Q. Cai, N. P. Brandon, and C. S. Adjiman, "Modelling the dynamic response of a solid oxide steam electrolyser to transient inputs during renewable hydrogen production," *Frontiers Energy Power Eng. China*, vol. 4, no. 2, pp. 211–222, 2010, doi: 10.1007/s11708-010-0037-6.

[47] Q. Cai, C. S. Adjiman, and N. P. Brandon, "Optimal control strategies for hydrogen production when coupling solid oxide electrolysers with intermittent renewable energies," *J. Power Sources*, vol. 268, pp. 212–224, 2014, doi: 10.1016/j.jpowsour.2014.06.028.

[48] S. Srikanth, M. P. Heddrich, S. Gupta, and K. A. Friedrich, "Transient reversible solid oxide cell reactor operation – experimentally validated modeling and analysis," *Appl. Energy*, vol. 232, pp. 473–488, Dec. 2018, doi: 10.1016/j.apenergy.2018.09.186.

[49] J. Ren, S. R. Gamble, A. J. Roscoe, J. T. S. Irvine, and G. Burt, "Modeling a reversible solid oxide fuel cell as a storage device within AC power networks," *Fuel Cells*, vol. 12, no. 5, pp. 773–786, Oct. 2012, doi: 10.1002/fuce.201100185.

[50] G. Botta, M. Romeo, A. Fernandes, S. Trabucchi, and P. V. Aravind, "Dynamic modeling of reversible solid oxide cell stack and control strategy development," *Energy Convers. Manage.*, vol. 185, pp. 636–653, Apr. 2019, doi: 10.1016/j.enconman.2019.01.082.

[51] A. Pohjoranta, M. Halinen, J. Pennanen, and J. Kiviaho, "Model predictive control of the solid oxide fuel cell stack temperature with models based on experimental data," *J. Power Sources*, vol. 277, pp. 239–250, 2015, doi: 10.1016/j.jpowsour.2014.11.126.

[52] F. Mueller, F. Jabbari, R. Gaynor, and J. Brouwer, "Novel solid oxide fuel cell system controller for rapid load following," *J. Power Sources*, vol. 172, no. 1, pp. 308–323, 2007, doi: 10.1016/j.jpowsour.2007.05.092.

[53] N. Chatrattanawet, S. Skogestad, and A. Arpornwichanop, "Control structure design and dynamic modeling for a solid oxide fuel cell with direct internal reforming of methane," *Chem. Eng. Res. Des.*, vol. 98, pp. 202–211, 2015, doi: 10.1016/j.cherd.2015.04.029.

[54] J. Jiang, T. Shen, Z. Deng, X. Fu, J. Li, and X. Li, "High efficiency thermoelectric cooperative control of a stand-alone solid oxide fuel cell system with an air bypass valve," *Energy*, vol. 152, pp. 13–26, Feb. 2018, doi: 10.1016/j.energy.2018.02.100.

[55] J. Larminie and A. L. Dicks, *Fuel Cell Systems Explained*, 2nd ed. Chichester, U.K.: Wiley, 2003.

[56] R. D. Knight, *Physics for Scientists and Engineers: A Strategic Approach with Modern Physics, Global Edition*, 4th ed. Harlow, U.K.: Pearson Education, 2017.

[57] NIST. "NIST Chemistry WebBook, Standard Reference Database Number 69." NIST.gov. https://webbook.nist.gov/chemistry/ (accessed Oct. 20, 2018).

[58] F. Mueller, J. Brouwer, F. Jabbari, and S. Samuelsen, "Dynamic simulation of an integrated solid oxide fuel cell system including current-based fuel flow control," *J. Fuel Cell Sci. Technol.*, vol. 3, no. 2, p. 144, May 2006, doi: 10.1115/1.2174063.

[59] Y. Qi, B. Huang, and J. Luo, "1-D dynamic modeling of SOFC with analytical solution for reacting gas-flow problem," *AIChE J.*, vol. 54, no. 6, pp. 1537–1553, Jun. 2008, doi: 10.1002/aic.11433.

[60] S. Campanari and P. Iora, "Comparison of finite volume SOFC models for the simulation of a planar cell geometry," *Fuel Cells*, vol. 5, no. 1, pp. 34–51, Feb. 2005, doi: 10.1002/fuce.200400057.

[61] B. Huang, Y. Qi, and A. K. M. M. Murshed, *Dynamic Modelling and Predictive Control in Solid Oxide Fuel Cells: First Principle and Data-Based Approaches*, 1st ed. Chichester, U.K.: Wiley, 2012.

[62] M. J. Moran, H. N. Shapiro, D. D. Boettner, and M. B. Bailey, *Principles of Engineering Thermodynamics*, 7th ed. Hoboken, NJ, USA: Wiley, 2012.

[63] J. Yang, X. Li, H.-G. Mou, and L. Jian, "Control-oriented thermal management of solid oxide fuel cells based on a modified Takagi-Sugeno fuzzy model," *J. Power Sources*, vol. 188, no. 2, pp. 475–482, 2009, doi: 10.1016/j.jpowsour.2008.12.012.

[64] F. Petipas, A. Brisse, and C. Bouallou, "Model-based behaviour of a high temperature electrolyser system operated at various loads," *J. Power Sources*, vol. 239, pp. 584–595, Oct. 2013, doi: 10.1016/j.jpowsour.2013.03.027.

[65] B. Shaffer and J. Brouwer, "Dynamic model for understanding spatial temperature and species distributions in internal-reforming solid oxide fuel cells," *J. Fuel Cell Sci. Technol.*, vol. 9, no. 4, p. 041 012, Aug. 2012, doi: 10.1115/1.4006477.

[66] J.-W. Kim, A. V. Virkar, K. Fung, K. Mehta, and S. C. Singhal, "Polarization effects in intermediate temperature, anode-supported solid oxide fuel cells," *J. Electrochem. Soc.*, vol. 146, no. 1, pp. 69–78, Jan. 1999, doi: 10.1149/1.1391566.

[67] E. J. Henley, J. D. Seader, and D. K. Roper, *Separation Process Principles*, 3rd ed. Hoboken, NJ, USA: Wiley, 2011.

[68] R. R. Remick and C. J. Geankoplis, "Binary diffusion of gases in capillaries in the transition region between Knudsen and molecular diffusion," *Ind. Eng. Chem. Fundam.*, vol. 12, no. 2, pp. 214–220, May 1973, doi: 10.1021/i160046a012.

[69] J. G. Calvert, "Glossary of atmospheric chemistry terms (recommendations 1990)," *Pure Appl. Chem.*, vol. 62, no. 11, pp. 2167–2219, Jan. 1990, doi: 10.1351/pac199062112167.

[70] S. Campanari and P. Iora, "Definition and sensitivity analysis of a finite volume SOFC model for a tubular cell geometry," *J. Power Sources*, vol. 132, no. 1-2, pp. 113–126, May 2004, doi: 10.1016/j.jpowsour.2004.01.043.

[71] A. F. Mills, *Mass Transfer*, 1st ed. Upper Saddle River, NJ, USA: Prentice Hall, 2001.

[72] MathWorks. "Choosing the Algorithm." MathWorks.com. https://www.mathworks.com/help/optim/ug/choosing-the-algorithm.html (accessed Nov. 10, 2018).

[73] A. Buttler and H. Spliethoff, "Current status of water electrolysis for energy storage, grid balancing and sector coupling via power-to-gas and power-to-liquids: A review," *Renewable Sustainable Energy Rev.*, vol. 82, pp. 2440–2454, 2018, doi: 10.1016/j.rser.2017.09.003.

[74] J. Udagawa, P. Aguiar, and N. P. Brandon, "Hydrogen production through steam electrolysis: Control strategies for a cathode-supported intermediate temperature solid oxide electrolysis cell," *J. Power Sources*, vol. 180, no. 1, pp. 354–364, 2008, doi: 10.1016/j.jpowsour.2008.01.069.

[75] M. H. Nehrir and W. Caisheng, *Modeling and Control of Fuel Cells: Distributed Generation Applications*. Hoboken, NJ, USA: Wiley-IEEE Press, 2009.

[76] MathWorks. "Fsolve." MathWorks.com. https://www.mathworks.com/help/optim/ug/fsolve.html (accessed Oct. 2, 2019).

[77] ——, "Linearize." MathWorks.com. https://www.mathworks.com/help/slcontrol/ug/linearize.html (accessed Oct. 2, 2019).

[78] H. K. Khalil, *Nonlinear Systems*, 3rd ed. Upper Saddle River, NJ, USA: Prentice Hall, 2002.

[79] G. Marsaglia, "Choosing a point from the surface of a sphere," *Ann. Math. Stat.*, vol. 43, no. 2, pp. 645–646, 1972, doi: 10.1214/aoms/1177692644.

[80] S. Skogestad and I. Postlethwaite, *Multivariable Feedback Control: Analysis & Design*, 2nd ed. Hoboken, NJ, USA: Wiley, 2005.

[81] P. Stoica and R. Moses, *Spectral Analysis of Signals*, 1st ed. Upper Saddle River, NJ, USA: Prentice Hall, 2005.

[82] K. J. Åström and B. Wittenmark, *Adaptive Control*, 2nd ed. Mineola, NY, USA: Dover, 2008.

[83] P. Ioannou and B. Fidan, *Adaptive Control Tutorial*, 1st ed. Philadelphia, PA, USA: SIAM, 2006.

[84] J. S. Shamma and M. Athans, "Gain scheduling: potential hazards and possible remedies," *IEEE Control Syst.*, vol. 12, no. 3, pp. 101–107, Jun. 1992, doi: 10.1109/37.165527.

[85] P. Swarnkar, S. K. Jain, and R. Nema, "Adaptive control schemes for improving the control system dynamics: a review," *IETE Tech. Rev.*, vol. 31, no. 1, pp. 17–33, Jan. 2014, doi: 10.1080/02564602.2014.890838.

[86] MathWorks. "Hinfstruct." MathWorks.com. https://www.mathworks.com/help/robust/ref/hinfstruct.html (accessed Oct. 2, 2019).

[87] C. Stiller, B. Thorud, O. Bolland, R. Kandepu, and L. Imsland, "Control strategy for a solid oxide fuel cell and gas turbine hybrid system," *J. Power Sources*, vol. 158, no. 1, pp. 303–315, Jul. 2006, doi: 10.1016/j.jpowsour.2005.09.010.

[88] thyssenkrupp Materials Services GmbH. "Stainless Steel 441 1.4509." thyssenkrupp-materials.co.uk. https://www.thyssenkrupp-materials.co.uk/stainless-steel-441-14509.html (accessed Jul. 24, 2018).

[89] E. N. Fuller, P. D. Schettler, and J. C. Giddings, "A new method for prediction of binary gas-phase diffusion coefficients," *Ind. Eng. Chem.*, vol. 58, no. 5, pp. 18–27, May 1966, doi: 10.1021/ie50677a007.

[90] A. F. Mills, *Basic Heat and Mass Transfer*, 2nd ed. Essex, U.K.: Pearson Education, 2014.

[91] B. E. Poling, J. M. Prausnitz, and J. P. O'Connel, *The Properties of Gases and Liquids*, 5th ed. New York, NY, USA: McGraw-Hill, 2000.

Glossary

List of acronyms

BOP	balance of plant
BV	Butler-Volmer
CEA	French Alternative Energies and Atomic Energy Commission
DFT	discrete Fourier transform
HEX	heat exchanger
ISE	integral of squared error
IUPAC	International Union of Pure and Applied Chemistry
MAPE	mean absolute percentage error
NRMSE	normalized root mean squared error
OCV	open circuit voltage
PEN	positive electrode, electrolyte, negative electrode
PI	proportional-integral
PID	proportional-integral-derivative
PSD	power spectral density
RES	renewable energy source
RGA	relative gain array
SOEC	solid oxide electrolysis cell
SOFC	solid oxide fuel cell
SORC	solid oxide reversible cell
STP	standard temperature and pressure as defined by IUPAC, 0 °C and 1 bar
TPB	triple phase boundary
U-j	cell voltage-current density

List of symbols

Latin symbols

A	state matrix	
a	activity of chemical species	-
A_s	cell active area	m^2
B	input matrix	
b	height of gas channel	m
B_d	disturbance matrix	
c	concentration	mol/m^3
C	output matrix	
c_p	molar heat capacity at constant pressure	$J/(mol\,K)$
c_p^*	specific heat capacity at constant pressure	$J/(kg\,K)$
c_v	molar heat capacity at constant volume	$J/(mol\,K)$
c_v^*	specific heat capacity at constant volume	$J/(kg\,K)$
D	input feedthrough matrix	
d	disturbance signal	
D_d	disturbance feedthrough matrix	
D_{eff}	effective diffusivity	m^2/s
d_h	hydraulic diameter	m
$D_{H_2-H_2O}$	binary molecular diffusivity for hydrogen - water	m^2/s
D_k	Knudsen diffusivity	m^2/s
$D_{O_2-N_2}$	binary molecular diffusivity for oxygen - nitrogen	m^2/s
E	molar internal energy	J/mol
E^*	specific internal energy	J/kg
e	error signal	
E_{act}	activation energy	J/mol
F	Faraday constant	$96\,485\,s\,A/mol$
f	frequency	Hz
f_1	state equation	
f_{exp}	expected peak frequency	Hz
f_{fit}	fitting function	
f_s	sampling frequency	Hz
G	plant model	
g_1	output equation	
G_d	disturbance model	
H	molar enthalpy	J/mol
H^*	specific enthalpy	J/kg
h	heat transfer coefficient	$W/(m^2\,K)$
i	cell current	A
i	imaginary number	
J	diffusion flux	$mol/(s\,m^2)$
j	current density	A/m^2
j_0	exchange current density	A/m^2
K	controller	

k	thermal conductivity	$\mathrm{W/(m\,K)}$
K_i	integral gain	
K_p	proportional gain	
L	length	m
M	molar mas	kg/mol
m	mass	kg
N	molar flux	$\mathrm{mol/(s\,m^2)}$
n	number of moles	mol
Nu	Nusselt number	-
P	power	W
$\bar{P}$	power density	$\mathrm{W/m^2}$
p	(partial) pressure	Pa
p_{amb}	ambient pressure	Pa
P_{SORC}	SORC power production	W
Q	heat transfer rate	W/s
R	universal gas constant	$8.314\,\mathrm{J/(K\,mol)}$
$\bar{r}$	average pore radius	m
r	reference signal	
R_{H_2}	hydrogen consumption rate	mol/s
R_{H_2O}	steam consumption rate	mol/s
R_{O_2}	oxygen consumption rate	mol/s
r_{ohm}	specific ohmic resistance	$\Omega\,\mathrm{m}$
$\mathcal{S}$	sensitivity function	
$\mathcal{T}$	complementary sensitivity function	
T	temperature	K
t	time	s
u	input signal	
U_0	reversible open circuit voltage at standard cconditions	V
U_{cell}	cell potential	V
U_{Nernst}	Nernst potential	V
V	volume	$\mathrm{m^3}$
w	width of gas channel	m
W_p	performance weighting filter	
W_u	input weighting filter	
x	state vector	
y	output vector	
z	distance	m

Greek symbols

∇	Jacobian matrix	
α_1	activation model parameter	-
α_2	activation model parameter	-
α_3	activation model parameter	-
β	charge transfer coefficient	-
γ	pre-factor for exchange current density	$\mathrm{A/m^2}$

Δ	difference	
δ	thickness	m
Δg_r	Gibbs free energy change of reaction	J/mol
ΔH_f	enthalpy of formation	J/mol
ΔH_r	enthalpy of reaction	J/mol
ϵ	emissivity	-
ε	porosity	-
η_{act}	activation overpotential	V
η_{conc}	concentration overpotential	V
η_{ohm}	ohmic overpotential	V
θ_d	scaling matrix based on maximum expected disturbance change	
θ_e	scaling matrix based on maximum allowed error	
θ_u	scaling matrix based on maximum allowed input change	
κ	electrical or ionic conductivity	$1/(\Omega\,\mathrm{m})$
$\sum \nu$	special atomic diffusion volume	$\mathrm{K}^{2.625}\,\mathrm{mol}^{3/4}\,\mathrm{s}^{9/2}/(\mathrm{kg}^{9/4}\,\mathrm{m}^{3/2})$
ξ	tortuosity	-
ρ	density	$\mathrm{kg/m^3}$
σ	singular value	
σ_{sb}	Stefan-Boltzmann constant	$5.670 \cdot 10^{-8}\,\mathrm{W}/(\mathrm{m}^2\,\mathrm{K}^4)$
ϕ	molar flow rate	mol/s
χ	mole fraction	-
Ψ	exogenous output	
ω	angular frequency	rad/s
ω_B	bandwidth	rad/s

Subscript

0	initial point
air	air channel or air side
el	electrode
$elec$	electrolyte
eq	equilibrium
$fuel$	fuel side or fuel channel
H_2	hydrogen
H_2O	water
in	inlet or inflow
int	interconnect
N_2	nitrogen
O_2	oxygen
out	outlet or outflow
p	perturbed
PEN	PEN structure
r	involved in the electrochemical reaction
TPB	triple phase boundary

Superscript

0	standard conditions
$conv$	convection
rad	radiation
$react$	reaction
ref	reference
$\hat{}$	scaled signal or system (diacritical mark)